On the study of fluid entry by solid objects and bubble column dynamics

by

Mohammadamin Ebrahimi

A thesis submitted to the Faculty of Graduate Studies and Research in partial fulfillment of the requirements for the degree of Doctor of Philosophy in Civil Engineering

Advisor:

Dr. Amir Azimi

Lakehead University

Faculty of Engineering

Department of Civil Engineering

Spring 2026

Author's Declaration Page

I hereby declare that I am the sole author of this thesis document. This is a true copy of this document, including any required revisions as accepted by my supervisor.

Abstract:

This research addresses the fluid-entry behavior of falling rigid bodies—specifically cylindrical disks and spheres—impacting a quiescent ambient fluid. With direct relevance to natural and engineered systems. The study resolves how variations in fluid properties such as fluid density, viscosity, and object geometry such as diameter, thickness, and edge profile, and the solid–fluid density ratio shape the entry process. Such entry processes are including splash/crown formation, cavity growth and pinch-off, added-mass effects, penetration trajectories, and the mixing field that develops behind the body. Framing the analysis with non-dimensional Froude, Reynolds, and Archimedes numbers. The study reveals the dominant scaling laws and furnish predictive correlations for impact-driven flow motion and mixing. Different fluids and mixtures were prepared to study the behavior of falling solid object in accordance with the variations in viscosity and yield stress. Several methods such as image analysis techniques, and flow measurement were implemented using in-house algorithms and MATLAB software codes to extract the required information for solid object movement, deceleration, crown geometries, and pinch-off time. The outcomes indicate that the behavior of the sinking solid object reveals valuable information about the dependence of the criteria that play an important role in the dynamics of the sinking objects. Additionally, the dynamics of rising bubble is investigated. The dynamics and characteristics of bubbles vary due to the properties of both solid objects and the ambient fluid. The influence of flow rates is investigated in a wide range, which could be nominated as a proper representative of many of its applications.

Acknowledgment

Firstly, I would like to sincerely thank my supervisor Dr. Amir Hossein Azimi for his endless guidance, patience, encouragement, and enthusiasm. This work would not have been completed without his support, motivation, and effort. I aspire to your thoughtfulness and admire your dedication, unparalleled work ethic, and passion.

I would like to thank my committee members Dr. Baoqiang Liao, Dr. Ahmed Elshaer, and Dr. Ram Balachandar (external examiner) who kindly agreed to evaluate the quality of my research work and gave me valuable suggestions and advice.

Last but not least, I would like to thank th**ose** who have supported me in any way in this journey, especially my beloved wife and family.

Table of Contents:

List of Tables:

List of Figures:

Chapter 1

Introduction

1.1 Fluid entry of solid objects

Water entry is a fundamental physical phenomenon that has attracted increasing attention in recent years, focusing on the processes that occur when a solid object impacts a water surface and subsequently penetrates the fluid surface. Understanding the dynamics of such event provides valuable insights with broad practical relevance across multiple fields. Among these, marine industries represent the most prominent domain in which solid-object water entry naturally occurs. Beyond marine applications, this phenomenon is also central to a wide range of sectors, including aerospace engineering, civil and coastal engineering, offshore construction, parcel delivery systems, oil and gas operations, and offshore drilling activities, where accurate prediction of impact, penetration, and fluid–structure interaction is essential (Faltinsen et al., 2004; Seddon and Moatamedi, 2006; Kapsenberg, 2011).

With continued technological advancement and increasing human interaction with complex natural environments, new criteria and governing mechanisms must be systematically explored. Many naturally occurring phenomena remain insufficiently understood or have been historically overlooked due to limitations in experimental capabilities or a lack of focused investigation. As measurement techniques and analytical tools continue to evolve, renewed and more detailed research efforts are required to uncover previously unresolved dynamics in this field of research and to refine existing physical understanding. Kim & Park (2019) inquire about the deformation of the water surface when a rounded cylindrical projectile with various aspects ratio enters the water. They investigated the influence of surface condition by conducting experiments on both smooth and rough surfaces, allowing a direct assessment of how surface roughness modifies the impact and subsequent fluid–structure interaction dynamics. The hemispherical object had a diameter of D = 40 mm and different aspect ratios of D/h = 1, 2, 4, and 8. The impact velocities of u_i = 2.5 m/s and 4.2 m/s were simulated to conduct the experiment. The time history

of liquid film height indicated that the film height initially increased, reached the peak, and decreased afterward. Moreover, decreasing the aspect ratio shortened the downward motion, while the reduction in liquid film thickness became more abrupt for objects with smaller aspect ratios.

Most of existing research studies has been focused on the entry of solid objects into water, as such phenomenon most commonly occurs in aquatic environments, with oceans and seas covering a large portion of the Earth's surface. However, given the broad range of applications involving fluids other than water, there is a clear need to investigate how fluid properties influence the entry dynamics of solid objects. Such conditions arise in environments including swamps, sewage systems, and the oil and gas industry where the surrounding media is differ markedly from water due to variations of fluid's density and its rheology (i.e., viscosity and yield stress) (Akbarzadeh et al., 2022; Akers and Belmonte, 2006; Ebrahimi and Sanati, 2021).

Several studies have probed the role of fluid properties in the water-entry of solid objects, yet the problem remains far from resolved. The challenge stems from the high dimensionality of the parameter space and the fact that key variables such as density, viscosity, surface tension, and geometric features do not act independently but interact in coupled, often nonlinear ways. These interdependencies obscure causal attribution and limit generalizability, leaving a significant gap that calls for coordinated, multivariate experiments and simulations, guided by dimensionless analysis and rigorous sensitivity assessment, to isolate controlling mechanisms. All in all, it could be deduced that a large number of experimental and numerical studies demand obtaining an accurate and acceptable overview of fluid entry of solid objects.

Akbarzadeh et al., (2022) performed research to investigate how the difference in the fluid properties affects the fluid entry characteristics of solid spheres. They conducted their study in two different Newtonian and non-Newtonian (i.e., Boger) fluids. The surface tension, density, and viscosity maintained the same for both fluids and the only variables were the properties of Newtonian and Boger fluids. Fluid mixtures were formulated to have matched density (ρ) and surface tension (σ) and a common dynamic viscosity of μ = 120 mPa·s. Release heights were chosen to span Froude numbers *Fr* ranging between 1.2 and 20. For the same Froude number, the body descended more slowly in the Boger fluid than in the Newtonian counterpart. The characteristic pinch-off time and length were measured for both fluids; in every case, occurred earlier in the Boger fluid, and exhibited the same decreasing trend relative to the Newtonian fluid.

Akers and Belmonte (2006) investigated the water-entry of solid spheres into viscoelastic wormlike micellar solutions composed of cetylpyridinium chloride (CPCl) and sodium salicylate (NaSal). To probe viscoelastic effects, they varied release height, sphere size, and the solid–fluid density ratio while holding the ambient viscosity fixed at μ = 430 mPa·s. Glass and steel spheres—spanning densities ρ_s = 1350-7970 kg.m^{-3} were released from heights h_r = 250-450 mm above the free surface. Across this parameter space, the penetration depth increased monotonically with the impact Froude number, indicating stronger inertial dominance at higher releases and/or larger characteristic lengths.

Tabuteau et al. (2011) investigated the falling of spherical projectiles into the yield-stress fluid which drastically changed the cavity pinch-off depth. The recent studies explored more complicated scenarios. They examined solid–fluid interactions for spheres impacting a non-Newtonian ambient prepared from Carbopol gels of varying concentration to adjust viscosity and yield stress. Sphere diameters spanned D = 0.0127-0.0254 m, with densities ρ_s = 1340-14970 kg.m^{-3}. Lower impact velocities reduced air entrainment around the body and, consequently, decreased the pinch-off depth. A threshold Reynolds number of $Re \approx 20$ was identified: for $Re < 20$, the crater diameter remained essentially constant, whereas for $Re \geq 20$ it increased approximately exponentially. Sun, et al. (2019) investigated a two-layer fluid system in a case a viscous fluid floats on top of water due to density difference. The difference in fluid also affects the phenomenon of entering a solid object into a fluid. Due to the above research, it is totally understandable that the fluid plays a very important role (de Goede et al. 2019). Thenceforth, from now on instead of using “water entry”, “fluid entry” is going to be applied.

Solid object entry can be affected by variations of many parameters such as density, shape, geometry, and surface treatment (i.e., hydrophilic versus hydrophobic). One of the most important factors that drastically affect the entry of fluid objects is the geometry of solid objects. Three common solid object geometries of sphere, disk, and projectile have been utilized in most research studies. The behavior of entering the solid objects for each of these objects is different. Each of these objects was explored in case of changing some of their aspects such as density, the height of releasing the objects, releasing, or throwing with a specific initial velocity, entering the water vertically or with an angle. Chaudhry et al. (2022) presented some recent improvements in the water entry of projectiles. Shi et al. (2019) studied the water entry of projectiles and they tried to

perform comprehensive research in which the shape of the nose, impact velocity, and angle have been investigated. They proved that all three investigated factors have some influence on the water entry characteristics such as cavity and pinch-off length. Du et al. (2022) illustrated that the geometrical shape of the object affects the cavity shape and size.

Despite decades of work on water entry of rigid bodies, key features remain unresolved because the phenomenon inertia, viscosity, surface tension, and geometry across a high-dimensional parameter space. The present thesis targets several specific knowledge gaps in this field of research. First, we isolate the effect of the solid–fluid density ratio on entry dynamics—splash formation, cavity growth and pinch-off, penetration depth, and post-impact mixing—using a consistent nondimensional framework. Second, the geometric control was assessed by testing annular disks with systematically varied hole ratios (d_h/D), relating porosity/solidity to canonical water-entry responses. By mapping these dependencies, we aim to produce transferable scaling laws and predictive correlations that can be relied upon for design and interpretation.

Most of previous research studies have focus on the entry of projectiles and spherical objects, however, the entry of disks received less attention. One of the features that are worth devoting time and energy to get deep into that is the annular forms of the disks, spheres, and projectiles. Zhou et al. (2021) perform a study on an eccentric disk falling. The trajectory of the falling disks in the water was recorded during the descend of thin eccentric annular disks. They proved that eccentricity highly affects the falling trajectory and modes. Bi et al. (2021) performed research on the flow structure of falling annular disks. The motion of the annular disks was monitored and the correlations between initial geometry and fluid parameters with the trajectory of the object were extracted.

Hou and his colleagues performed studies to examine the dynamics of water entry of the hollow cylinder both numerically and experimentally. They reveal the characteristics such as through-hole jets and secondary jets (Hou et al., 2022, 2019). Hou et al., (2021) tried to determine the patterns of the closure of the cavity that produce in the reaction of the entering a solid object into a water. They applied hollow cylinders; however, the concentration is on the different water entry velocities. Their study reveals the impact of water entry velocity of hollow cylinders. Jafari & Akbarzadeh (2022) designed an experiment to assess the impacts of hole geometry of hollow cylinders. Other parameters such as mass, outer diameter cones, etc were kept constant in order

eliminate the influence of other parameters on the results and the only undergoing variables that are studied is hole geometry. Janati & Azimi (2023) inspected the cavity dynamics and crown formation of relatively thick disks. Both solid and annular disks with different cavity diameters were tested. The difference between the annular disks and the impacts of the hole were assessed as well.

In this thesis, a comprehensive study was conducted in order to investigate the characteristics related to the fluid entry of solid objects. The entry of both solid and annular disks were examined when they are freely falling into a stagnant fluid. The behavior of the annular disks with a hole in the middle of solid disks was assessed to investigate the impacts of hole size and three different hole sizes were chosen. In addition, the effects of fluid viscosity on the entry of solid and annular disks were explored as well. Three disks with different densities were chosen to further study the effect of solid object density on cavity formation, pinch-off, and energy transfer from the disks to the ambient water. In the following, at first, all the performed experiments are explained. Thereafter the characteristic of the prepared fluid is enucleated. In the results section, the results and the figures are represented.

1.2 Bubble plume dynamics

The abundance of bubble plume applications in nature and industry is undeniable, therefore, conducting research studies to investigate the behavior of bubble plume and the controlling factors that affect this phenomenon requires crucial attention. This topic could be counted as one of the most applicable topics, which is very important due to its practical applications both in nature and industries. This topic is very wide and categorized into several subjects to make it plausible to study. Multiphase flow is one of its most common subjects that covers liquid-liquid, solid-liquid, gas-liquid, and other types of interactions.

Bubble plume is nominated to have a wide variety of applications in civil, mechanical, chemical, environmental, wastewater treatment, gas mixing and resolution, biochemical reactions, etc. Moreover, bubble plumes have been utilized to enhance dissolved oxygen and to improve water quality, impede the channel and other facilities from freezing, decrease wave damage, etc. According to recent explorations, bubble plumes are also applicable in alleviating the pollution

that oil and gas exploitation could cause under the sea. Due to the mentioned applications and other listed in the study bu Abdulmouti (2022) the prominence of the bubble plume cannot be overlooked.

Bubble columns are a common system in a lot of industries, especially in chemical and biochemical reactors. In these industries, a bubble column is exerted due to its very well-known advantages. Preparation of a bubble column setup is certainly easy and affordable compared to all other methodologies. Contrary to its simplicity, it has been proven to be very practical, which is why it is the most applicable system that has been used in related industries. There are differences between some of the factors that are controllable in these reactors such as injection condition, column dimensions, injection rate, injection pressure, number of nozzles and placement of spargers, fluid properties, etc. These noted elements have the capability to control the efficiency of transfer of oxygen, mixing ability, and other desired features that are the priority to the demanded usage.

One of the uses of bubble reactors is in petrochemistry in which the bubble column is exerted to provoke the formation of the oil through the shales, oxidation of hydrocarbons, cultivation of algae, and cosmetic production are other applications of bubble columns. The noted application requires homogenous aeration whereas some other applications may operate in non-uniform bubble structure. For instance, in wastewater treatment, ice prevention, mechanization reactors, and sedimentation of particles, mass transfer is the prior goal. In some cases, some criteria such as flow rates, bubble geometry, sparger distance, and number of spargers are important. In some other applications, such as fermentation, viscosity, surface tension and other fluid properties are the key parameters.

One of the most crucial applications of bubble dynamics is in water and wastewater treatment facilities. There are many studies that have concentrated on developing methods for the blackening and odorization of rivers such as chemical oxidation, water cycle, microbial technology, chemical precipitation, artificial aeration, etc. Among all of them, artificial aeration has been represented as a very practical methodology due to its potential for high oxygen transfer, long retention time, high surface area, etc. The crucial treatment for black-odorous water is aeration (Cao et al., 2020). Therefore, improvement in aeration is one of the most important

beneficial treatments for not only the black-odorous pollution but also for the other pollutions of the other water bodies.

One of the methods that are provided for water and wastewater treatment is the application of the bubble which in most cases plays an important role in the removal of water pollutants. The aeration process can be carried out by two methods; the first method is called traditional artificial aeration and the second method uses micro and nanobubbles. A traditional method of aeration is achieved by air blower, mechanical stirring, turbulent jet and mixing. The drawback in traditional aeration is low efficiency in oxygen transfer and oxygen retention. Therefore, it requires relatively large facilities and equipment which demand high energy and cost of operation (Cao et al., 2020; Chen et al., 2022; Shi et al., 2022). Based on a research study by Zhang et al. (2022), dissolved oxygen demand was utilized as an appropriate representative of pollutants in water. Yin et al. (2019) also represented that artificial aeration has an effective impact. It should be mentioned that the other methodology, rather than the new micro and nanobubble technology, could produce some secondary pollutants and some of them require extra chemical agents.

Recently, Behzadipour et al. (2022a, 2023a) studied the impacts of a grid screen structure on variations of bubble characteristics and the effect of air discharge on bubble dynamics. As bubble dynamics and mixing is a very wide and complicated topic of research and many factors affect the phenomena, more research studies should be carried out. Most research studies in this field focused on the effects of air discharge, nozzle size, and nozzle arrangement (Behzadipour et al., 2023b, 2022b; Simiano et al., 2006; Wang and Socolofsky, 2019, 2015; Xu et al. (2017);Wu et al., 2021). Integral models have been proven to be successful and more practical by applying some methods to solve the mass, momentum and buoyancy equations (Dissanayake et al., 2018; Poojitha Yapa et al., 1999; Socolofsky et al., 2008). Notwithstanding the usage of integral models, it should be noted that there are some drawbacks that hold this method from being the universal method to solve such models. Transition regimes are the main problem of such methodology which causes the disconnect between bubble plume and turbulence (Jirka, 2004).

As noted previously, bubble size is one of the factors that has a great impact on bubble plume characterization. It should be noted a few studies have been conducted on the impacts of bubble size in the water plume. Fraga and Stoesser, (2016) focused on the effect of bubble size by applying Large Eddy Simulation (LES) numerical method. The defect of this study is that the

bubble size has not been studied directly. Accordingly, (Li et al., 2020) by using the numerical method and experimentally investigate the impacts of the bubble size in the bubble plume. The following studies have been conducted in order to discover the impacts of nozzle size, and the relationship of the centerline velocity with the distance from the nozzle which is a nonlinear correlation (Behzadipour et al., 2022b; Bohne et al., 2020; Bombardelli et al., 2007; Lai and Socolofsky, 2019; Lima and Lima Neto, 2018; Lima Neto et al.,2008; Ruzicka et al. (2008); Cachaza et al. (2011)).

Milgram, (1983) carried out several experiments to test the different air discharges to discover the variation of the centerline velocity of the bubbles in which it has been revealed that the centerline bubble velocity experienced a reduction of about 45 % at the distance of 1.5 m above the release point. In another study, it has been shown that there is a correlation between flow rates and bubble size. Bubble size distribution is more uniform in higher airflow (Bohne et al., 2020; Ziegenhein and Lucas, 2017).

So far, most of the research and studies conducted for the atmosphere where the water is the fluid and the bubble, could be air or other gas, release in that. However, as far as it is understood, the application of bubble plumes contains a wide variety of industries in which water is not the sole fluid that the bubble should be released in. On the other hand, different types of fluid with varying properties are used. Consequently, it has been found that the domain of studies must widen to be able to cover all aspects. In some studies that are not sufficient absolutely, some of the researchers have shown some passion for investigating the behavior of bubble columns in other fluids rather than water.

Ruzicka et al. (2003) investigated the effects of viscosity on bubble dynamics in bubble columns. The gas hold-up and the transition flow regime were studied and the results showed that low viscosity supported the stability of bubbles. On the contrary, fluid with a viscosity range between 5 and 20 mPa.s could ease the transition of the flow regime by destabilizing the homogeneous regime. Additionally, they proved that increasing the gas inlet flow rate leads the gas hold up to increments as well.

Besagni and Inzoli (2017) performed a study to probe the impacts of fluid phase characteristics on bubble dynamics in bubble column. The parameters that were studied were flow regime, bubble size distribution and shapes, and gas holdup. Different fluids of tap water, water

with NaCl, water-mono ethylene glycol, and water-ethanol were tested. The results indicate that increasing the gas velocity leads the gas hold up to rise as well.

Laupsien et al. (2022, 2017) assessed the effects of fluid's viscosity ranged between 1 and 100 mPa.s on variations of bubble size. Accordingly, two different spargers were exerted to generate two types of bubbles that were ellipsoidal and spherical cap bubbles. They discovered that the bubble plume dynamics rely on the fluid viscosity significantly. In high viscosity range, the oscillation of bubble plume was suppressed easily and at a high pace in both the plume expansion and period. Additionally, the effect of sparger on bubble dynamics significantly decreased in high viscose fluids. Glycerine-water solutions were used by Lee et al. (2021) to provide a media to examine the impacts of the liquid viscosity on the bubble column. Two main variables that have been inquired were liquid viscosity and inlet flow rate which were in the range of around 5 to 800 cP and 300 to 1500 cc/min, respectively. They have concluded that while the viscosity of the fluid mixture increased, the bound expansion stage acceleration expansion stage incremented as well. Bubble rising velocity decreased when the viscosity of the fluid experienced an increasing trend.

This thesis is organized as a paper-based dissertation consisting of five interconnected research studies. The overall theme of the thesis is the experimental investigation of multiphase fluid–structure interactions in Newtonian and non-Newtonian ambient fluids, with emphasis on the role of solid-body geometry, fluid rheology, impact conditions, energy transfer, cavity dynamics, and gas–liquid interaction. Although each chapter addresses a specific research question, the chapters are connected through a progressive development of the same physical framework: how an object or gas phase interacts with a complex ambient fluid and how this interaction controls free-surface deformation, cavity formation, energy dissipation, sinking/rising motion, and bubble evolution.

Chapter 2 establishes the foundation of the thesis by investigating the entry of cylindrical solid disks into water and non-Newtonian fluid mixtures. This chapter examines how disk density, disk aspect ratio, and ambient rheology affect crown formation, splash evolution, pinch-off characteristics, sinking time, and energy losses. The results of this chapter define the baseline fluid-entry problem and identify the main controlling parameters governing the interaction between falling cylindrical objects and complex fluids. In this stage, the focus is placed on solid disks without central openings, providing a reference for later chapters where additional geometric and

dynamic complexities are introduced. This chapter is particularly important because previous studies were mainly focused on spheres, projectiles, or disks in water, while fewer studies considered cylindrical disks entering non-Newtonian fluids with controlled rheological properties.

Chapter 3 extends the baseline problem by introducing annular disks with central openings. In this chapter, the role of disk geometry is further examined by studying how opening diameter, relative disk density, and non-Newtonian rheology affect cavity development, crown formation, through-hole jet formation, pinch-off depth, pinch-off time, and sinking velocity. This chapter builds directly on Chapter 2 by moving from solid disks to annular disks and showing that the central opening modifies the pressure distribution, fluid passage through the disk, and the overall energy transfer between the disk and the surrounding fluid. Therefore, it provides a deeper understanding of how internal geometric modification changes the fluid-entry process.

Chapter 4 then shifts the focus from describing the visible dynamics of disk entry to quantifying the mechanical energy transfer during the process. Using the solid and annular disk cases developed in the previous chapters, this chapter evaluates the energy losses at three key stages: immersion/collision, pinch-off, and sinking. This stage-based energy analysis provides a mechanistic explanation for the observed differences in crown formation, cavity development, and disk motion. In particular, it clarifies how disk density, central opening, and ambient viscosity redistribute the initial potential and kinetic energy into splash formation, cavity growth, viscous dissipation, wake formation, and sinking motion. Therefore, Chapter 4 connects the kinematic observations of Chapters 2 and 3 to the underlying energy-transfer mechanisms.

Chapter 5 further develops the disk-entry framework by examining the effect of impact orientation. While the previous chapters focus mainly on face-on entry, Chapter 5 investigates edge-on disk entry and compares it with the corresponding face-on cases. This chapter addresses how the projected collision area and impact geometry influence splash asymmetry, cavity development, pinch-off behavior, sinking velocity, and energy loss. In this way, Chapter 5 completes the solid-entry part of the thesis by showing that not only the disk geometry and ambient rheology, but also the release orientation and impact surface area, strongly control the fluid-entry response. This chapter also links back to Chapters 2–4 by using the earlier face-on studies as the reference cases for interpreting the edge-on results.

Chapter 6 extends the thesis from solid-object entry to bubble plume dynamics in non-Newtonian ambient fluids. Although this chapter appears different from the previous disk-entry chapters, it is connected to the same broader multiphase-flow theme. During solid entry, cavity formation, air entrainment, pinch-off, and bubble formation are important features of the fluid–structure interaction. Chapter 6 isolates the gas–liquid interaction aspect by directly studying bubble generation, bubble morphology, rising velocity, and coalescence in shear-thinning non-Newtonian fluids. The controlling parameters in this chapter, including ambient rheology, air discharge, and nozzle diameter, are analogous to the controlling parameters in the solid-entry chapters, where geometry, density, and fluid viscosity govern the motion and energy exchange. Therefore, Chapter 6 expands the thesis from the motion of solid bodies into complex fluids to the motion and evolution of gas bubbles within similar non-Newtonian environments.

Overall, the thesis progresses from simple to more complex multiphase interactions. Chapter 2 introduces solid disk entry into non-Newtonian fluids, Chapter 3 adds annular geometry and through-hole flow, Chapter 4 explains the observed behavior through stage-specific energy losses, Chapter 5 introduces the influence of impact orientation and collision geometry, and Chapter 6 extends the investigation to bubble plume dynamics. Together, these chapters provide a unified experimental framework for understanding how geometry, rheology, and phase interaction control the dynamics of objects and bubbles moving through Newtonian and non-Newtonian fluids.

Chapter 2

On the entry of cylindrical disks in non-Newtonian fluid mixtures

2.1 Introduction

Water entry of a solid object is a complex fluid dynamics phenomenon, which has many applications in aerospace, military, marine science, engineering, and the environment. Many experimental studies have been conducted in the past to investigate different aspects of water entry such as reduction of energy, trajectory prediction, momentum transfer, splash curtain, and crown formation. Some important parameters in the water entry of solid objects are the cavity dimensions, which are characterized by the pinch-off depth and time, crown evolution and its dimensions, and formation of the Worthington jet (Worthington, 1908; Faltinsen et al., 2004; Seddon and Moatamedi, 2006; Aristoff and Bush, 2009; Truscott and Techet, 2009; Gekle and Gordillo, 2009, 2010; Kapsenberg, 2011; Chrust et al., 2013; Eshraghi et al., 2020; Shokri and Akbarzadeh, 2022; Wang et al., 2022; Janati and Azimi, (2022). Such dynamic characteristics have been studied in the past and useful correlations have been developed to better understand the solid-fluid interaction phenomena such as cavity dynamics and crown formation with the related solid objects and ambient fluid parameters. In recent years, more complex configurations of solid entry have been studied such as the water entry of solid spheres in a tandem configuration and the side-by-side release of solid objects in water (Sooraj et al., 2019; Yun et al., 2020; Wang and Lyu, 2021; Lyu et al., 2022, 2021a, 2021b; Du et al., 2022; and Jafari and Akbarzadeh, 2022).

Most research studies in the past have focused on the free-falling release of solid objects (i.e., spheres, projectiles, and disks) in water and less attention has been paid to include the effects of energy transfer in the water entry of solid objects.

A paper based on the content of this chapter is published in the Physics of Fluids: Ebrahimi, M., Azimi, A.H., 2024. On the entry of cylindrical disks into non-Newtonian fluid mixtures. Physics of Fluids 36

Aristoff and Bush (2009) investigated the water entry of hydrophobic spheres with a diameter ranging from 1.2 mm to 1.8 mm and a density of 7700 kg/m^3. They studied the pinch-off behavior and proposed a regime plot that classifies pinch-off as a function of Weber number (i.e., $We = \rho_d U^2 R/\sigma$), where ρ_d is the density of disk, U is the velocity of disk, R is the radius of disk, and σ is the surface tension at the interface. Four regimes of quasi-static, shallow seal, deep seal, and surface seal were introduced for regime classification. It was found that the Weber number, which is highly correlated with the disk density and velocity, results in the traveling of pinch-off depth from the quasi-static regime towards the shallow seal and continuing to approach the deep seal regime. Truscott and Techet (2009) investigated the water entry and hydrodynamics of a spinning sphere. Spherical objects were half-hydrophilic and half-hydrophobic and the cavity formation by such spheres was studied. Their results indicated that the hydrophobic surface formed a deeper cavity and higher crown in comparison to the hydrophilic surface treatment. Mansoor et al. (2014) performed a series of experiments to investigate cavity formation by super-hydrophobic spheres entering the ambient water. The diameter of spheres ranged from 15 mm to 25 mm and the impact velocity of spheres varied between 1.5 m/s and 8.5 m/s. Such variations of impact velocities are translated to relatively wide range of Froude numbers (i.e., $18 < Fr < 960$). It was found that the ratio of pinch-off depth to disk diameter at the time of pinch-off is equal to 0.5, which was in agreement with the observations of Duclaux et al. (2007). They reported a value of 0.45 for spheres with diameters ranging between 12 mm and 40 mm, and Froude number ranging from $Fr = 10$ to 330.

Besides spherical geometry, projectile geometry has been recently tested by many researchers (Truscott et al., 2014; Song et al., 2020). Other than spheres and projectiles, several studies have focused on the water entry and hydrodynamics of disks with different aspect ratios, D/H, where H is the disk thickness and D is the disk diameter(Auguste et al., 2013; Lee et al., 2013; Zhong et al., 2013; Vincent et al., 2016; Bi et al., 2018; Xu et al., 2021; Janati and Azimi, 2022). Zhong et al. (2013) studied the entry of thin disks with a relatively wide range of aspect ratios of $H/D = 0.0125$, 0.025, 0.05, 0.1, and tested the effects of release angle to observe the motion and trajectory of thin disks in water. The initial Reynolds number ($Re = \rho_d UD/\mu$) of the disks varied with a relatively wide range from $Re = 500$ to 5500, while the density ratio of disks was fixed at $\rho_d/\rho_w = 1.2$, ρ_w is the density of water. It was found that the aspect ratio of disks plays a key role in the motion and trajectory of thin disks in water. Willmarth et al., (1964) studied the

impacts of disk density and aspect ratio on the motion of a free-falling disk in water. Such motion was represented by variations of two dimensionless parameters, Re and I^*, where $I^* = (\pi\rho_d U)/(64\rho_w D)$. The relationship between dimensionless parameters defined the boundaries of different motion regimes initially named as tumbling, stable, and pitching. Figure 1 shows Willmarth's regime plot and the boundaries of the present study in relationship with other studies in the literature. In this regime map, four domains of steady, tumbling, chaotic, and fluttering are labeled. As can be seen in Figure 2.1, the present study is located in the chaotic region, and it moves toward the steady regime as the mixture's viscosity increases due to increasing polymer concentration.

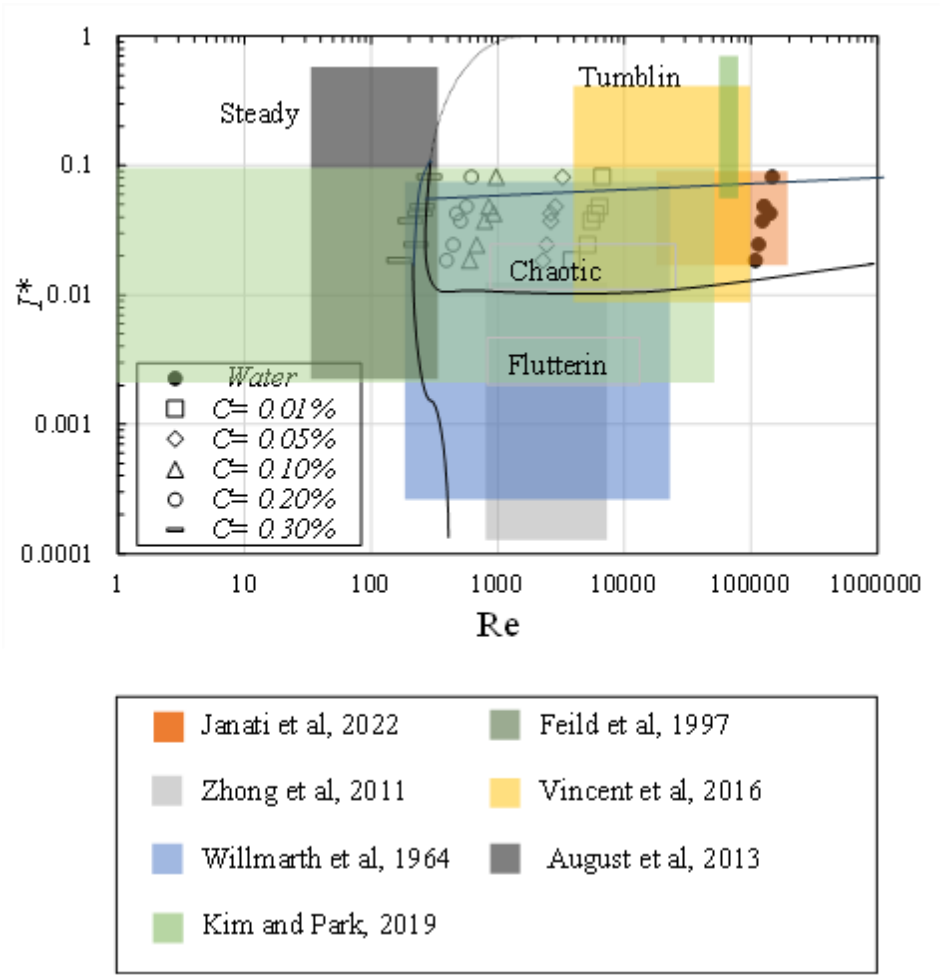

Figure 2.1: A regime plot indicating the correlation between I^* and disk Reynolds number, Re, in the present study and other studies in the literature.

Glasheen and McMahon, (1996) have characterized the water entry of disks with three dimensionless numbers of: 1) the virtual mass ($M = m(\Delta u/u)/(4/3)\pi\rho_w r^3$) where m is the mass of disk, u is the velocity, ρ_w is the density of water, 2) the dimensionless force ($C_D^* = F_d(t)/[\rho_w Sgh(t)+0.5\rho_w Su^2]$), where $S = \pi r^2$, $F_D(t)$ is time-variant force, which is recorded by the force transducer, and 3) dimensionless time, $\tau = T_s(g/r)^{1/2}$, where T_s is the period between the impact and cavity closure. It was reported that the correlation between the mentioned dimensionless parameters is valid when disks enter the water at a relatively low-speed equivalent to *Fr* between 1 and 80. The study on the motion and trajectory of falling disks indicated that disks tend to undergo a helical motion and the horizontal drift pattern is associated with the length and aspect ratio of the disks (Kim et al., 2018).

Most research studies in the past have focused on the entry of solid objects into water, and less attempts have been made to study the entry of solid objects in viscoelastic fluids or non-Newtonian mixtures. Some research studies investigated the motion of particles in viscoelastic fluids such as drilling fluids, production fluids, and swamps (Arigo and McKinley, 1997; McKinley, 2002; Gupta et al., 2005; Akbarzadeh et al., 2022). Akbarzadeh et al. (2022)studied the entry of solid spheres in both Newtonian and non-Newtonian fluids. They used a mixture of glycerin and water to form highly viscous Newtonian fluid mixtures with different viscosities and added Polyacrylamide (PAA) to form non-Newtonian Boger fluid mixtures. The fluid properties such as density and viscosity were kept approximately constant for both Newtonian and non-Newtoniam (i.e., Boger) fluid mixtures in a range between 1206 and 1242 kg/m^3, and 120 mPa.s. Five different release heights ranging from 0.05 m to 1 m were chosen to form various impact velocities ranging between 0.31 m/s and 4.4 m/s. It was observed that the Worthington jet does not form in Boger fluids and spheres descended at a slower rate in Boger fluid in comparison with spheres descending in Newtonian fluid despite having the same density and viscosity. More air volume was also drawn from the interaction of sphere with Boger fluid than that of Newtonian fluid. It was found that the values of pinch-off depths in Boger fluids were smaller than those of Newtonian fluid mixtures.

Akers and Belmonte, (2006) conducted a series of experimental studies on the entry of solid spheres into a viscoelastic wormlike micellar fluid that was formed by using Cetylpyridinium Chloride and Sodium Salicylate (i.e., NaSal) with a viscosity of 430 mPa.s. The density of the

tested spheres ranged between 1400 kg/m^3 and 8000 kg/m^3. The effects of impact energy were studied by selecting a wide range of release heights from 0.01 m to 1.30 m. Different features have been spotted in the solid entry of Newtonian and non-Newtonian fluids. For instance, smooth pinch-offs were formed in Newtonian fluids, which is highly dependent on the sphere's velocity, whereas a transition between smooth to rough surface texture was observed on entry to viscoelastic fluids. The formation of Worthington jet and splash patterns by the entry of spheres into viscoelastic fluids were studied in the literature (Cheny and Walters, 1999, 1996; Nigen and Walters, 2001). Tabuteau et al., (2011) stated that the entry of spherical objects into a viscoelastic fluid is different from the entry of the same object into water. The pinch-off depth and the height of the jet were significantly altered by spheres that entered into a Carbopol mixture with a wide range of concentrations ranged between 0.3 wt.% and 2.2 wt.% and with a release height ranging from 0.002 m to 1.8 m. At a high Reynolds number (i.e., $Re \geq 20$), the cavity size decreased in comparison to tests with low Re (i.e., $Re < 20$) due to significant viscous effects. It was also found that the height of the jet increased with increasing the release height of the solid object.

De Goede et al. (2019) investigated the velocity decay of a high-speed spherical object entering into a shear-thickening fluid. Two fluid mixtures of water-cornstarch and polyvinyl alcohol borax solution were used, which both behave as shear-thickening fluid. The results denoted that the penetration depth is highly dependent on the fluid properties, and the penetration depth in the cornstarch-water mixture was found to be lower than that of the polyvinyl alcohol borax solution and water. Sun et al. (2019) studied the fluid entry of a sphere into a two-layer fluid. The system included water and a thin layer of dimethicone, which rested at the water surface. The viscosity and surface tension of the dimethicone were 10 mPa.s and 19.4 mN/m, respectively. The formation of crown changed by the presence of the second fluid and some specific shapes such as flowerpot-shape, and diamond-shape were formed on the crown when the dimethicone was placed on the water surface. In addition, the cavity wall for the water-dimethicone interface showed some waves, while the cavity at the water layer was smooth.

The present study aims at understanding the effects of density and aspect ratio of cylindrical objects on the interface motion and fluid dynamics as they enter water and non-Newtonian fluid mixtures. To investigate the effects of ambient fluid properties, five fluid mixtures with different viscosities and yield stresses were prepared by using a water-soluble polymer with different weight

concentrations of the selected polymer. The solid entry of cylindrical objects with different densities and aspect ratios in water were also tested to use as benchmark experiments. Due to the change in the media from water to other fluid mixtures with different properties, a phrase substitution is made from "water entry" to "fluid entry". In this study, a very wide range of fluid viscosities are examined in addition to the density and aspect ratio of cylinders. The impacts of fluid viscosity and the transition from Newtonian to non-Newtonian fluid domain on cavity size and splash evolution are studied.

2.2 **Materials and Methods**

2.2.1 Experimental Setup

A series of laboratory experiments was conducted in the Multiphase Flow Research Laboratory (MFRL) at Lakehead University, Canada. A glass-walled tank with dimensions of 400 mm × 400 mm and a depth of 1000 mm was used to perform the experiments. The tank was filled up to the height of 700 mm, and the 300 mm height above the fluid surface was left to observe the crown formation after the object entry. The fluid in the tank was maintained at a constant level to ensure the repeatability of experiments. In this study, six different disks with different densities and disk aspect ratios were tested. The disks were categorized into two aspect ratios of 1.5 (i.e., thick disk) and 3 (i.e., thin disk), and in each group, three disks with different densities were tested. All disks had the same diameter of D = 75 mm, and the thicknesses of the thick and thin disks, H, were 50 mm and 25 mm, respectively. The disks were homogeneous and made of compressed rubber with densities of ρ_d = 1140, 1480, and 2500 kg/m^3. The flat solid disks had a rounded rim, and the side edge had some roughness with a roughness height of 1 ± 0.1 mm.

All disks were released through a 300 mm long lubricated pipe to minimize solid-air interaction, and the short pipe was installed 200 mm above the fluid surface giving a total release height of 500 mm. Such release condition ensures the stability of the released disk to form a symmetrical crown and cavity. The short pipe was located exactly at the center of the tank to minimize the wall effect. To ensure the repeatability of experiments, each test was repeated three times, and the average value of results such as crown and cavity dimensions, pinch-off time, and depth were recorded. The minimum and maximum values in some experiments were shown as overbars to show the experimental uncertainties. Six light sources (Woods 166 L13, 1,000-W

telescope work light, CA) were used to generate sufficient and uniform brightness all over the tank and to capture high-quality images. Two high-speed cameras (Phantom, Miro Lab 110, New Jersey, Wayne, USA) were utilized to capture high quality time-series images. The first camera was pointed perpendicular to the intersection of the fluid surface and the air, and the second camera was located below the first camera, pointed just below the fluid surface, to capture the formed cavities. The high-speed cameras captured images with a frequency of 1000 fps and a resolution of 1280 × 800 pixels (Phantom, Miro Lab 110, New Jersey, Wayne, USA) using a proper camera lens (AF Nikkor 50 mm, f/1.4D, Nikon, Tokyo, Japan). A proper relaxation time of at least 15 minutes between each experiment was given to eliminate the fluid fluctuations and to stabilize the fluid surface. Figure 2 shows the experimental setup and the disk's geometries that were utilized in this study.

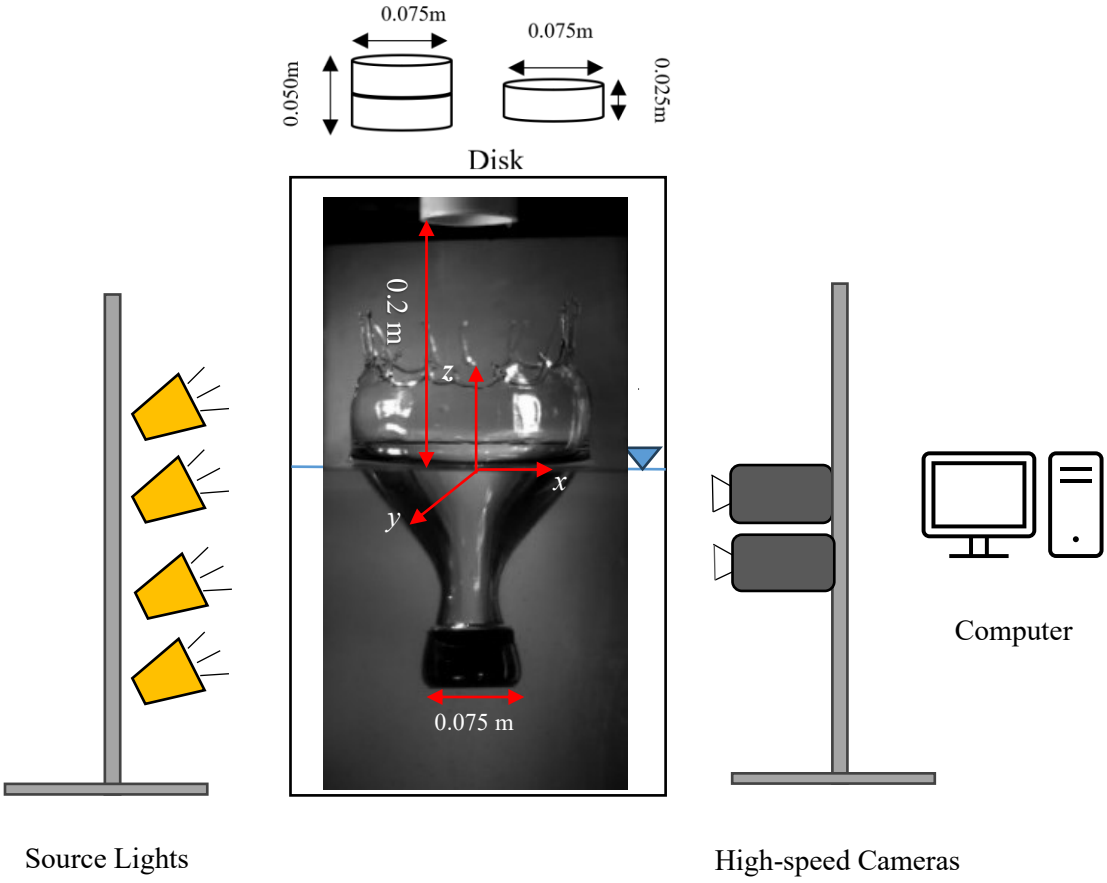

Figure 2.2: Experimental setup and disk geometry in free falling of a cylindrical disk in stagnant ambient.

2.2.2 Fluid Properties and Preparation

To investigate the effects of fluid viscosity on the fluid entry and characteristics of free-falling disks such as crown and cavity formation, six different fluid mixtures were prepared to assess a wide range of mixture's viscosity. The condition that restricted the window of choice for additives was the transparency of the final mixture. Due to the method of investigation and the use of flow visualization, a substance should be used to provide the desired viscosity and it should be transparent. To prepare the fluid mixtures with different viscosities, a mixture of Polyacrylamide (PAM) with water was chosen. Different volumetric concentrations of PAM polymer provide a reliable range of viscosities and such a mixture has been employed in other studies in the literature

(Bleier, 1990; Ebrahimi et al., 2020; Ebrahimi and Sanati, 2021 Gao, 2013; Pei et al., 2016). The Polyacrylamide (PAM) mixture that was applied in this study was supplied by the SNF Corporation, France, and its commercial name is FLOPAM AN 934 VHM.

The lowest mixture viscosity was 24 mPa.s for 0.01 wt.% concentration of PAM and the highest viscosity of the mixture was 580 mPa.s formed by adding 0.3 wt.% concentration of PAM. Three other fluid mixtures were prepared with a polymer weight concentration of 0.05 wt.%, 0.1 wt.%, and 0.2 wt.%. The pure water with zero concentration of PAM was also used as a benchmark fluid. The mixture of PAM and water showed a shear thinning behaviour in which both yield stress and viscosity increased with increasing PAM concentration. Figure 2.3 shows the rheological characteristics of the PAM-water mixture. Figure 2.3a illustrates the correlation between shear stress versus shear rate for all six fluid mixtures. As can be seen, the yield stress increments with increasing PAM concentration and reaches to 28 Pa for the mixture with 0.5 wt.% of polymer. The viscosity of the fluid was measured up to 0.50 wt.% of PAM. This was more than the concentration selected for the solid entry tests (i.e., 0.3 wt.% PAM), to ensure that the rheological data is consistence in higher polymer concentrations. Figure 2.3b shows the correlation between shear rate and apparent viscosity of fluid mixtures in the log-log scale. As can be seen, apparent viscosity of the mixtures increases non-linearly with polymer concentration and a small addition of polymer increases the viscosity of the mixture more than twenty times the viscosity of water.

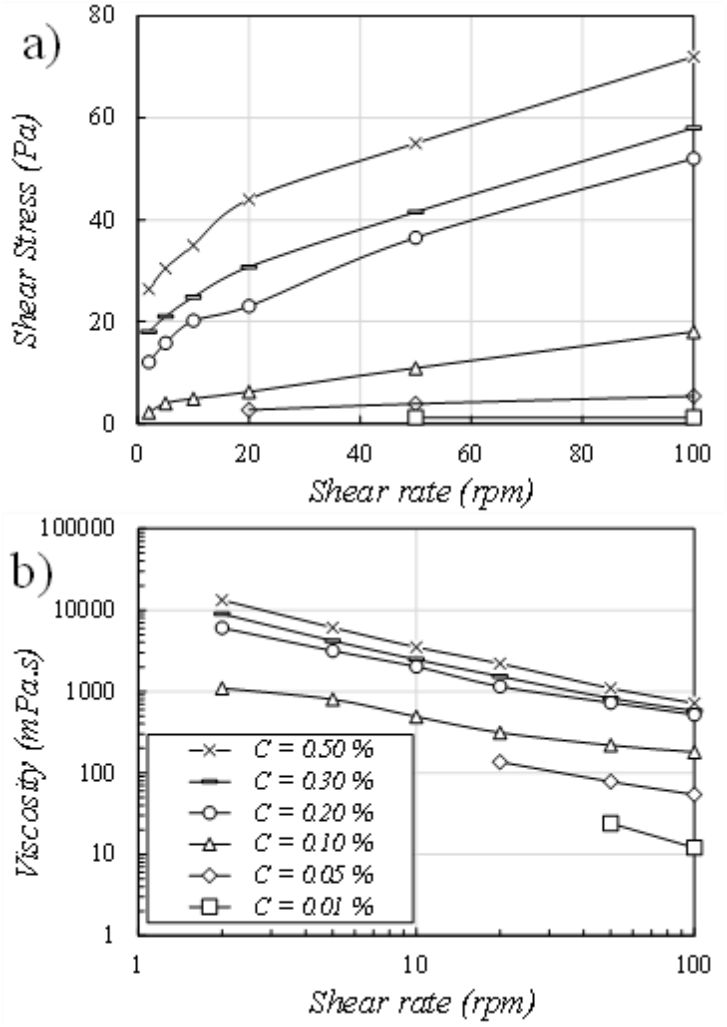

Figure 2.3: Effects of polymer concentration on the rheology of the mixture: a) variations of shear stress with shear rate; b) variations of mixture viscosity with shear rate.

Achieving a homogeneous mixture is a meticulous process and requires considerable time and effort. The polymer powders were first mixed with a small volume of water to form a concentrated mixture. Then, the concentrated mixture was gradually diluted with water and continuously mixed to achieve a uniform mixture. The consistency tests and the time of aging were examined in preliminary experiments. It was found that each fluid mixture should undergo a minimum of one week for the aging process to ensure a complete dissolution of polymers and to guarantee that the fluid attained its desired properties. The experiments were conducted at atmospheric pressure and a room temperature of 25 ^{o}C. In the following, the results that are significant for the fluid entry of

solid objects such as cavity formation, pinch-off, crown formation, and splash curtain are presented. Overall, 36 experiments were conducted to study the solid interface interaction of six disks with different densities and aspect ratios falling into six different types of fluid mixtures. Detailed information on the initial solid object and fluid mixture properties are listed in Table 2.2.

To analyze the outcomes of experiments, an in-house image processing code was developed using the MATLAB (R2018b) software. Based on the quality and condition of the captured images, some preliminary processes such as picture resizing, contrast enhancement, and background subtraction were implemented before converting the images into binary format. After image preparation, specific codes were prepared to extract different parameters from binarized images. The time-history of some parameters such as penetration depth, crown geometry, velocity of falling disk, and cavity volume were extracted from the time-series of images, and other information such as pinch-off depth, disk depth at the pinch-off, and maximum crown height were extracted from particular images as well.

Table 2.2: Variations of fluid entry properties such as pinch-off time and depth, crown diameter, maximum crown height, crown diameter at the maximum crown height with the geometry of the disk, disk density, and polymer concentration.

Test No.	*Disk Density* (kg/m^3)	*Disk aspect ratio*	*C* (%)	t_p (ms)	t_s (ms)	h_p (mm)	h_d (mm)	d_c (mm)	h_c (mm)	*Re*	*I**
1	1120	1.5	0	139	1078	131.9	165.2	260.1	132.0	122768	0.0373
2	1480			143	632	149.1	209.0	266.4	134.1	127001	0.0483
3	2500			149	334	179.1	301.7	286.6	107.9	147321	0.0814
4	1120	3		135	1815	87.6	99.2	239.6	91.5	108325	0.0185
5	1480			137	1099	116.5	154.2	257.8	133.1	115095	0.0244

6	2500			143	562	141.4	223.5	265.7	127.6	141655	0.0426
7	1120	1.5	0.01	136	1140	126.4	163.6	243.3	111.7	5481	0.0372
8	1480			142	644	146.4	194.2	245.0	102.0	6395	0.0482
9	2500			149	360	169.2	283.9	257.3	99.2	6673	0.0813
10	1120	3		133	1861	89.6	105.9	233.3	115.4	3837	0.0184
11	1480			135	1059	110.5	133.6	240.7	135.3	5116	0.0244
12	2500			142	601	137.0	202.4	250.1	118.7	5903	0.0425
13	1120	1.5	0.05	138	952	136.3	170.9	272.4	124.7	2625	0.0371
14	1480			143	560	163.5	214.7	279.4	122.8	2843	0.0480
15	2500			149	340	188.6	313.3	280.1	122.1	3249	0.0810
16	1120	3		133	1715	97.6	110.4	252.9	87.9	2275	0.0184
17	1480			136	993	124.4	152.5	272.8	164.7	2437	0.0243
18	2500			141	519	154.2	238.0	286.7	163.1	2625	0.0424
19	1120	1.5	0.1	138	1044	124.7	162.8	275.8	129.8	788	0.0372
20	1480			141	570	161.4	200.7	284.8	109.2	853	0.0482
21	2500			147	344	180.8	297.3	296.2	122.8	975	0.0813
22	1120	3		133	1932	92.7	111.0	254.5	62.4	602	0.0184

23	1480			134	976	125.7	149.0	263.9	89.1	683	0.0244
24	2500			141	543	155.3	202.4	280.1	127.7	931	0.0425
25	1120			136	1362	129.7	158.7	278.4	53.2	507	0.0372
26	1480	1.5		139	657	147.0	180.8	294.5	76.9	568	0.0482
27	2500			146	348	181.0	280.6	298.9	92.2	617	0.0812
28	1120		0.2	134	3357	87.0	102.6	271.6	15.5	394	0.0184
29	1480	3		134	1108	111.95	131.6	281.5	33.7	444	0.0244
30	2500			141	542	152.8	212.9	316.2	64.9	473	0.0425
31	1120			138	1934	126.4	155.4	287.5	31.1	205	0.0372
32	1480	1.5		140	690	152.5	191.3	284.6	42.9	255	0.0481
33	2500			145	355	190.8	291.7	295.2	48.6	290	0.0812
34	1120		0.3	135	5565	94.1	107.9	284.9	28.7	168	0.0184
35	1480	3		135	1161	110.4	131.1	272.5	31.1	227	0.0244
36	2500			137	588	153.8	216.5	294.5	46.4	245	0.0424

2.3 Results and Discussion

2.3.1 Splash evolution and crown formation

The effects of mixture's rheological characteristics and disk geometry on the shape and size of the crown and splash are investigated to assess the splash curtain and track the splash evolution as each shape enucleates valuable information on the geometry and density of solid objects, fluid

properties, and solid object drop condition. From the moment that a disk impacts the surface of the fluid, the energy from the solid object is transferred to the fluid and the energy transfer causes the fluid to move upward and form a crown shape. In addition to the crown, a cavity is formed due to downward motion of the solid object at the collision point. The surface closure happens based on the magnitude of impact, fluid viscosity, and surface tension of the interface.

Figure 2.4 shows the time-history images of a free-falling disk impacting with stagnant water. The images belong to Test No. 2 with a density ratio of 1.48 and disk aspect ratio of 1.5 (see Table 2). The first image in the time-history shows the impact time and the time interval between each consecutive images is constant with a value of 10 milliseconds. As can be seen, a crown is formed as the disk plunged into the water surface and it grows after 50 ms from the impact. The size of the crown remains constant, and the crown wall forms a dome as the disk continued to penetrate the fluid. A complete sealing of the dome and a pinch-off occur at approximately 100 ms and 170 ms after the impact, respectively. The cavity volume continues to grow from the impact and reaches the maximum volume before the pinch-off at approximately 100 ms. Then, the cavity volume reduces due to pressure exerted from the boundaries of the under-surface cavity and gravitational force to demolish the dome above the interface. The Worthington jet is formed at 210 ms, which is 40 ms after the occurrence of the pinch-off.

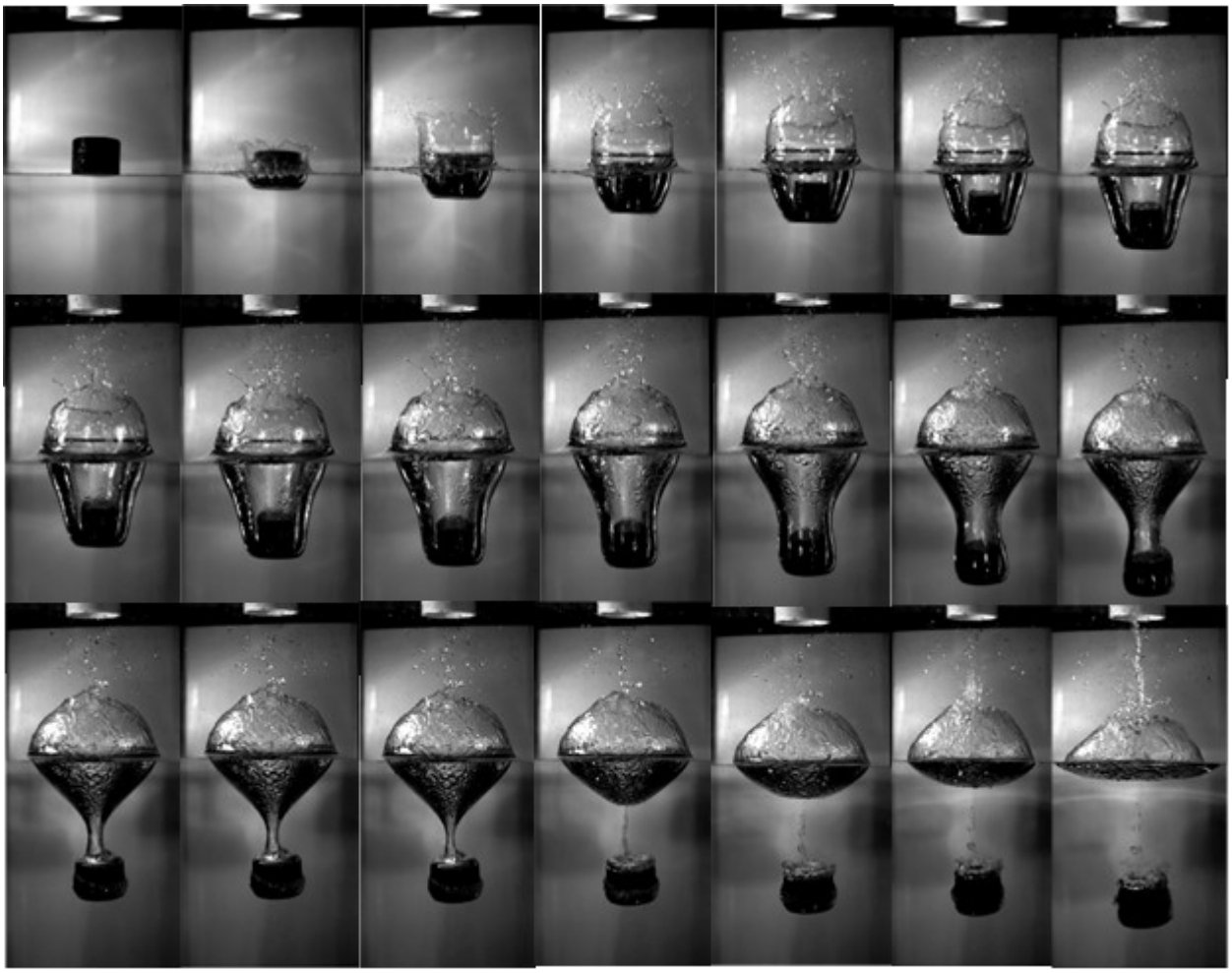

Figure 2.4: Time history images of a free-falling disk in stagnant water with a density ratio of 1.48 and an aspect ratio of 1.5. The time interval between each image is 0.01 seconds.

Figure 2.5 shows the time-history images of the same free-falling disk impacting with a fluid mixture having the minimum polymer concentration of 0.01 wt.% of PAM. A small addition of polymer to the ambient water shows that the splash curtain above the crown becomes more arranged and the splash fingers are uniformly spread around the disk. This phenomenon is evident between 40 and 60 milliseconds after the impact. Due to the addition of polymer, the cavity wall becomes smoother and the ripples on the wall are significantly reduced, indicating that a slight increase in the mixture's viscosity dissipates the ripples on the cavity walls. The higher viscosity of the ambient fluid also reduced the height of the dome by approximately 30% which occurs at 140 ms from the impact. The slight increase in the viscosity of the ambient fluid, as a result of

increasing polymer concentration, reduced the time of pinch-off and formation of the Worthington jet by 20 ms and 30 ms, respectively. The timing between the pinch-off and formation of the Worthington jet was also reduced by 30 ms due to increasing the mixture's viscosity.

Figure 2.5: Time history images of a free-falling disk with a density ratio of 1.45 and an aspect ratio of 1.5 in a stagnant fluid mixture with 0.01 wt. % PAM concentration. The time interval between each image is 0.01 seconds.

Figure 2.6 shows the time series of images of cavity formations and crown evolution by the impact of a thick disk in a non-Newtonian fluid mixture having 0.10 wt.% PAM concentration. A clear difference in the solid entry of a thick disk in this figure in comparison with the same disk entry in water (see Figure 2.4) is the crown formation. Due to energy transfer and relatively low

viscous resistance from the ambient water, the crown is formed, and splash fingers collide with each other resulting in sealing the crown into a dome. High viscous resistance was observed in the disk entry to a fluid mixture with 0.10 wt.% PAM concentration. Such viscous resistance limits the evolution of splash fingers and does not close the crown's wall to form a dome. Although polymer's concentration increased tenfold (i.e., from 0.01 wt.% to 0.10 wt.% in Figures 2.5 and 2.6), the pinch-off and Worthington jet times were unchanged. A further increase in polymer concentration significantly reduces the crown height, which may be due to the sudden rise of the yield stress in the ambient mixture. Figure 2.7 shows the time history of a free-falling disk into a stagnant fluid mixture with 0.30 wt.% of polymer concentration. Rheological data show that the yield stress of the fluid mixture significantly increases as the polymer concentration goes beyond 0.10 wt.% (see Figure 2.3a). Although the crown diameter remains almost constant in all tests, the curtain walls and splash fingers significantly reduced as viscosity and yield stress of fluid mixtures increased.

Figure 2.6: Time history images of a free-falling disk with a density ratio of 1.45 and an aspect ratio of 1.5 in a stagnant fluid mixture with 0.1 wt. % PAM concentration. The time interval between each image is 0.01 seconds.

Figure 2.7: Time history images of a free-falling disk with a density ratio of 1.45 and an aspect ratio of 1.5 in a stagnant fluid mixture with 0.3 wt. % PAM concentration. The time interval between each image is 0.01 seconds.

Figure 2.8 shows the images of cavity and crown formation of all tests when the crown height was at the maximum. The top row of images in each subplot belong to thick disks with an aspect ratio of 1.5 and the bottom row in each subplot represents thin disks with an aspect ratio of 3. In each subplot, the density ratio decreased from left to right as 2.5, 1.48, and 1.14, respectively. As can be deduced from Figure 8, a reduction in the disk aspect ratio slightly increased the crown

height. The maximum crown height forms earlier than the pinch-off time. The dome forms during the time when the crown reaches its maximum and when the pinch-off occurs.

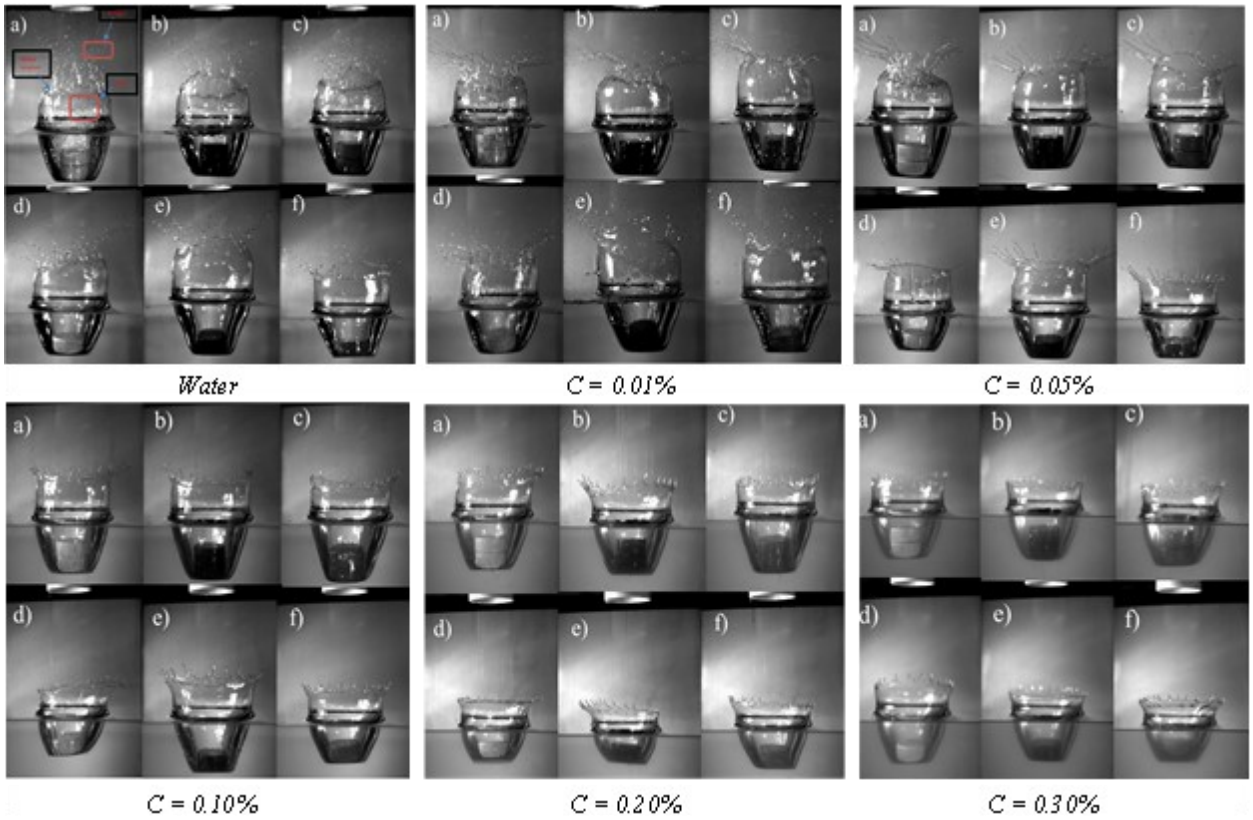

Figure 2.8: Effect of fluids characteristics on different stages of crown development such as formation of ribbed structure, waves, fingers, strings, and droplets.

According to Yang et al. (2021), the splash evolution is categorized into three forms of splash curtain, demo-over, and sealing. Table 2.3 shows the disk's features, polymer concentration, and splash evolution in all tests. By assessing the photos, the splash evolutions were determined and the results listed in Table 2.3. At the maximum crown height, the sealing formed in most cases except for density ratios of 1.14 and 1.48 and for aspect ratio of 3. For the disks with a density of 1.14 and aspect ratio of 3, the sealing did not form at all, and the curtain did not form a dome. In this situation, the crown went up and returned without formation of curved wall towards the inside. For the test having a disk with a density of 1.14 and aspect ratio of 1.5, the curtain went up and formed a dome; however the curtain edges did not touch each other at the end. A complete dome was formed in the rest of the tests. Therefore, except for two tests that are classified as demo-over, the rest of experiments fall in the sealing regime.

Table 2.3: Effect of disk geometry and fluid properties on splash evolution by free fall entry of a cylindrical disk.

Polymer concentration C (%)	Disk aspect ratio D/H	ρ_d/ρ_w	Splash evolution
0	1.5	1.14	Sealing
		1.48	Sealing
		2.50	Sealing
	3	1.14	Demo-over
		1.48	Demo-over
		2.50	Sealing
0.01	1.5	1.14	Sealing
		1.48	Sealing
		2.50	Sealing
	3	1.14	Demo-over
		1.48	Demo-over
		2.50	Sealing
0.05	1.5	1.14	Sealing
		1.48	Sealing
		2.50	Sealing
	3	1.14	Splash Curtain
		1.48	Demo-over
		2.50	Sealing
0.1	1.5	1.14	Splash Curtain
		1.48	Demo-over
		2.50	Sealing
	3	1.14	Splash Curtain
		1.48	Splash Curtain
		2.50	Splash Curtain
0.2	1.5	1.14	Splash Curtain
		1.48	Splash Curtain
		2.50	Demo-over
	3	1.14	Splash Curtain
		1.48	Splash Curtain
		2.50	Splash Curtain
0.3	1.5	1.14	Splash Curtain
		1.48	Splash Curtain
		2.50	Demo-over
	3	1.14	Splash Curtain
		1.48	Splash Curtain
		2.50	Splash Curtain

For the entry of disks into a fluid mixture with 0.01 wt.% of polymer concentration, sealing formation was observed for all the disks with an aspect ratio of 1.5 and also disks with an aspect

ratio of 3 and density ratio of 2.5. The disks with an aspect ratio of 3 and density ratios of 1.14 and 1.48 did not form the sealing and demo-over regime was observed. For the fluid with polymer concentration of 0.05 wt.%, the splash evolutions for the disks were almost the same as the tests with the polymer concentration of 0.01 wt.% except for the disk with the aspect ratio of 3 and density ratio of 1.14, at which a splash curtain was formed. For tests with a polymer concentration of 0.10 wt.%, all three disks with the aspect ratio of 3 did not form a seal and the edges of the fluid did not even show an inward motion. Therefore, these three disks in addition to the disk with a density and aspect ratio of 1.14 and 1.5 were categorized into splash curtain regime. The two remaining disks with an aspect ratio of 1.5 and density ratio of 1.48 and 2.50, showed different behavior in splash evolution. The disk with a density ratio of 1.48 formed an incomplete crown and it was categorized as the demo-over regime. Finally, the disk with a density ratio of 2.5 formed a complete seal. For tests with a polymer concentration of 0.20 wt.%, the seal did not form for disks with all ranges of densities. All disks with different aspect ratios, except the disks with the density ratio of 2.5 and aspect ratio of 1.5 which are classified as demo-over, fall into the splash curtain regime. Similar classifications were observed for the polymer concentration of 0.3 wt.%.

Figure 2.9 shows the effect of fluid characteristics and disk density on variations of normalized crown diameter. This figure revealed important information on the behavior of falling disks into fluid mixtures with different fluid viscosity, disk density, and aspect ratio. The normalized crown diameter was plotted for disks with aspect ratios of 3 and 1.5 in Figures 2.9a and 2.9b, respectively. Experimental data shows a direct correlation between normalized disk density and crown diameter regardless of ambient fluid characteristics and disk aspect ratio. A comparison between the tests with different aspect ratios indicates that disks with an aspect ratio of 1.5 creates a larger crown than that of disks with an aspect ratio of 3.

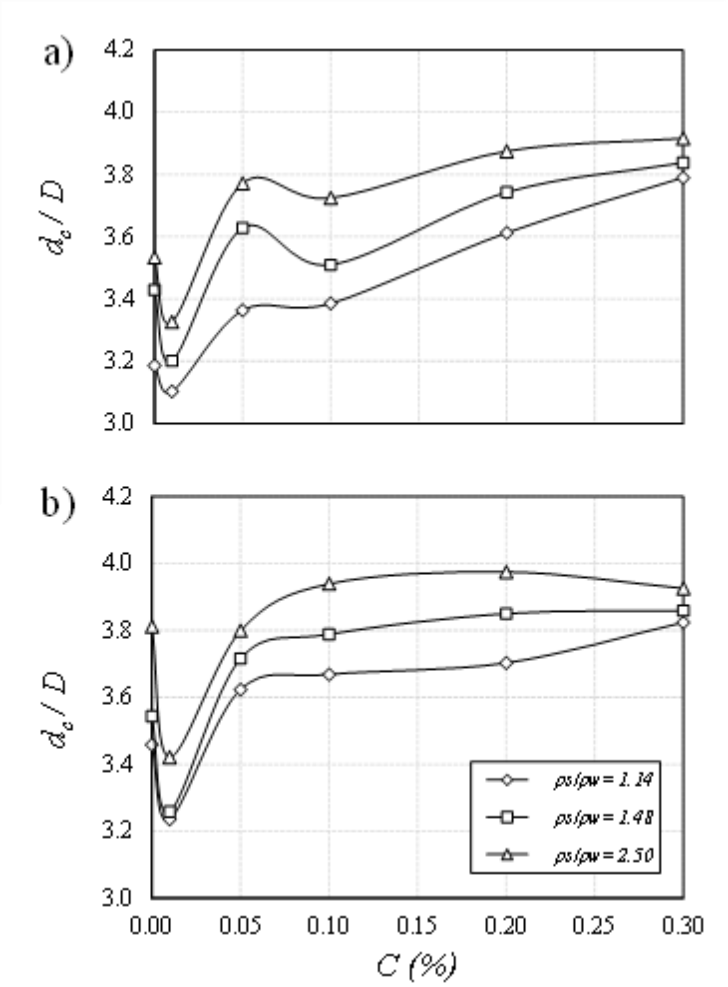

Figure 2.9: Effects of fluid characteristics and disk density ratio on normalized crown diameter: a) disk aspect ratio of 3; b) disk aspect ratio of 1.5.

The rheological data and image analysis in Figures 2.3 to 2.7 have shown two different behaviors in relatively low and high polymer concentrations with a threshold value of $C = 0.1$ wt. %. Three different trends were also observed in variations of normalized crown diameter with polymer concentration at which for $C \leq 0.01$ wt.%, the crown diameter reduced with polymer concentration, and the crown diameter sharply increased with increasing polymer concentration for 0.01 wt. %$< C <$ 0.1 wt. %. For relatively thin disks, the crown diameter slightly increases linearly with polymer concentration for $C \geq 0.1$ wt. %. However, for relatively thick disks, the normalized crown diameter became independent of polymer concentration for $C \geq 0.1$ wt. %. This

indicates that increasing fluid viscosity does not reduce the cavity size and it may reduce the depth of the cavity and shorten the pinch-off time.

Another regime plot is formed based on the correlation between normalized crown diameter in form of $d_c/(h_oD)^{1/2}$, where h_o is the release height, and a dimensionless number expressed as $I^* = (\pi\rho_d U)/(64\rho_w D)$. Figure 2.10 shows the relationship between the two defined dimensionless parameters for this study and other experimental studies in the literature. A comparison between experimental studies from the literature indicates that the normalized crown diameter is below unity for free-falling spheres, whereas the present study and the study of Janati and Azimi, (2022) on the entry of disks show that the normalized crown diameter is larger than unity. The difference between the present data and the ones from the study of Janati and Azimi, (2022) is the rheological characteristics of the ambient fluid as the study of Janati and Azimi, (2022) was performed in water. As can be seen, the normalized crown diameter is larger in disks that enter in non-Newtonian viscous fluid mixture. More data is required to complete the regime plot for tests with relatively larger values of I^*, which can be achieved by releasing the disks from higher distances from the interface.

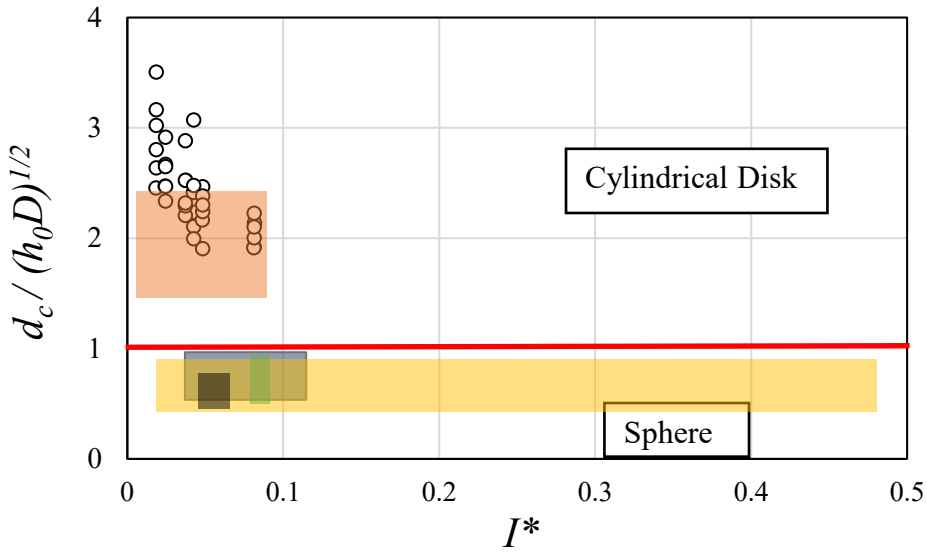

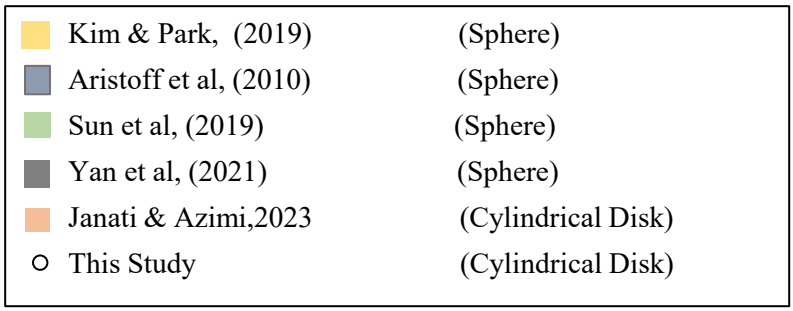

Figure 2.10: Regime plot illustrates the variations of normalized crown diameter with I^* in this study and a comparison with other studies in the literature.

2.3.2 Cavity formation

In this section, the shapes of crown and cavity, formation of curtain wall and its demolition are investigated. The evolution of crown and cavity formation are analyzed by studying the crown and cavity features such as crown and cavity dimensions, pinch-off time and depth, and variations of disk velocity at different stages of evolution.

2.3.1.1 Pinch-off time

The solid-liquid interaction and momentum transfer in the fluid entry of free-falling objects are characterized by the evolution of crown, cavity formation, and pinch-off. The magnitude of the energy transfer between the moving object and the ambient fluid and the dynamics of the mentioned parameters such as pinch-off depth and time are functions of disk parameters and ambient characteristics as:

$$t_p = f_1(\rho_d, \rho_f, \mu_f, D, H, g, u_i) \tag{2.1}$$

where ρ_d, and ρ_f are the densities of disk and fluid, respectively, μ_f is the viscosity of fluid mixture, D and H are the diameter and thickness of the disk, respectively, g is the gravitational acceleration, and u_i is the impact velocity of disk. The impact velocity of disk is linked with the disk's mass and release height and it is correlated as $u_i = \varepsilon(2gh_o)^{1/2}$, where ε is a coefficient and h_o is the release height. Since in this study, the release height and disk's geometry are constant, the impact momentum of the disk is only correlated with the density of the disk, and the pinch-off time can be correlated with the following dimensional parameters as:

$$t_p = f_2(\rho_d, \rho_f, \mu_f, D, H, g) \tag{2.2}$$

Similar dimensional consideration can be written for other dependent variables such as pinch-off depth, crown and cavity dimensions. Based on the number of independent variables and fundamental units, the π-theorem suggests the formation of three dimensionless parameters. Based on dimensional analysis, pinch-off time in free falling of solid disks in stagnant fluid can be modeled as:

$$t_p = f_3\left(\frac{gD^3\rho_f(\rho_d-\rho_f)}{\mu_f^2}, \frac{D}{H}, \frac{\rho_d}{\rho_f}\right) \tag{2.3}$$

The first non-dimensional parameter in Eq. (3) is Archimedes number, the second non-dimensional parameter is the disk's aspect ratio, and the last parameter is the density ratio. A time scale, *T*, is introduced to describe the effects of disk density, disk aspect ratio, and ambient fluid properties on crown formation and cavity dynamics in non-dimensional form. The time scale, *T*, is defined as $T = (D/g)^{1/2}$. Figure 2.11 shows the correlation between the Archimedes number and non-dimensional pinch-off time for disks with different aspect ratios. It should be noted that the horizontal axis in Figure 2.11 is logarithmic. The solid symbol shows the pinch-off times for cylindrical disks in water and the open symbols show the fluid entry of a solid disk into non-Newtonian fluid mixtures with different polymer concentrations. Figures 2.11a and 2.11b show the correlation between Archimedes number and non-dimensional pinch-off time for disk aspect ratios of 3 and 1.5, respectively. As can be seen, the range of non-dimensional pinch-off time was between 1.5 to 1.7 regardless of Archimedes number and disk aspect ratio. The multivariable regression analysis showed a unique combination between density ratio and Archimedes number as $Ar^{-1/8}(\rho_d/\rho_f)^{-5/2}$, which such a combination can predict the pinch-off time in the free flow entry of cylindrical disks.

Figure 2.11c shows the correlation between normalized pinch-off time and the governing parameters listed in Eq. (3). The experimental data from other studies in the literature such as Mansoor et al. (2014), Kim and Park (2019), Janati and Azimi (2023) for solid objects falling in stagnant water were also included in Figure 11c for comparison. The theoretical estimation of normalized pinch-off time from the study of Duclaux et al. (2007) was also added. Data points with black borders represent the disks with an aspect ratio of 1.5 and data points with red borders depict the disks with the aspect ratio of 3. As can be seen, the normalized pinch-off time in disk insertion into non-Newtonian fluid mixture is relatively larger than the solid entry of a free-falling

object in stagnant water. Experimental data indicate that normalized pinch-off times are smaller in disks with smaller aspect ratios. Two logarithmic equations were developed to describe the correlation between normalized pinch-off time and the controlling parameters for disk aspect ratios of 1.5 and 3 as:

$$\frac{t_p}{T} = -0.048\, ln\left[Ar^{-\frac{1}{8}}\left(\frac{\rho_s}{\rho_f}\right)^{-5/2}\right] + 1.46 \qquad \text{For } D/H = 3 \qquad (2.4a)$$

$$\frac{t_p}{T} = -0.033\, ln\left[Ar^{-\frac{1}{8}}\left(\frac{\rho_s}{\rho_f}\right)^{-5/2}\right] + 1.45 \qquad \text{For } D/H = 1.5 \qquad (2.4b)$$

The differences between the outcomes of this study with other experimental data may be due to non-linear effects of other variables that were constant in our study. For example, the release height in present study is 0.5 m whereas it was 0.3 m in the study of Janati & Azimi (2023). The overlaps data belong to the experiments which dropped into the water for this study. The geometry of solid object in the study of Kim & Park (2019), Mansoor et al, (2014), and Duclaux (2007) was sphere and the ambient fluid was water. A comparison between the results from the literature and pinch-off time of disks in water indicates that the normalized pinch-off time of solid spheres are smaller than that of disks.

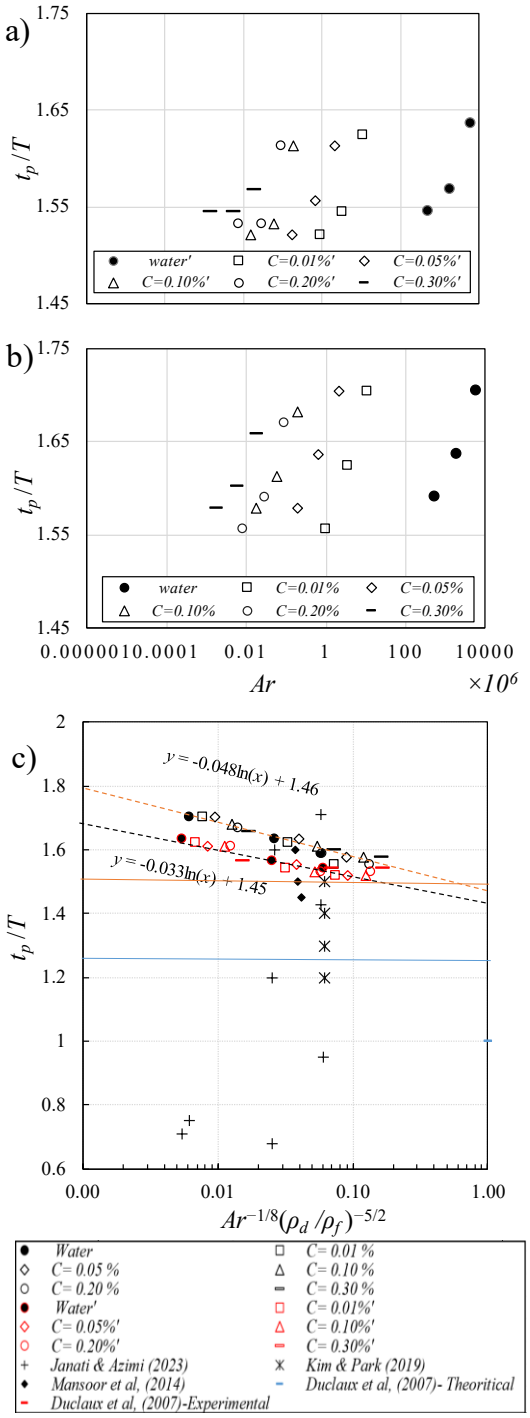

Figure 2.11: Effects of aspect ratio, disk density, and fluid characteristics on variations of pinch-off time: a) variations of normalized pinch-off time with Archimedes number for aspect ratio of 3; b) variations of normalized pinch-off time with Archimedes number for aspect ratio of 1.5; c) variations of normalized pinch-off time with Archimedes number for all disks. Red markers are

dedicated to the disks with the aspect ratio of 3 and the black ones are regarding to the ones with the aspect ratio of 1.5.

2.3.2.2 Pinch-off depth

The pinch-off depth was normalized with the disk diameter and the correlation between normalized pinch-off depth and Archimedes number are shown in Figure 2.12. Figure 2.12a shows the variations of normalized pinch-off depth with Archimedes number for disk with an aspect ratio of 3. As can be seen, the normalized pinch-off depth ranged between 1 and 2 and they were independent of polymer concentration. Figure 2.12b shows that the pinch-off depth in relatively thicker disks (i.e., D/H = 1.5) increased and normalized pinch-off depth ranged between 1.5 and 2.5. The three data points in each test series indicate the variations in disk density showing that the normalized pinch-off depths are smaller in disks with smaller density ratios.

The effects of disk density are combined with the rheological characteristics of ambient fluid mixture and a unique combination between density ratio and Archimedes number was found to develop a robust correlation between pinch-off depth and other controlling parameters. Figure 12c shows the relationship between dimensionless pinch-off depth and the combination of Archimedes number and density ratio in form of $AR^{-1/8}(\rho_d/\rho_f)^{-5/2}$. As can be seen in Figure 2.12c, the horizontal axis of the plot is in logarithmic format. It is worth noting that Figure 2.12c includes data for both aspect ratios of 1.5 and 3 and other data from the literature. The experimental data for disks with an aspect ratio of 1.5 are shown with open black symbols and data for disks with the aspect ratio of 3 are shown with the open red symbols. The solid symbols show the data for the disk entering water. The data with red border markers are all below the black border markers indicating that the aspect ratio has a noticeable impact on pinch-off depth and a higher aspect ratio cause a smaller pinch-off depth. Since the Archimedes number on the horizontal axis depends on the fluid's viscosity and density as well as the solid object's density and geometry, the Archimedes number for other experiments remains constant since the same fluid and solid object were used. The normalized pinch-off depths in other studies except for Janati & Azimi (2023) were higher than the current study due to existence of higher impact velocities and spherical solid objects. However, since the density ratio and geometry of the solid object in the study of Janati & Azimi were almost the same as the current study unlike the impact velocity (i.e., 1.72 m s^{-1}) compared to the impact velocity of the present study (i.e., 3.2 m s^{-1}), the normalized pinch-off depth of in present study stand above the data from the study of Janati & Azimi. A series of experiments in free-falling of

disks from different impact velocities (i.e., release heights) is suggested to better understand the correlation between impact velocity and pinch-off. The correlations between normalized pinch-off depth and controlling parameters are non-linear and two formulas were developed to show the correlations as:

$$h_p/D = -0.241\, ln(\, Ar^{-1/8}(\rho_s/\rho_f)^{-2.5}) + 0.8803 \qquad \text{For } D/H = 3 \tag{2.5a}$$

$$h_p/D = -0.224\, ln(\, Ar^{-1/8}(\rho_s/\rho_f)^{-2.5}) + 1.4198 \qquad \text{For } D/H = 1.5 \tag{2.5b}$$

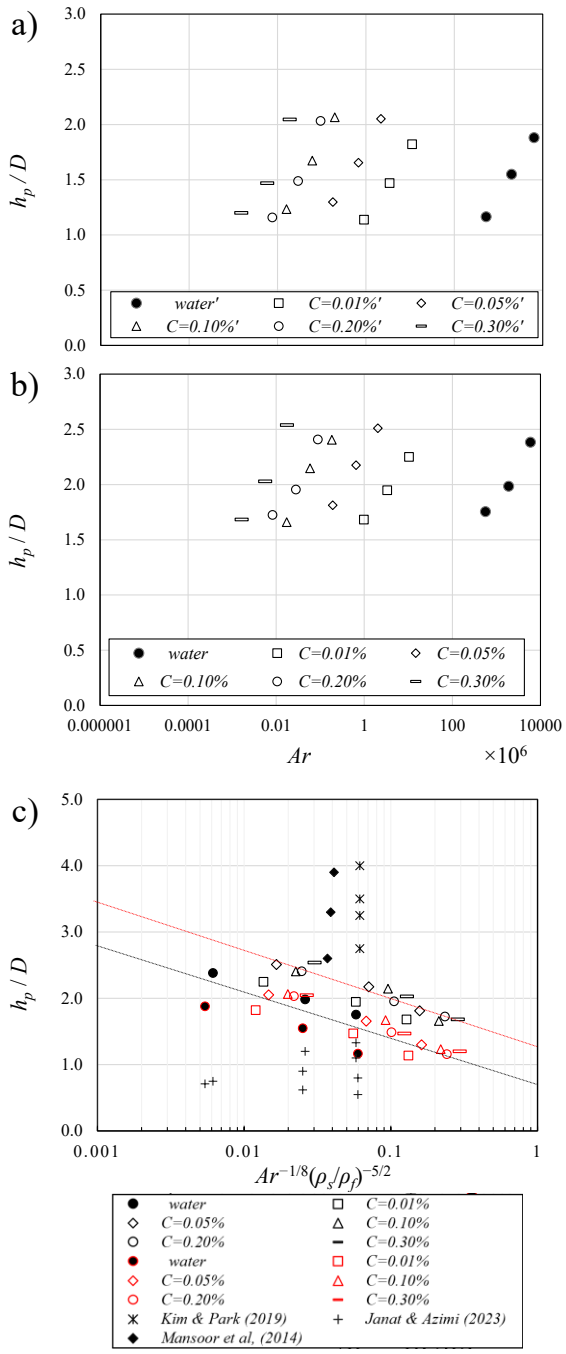

Figure 2.12: Effects of aspect ratio, disk density, and fluid characteristics on variations of pinch-off depth: a) variations of normalized pinch-off depth with Archimedes number for aspect ratio of 3; b) variations of normalized pinch-off depth with Archimedes number for aspect ratio of 1.5; c) variations of normalized pinch-off depth with Archimedes number for all disks.

2.3.3 Disk's kinetic

The inertia and gravitational forces play major roles on the motion of solid objects in water and viscoplastic fluid mixtures. Other forces such as buoyancy, surface tension, and hydrodynamic forces are also important in crown formation and penetration of solid objects in Newtonian and non-Newtonian fluid mixtures. To elucidate the dependence of cylindrical objects on three main elements of liquid viscosity, disk density, and aspect ratio of free-falling disks, the time and velocity variations of sinking disks are studied in this section. Figure 2.13 shows the effects of disk density and rheological characteristics of the fluid mixture on the sinking time of cylindrical disks for both disk aspect ratios. The sinking time is measured from the time of collision to the time the disk reaches the bottom of the tank. Figures 2.13a and 2.13b belong to disks with the aspect ratios of 3 and 1.5, respectively. The overbars were also added to depict measurement uncertainties. As can be seen from Figure 2.13, the effect of polymer concentration on sinking time was found to be negligible in disks with a relatively high-density ratio of $\rho_s/\rho_w = 2.5$; it was slightly noticeable for $\rho_s/\rho_w = 1.48$; and it was significant for $\rho_s/\rho_w = 1.14$. The normalized sinking time increased non-linearly with polymer concentration. The gravitational force due to the mass of cylindrical disks overcomes the resistive viscous force for $\rho_s/\rho_w \geq 1.5$ and the effects of polymer concentration become negligible in such a range of density. On the other hand, for relatively small density ratios, the effect of mixture's viscosity on sinking time and velocity is not trivial and increases with increasing polymer concentration. Figure 2.13 also shows the effect of aspect ratio on normalized sinking time. A comparison between the two subplots in Figure 2.13 shows that the sinking time diminished as the disk's aspect ratio reduces and such reduction continued for all tests with different mixture's viscosity.

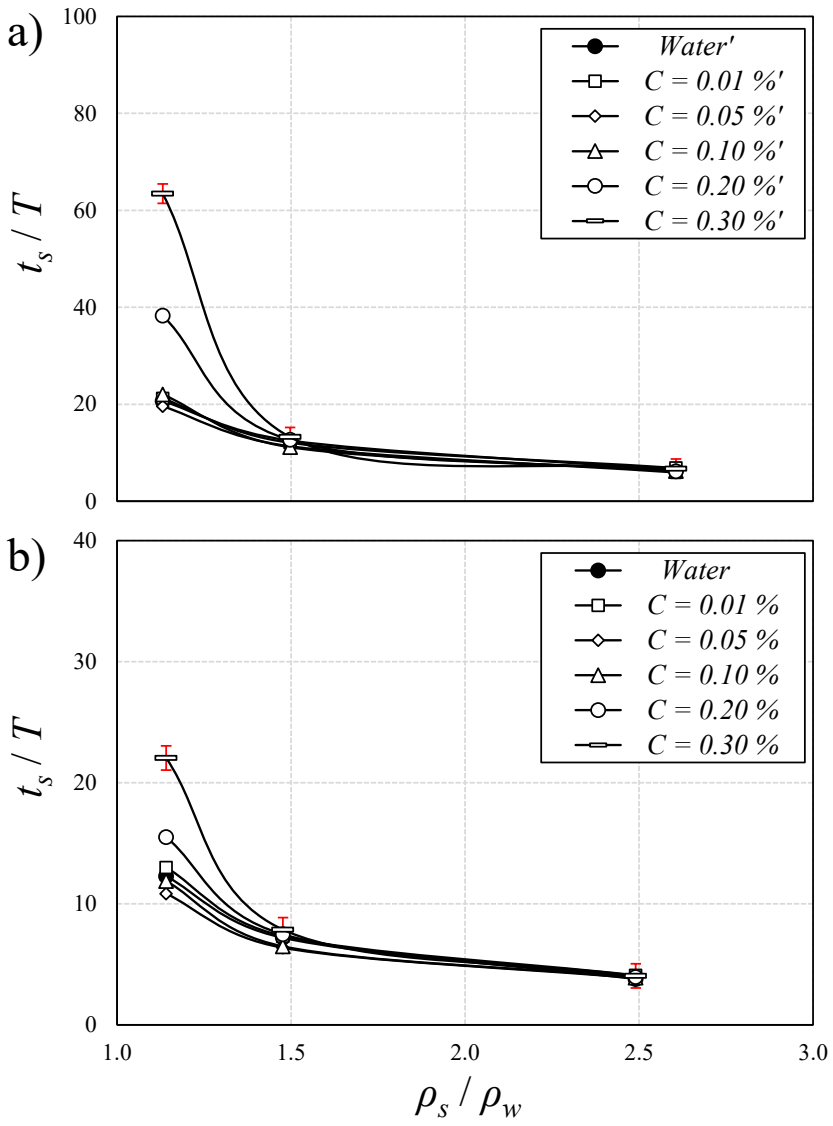

Figure 2.13: Correlations of normalized sinking time versus dimensionless disk density for different concentrations of PAM in the fluid mixture: a) $D/H = 3$; b) $D/H = 1.5$.

Figure 2.14 depicts the correlation between dimensionless sinking velocity and controlling parameters in form of $Ar^{-1/8}(\rho_s/\rho_f)^{-5/2}$ for all disks with different densities and aspect ratios. The sinking velocity was normalized with $V\infty = (\rho_d A/2mg)^{1/2}$ where m is the mass of disk, A is the area of disk, and ρ_d is the density of disk. The slope of variation in settling velocity is different for disks with different aspect ratios and it decreases with increasing aspect ratio. Disks with an aspect ratio of 1.5 have a steeper slope in comparison to disks with an aspect ratio of 3. This indicates that a

relatively thicker disk has a higher momentum and a higher rate of momentum transfer. Therefore, such disks lose their velocity at a higher rate than that of a relatively thin disk (i.e., D/H = 3). According to Figure 2.14, the disks with an aspect ratio of 1.5 have a higher sinking velocity in comparison to disks with the aspect ratio of 3. Two non-linear equations were proposed to predict the sinking velocity of cylindrical disks in water and viscous mixtures as:

$$V_s/V_\infty = -2.05\, ln(\, Ar^{-1/8}(\rho_s/\rho_f)^{-2.5}) - 1.13 \qquad \text{For } D/H = 3 \tag{2.6a}$$

$$V_s/V_\infty = -4.56\, ln(\, Ar^{-1/8}(\rho_s/\rho_f)^{-2.5}) - 1.56 \qquad \text{For } D/H = 1.5 \tag{2.6b}$$

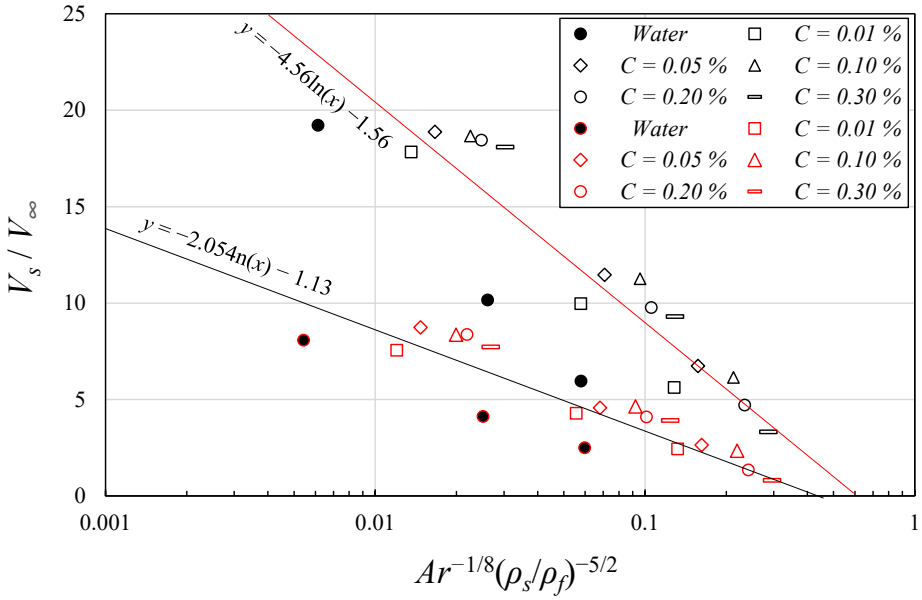

Figure 2.14: Variations of normalized sinking velocity with Archimedes number for disks with different aspect ratios and mixture concentration.

2.3.4 Energy losses

The variations of energy budget during different stages of interaction such as impact, crown formation, pinch-off, and descend provide valuable information about the hydrodynamics and energy transfer. Such information are important in determination of design parameters such as impact velocity, release height, and disk geometry. The energy loss is calculated by equating the energy budgets from the time a disk collides with the fluid surface and the time that it settles down with a relatively constant sinking velocity. The interface was selected as the datum for energy

consideration. Figure 2.15 shows the correlation between the density ratio of disks and normalized energy losses. The energy losses were normalized with the initial potential energy of disks at the release elevation. The overbars were also added to depict measurement uncertainties. Experimental results indicate that the thick dense disks have less energy losses in comparison with thin and light disks. As can be seen, three fluid mixtures having polymer concentrations of 0.10 wt.%, 0.20 wt.%, and 0.30 wt.% are shown in Figure 2.15. As can be seen, polymer concentration increases the energy losses, as the potential and kinetic energies in a highly viscous fluid mixture dissipate at a higher rate.

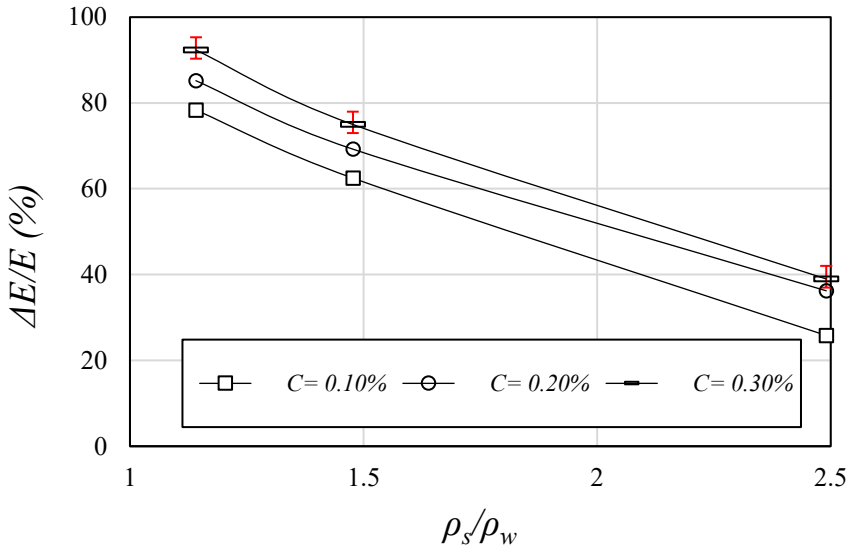

Figure 2.15: Effects of polymer concentration and normalized density of disks on the energy losses.

Figure 2.16 shows the variations of energy losses with Archimedes number for disks with different densities and aspect ratios. A comparison between Figures 2.16a and 2.16b indicates that the energy loss for disks with aspect ratio of 3 (Figure 2.16b) is higher than that of disks with aspect ratio of 1.5. Figure 2.16c shows the variation of the energy losses with the proposed combination of density ratio and Archimedes number in the form of $Ar^{-1/8}(\rho_s/\rho_f)^{-5/2}$. The black markers are related to disks with aspect ratio of 1.5 and the red markers represent disks with aspect ratio of 3. As can be seen, all disks with aspect ratio of 3 are located on top of black markers indicating that the energy losses are highly dependent on the aspect ratio. Two equations were proposed for prediction of energy losses for free-falling disks in non-Newtonian fluid mixture as:

$$\frac{\Delta E}{E} = 16.38\, ln(\, Ar^{-1/8}(\rho_s/\rho_f)^{-5/2}) + 108.5 \qquad \text{For } D/H = 1.5 \qquad (2.7a)$$

$$\frac{\Delta E}{E} = 7.643\, ln(\, Ar^{-1/8}(\rho_s/\rho_f)^{-5/2}) + 104.1 \qquad \text{For } D/H = 3 \qquad (2.7b)$$

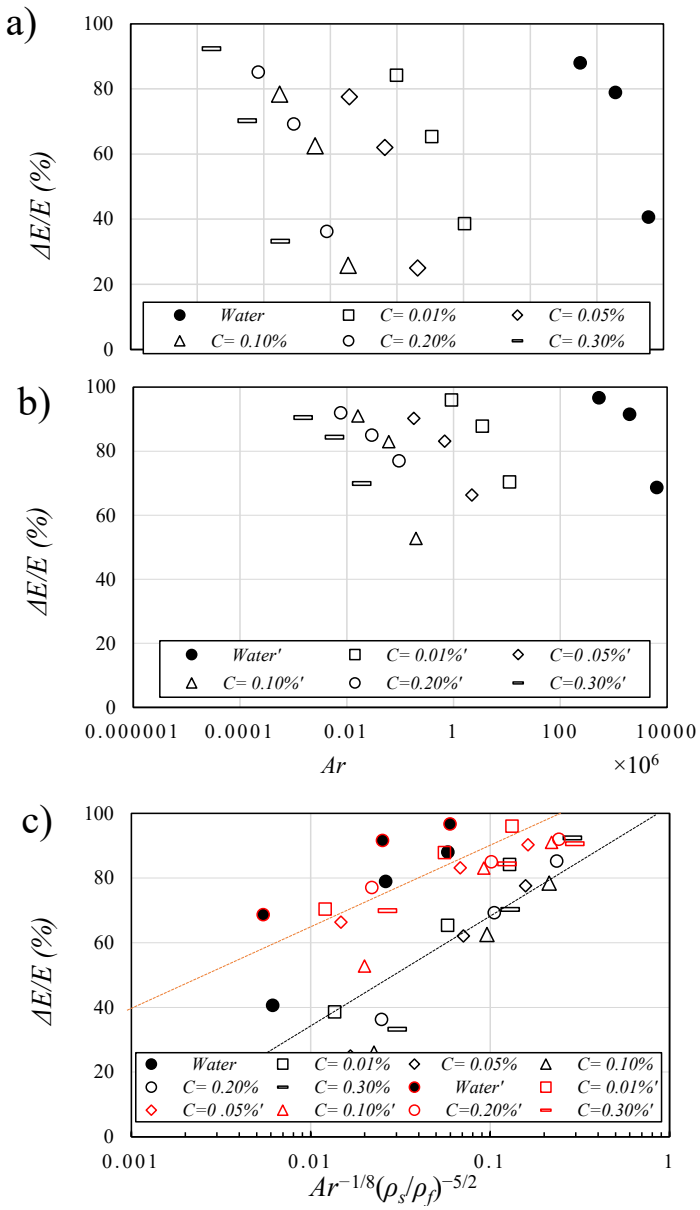

Figure 2.16: Effects of ambient fluid properties and disk characteristics on variations of energy losses: a) variations of normalized energy losses with Archimedes number for aspect ratio of 1.5; b) variations of normalized energy losses with Archimedes number for aspect ratio of 3; c) variations of normalized energy losses with Archimedes number for all disks.

2.4. Conclusion

A series of laboratory experiments was conducted to study the fluid entry of cylindrical disks in water and non-Newtonian fluid mixtures. The effects of disk mass and aspect ratio on cavity dynamics, crown formation, and energy dissipation of solid disks in stagnant fluid mixtures with different viscosity and yield stresses were investigated. A small increment of fluid viscosity showed that the splash curtain above the crown became well arranged, symmetrical, and the splash fingers were uniformly spread around the disk. In addition, the cavity wall became smoother and the ripples on the wall were significantly reduced, indicating that a slight increase in the mixture's viscosity dampened the ripples of the cavity walls. It was found that a slight increase on the viscosity of the ambient fluid reduced the height of the dome by approximately 30%. A further increase in viscosity and yield stress of the ambient fluid mixture significantly reduced the crown height. Although the crown diameter remained almost constant with variations of fluid's rheological characteristics, the curtain walls and splash fingers significantly reduced as viscosity and yield stress of fluid mixtures increased.

Dimensional analysis indicated that the pinch-off time and depth are correlated with the Archimedes number, disk aspect ratio, and relative disk density. The normalized pinch-off time was found to be larger than that of spheres in water and normalized pinch-off times were found to be smaller in disks with smaller aspect ratios. Experimental data indicated that the normalized pinch-off times and depths were smaller in disks with larger aspect ratios. In addition, both normalized pinch-off times and depths increased non-linearly with increasing disk's density. Multivariable regression analysis was performed to determine functional correlations between pinch-off time and depth and controlling parameters.

The settling time and velocity were measured for disks with different geometries and entering different fluid mixtures. It was observed that the sinking time diminished as the disk's aspect ratio reduced and such reduction continued for all tests with different mixture's viscosity. The normalized sinking velocity decreased non-linearly with decreasing Archimedes number and density ratio. The slope of variation in settling velocity was found to be different for disks with different aspect ratios and the slope of variation decreased with increasing aspect ratio. Experimental results indicated that the thick dense disks had less normalized energy dissipation in comparison with thin and light disks. In other words, normalized energy losses in disks with aspect ratio of 3 was higher than that of disks with aspect ratio of 1.5.

Chapter 3

Cavity dynamics by the entry of annular disks into non-Newtonian ambient

3.1. Introduction

The entry of rigid bodies into water has gained significant attention due to its numerous applications, both in naturally occurring phenomena and solid entry induced by human activities. The entry of cylindrical objects is particularly relevant to the marine industry, and in other fields such as aerospace, ocean engineering, parcel delivery, oil and gas industry, and offshore drilling (Faltinsen et al., 2004; Seddon & Moatamedi, 2006; Kapsenberg, 2011). Water entry refers to the phenomenon where a solid object penetrates the surface of a water body, initiating complex interactions between the object and the fluid. Cavity in this context is the void or hollow space created in the fluid as the object moves through it. The complexities in formation of cavity and splash curtain as a result of solid entry are due to correlations between many controlling factors such as the geometry of rigid body, object density, shape of the object, rheological characteristics of the ambient, and release conditions (Belden et al., 2023; Janati & Azimi, 2023; Shokri & Akbarzadeh, 2022; Vincent et al., 2018; Wang et al., 2022; Yuan et al., 2022; Zhang et al., 2022;Lu et al., 2024). Recent research studies explored the effects of ambient fluid characteristics and fluid rheology on cavity dynamics and splash formation. The examples of solid entry in non-Newtonian fluid mixtures can be found in the analysis of swamp, sewage, and oil industries (Akers & Belmonte., 2006; de Goede et al., 2019; Ebrahimi & Sanati., 2021; Akbarzadeh et al., 2022). Tabuteau et al., (2011) investigated the solid-fluid interactions of falling spheres into a non-Newtonian ambient.

A paper based on the content of this chapter is published in the *Ocean Engineering*: Ebrahimi, M., & Azimi, A. H. (2025a). Cavity dynamics by the entry of annular disks into non-Newtonian ambient. *Ocean Engineering*

The diameters of spheres ranged from 0.0127 m to 0.0254 m and their densities varied between 1340 kg/m³ and 14970 kg/m³. The ambient fluid was prepared by the variations of Carbopol gel concentration to develop ambient mixture with different viscosities and yield stresses. It was found that a reduction in impact velocity reduced the amount of air entrained by the solid object, which in return led to a decrease in the pinch-off depth. A threshold Reynolds number of 20 was identified at which the crater diameter remained constant for Re < 20 and for Re ≥ 20, the crater diameter increased exponentially. Here $Re = \rho_d u_i D/\mu$, where ρ_d, u_i, and D are the density, velocity, and diameter of the disk, respectively and μ represents the viscosity of the fluid mixture. Sun, et al., (2019) investigated the crown formation and cavity dynamics by solid spheres into two-layered immiscible fluids. The two-layer fluid system consists of water and a viscous layer made of dimethicone with a viscosity of 10 mPa.s and density of 941 kg/m^3. The initial Froude number ($Fr = u_i/(gD)^{1/2}$, where u_i is the impact velocity, g, is the gravitational acceleration, and D is the sphere diameter) varied between 6 and 9. The results indicated that the presence of the top viscous layer significantly changed the crown formation and cavity dynamics, leading to waves and instabilities in both the cavity and crown while the viscous fluid rested on top of the water. Prasad et al., (2024) also conduct a review study on the multiphase analysis of water entry.

The entry of three solid objects (i.e., spheres, disks, and projectiles) in stagnant water and non-Newtonian fluid mixtures have been predominantly studied in the literature (Shi et al., 2019; Kim and Park, 2019; Du et al., 2022). Each of these objects has been assessed by many researchers and the effects of controlling factors such as object density, initial energy (i.e., release height), initial impact velocity, and the angle of entry have been explored. Shi et al., (2019) performed comprehensive research on the effects of shape, impact velocity, and release angle on the entry of a solid object. The impact velocity ranged between 8 m/s and 14 m/s and the release angle varied between zero and 90 degrees. The analysis revealed that the pinch-off depth increased with the Froude number. Such escalation was initially marked by a sharp increase, which gradually tapered off as the impact velocities reached higher to u_i = 10 m/s. Du et al., (2022) performed a series of experiments to study the effect of object's geometry on the shape and size of the cavity. All solid geometries had the same diameter of D = 20 mm but different geometries of circle, semicircle, square, and trapezoidal were tested. It was found that the effect of object shape on variations of pinch-off depth was significant. Amongst all sections, the square section had the highest pinch-off depth, and the trapezoidal section was the second.

Kim & Park, (2019) studied the deformation of water surface when a rounded cylindrical projectile with various aspect ratios and surface roughness entered the water. The hemispherical object had a diameter of D = 40 mm and different aspect ratios of D/h = 1, 2, 4, and 8 with impact velocities of u_i = 2.5 m/s and 4.2 m/s were tested. The time history of liquid film height indicated that the film height initially increased, reached the peak, and decreased afterward. Additionally, a decrease in the aspect ratio shortened the downward motion, and the reduction in liquid film height became steeper in objects with smaller aspect ratios. Zhou et al., (2021) performed a series of experiments on the falling and entry of eccentric annular disks in water. The trajectory of the falling disks in water was measured, and it was found that the eccentricity of the disks significantly altered the falling trajectories and the modes of falling. The studies focused on the flow structure of the falling annular disks and the motion of the dropping annular disks was monitored.

Hou et al. (2019, 2022) conducted a series of experimental and numerical studies to examine the entry of hollow cylinders in water. The exerted hollow cylinder had a diameter of D = 30 mm, and the mass of cylinders ranged between m = 0.128 kg and 0.328 kg while the Froude number ranged between Fr = 5 and 10. It was found that the augmentation of cylinder's mass increased the submergence distance (i.e., penetration depth). Hou et al. (2021) studied the patterns of closure in cavities and used hollow cylinders with different water entry scenarios. The density of the disk was 7.8 kg/m³, the thickness of the cylinder was h = 80 mm, the hole diameter ratio was 0.84, and the impact velocity was 4 m/s. It was found that the settling velocity of the hollow cylinders increased non-linearly with the initial impact velocity at the water surface. Many other studies elaborate on the oblique entry of solid object into water such as (Z. Li et al., 2024; H. Liu et al., 2023). Also, the cavity dynamics of sinking solid object into a fluid was studied by many researchers (Lu et al., 2022; Wang et al., 2024; Zhang et al., 2021). Duan et al., (2022); X. Wang et al., (2022); and Zhang et al., (2023) studied bubble dynamics in fluid mixture using both numerical simulation and laboratory experiments.

Akbarzadeh et al. (2022) performed a series of experimental studies to investigate the effects of ambient fluid properties on the fluid entry of solid spheres. Two ambient fluids of glycerin (Newtonian), and polyacrylamide (non-Newtonian, Boger) with different concentrations were utilized. The surface tension, density, and viscosity of the selected fluid mixtures were kept constant with a value of 120 mPa.s. The chosen released heights covered a wide range of Froude

numbers, Fr = 1.2 to 20. The solid object moved at a slower rate in Boger fluid in comparison to the Newtonian fluid. The characteristic length and time of pinch-off were measured in both Newtonian and non-Newtonian (Boger) fluid mixtures. The pinch-off time was measured in all experiments, and it occurred earlier in Boger fluid than those in Newtonian fluids. A similar trend was observed in variations of pinch-off length.

Akers and Belmonte (2006) studied the entry of solid spheres into viscoelastic wormlike micellar fluids that were made of Cetylpyridinium Chloride (CPCl) and Sodium Salicylate (NaSal). The effects of object entry into viscoelastic fluids were explored by the variation of release height, object size, and the relative disk density. The ambient viscosity was kept constant with a value of 430 mPa.s and different glass and steel spheres were released from a height above the mixture's surface and the release heights ranged between 250 mm and 450 mm. The density of the solid objects varied between 1350 kg/m^3 and 7970 kg/m^3. It was found that the penetration depth of the solid object increased with increasing Froude number.

Jafari and Akbarzadeh, (2022) investigated the impacts of opening diameter on the water entry of hollow cylinders. To isolate the effect of opening on cavity formation, many parameters such as the mass and the outer diameter of the cylinders were kept constant. The equivalent cylinder diameter was 18 mm and the Froude number in all experiments ranged from 0.74 to 10.2. Three geometries were tested and the shape and height of the through-hole jets were measured. It was found that the geometry of the through-hole jets varied with the hole geometry. A direct correlation was found between the pinch-off depth, penetration depth, and cavity diameter. In addition, a linear relationship was observed between the pinch-off time and the impact velocity. Janati and Azimi, (2023) examined the cavity dynamics and crown formation of thick solid and annular disks falling into water. The effect of opening diameter (d_h = 38 mm), outer disk diameter (D = 78 mm), and disk aspect ratio on cavity dynamics and crown formation were investigated. The density ratio of the disks varied between 1 and 2.3 times of the density of water. The applied fluid was water with a density of 999 kg/m^3 and the viscosity of water was 1.02×10^{-6} m^2/s. The Froude number for conducting their experiments varied between 1 to 3.5. It was found that the crown diameter formed by the solid disks was larger by 10% to 20% more than that of the annular disks. Unanimous to the previous studies, they showed that increasing the Froude number increased the pinch-off depth as well.

The recent study by authors (Ebrahimi and Azimi, 2024) presented the results of a comprehensive study on the behaviour of free-falling disks entering in non-Newtonian fluid mixture. The density of the falling disk varied from 1000 kg/m^3 to 2500 kg/m^3 and the disks had two aspect ratios of D/h = 1.5 and 3. The disks were released from a constant height of H = 500 mm and the viscosity of the fluid mixture ranged from 15 mPa.s to 600 mPa.s. The results indicated that the crown diameter increased with increasing the viscosity of the fluid mixture in disks with aspect ratios of 1.5 and 3. It was found that the sinking time reduced with increasing the density of the disks and sinking time experienced a reduction with a reduction in viscosity of the fluid mixture. Moreover, the effect of controlling parameters on variations of energy losses was studied and a correlation was formulated between the rheological characteristics of the fluid mixture and energy losses at different stages of the descending disk motion.

The cavity dynamics has also been investigated numerically and theoretically. The numerical methodology mostly consists of applying the commercial software such as Ansys Fluent (Ping et al., 2025; Xia et al., 2023; Yang et al., 2023; C. Zhao et al., 2023; Z. X. Zhao et al., 2023). The theoretical approach has been explored in multiple studies, introducing various equations designed to track the growth and collapse of cavities. These proposed equations are critical for understanding the underlying physical phenomena and for validating the numerical simulations by providing a theoretical framework for the observed behaviors (Duclaux et al., 2007; Guo et al., 2012; Zhang et al., 2021; Tavakoli et al., 2023; Khabakhpasheva et al., 2024). However, the proposed correlations are only dedicated to the certain situation such as water media.

Due to the complexity of fluid properties and the impact of numerous variables on the fluid entry phenomenon, more research study is required to provide a better understanding of the correlation between disk dynamics such as pinch-off, crown formation, and the controlling parameters of the solid disk and the ambient fluid. Hereby, a comprehensive study is conducted to investigate the characteristics related to the fluid entry of annular solid objects in both stagnant Newtonian and non-Newtonian ambient. The solid objects used in the experiments included both solid and annular disks with various densities and opening diameters. The behavior of annular disks with a central hole in a flat and homogeneous disk was assessed. The solid entry of annular disks was tested in different ambient with non-Newtonian rheological characteristics and the results were compared with the solid entry of annular disks in water.

By testing nine different disks with varying central hole diameter and density ratio across six fluid mixtures with varying viscosities, our work reveals new insights into the interplay between disk geometry and density, and fluid rheology. These findings enhance the understanding of fluid-structure interactions in complex fluids, contributing valuable knowledge applicable to ocean engineering and related fields. This study is highly relevant to ocean engineering that could be addressed in plethora of examples such as: offshore drilling and subsea operations, equipment often interacts with non-Newtonian fluids like drilling muds, making it crucial to understand the entry dynamics of solid objects to ensure the safe design and operation of marine equipment (Ebrahimi et al., 2020; Hemphill et al., 1993). Studying how objects penetrate non-Newtonian marine sediments aids in designing foundations for offshore structures and anchors (Winterwerp and van Kesteren, 2004). In environmental and spill response, knowledge of interactions between solid particles and non-Newtonian fluids enhances remediation strategies for oil spills and pollutants (Fingas, 2010). Additionally, insights into operations within swampy environments involving non-Newtonian muds which can improve the design of vessels and equipment in such challenging conditions (Mitsch and Gosselink, 2015).

3.2 Methodology

3.2.1 Experimental setup

A series of laboratory experiments was carried out in the Multiphase Flow Research Laboratory (MFRL) at Lakehead University, Canada. The experimental setup consists of a tank with dimensions of $400 \times 400 \times 1000$ mm^3. The depth of fluid mixture was 700 mm and 300 mm free space was allocated above the fluid surface to capture crown evolution and splash curtain formation after the water entry of the annular disks. The disks had a diameter of $D = 75$ mm, height of $h = 50$mm and they were released from a constant height of $H = 500$ mm above the fluid surface. The disks collide with the fluid surface perpendicularly which means that the contact angle of the disk collision is 90^o. Nine different disks with three opening diameters of $d_h = 15$, 25, 40 mm and three density ratios of 1.14, 1.48, and 2.5 were tested. The flat solid disks included a rounded rim, and the side edge had some roughness with a height of 1±0.1 mm. The collision spot of the disks with the fluid's surface is located precisely at the center of the tank to avoid any bias from wall effects. The disk diameter, D, and height, h, were selected to minimize boundary effects in a $400 \times 400 \times 1000$ mm^3 tank, ensuring accurate fluid interaction and allowing high-resolution

observations of flow phenomena like cavity dynamics using high-speed cameras. Annular disks with the mentioned central openings simulated engineering structures such as hollow cylinders, affecting mass distribution and descent dynamics. Studying such variations provide insights into how geometry influences fluid flow patterns during water entry to optimize the mentioned engineering applications. Also, the disk density ratio and fluid properties were guided by the need to replicate and study phenomena relevant to engineering applications while ensuring experimental feasibility and accuracy.

To investigate the behavior of free-falling disk into water and non-Newtonian fluid mixtures, two high-speed cameras (Phantom, Miro Lab 110, New Jersey, Wayne, USA) with the camera lens AF Nikkor 50 mm, f/1.4D (Nikon, Tokyo, Japan) were applied. The usage of the camera demanded some source light to provide adequate brightness. Consequently, six source lights (Woods 166 L13, 1,000-W telescope work light, CA) were employed in the surroundings of the tank. The credibility of the experiments was verified by three repetitions of all experiments and the uncertainty of the results was shown in different figures by overbars. The high-speed cameras were set to capture images with a frequency of 1000 fps and a resolution of 1280 × 800 pixels. A proper relaxation time of approximately 15 minutes between each experiment was given to eliminate fluid fluctuations and have a stable fluid level. The sketch of experimental setup which includes the position of cameras, source light, side and top views of the solid and annular disks, and the coordinate system are shown in Figure 3.1.

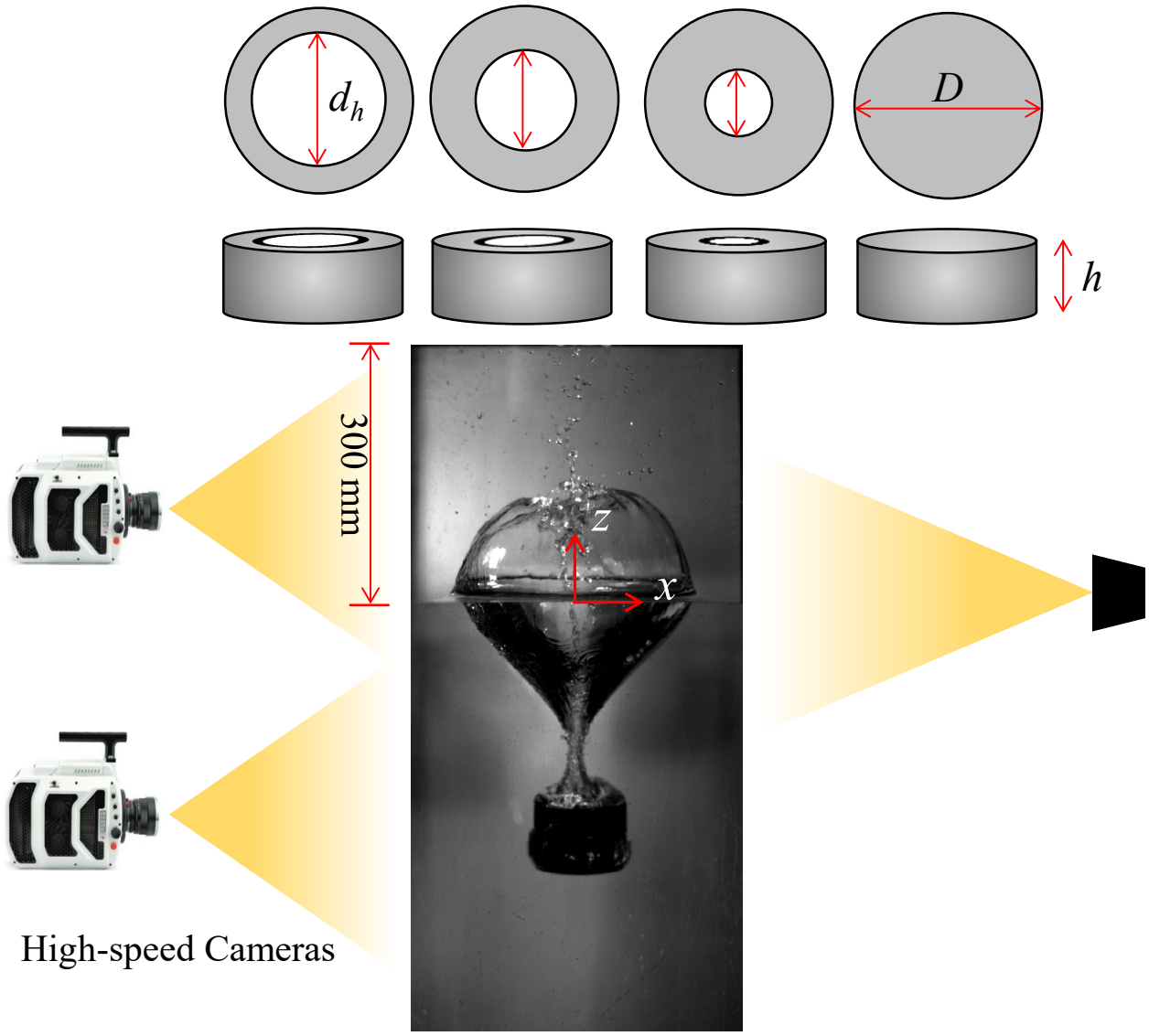

Figure 3.1: Experimental setup of the cylindrical disk entry in stagnant ambient, disk geometry, and the coordinate system.

3.2.2 Fluid properties

Six different fluid mixtures with varying viscosities were prepared to investigate the effects of fluid properties on the entry of solid and annular disks. Preliminary research was conducted to determine the most suitable additives to create fluid mixtures with specific properties. Most of the additives suitable for increasing the viscosity of water without significantly impacting other fluid properties may alter the color and transparency of water and are not environmentally friendly. Additionally, nano additives, are costly, making them impractical for real-world applications and laboratory use. Based on the mentioned constraints, Polyacrylamide (PAM) with different

concentrations was selected and such additive has been successfully used in other research studies Akbarzadeh et al., 2022; Ebrahimi & Sanati, 2021; Ebrahimi et al., 2020; Akers & Belmonte, 2006; de De Goede et al., 2019; Sun, et al., 2019a; Sun, et al., 2019b; Tabuteau et al., 2011). Even at high concentrations, the final fluid remains transparent, it is cost-effective and is considered an eco-friendly additive since it is used for water treatment (Gao, 2013; Jung et al., 2013; Pei et al., 2016; Hu et al., 2017; Kumar et al., 2020; Lu et al., 2021). The Polyacrylamide (PAM) that is used for this study was supplied by the SNF Corporation and its commercial name is FLOPAM AN 934 VHM.

To prepare fluid mixtures with varying viscosities, a known mass of PAM powder was added to a specified volume of water. The PAM concentrations that were exerted to prepare the fluids were C = 0.01% wt.%, 0.05 wt.%, 0.10 wt.%, 0.20 wt.%, and 0.30 wt.%. The viscosities of the prepared fluid mixtures were measured using a Brookfield viscometer (DVPlus viscometer, Massachusetts, USA). Table 3.1 provides the rheological characteristics of the fluid mixture for different polymer concentrations which includes shear stress, shear rate, and viscosity. For a fluid mixture with polymer concentrations of above 0.1 wt.%, the fluid begins to exhibit non-Newtonian behaviour. However, by increasing the polymer concentration from 0 to 0.1 wt.% of PAM, the fluid experiences unstable features, indicating a transition stage to a non-Newtonian flow behaviour. Therefore, in the following, the behavior of the fluid with a polymer concentration below 0.1% follows a different pattern than the fluid with a polymer concentration of more than 0.1 wt.%. The maximum polymer concentration in this study was 0.30 wt.% of PAM.

Table 3.1. Rheological characteristics of the fluid mixture for different polymer concentrations, C (%)

C (%)	*Shear rate* (rpm)	*Shear Stress* (Pa)	*Viscosity* (Pa.s)
0.01	100	1.2	0.012
	50	1.2	0.024
0.05	100	5.4	0.054
	50	3.9	0.078
	20	2.72	0.136
0.10	100	18	0.18
	50	10.9	0.218
	20	6.24	0.312

	10	4.9	0.49
	5	4	0.80
	2	2.2	1.1
0.20	100	52	0.52
	50	36.5	0.73
	20	23.1	1.15
	10	20.2	2.02
	5	15.8	3.16
	2	12.1	6.05
0.30	100	58	0.58
	50	41.5	0.83
	20	30.7	1.53
	10	24.8	2.48
	5	21	4.2
	2	18	9

The aging time for all fluid mixtures was seven days to ensure that all polymer particles were homogeneously placed in the water. The experiments were conducted at the atmospheric pressure and the temperature was kept constant at 25 ^{o}C. The experiments commence with the water entry of all nine disks, followed by repetitions of the same disks in the five pre-prepared fluids to investigate the impacts of viscosity, as well as the influence of density and opening diameter. In total, 72 experiments, excluding the repetition tests, were conducted. An in-house MATLAB code (Mathworks, R2018b, Natick, USA) was used for image analysis and extract the necessary information from the images. In the following, the results of the conducted experiments are presented through identifying features such as pinch-off characteristics, crown properties, disk position and its derivatives.

3.3 Results and Discussion

3.3.1 Fluid viscosity

The time series images of the free-falling solid and annular disks with opening diameters of d_h = 0.015, 0.025, and 0.04 m in stagnant water with various density ratios, and an aspect ratio of D/h = 1.5 are shown in Figures 3.2 to 3.5. The time interval between each image is 0.01 seconds. Four different time histories are chosen to represent the impacts of varying opening diameters on the entry characteristics of annular cylinders. Each time history corresponds to one of the four different opening size, allowing for a detailed analysis, and understanding the effect of opening size on the

entry of solid objects. The time history images are chosen for four different fluid mixtures to study the effect of ambient fluid rheology on crown formation and pinch-off time. The fluid interface phenomena such as crown formation, cavity dynamics, and development of the through-hole jets are visible in these time-series images.

Figure 3.2 illustrates the time-series images of a free-falling annular disk with an opening diameter ratio of d_h/D = 0.53 and a density ratio of ρ_d/ρ_w = 2.50. The sequence begins with the collision of the annular disk with the stagnant fluid. From the early stages of the collision, the formation of a through-hole jet is evident due to the presence of a large hole in the annular disk, and droplets are visible on top of the splash. As time passes, the height of the rising through-hole jet and droplets increases until the advancement reaches the stagnation point. At this point, a dome on the top of the cavity reaches its maximum size and starts to fall due to gravity. Assuming the initial collision time, as captured in the first image, as a reference time of t = 0, the entire disk submerges into the water within 20 milliseconds. Forty milliseconds post-submersion, the splash curtain peaks in height. Subsequently, the height of the splash begins to decrease. It takes a total of 130 milliseconds from the start for the pinch-off event to occur.

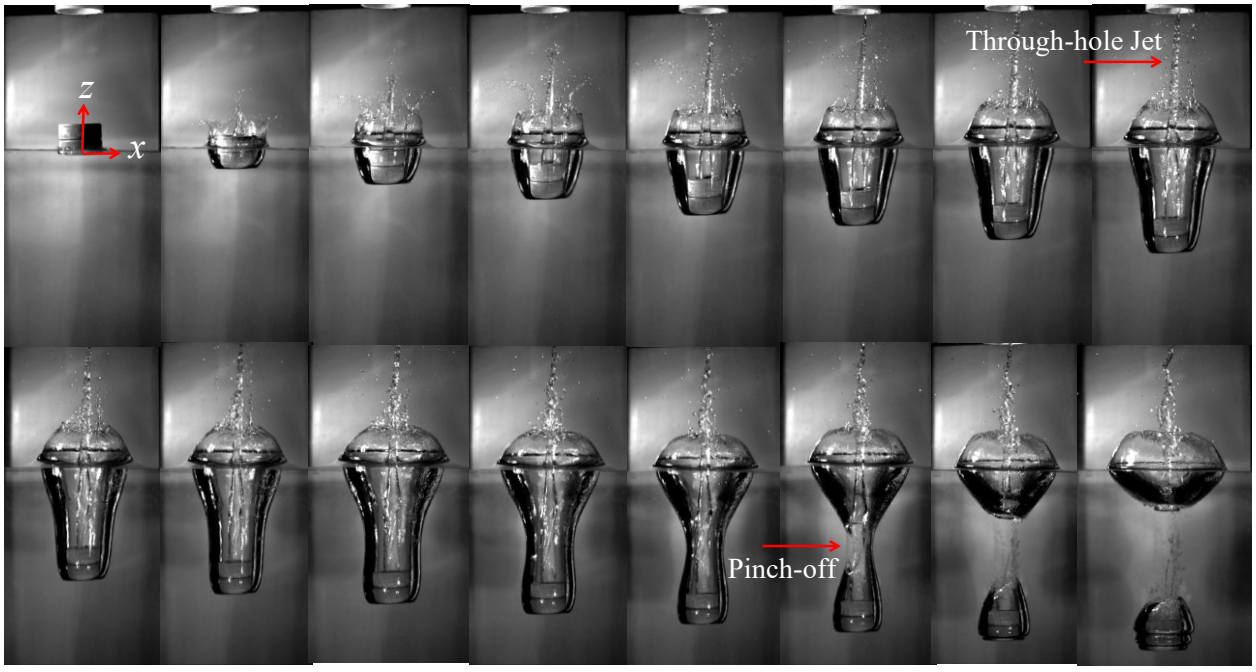

Figure 3.2: Time history images of a free-falling annular disk in stagnant water. The hole diameter ratio of the test, d_h/D = 0.53, ρ_d/ρ_w = 2.50, D/h = 1.5. The time interval between each image is 0.01 seconds.

Time history images of a free-falling annular disk with an opening diameter ratio of d_h/D = 0.33 and density ratio of ρ_d/ρ_w = 2.50 in a fluid mixture with C = 0.10 wt. % PAM concentration is shown in Figure 3. It takes more than 20 milliseconds for the disk with the same features to sink into the fluid mixture when it enters a fluid with a higher viscosity, in comparison with the same disk entering in water (see Figure 3.2). The maximum crown height is observed at 60 milliseconds following the disk's entry into the fluid mixture. The pinch-off occurs at 140 milliseconds, indicating a delay compared to the earlier measurement. It is evident that the crown and splash curtain became smoother, with no further droplets or waves are being visible. By increasing the viscosity, the droplets disappear and change into shapes that are well-known as crown fingers due to the similarities. With the increment in viscosity, the through-hole jet height decreases and is suppressed more quickly (see Figures 3.3 and 3.4). The diameter of the through-hole jet depends on the opening diameter and after the occurrence of the pinch-off, the through-hole jet begins to vanish.

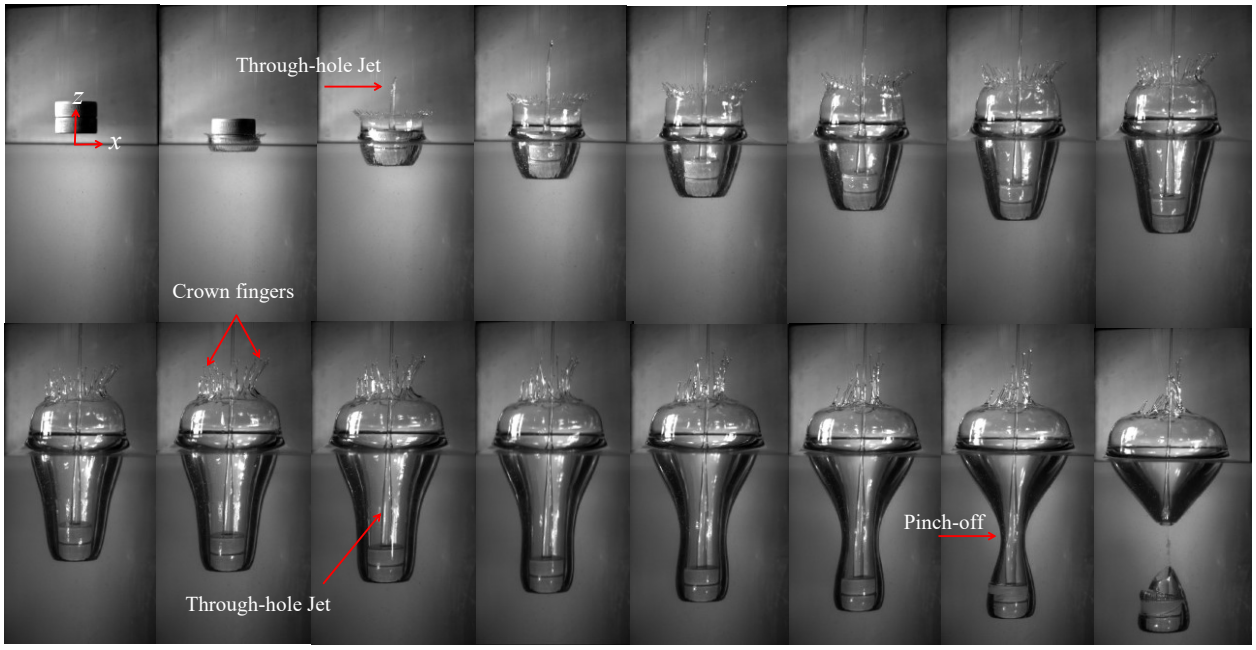

Figure 3.3: Time history images of a free-falling annular disk with a hole diameter ratio of d_h/D = 0.33 in a stagnant fluid mixture with C = 0.10 wt. % PAM concentration. In this test, the density ratio, ρ_d/ρ_w, is 2.50. The time interval between each image is 0.01 seconds.

Figure 3.4 shows the time history images of a free-falling annular disk with an opening diameter ratio of d_h/D = 0.20 and density ratio of ρ_d/ρ_w = 2.50 in a stagnant fluid mixture with C =

0.20 wt. % of PAM concentration. The pinch-off occurs at 140 milliseconds after the collision of the disks with the fluid mixtures and the formation of the through-hole jet is not as intense as the tests with lower polymer concentration. The through-hole jet attenuates fast at approximately 90 milliseconds after the collision of the disks with the fluid mixture. Figure 3.5 shows the time history images of a solid free-falling disk with a density ratio of ρ_d/ρ_w = 2.50 in a fluid mixture with C = 0.3 wt. % PAM concentration. It takes more than 140 milliseconds for the pinch-off moment to occur and since no through-hole jet forms in this test, the pinch-off moment is clear and represents very well in comparison to the situation where there is a through-hole jet. No strings can be seen on top of the crown and the maximum height of the crown is lower than that of previous tests due to relatively high ambient viscosity.

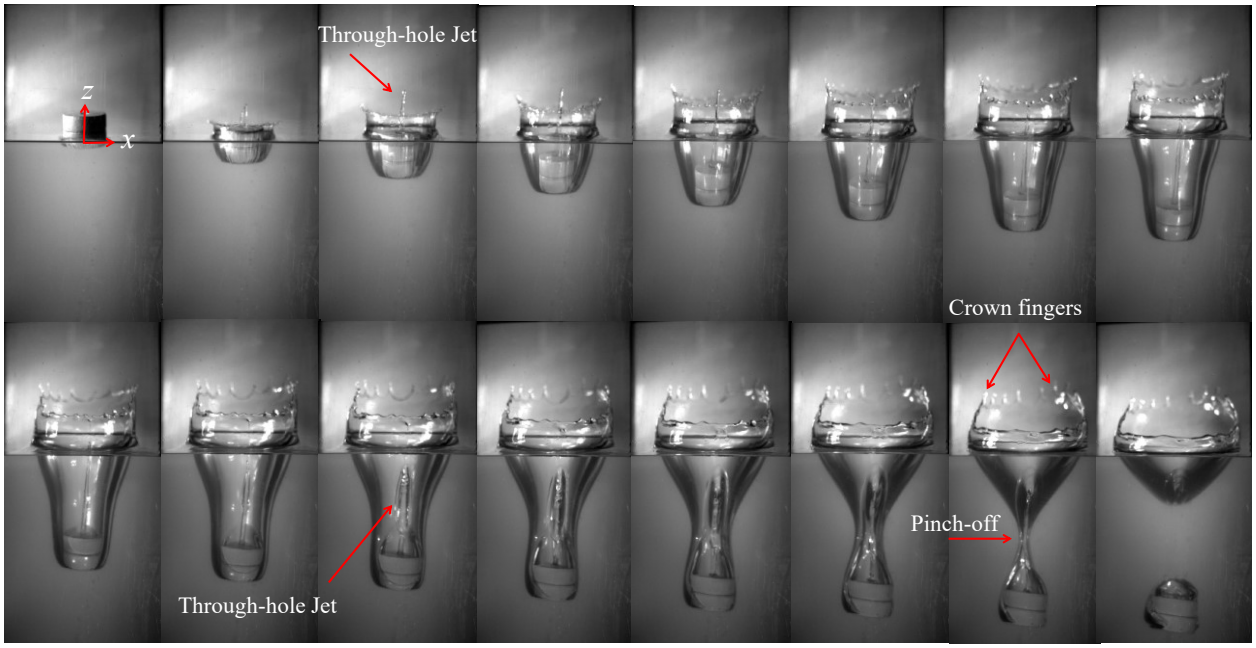

Figure 3.4: Time history images of a free-falling annular disk with a hole diameter ratio of d_h/D = 0.20 in a stagnant fluid mixture with C = 0.2 wt. % PAM concentration. In this test, the density ratio, ρ_d/ρ_w, is 2.50. The time interval between each image is 0.01 seconds.

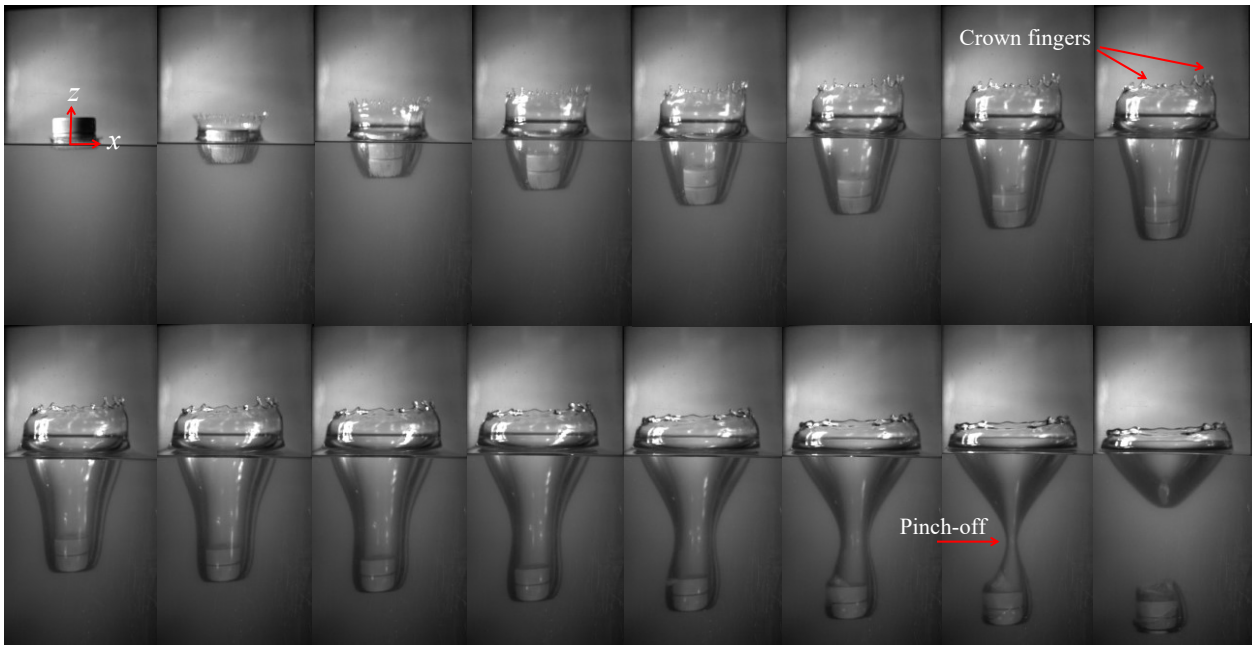

Figure 3.5: Time history images of a free-falling annular disk without hole in a stagnant fluid mixture with $C = 0.3$ wt. % PAM concentration. In this test, $\rho_d/\rho_w = 2.50$. The time interval between each image is 0.01 seconds.

3.3.2 Cavity Pinch-off

Table 3.2 shows the variations of pinch-off and crown characteristics with the geometry of the disk, density ratio, and polymer concentration. Both the pinch-off time and pinch-off depth were measured in all 72 experiments, each considering three different factors of disk density, opening diameter, and fluid viscosity. Figure 3.6 shows the variations of normalized pinch-off time with normalized opening diameter for a wide range of polymer concentrations. The opening diameter was normalized with the diameter of the disk, d_h/D, and pinch-off time was normalized with a characteristic time scale, which is defined as $T = (D/g)^{0.5}$ where g is the gravitational acceleration. The subplots in Figure 3.6, show the correlation between normalized pinch-off time and opening diameter in fluid mixtures with different polymer concentrations. As can be seen, increasing the values of opening size resulted in the reduction of normalized pinch-off time. However, no significant changes were observed for $d_h/D \leq 0.2$ and the reduction of normalized pinch-off time was linear with increasing normalized opening diameter for $d_h/D > 0.2$.

Table 3.2: Variations of pinch-off and crown characteristics with the geometry of the disk, density ratio, and polymer concentration.

Test No.	*C* (%)	ρ_d/ρ_w	d_h/D	t_p/T	h_p/D	h_d/D	V_c/v_e	*Fr*	*Re*
1	0	1.14	0	1.59	1.75	2.20	5.95	2.65	1.67E+05
2		1.48		1.64	1.98	2.78	10.16	3.07	1.94E+05
3		2.50		1.70	2.38	4.01	19.22	3.43	2.17E+05
4		1.14	0.2	1.54	1.80	2.65	7.32	2.33	1.47E+05
5		1.48		1.62	2.07	3.10	10.05	2.91	1.84E+05
6		2.50		1.68	2.39	4.31	19.50	3.64	2.30E+05
7		1.14	0.33	1.49	1.76	2.62	4.95	2.77	1.75E+05
8		1.48		1.59	1.83	3.01	9.89	3.07	1.94E+05
9		2.50		1.66	2.18	4.42	18.71	3.64	2.30E+05
10		1.14	0.53	1.38	1.61	2.38	5.32	2.53	6.37E+03
11		1.48		1.42	2.05	2.94	9.06	2.43	6.89E+03
12		2.50		1.50	2.29	4.11	17.05	3.07	8.08E+03
13	0.01	1.14	0	1.56	1.68	2.18	5.63	2.65	6.98E+03
14		1.48		1.62	1.95	2.58	9.97	2.91	7.67E+03
15		2.50		1.70	2.25	3.78	17.83	3.64	9.59E+03
16		1.14	0.2	1.57	1.61	2.41	5.50	2.91	7.67E+03
17		1.48		1.60	1.89	2.89	9.84	3.24	8.53E+03
18		2.50		1.68	2.15	4.14	17.46	3.64	9.59E+03
19		1.14	0.33	1.51	1.70	2.45	5.43	2.91	3.41E+03
20		1.48		1.54	1.83	2.87	9.74	3.07	3.59E+03
21		2.50		1.61	2.04	3.96	17.18	3.64	4.26E+03
22		1.14	0.53	1.40	1.60	2.34	4.98	3.07	3.59E+03
23		1.48		1.46	1.87	2.84	8.81	3.24	3.79E+03
24		2.50		1.50	2.11	3.80	15.37	3.88	4.55E+03
25	0.05	1.162	0	1.58	1.81	2.27	6.74	2.91	3.41E+03

26		1.498		1.64	2.17	2.86	11.46	3.07	3.59E+03
27		2.551		1.70	2.51	4.17	18.88	3.64	4.26E+03
28		1.137		1.57	1.84	2.73	6.85	2.53	8.91E+02
29		1.466	0.2	1.61	2.20	3.25	11.59	2.77	9.75E+02
30		2.48		1.68	2.40	4.52	21.13	3.43	1.20E+03
31		1.122		1.46	1.70	2.57	6.10	2.77	9.75E+02
32		1.452	0.33	1.51	2.11	3.07	10.47	2.91	1.02E+03
33		2.45		1.61	2.46	4.35	18.37	3.43	1.20E+03
34		1.162		1.36	1.82	2.50	5.33	2.77	9.75E+02
35		1.498	0.53	1.44	2.18	2.90	8.89	2.91	1.02E+03
36		2.551		1.48	2.50	4.08	16.48	3.64	1.28E+03
37		1.14		1.58	1.66	2.16	6.15	2.65	6.45E+02
38		1.48	0	1.61	2.15	2.67	11.26	2.77	6.76E+02
39		2.50		1.68	2.40	3.95	18.66	3.07	7.47E+02
40		1.14		1.57	1.81	2.77	6.34	2.53	6.17E+02
41		1.48	0.2	1.59	2.13	3.12	10.58	2.77	6.76E+02
42	0.1	2.50		1.66	2.44	4.45	18.53	3.07	7.47E+02
43		1.14		1.46	1.71	2.48	5.45	2.16	5.26E+02
44		1.48	0.33	1.53	2.04	2.94	9.85	2.65	6.45E+02
45		2.50		1.60	2.41	4.20	17.88	3.43	8.35E+02
46		1.14		1.34	1.58	2.30	4.11	2.77	3.03E+02
47		1.48	0.53	1.36	1.89	2.66	7.48	2.91	3.18E+02
48		2.50		1.50	2.28	3.89	14.78	3.43	3.75E+02
49		1.14		1.56	1.73	2.11	4.90	2.65	2.90E+02
50	0.2	1.48	0	1.59	1.95	2.40	9.77	2.91	3.18E+02
51		2.50		1.67	2.41	3.73	18.45	3.43	3.75E+02
52		1.14	0.2	1.53	1.61	2.49	4.16	2.77	3.03E+02

53		1.48		1.57	1.93	2.86	9.71	3.07	3.35E+02
54		2.50		1.65	2.32	4.09	18.32	3.64	3.98E+02
55		1.14		1.51	1.53	2.34	3.90	2.65	1.67E+05
56		1.48	0.33	1.52	1.80	2.79	8.55	3.07	1.94E+05
57		2.50		1.57	2.18	3.73	16.48	3.43	2.17E+05
58		1.14		1.49	1.26	1.97	3.00	2.33	1.47E+05
59		1.48	0.53	1.44	1.63	2.44	6.14	2.91	1.84E+05
60		2.50		1.48	2.43	3.68	13.02	3.64	2.30E+05
61		1.14		1.58	1.68	2.07	3.32	2.77	1.75E+05
62		1.48	0	1.60	2.03	2.54	9.30	3.07	1.94E+05
63		2.50		1.66	2.54	3.88	18.08	3.64	2.30E+05
64		1.14		1.54	1.68	2.57	2.60	2.53	6.37E+03
65		1.48	0.2	1.54	2.00	2.57	8.47	2.43	6.89E+03
66		2.50		1.65	2.51	4.29	17.95	3.07	8.08E+03
67	0.3	1.14		1.52	1.41	2.34	2.47	2.65	6.98E+03
68		1.48	0.33	1.49	1.79	2.78	7.70	2.91	7.67E+03
69		2.50		1.57	2.49	3.91	15.59	3.64	9.59E+03
70		1.14		1.42	1.32	2.10	1.04	2.91	7.67E+03
71		1.48	0.53	1.36	1.66	2.46	6.10	3.24	8.53E+03
72		2.50		1.44	2.39	3.58	11.86	3.64	9.59E+03

Disks with higher density experienced a longer pinch-off time, indicating a direct relationship between the density of a solid object and the pinch-off time. These trends are consistent across all fluid mixtures. As the viscosity of the ambient fluid increased, the normalized pinch-off time slightly reduced, and the effect of disk density became less effective. For the fluid with the polymer concentration of 0.20 wt.% and 0.30 wt.%, (see Figures 3.6e and 3.6f), the effects of disk density and opening diameter become non-linear and the pinch-off time in relatively light annular disks became longer than that of relatively dense annular disks. Such contradicting behaviour became

more evident in disks with larger hole diameters (i.e., d_h/D = 0.53). The dependency of pinch-off time on the three understudy factors of density ratio, relative opening diameter, and Reynolds number is illustrated in Figure 3.7. As can be seen, the effect of density ratio is more announced in variations of pinch-off time and the Reynolds number and opening diameter ratio are the secondary and tertiary important parameters. The relationships between the pinch-off time and the understudy parameters are expressed as:

$$t_p/T = 0.136\left[Re^{0.05}(\rho_d/\rho_f)^{0.5}(d_h/D)^{0.005}\right] + 1.295 \quad (1)$$

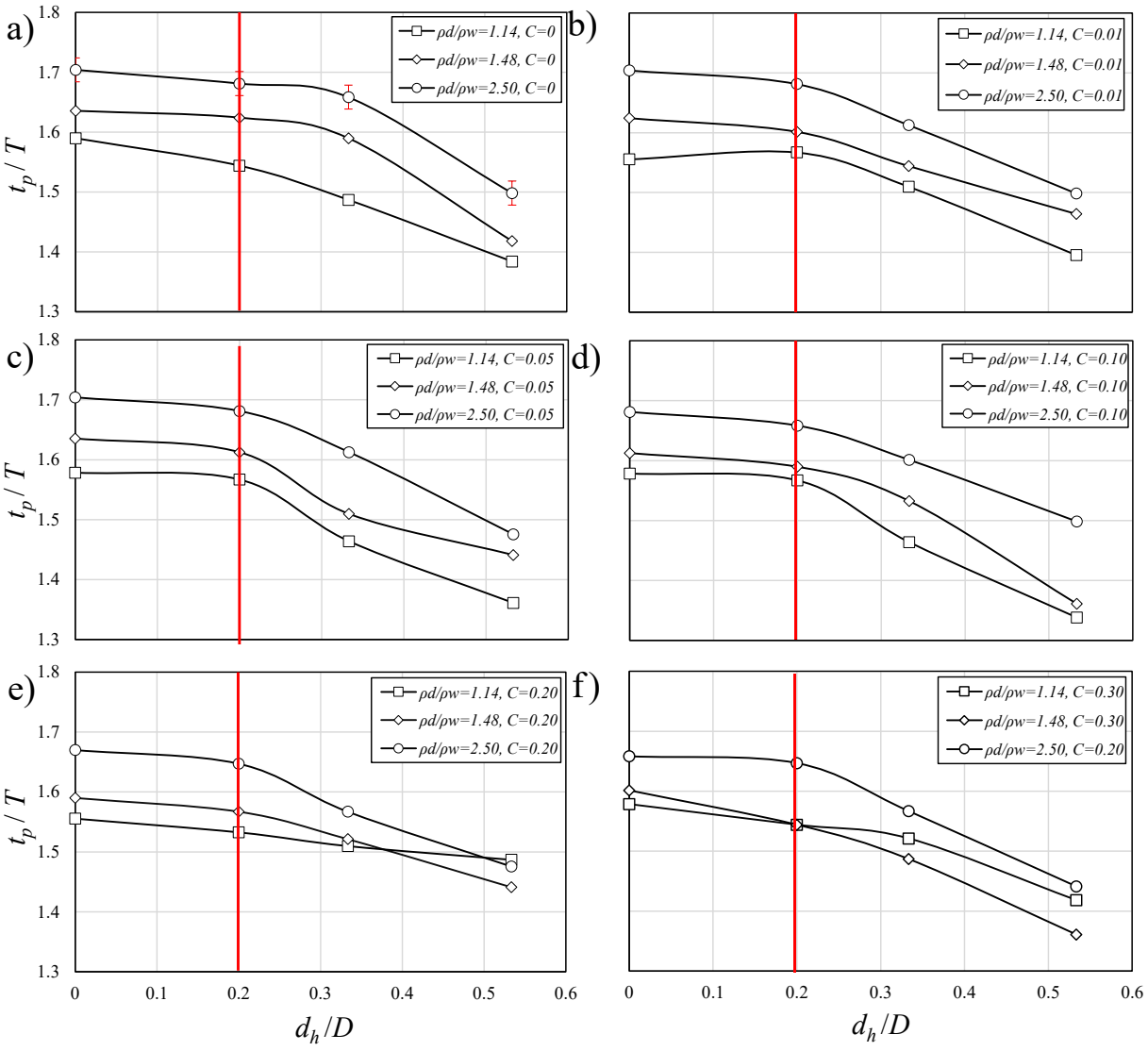

Figure 3.6: Effects of normalized hole diameter, density ratio, and rheological characteristics of the ambient fluid mixture on variations of normalized pinch-off time with the different polymer

concentrations: a) C = 0, b) C = 0.01 % PAM, c) C = 0.05 % PAM, d) C = 0.10 % PAM, e) C = 0.20 % PAM, f) C = 0.30 % PAM.

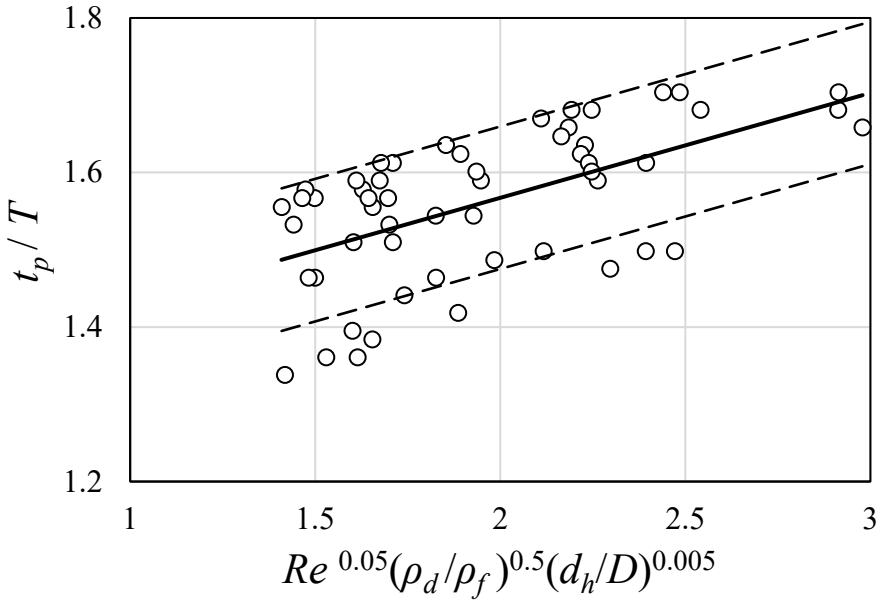

Figure 3.7: Variations of the pinch-off time with combined non-dimensional parameters including relative disk density, normalized disk opening, and Reynolds number, *Re*.

The proposed equation for prediction of normalized pinch-off time is applicable for $1.4 < Re^{0.05}(\rho_d/\rho_w)^{0.5}(d_h/D)^{0.005} < 3$. The two dashed lines show the domain of the variation of the pinch-off time based on the standard deviation of data. Most of the data points seem to be clustered relatively close to the regression line, indicating a reasonably good fit. Most of the data points fall between the dashed lines, indicating that the majority of the data lies within one standard deviation from the mean. This suggests that the data is relatively well clustered around the regression line. The pinch-off moment is governed by the dynamics of cavity formed behind the disk as it enters the fluid. In non-Newtonian fluids, high viscosity reduces the closure of cavity process. The disk's density and impact velocity contribute to the initial cavity size and depth. A denser disk and higher impact velocity leads to a deeper cavity leads to delaying the pinch-off. The equation relates the pinch-off time to the Froude number and the fluid's rheological properties, capturing how momentum transfer and fluid resistance interact during cavity collapse.

3.3.4 Cavity and Crown Evolution

Based on the observation from the time series and snapshot images, the effects of polymer concentration on crown formation and cavity evolution, three different regimes can be identified. From experimental results, it can be deduced that from a polymer concentration range of $C = 0$ (i.e., water) to 0.01 wt.%, there is a discernible decrease on crown dimensions. This indicates that the addition of small concentration of polymer changes the viscosity and yield stress of the fluid mixture, which can reduce the crown dimension due to excess energy losses and fluid resistance as a result of higher viscosity and yield stress. As polymer concentration increases from $C = 0.01$ wt.% to 0.05 wt.%, the crown dimensions expand and achieve their maximum value. It is important to note that the experimental results demonstrate variability across different disk types, indicating that the observed trends are not universally consistent for all applied disks. The energy transferred to the fluid upon collision affects crown formation and energy loss due to viscous dissipation. Higher viscosity leads to greater energy absorption by the fluid and diminishing splash intensity.

For dense disks characterized by a density ratio of $\rho_d/\rho_w = 2.50$, across all three varied opening diameters, the maximum crown height is consistently observed at a polymer concentration of $C =$ 0.1 wt.%. This finding suggests a specific interaction between disk density, opening diameter, and polymer concentration that maximizes the crown height under these conditions. Due to the noticeable increase in the viscosity of the fluid mixture for $C \geq 0.1$ wt.%, the crown height decreases with polymer concentration. As it was mentioned, the trend for the polymer concentration ranging from 0 to 0.01 wt.% caused a reduction in crown size, however such trend is not valid for disks with $d_h / D = 0.53$. It appears that with an increase in the diameter of the opening, the previously mentioned behavior does not follow a linear trend, and the intensity of all measured features diminishes. Such deviation suggests that the opening size significantly influences the dynamics of flow around solid cylinders, resulting in a reduction on the crown height. The cavity formation is primarily driven by the inertial force of the disk overcoming the gravitational force and viscous resistance of the fluid. In non-Newtonian fluids, the viscous behavior facilitates deeper penetration and smaller cavity formation compared to Newtonian fluids. The annular geometry introduces additional complexities, as the central opening allows fluid to flow through the disk, altering the pressure distribution at the cavity. The produced vortex ring affects the stability of the cavity walls and accelerates the pinch-off process (Sarpkaya et al., 1982). The non-Newtonian fluid's elastic properties store part of the kinetic energy, leading to

delayed and dampened crown evolution compared to water. Also, the opening diameter significantly affects the flow through the disk.

Figure 3.8 shows the snapshot images of the water entry of solid and annular disks at the pinch-off moment. The horizontal row (e.g., Figures 3.8a, 3.8b, and 3.8c) shows the effect of disk density for a constant opening diameter ratio and the vertical column (e.g. Figures 3.8a, 3.8d, and 3.8g) shows the effect of opening diameter for a constant density ratio. The pinch-off depth, h_p, and the depth of the disk at the pinch-off, h_d, are shown in Figure 3.8. As can be seen, the pinch-off depth and the size of the crown are directly correlated with the density of the disks. Observations indicate that the pinch-off depth increased with increasing disk density and the crown height slightly decreased with increasing disk density. In addition, increasing density ratio increased the cavity size, which is representative of both pinch-off time and depth. Figure 8 shows that the opening size did not change the pinch-off depth, and it mostly controls the height of the through-hole jet.

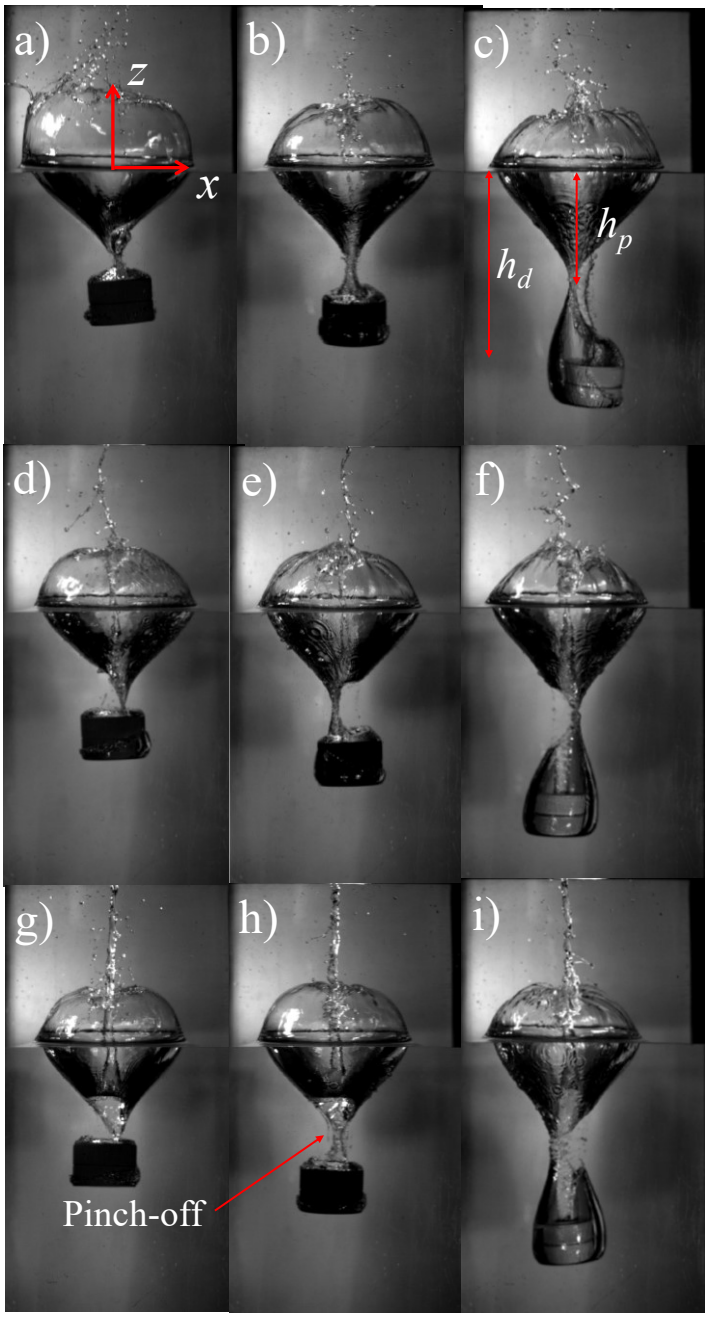

Figure 3.8: Images of fluid entry of disks with different densities and disk hole sizes into water at the pinch-off time: a) $\rho_d/\rho_w = 1.14$ and $d_h/D = 0.20$, b) $\rho_d/\rho_w = 1.48$ and $d_h/D = 0.20$, c) $\rho_d/\rho_w = 2.50$ and $d_h/D = 0.20$, d) $\rho_d/\rho_w = 1.14$ and $d_h/D = 0.33$, e) $\rho_d/\rho_w = 1.48$ and $d_h/D = 0.33$, f) $\rho_d/\rho_w = 2.50$ and $d_h/D = 0.33$, g) $\rho_d/\rho_w = 1.14$ and $d_h/D = 0.53$, h) $\rho_d/\rho_w = 1.48$ and $d_h/D = 0.53$, i) $\rho_d/\rho_w = 2.50$ and $d_h/D = 0.53$.

Figure 3.9 shows the effects of disk density and opening diameter on the entry of annular disks into a non-Newtonian fluid mixture with a polymer concentration of $C = 0.30$ wt.%. The

pinch-off depth, h_p, and the depth of the disk at the pinch-off, h_d, are labeled in one of the images in Figure 3.9. As can be seen, increasing the viscosity of fluid mixture reduced the height of the curtain wall. The size of the formed curtain and the height of the through-hole jets became smaller in the solid entry into a fluid mixture with a polymer concentration of $C = 0.30$ wt.%. The through-hole jet did not form for $d_h/D \geq 0.33$ except in a relatively light disk (see Figure 3.9d). The height of the through hole jet was found to be proportional to the disk density ratio and it increased with increasing ρ_d/ρ_w.

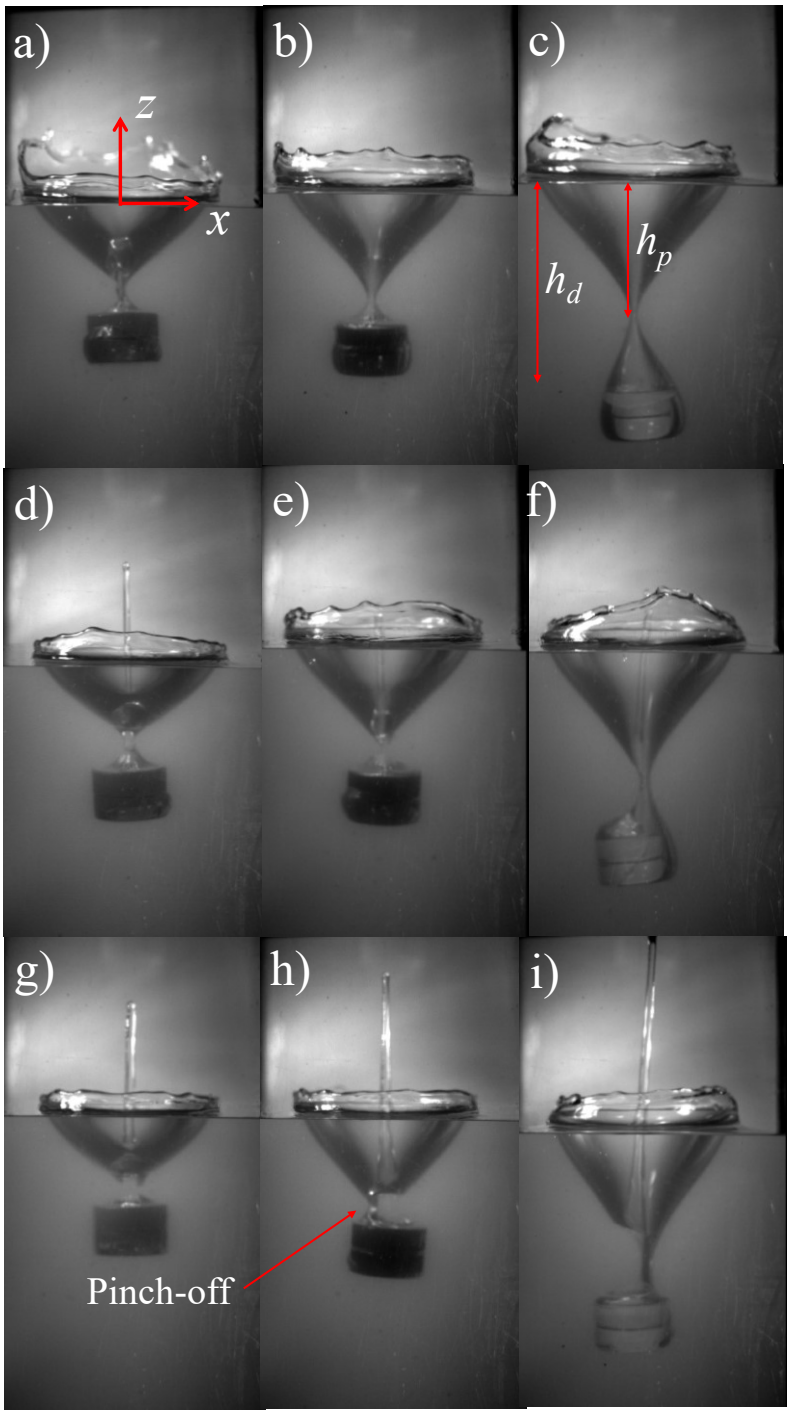

Figure 3.9: photos of the fluid entry of the disks with different densities and disk hole sizes into a fluid mixture with polymer concentration of 0.30 wt.% at the pinch-off time: a) $\rho_d/\rho_w = 1.14$ and $d_h/D = 0.20$, b) $\rho_d/\rho_w = 1.48$ and $d_h/D = 0.20$, c) $\rho_d/\rho_w = 2.50$ and $d_h/D = 0.20$, d) $\rho_d/\rho_w = 1.14$ and $d_h/D = 0.33$, e) $\rho_d/\rho_w = 1.48$ and $d_h/D = 0.33$, f) $\rho_d/\rho_w = 2.50$ and $d_h/D = 0.33$, g) $\rho_d/\rho_w = 1.14$ and $d_h/D = 0.53$, h) $\rho_d/\rho_w = 1.48$ and $d_h/D = 0.53$, i) $\rho_d/\rho_w = 2.50$ and $d_h/D = 0.53$.

The dimensions of through-hole jets vary with changes in the rheological characteristics of fluid mixture, disk opening diameter, and disk relative density. As the disk density increases, the height of the through-hole jet increases as well, indicating a direct relationship between disk density and jet vertical extension (see Figure 3.9g-3.9i). Additionally, the disk opening plays a critical role; a reduction on disk opening diameter leads to a decrease in the diameter of the through-hole jet. This suggests that the geometrical configuration of the disk significantly influences the fluid dynamics, particularly affecting the spatial characteristics of the jet ejecting from the disk's opening. The polymer concentration significantly impacts the dynamics of the through-hole jet, exhibiting a variety of trends. The impact of a disk with an opening generates an unstable through-hole jet with several droplets indicating a high level of turbulence and energy losses (Figure 8). As the viscosity of the mixture slightly increases, the height of the through-hole jet increases and the surrounding surface of the jet and the crown's surface become more stable and smoother. It is expected that a slight increase in the viscosity of the fluid mixture reduces the instability and turbulence level hence decreases the energy losses and therefore, a higher through-hole jet may result in. A further increase on polymer concentration (i.e., larger than 0.20 wt.%), showed a discernible decrease in the height of the through-hole jets. At higher range of polymer concentration, the addition of viscosity and yield stress overcomes the fluid stability and the height of the through-hole jet decreases with increasing polymer concentration. A complex relationship exists between the addition of viscosity due to polymer concentration and the dynamics of the though-hole jet and crown formations which requires further attention.

Cavity bubble dynamics has been studied comprehensively (theoretically, numerically, and experimentally) in a variety of conditions such as liquid compressibility, phase transition, migration, ambient flow field (Yu et al., 2022, 2021; Bokman et al., 2022; Choi et al., 2023; Wang et al., 2023; Han et al., 2024; Zhang et al., 2024). The transient dynamics model is fundamental to investigate the physics of a single cavitation bubble. However, the introduced models cannot be employed to investigate the cavity bubble dynamics that is formed due to the entry of solid objects into a fluid since the bubble generation is different to the ones that have already known.

The formation of the bubble is not concurrent with the initial collision of the solid object with the fluid surface. Instead, the bubble forms as the solid object continues to sink into the fluid, indicating a delayed onset of cavitation. Based on the observations through this study, the

formation of the bubble is highly dependant on the fluid properties, disk density, and the disk hole size ratio. While the density of the disk increase, the number of the formed bubble increments as well because the denser disk entraining more air into the fluid mixture. Also, rising the fluid viscosity cause the bubble formation to lesson since the higher viscosity cease the bubble to be detached from the disk. The bubble detached from the disk in later time than then ones with lower viscosity. Also, While the fluid viscosity is low (water and C < 0.10 wt.%), bubbles are formed in a shedding formation where they appear densely packed at the top of the disk. Conversely, this phenomenon is scarcely observed in fluids with higher viscosity, where the denser medium inhibits such extensive bubble formation. An increase in the viscosity of the fluid mixture causes the formed bubbles to be larger in its size in comparison to the ones that are formed in the fluid with lower viscosity.

3.3.5 Disk depth at Pinch-off time

The dependency of the normalized pinch-off depth with the understudy factors and for the disk entry into a fluid mixture with C = 0.3 wt.% PAM is shown in Figure 3.10. The vertical axis shows the variations of normalized pinch-off depth, h_p/D, and the horizontal axis shows the variations of normalized disk opening diameter, d_h/D. Each subplot in Figure 10 shows the correlation between the pinch-off depth and normalized opening diameter for different values of disk density ratio. The overbars in Figure 3.10a show the range of experimental uncertainty for measuring the pinch-off depth. As can be seen, normalized pinch-off depth remained almost invariant with the variations of normalized opening diameter for $d_h/D \leq 0.20$ and it dropped with increasing the opening diameter ratio. For the transition of the opening size ratio from 0.20 to 0.33, while the density ratios are equal to 1.14, and 1.48, the pinch-off depth experiences a sharp drop in its magnitudes. For the disks with a density ratio of 2.50, the pinch-off depth decreased with a smaller rate than that of relatively lighter disks. Regardless of the variations of normalized opening diameter, the normalized pinch-off depths were higher due to the entry of denser disks. The ranges of pinch-off depth were between 2.3 and 2.55, 1.6 and 2, and 1.3 and 1.7 times of the disk diameter for ρ_d/ρ_w = 2.50, 1.48, and 1.14, respectively. However, the intensity of reduction in values of normalized pinch-off depth was found to be correlated with other factors such as fluid viscosity and disk density. The reduction in the magnitude of pinch-off depth for disks with a density ratio

of 1.14 was found to be higher than that of relatively denser disks. The disks with a density ratio of 2.50 was found to be less variant on the pinch-off depth in comparison to relatively lighter disks.

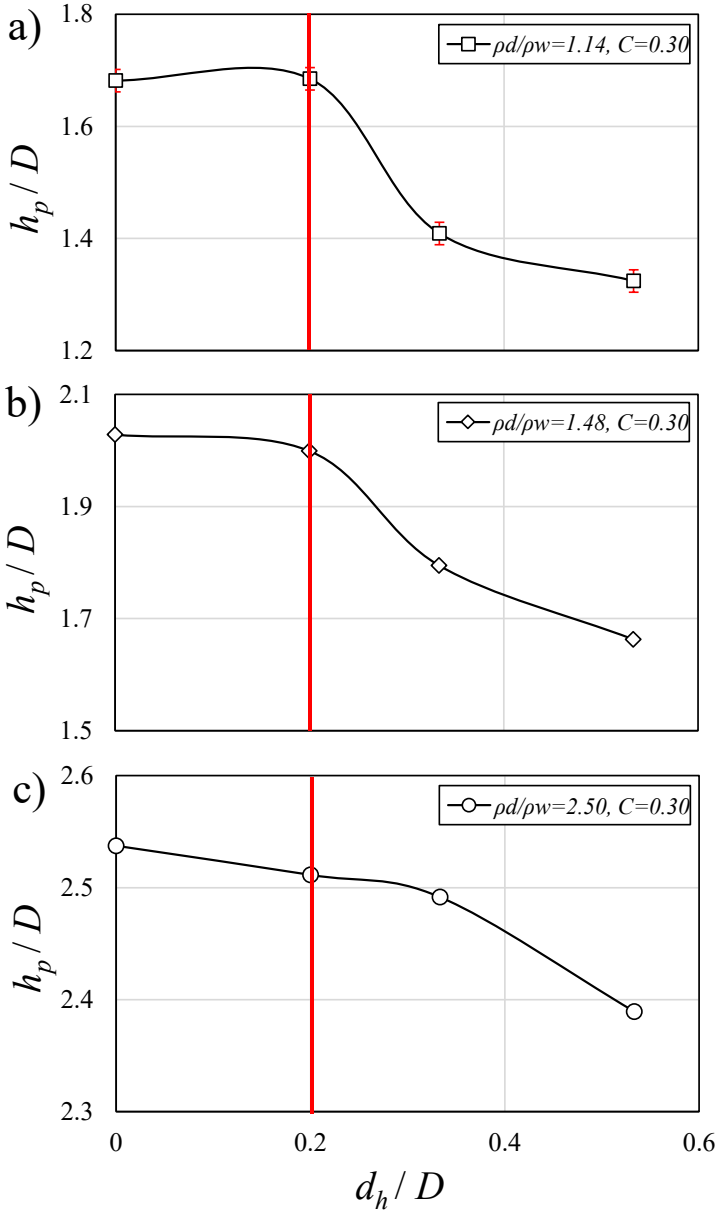

Figure 3.10: Effects of hole diameter and density ratio on variations of the normalized pinch-off depth for disk entry into a stagnant fluid mixture with C = 0.3 wt.% PAM concentration while the disk density ratio varies: a) ρ_d/ρ_w = 1.14, b) ρ_d/ρ_w = 1.48, c) ρ_d/ρ_w = 2.50.

The values of the disk depth at the pinch-off moment were extracted from the images and the results were listed in Table 3.2. The trend and variations of the disk depth at the pinch-off time

were almost the same as the variations of the pinch-off depth. This can be seen in correlation of normalized pinch-off depth with disk density ratio in Figure 3.11a where the pinch-off depth, h_p, and disk depth at the pinch-off, h_d, were normalized with the disk diameter, D. Dimensionless pinch-off depths, h_p/D, are shown by solid circles, and dimensionless disk depths, h_d/D, are shown by open circles in Figure 3.11a. The trendlines are plotted for both dimensionless pinch-off depth and disk depth at the pinch-off. The best-fitted equations for both trends were exponential models, and the curves are plotted in Figure 3.11a as well. As can be seen, increasing the disk density ratio has a greater impact on variations of the disk depth at the pinch-off moment than the pinch-off depth since the slope of correlation regarding the disk depth at the pinch-off is higher than that of the pinch-off depth. Two equations were proposed for prediction of normalized pinch-off depth and disk depth at the pinch-off moment which are expressed as:

$$h_p/D = 1.30exp^{0.242(\rho_d/\rho_w)} \tag{3.2}$$

$$h_d/D = 1.59exp^{0.383(\rho_d/\rho_w)} \tag{3.3}$$

The relationship between the disk depth at the pinch-off time and the pinch-off depth was plotted and the results are shown in Figure 11b. The proposed equations for prediction of pinch-off depth by Duclaux et al. (2007) and Mansoor et al. (2014) are also added for comparison. Experimental data indicated an exponential correlation between h_p and h_d and the correlation can be expressed by an exponential model as:

$$h_d/D = 0.80exp^{0.661(h_p/D)} \tag{3.4}$$

The ratio of the pinch-off depth over the disk depth at the pinch-off was modeled by Mansoor et al. (2014) who illustrates that the ratio of pinch-off depth over the disk depth at the pinch-off time is $h_p/h_d = 0.5$. Duclaux et al., (2007) claimed that this ratio is equal to $h_p/h_d = 0.45$. As can be seen, the values of h_p/h_d in this study vary between 0.49 and 0.78 where the influence of the fluid properties and opening size can be seen by comparing the range values of the current study and the presented models.

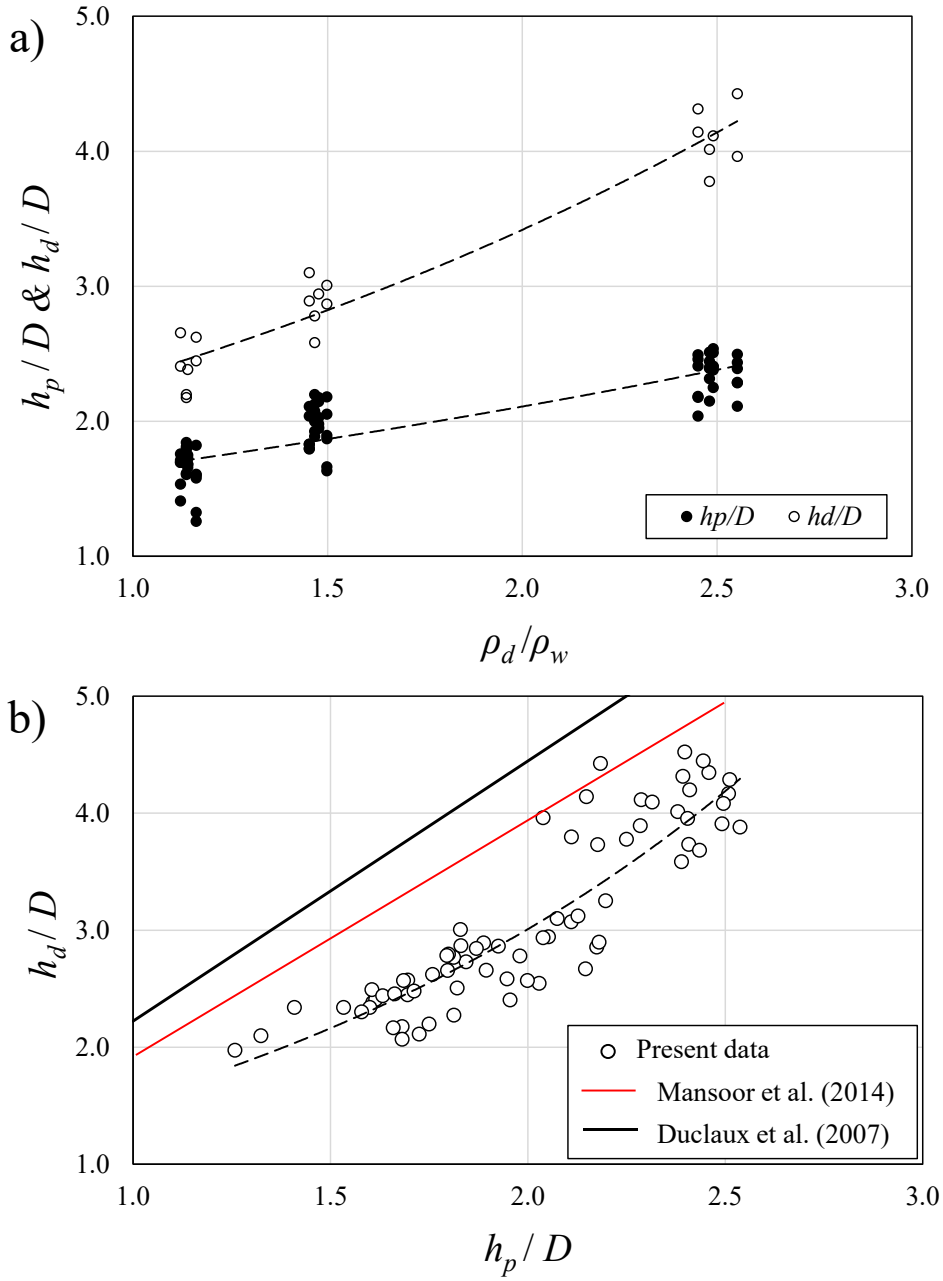

Figure 3.11: Variations of normalized pinch-off depth and disk depth with density ratio: a) effect of density ratio on variations of pinch-off and disk depths, b) correlation between pinch-off depth and disk depth at the pinch-off time.

Variations of the pinch-off depth, disk depth at the pinch-off moment, and their ratio with the combined non-dimensional parameters including the relative disk density, normalized disk opening diameter, and Reynolds number are shown in Figure 3.12. As can be seen, a combination of the mentioned parameters with different powers indicates the relative importance of the

controlling parameters. The sold line in Figure 3.12 representing the best fit of data and the dashed lines shows the ±1 standard deviation from the average. As can be seen from Figure 3.12a, both normalized pinch-off depth and disk depth at the pinch-off increases linearly with the disk Reynolds number, density ratio, and normalized opening diameter and considering the powers of variables in horizontal axis indicates that the effect of relative disk density is more pronounced. Figure 3.12b shows the correlation between the ratio of pinch-off depth to disk depth at the pinch-off (see Figure 3.9c) with the controlling parameters. As can be seen, the correlation between h_p/h_d is linear with an adverse slope. The boundaries of ±1 standard deviation from the average indicate the spread of data around the regression line. Most data points are located within the two dashed lines, indicating a moderate variability in the dataset. The quite narrow gap between these bounds suggests that the data is tightly clustered around the regression line, with minimal deviation. This implies that the model effectively captures the underlying linear trend as:

$$h_p/D = 0.488\, Re^{0.05}(\rho_s/\rho_f)^{0.5}(d_h/D)^{0.005} + 1.064 \tag{3.5a}$$

$$h_d/D = 1.538\, Re^{0.05}(\rho_s/\rho_f)^{0.5}(d_h/D)^{0.005} + 0.138 \tag{3.5b}$$

$$h_p/h_d = -0.148\, Re^{0.05}(\rho_s/\rho_f)^{0.5}(d_h/D)^{0.005} + 0.948 \tag{3.5c}$$

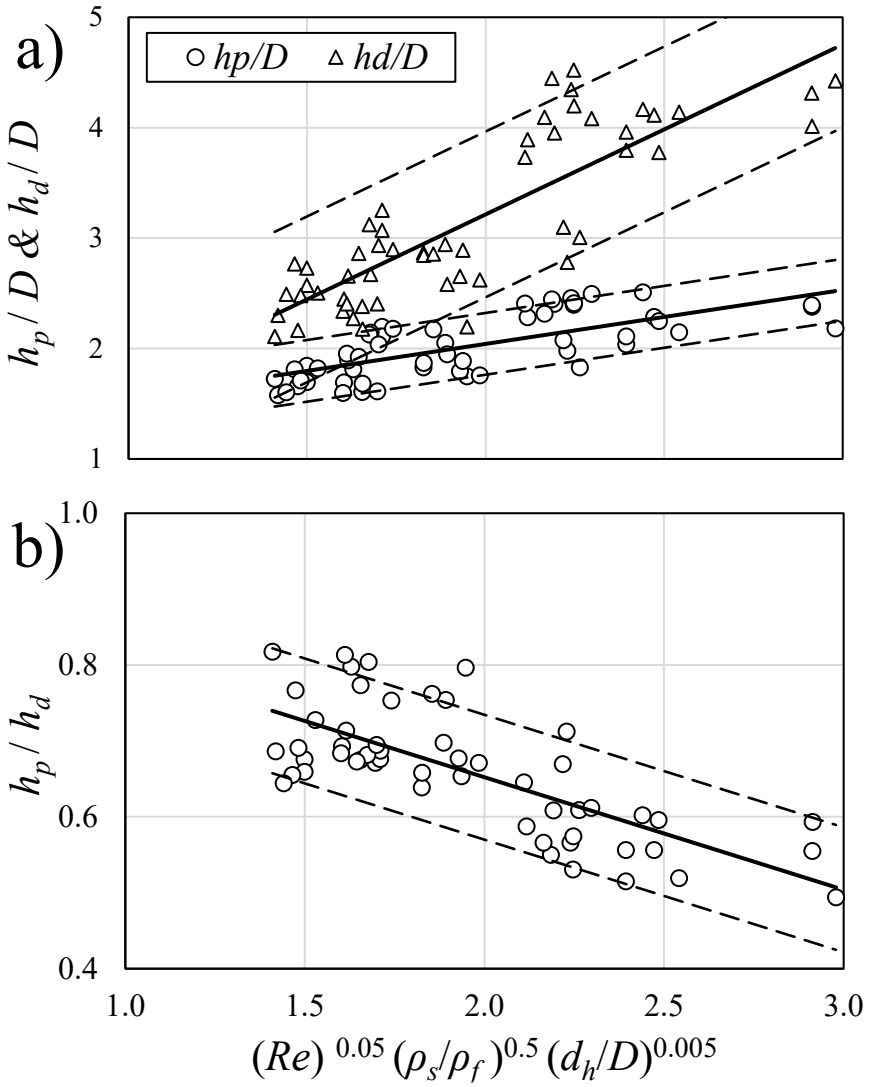

Figure 3.12: Variations of the pinch-off depth, disk depth at pinch-off moment, and their ratio with combined non-dimensional parameters including relative disk density, normalized disk opening, and Reynolds number

3.3.6 Sinking Velocity

The effect of controlling parameters and disk geometry on the surface impact and dynamics of cylindrical disks are studied by focusing on variations of the sinking velocity of disks. Figure 13 shows the variation of sinking velocity with polymer concentration for cylindrical disk with different density ratio and opening diameters. The sinking velocity was normalized with the characteristic disk velocity (i.e., $Ve = \sqrt{\rho_d A/2mg}$, where m is the mass of the disk, ρ_d is the disk

density, A, and g are the area of the disk and gravitational acceleration, respectively). Figure 13 consists of four plots, each showing the variations of dimensionless sinking velocity versus polymer concentration as a representative of fluid viscosity. The impacts of opening diameter and disk density are also investigated in Figure 3.13. The variations of sinking velocity with polymer concentration indicate the existence of two different dynamic regimes. As polymer concentration increases from 0 (i.e., water) to 0.01 wt.% of PAM, normalized sinking velocity decreases in all experiments. Such reduction in normalized sinking velocity reaches to a local minimum at the polymer concentration of 0.01 wt.%. Subsequently, as polymer concentration increases from 0.01 wt.% to 0.05 wt.%, an intense growth of sinking velocity is observed, contrasting with the previous reduction. Upon reaching a concentration of 0.05 wt.% and higher, the sinking velocity begins to decrease again, but at nearly a constant rate. However, by comparing Figures 3.13a, 3.13b, and 3.13c, it can be deduced that the intensity of variations in normalized sinking velocity is affected by other parameters, such as opening size and disk density.

As it was mentioned on the dynamics of through-hole jets, a slight addition of polymer concentration increases the height of the through-hole jet and such high displacement of fluid causes higher rate of energy losses. As a result, the remaining energy after cavity, crown formation and the motion of through-hole jet becomes smaller which results in slightly smaller sinking velocity. As polymer concentration increases, the viscosity effect overcomes the surface instability, and less energy is dissipated through impact and crown formation. Therefore, the remaining energy becomes higher at the sinking stage and the sinking velocity of the disk increases. Further increase in polymer concentration increases the viscosity of the fluid mixture and increases energy losses not only during impact and crown formation, but also during the descending phase. As a result, further increasing polymer concentration directly reduces the normalized sinking velocity.

As can be seen in Figure 3.13, the magnitude of normalized sinking velocity is directly correlated with the disk density and an adverse correlation was observed with the opening diameter of the disks. Figure 3.13a shows that the domain of normalized sinking velocity for the light disks varies between 1 and 7, with three graphs representing different disk opening diameters. For the medium-density disks, normalized sinking velocity varies between 6 and 12 (Figure 3.13b), and for the dense disks, it varies between 12 and 21 (Figure 3.13c). Figure 3.13d shows the effect of

disk density on variations of normalized sinking velocity with variations of polymer concentration for d_h/D = 0.53. The rate of reduction of normalized sinking velocity with increasing polymer concentration is similar for disks with different densities and the magnitude of sinking velocity is affected by the density of disks. For a polymer concentration of 0.1 wt. %, by increasing the density of disks by 1.7 and 2.2 times the normalized sinking velocity increased by 2 and 3.3 times, respectively. The same relationships can be extracted from Figure 3.13d for higher polymer concentrations.

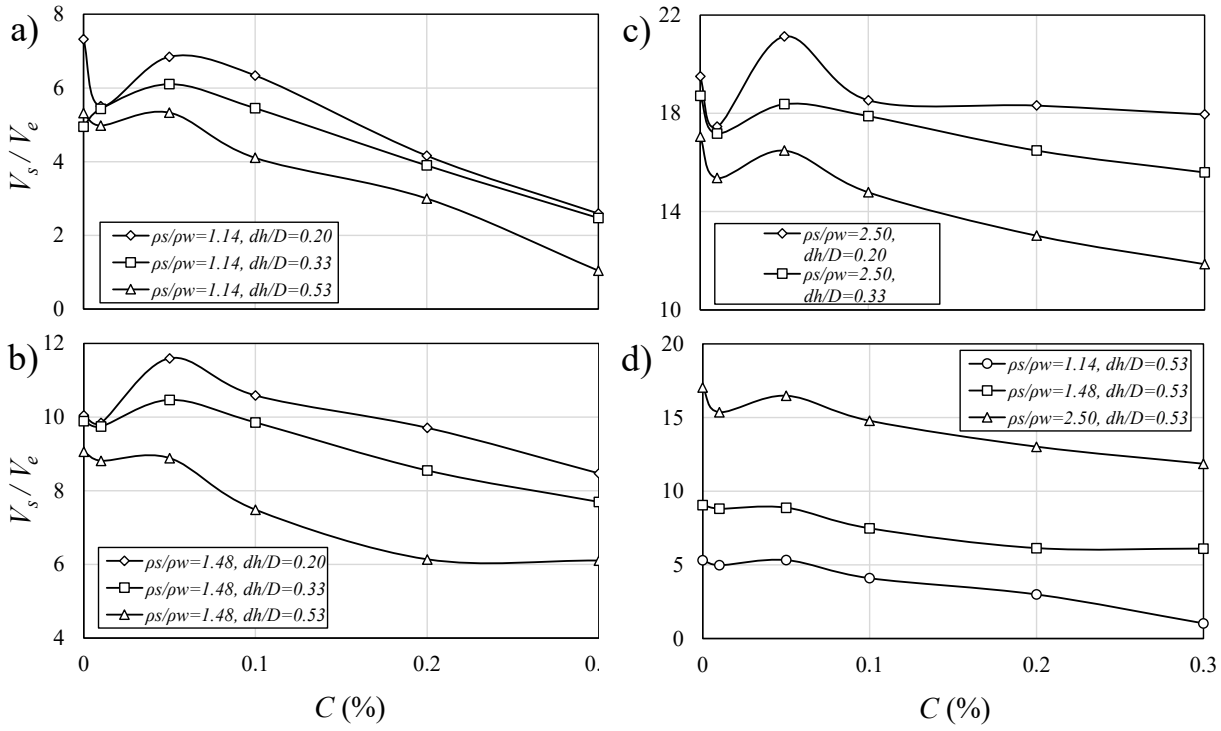

Figure 3.13: Effects of disk opening and density ratio on variations of the dimensionless sinking velocity for different and constant hole size ratio of d_h/D = 0.53.

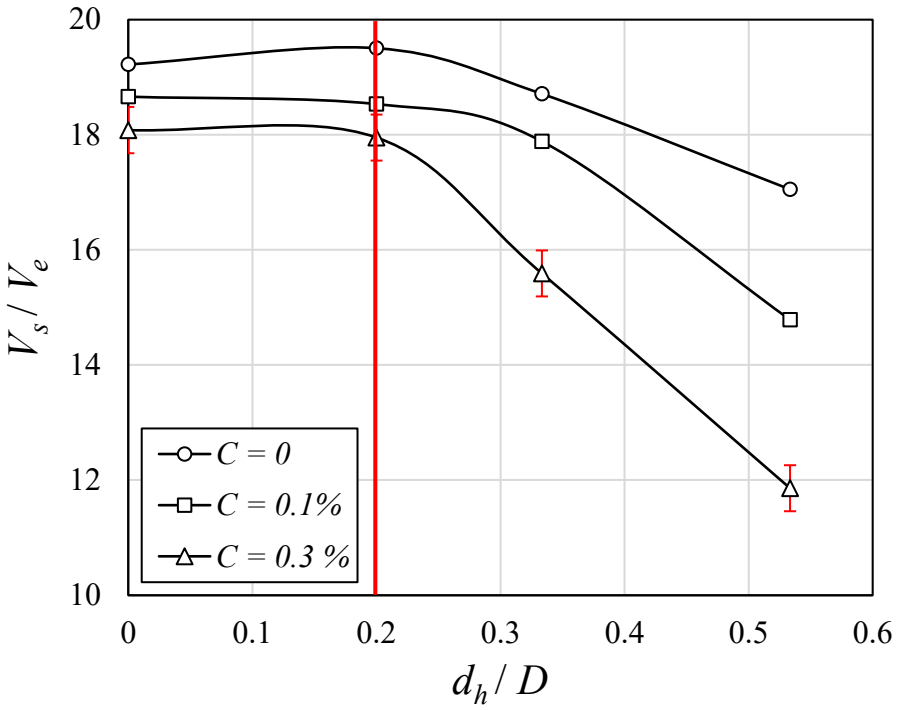

Figure 3.14: Effect of polymer concentration on correlation between normalized sinking velocity and normalized opening diameter of disks for $\rho_d/\rho_w = 2.50$.

Figure 3.14 shows the effect of opening diameter on variations of normalized sinking velocity with different polymer concentration, C for $\rho_d/\rho_w = 2.50$. The three fluid mixtures illustrated are water (i.e., 0 wt.% polymer concentration), a fluid mixture with a medium polymer concentration of 0.10 wt.%, and a fluid mixture with the highest polymer concentration of $C = 0.3$ wt.%. As can be seen, the opening diameter is ineffective for $d_h/D \leq 0.2$ and once the normalized opening passed the threshold, normalized sinking velocity decreased with increasing normalized opening diameter. In other words, an increase in opening diameter ratio results in a decrease in normalized sinking velocity, and such observation is valid across all disks relative densities. However, the magnitude and intensity of such reduction vary with polymer concentration. Among the three different disk opening diameters, the variation in sinking velocity shows that the smallest hole size ratio ($d_h/D = 0.2$) exhibits the lowest reduction. On the other hand, the reduction in sinking velocity becomes more significant as the hole size diameter ratio increases from 0.2 to 0.53. The formation of relatively large through-hole jet and flow disturbance at the wake of the disk cause additional turbulence and hence higher rate of energy dissipation. The higher energy dissipation due to fluid

instability and vortex formation at the rear of the disk may results in higher energy losses and the remaining energy results in smaller sinking velocity. It can also be deduced that increasing fluid mixture viscosity due to higher polymer concentration causes a further reduction in sinking velocity compared to an ambient with lower fluid viscosity. While the disk opening size ratio increases from 0 to 0.53, the sinking velocity diminishes by approximately 33%, 19%, and 10.5% for fluid mixtures with a polymer concentration of 0.30, 0.10, and 0 wt.% of PAM, respectively. Figure 3.15 represents the variations of the normalized sinking velocity with variations of all the understudy parameters. Similar to pinch-off depth, variation of sinking velocity is mostly affected by the disk's density ratio and less affected by the opening diameter. As linear correlation was obtained from multi-regression analysis to predict sinking velocity of cylindrical disks with different density and opening diameters as:

$$V_s/V_e = 10.99\left[Re^{0.05}(\rho_s/\rho_f)^{0.5}(d_h/D)^{0.005}\right] - 10.26 \quad (3.6)$$

It is important to predict the impact velocity of a cylindrical disk knowing the disk's geometry such as disk's diameter, density, opening diameter and the rheological characteristics of the ambient fluid. The impact velocity and disk's diameter are represented by the Froude number at the impact as $Fr = u_i/(gD)^{1/2}$. Figure 16 shows the variations of Froude number with combined non-dimensional parameters including relative disk density, normalized disk opening, and Reynolds number. The relationship between the variables appears to be positive, as the Froude number increases with the combined parameter on the horizonal axis of Figure 16. The data points are scattered but generally follow the fitted trend line. Most of the data points are contained within a standard deviation from the average indicating that the variability of the data is moderate. A linear equation was proposed for prediction of impact velocity and the standard deviation domain suggests that the fitted model captures the data trend effectively.

$$Fr = 0.76\left[Re^{0.05}(\rho_s/\rho_f)^{0.5}(d_h/D)^{0.005}\right] + 1.55 \quad (3.7)$$

The sinking velocity results from the balance between gravitational forces and resistive forces from the fluid (i.e., viscous drag and elastic stresses in non-Newtonian fluids). The hole size in annular disks affects the flow of fluid through the disk, altering pressure distribution and reducing drag forces compared to solid disks. The equation connects sinking velocity with disk density, hole size, and fluid viscosity, reflecting how such parameters influence the net force acting on the disk.

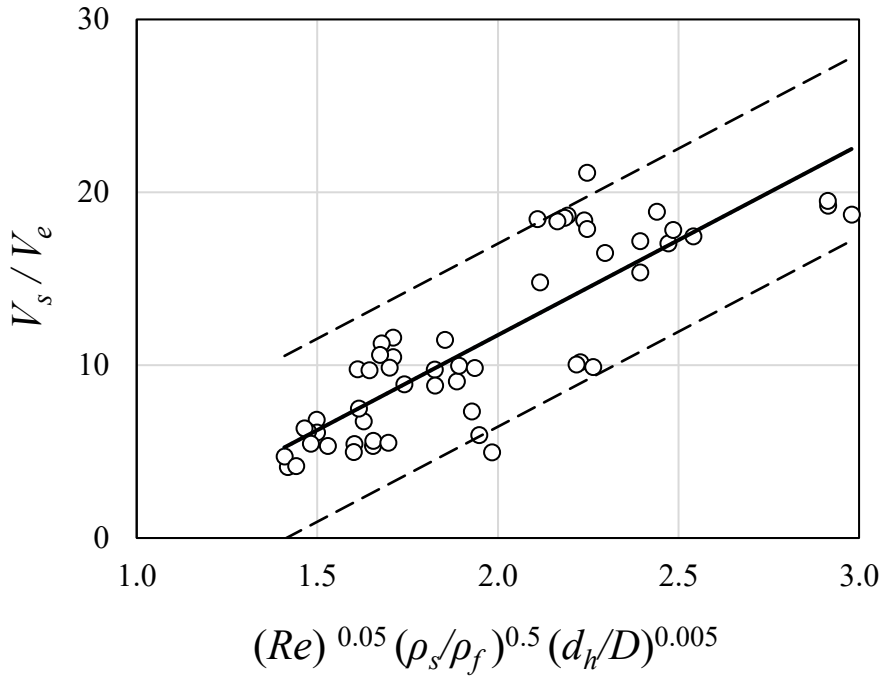

Figure 3.15: Variations of the normalized sinking velocity with combined non-dimensional parameters including relative disk density, normalized disk opening, and Reynolds number

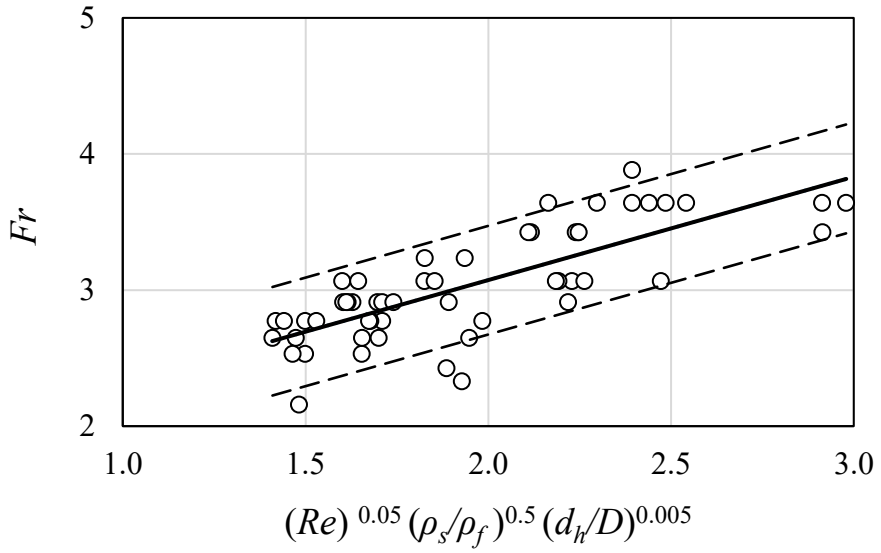

Figure 3.16: Variations of the Froude number with combined non-dimensional parameters including relative disk density, normalized disk opening, and Reynolds number.

3.3.6 Through-hole jet

The through-hole jet dimensions are illustrated in Figure 3.17 where three plots regarding the dimensionless through-hole jet diameter (D_{THJ}/D) and normalized height (H_{THJ}/D), which are

normalized with diameter of the disk concerning the disk density ratio, disk hole size ratio, and fluid properties in figures 3.17a, 3.17b, and 3.17c, respectively. Figure 3.17a represents the disk hole size ratio and fluid mixture kept constant and equal to 0.53 and water while the disk density ratio varies with the three under-study available densities. as can be seen in Figure 3.17a, both diameter and height of the through-hole jet vary with the density ratio of the disks and both parameters increase with increments on the disk density ratio. Figure 3.17b presents the through-hole jet diameter and height with respect to the disk hole size ratio for water and disk density ratio of 1.14. The graph belongs to the disk hole size ratio of 0.53 stands on top of the other followed by the density ratios of 0.33 and 0.20. The variations of through-hole jet diameter and height in different fluid properties are complicated. As the concentration increases, the jet diameter ratio decreases more rapidly. This implies that higher concentrations of the polymer in the fluid contribute to a faster reduction in jet diameter with height in the beginning, which could be due to increased viscosity or other rheological changes affecting the fluid flow dynamics through the hole. Such variation changes after a certain height of the jet, which indicates that the jet diameter formed in a higher threshold fluid viscosity, the tendency of the jet to maintain its shape and size due to higher cohesion between the fluid. It was observed that the increment in the height of the through-hole jet leads the through-hole jet diameter to decrease unanimously, which starts with a diameter equal to the disk hole diameter and zero through-hole jet height. It was observed that annular disks entering non-Newtonian fluids produce unique through-hole jets whose characteristics depend on the hole size and fluid viscosity. The jets in non-Newtonian fluids exhibit different shapes and velocities compared to those in Newtonian fluids, due to the fluid's viscoelastic properties.

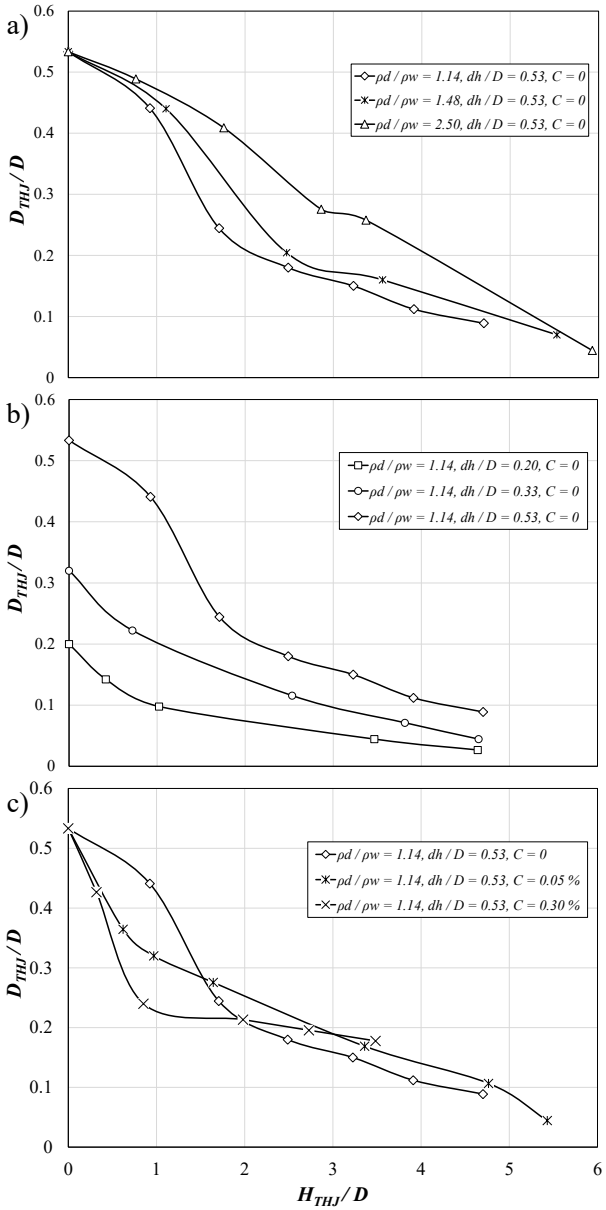

Figure 3.17: Variation of the dimensionless through-hole jet diameter with the dimensionless through-hole jet height concerning the a) disk density ratio; b) disk hole size ratio; c) fluid properties.

3.3.7 Time variations of z, V, a

Many researchers have used the time variations of object's positions and its derivatives as indicators of solid entry and energy balance. Figure 3.18 tracks the time history of the disk displacement, z, along the depth (i.e., z-axis), the downward velocity of the disks, and time variations of deceleration are obtained from the first and second derivatives of the disk's position.

Figure 3.18a details the time-history displacement of disks along the z-axis for disks with different disk density ratios and opening diameters. The polymer concentration of the liquid mixtures is constant with a value of C = 0.30 wt.% PAM. As depicted in Figure 3.18a, the time-history of position of solid objects with different ambient fluid conditions and disk geometry from the studies of (Akbarzadeh et al., 2022; Jafari and Akbarzadeh, 2022; Shokri and Akbarzadeh, 2022) are included. In comparison, the experimental curves generally follow similar trends, showing increasing displacement over time. As can be seen in Figure 3.18a, since Akbarzadeh et al., (2022) conducted their experiments in Boger fluid with the specific features which are already explained in the introduction section, it takes more time for the solid object to travel a specific distance compare to the ones conducted by Jafari et al. (2022), and Shokri et al, (2022) where the media was water.

Figure 3.18b shows the time-history of disk velocity for the same disks and ambient flow conditions as presented in Figure 3.18a. The graph illustrates that while the disk descends downward, its velocity decreases non-linearly with time due to constant energy losses. The reduction in velocity exhibits significant fluctuations; however, after a certain duration following the pinch-off moment, it stabilizes at a constant value. Initially, the velocity experiences a sharp decline upon the disk's collision with the liquid. Notably, the trend of velocity reduction ceases, and between approximately 50 to 75 milliseconds, the rate of velocity decrease markedly diminishes due to the drag force exerted by the cavity prior to the pinch-off event, which occurs around 130 to 140 milliseconds. At around 75 milliseconds, the trend of sinking velocity begins to decrease again, and following the pinch-off moment at approximately 150 milliseconds, the velocity becomes constant. Also, dropping in the velocity of the descending disk in the fluid with the polymer concentration of 0.10 wt.% is lower than the ones in the liquid with the polymer concentration of 0.20 wt.%. This represents the importance of fluid viscosity on the solid object entry in fluid. The research conducted by Jafari et al. (2022) stands out among others due to its findings that the solid object used a hollow cylinder and the medium introduced water resulted in the least velocity reduction compared to other studies. The experimental data of Akbarzadeh et al. (2022) locates below the rests due to the used of the Boger fluid as an ambient medium. The energy losses due to impact, crown formation and viscous fluid motion are relatively higher in the motion of disk in Boger fluid which resulted is significantly smaller disk velocity in the study of Akbarzadeh et al. (2022).

The time-variations of disk's deceleration for disks with a density ratio of 2.50, disk opening diameter ratios of 0.20 and 0.33, and constant polymer concentration of C = 0.3 wt.% is shown in Figure 18c. The graph reveals that the disk initially experiences a sharp deceleration due to impact, reaching a minimum value of approximately −45 m/s^2 (i.e., −4.5g). The experimental data from Shokri et al. (2022) indicates a near-constant deceleration close to zero throughout the entire time indicating a minor energy loss due to impact, crown formation, and cavity formation. Following the initial impact, the deceleration reduces after the cavity and pinch-off phenomena and finally reaching near zero acceleration (i.e., constant sinking velocity) at approximately 50 milliseconds after the impact. Beyond this point, the rate of change in acceleration becomes much less stated, exhibiting minor fluctuations between 50 ms and 150 ms. Eventually, the acceleration stabilizes at a value close to zero, maintaining this steady state until the end of the observed period (300 milliseconds). This trend suggests that the disk undergoes a significant deceleration shortly after entering the fluid, likely due to impact at the early stages of descent. As time progresses, the fluid's resistance diminishes, allowing the disk to approach a state of constant velocity, where the net force acting on the disk approaches to a constant equilibrium value. The disk imparts momentum to the fluid and initiates cavity formation. The rate of momentum transfer depends on disk mass, impact velocity, and fluid resistance. Non-Newtonian fluids exhibit shear-dependent viscosity and elasticity, affecting how the fluid deforms and flows around the disk. Such properties influence drag forces and cavity behavior. Fluid flow through the disk's hole alters pressure distribution, reducing the pressure difference across the disk and affecting sinking velocity and cavity collapse.

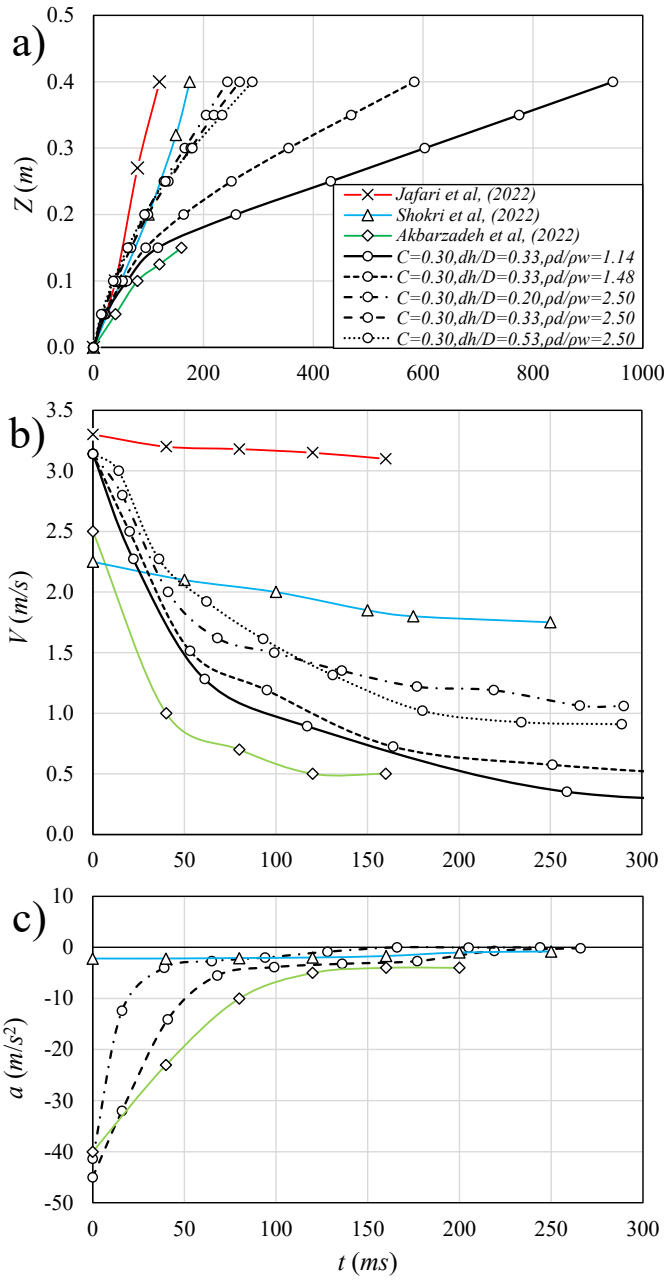

Figure 3.18: Variation of the disk position, velocity, and acceleration with time: a) disk displacement; b) velocity reduction; c) acceleration.

3.4 Future Work

The following items are suggested for future works on this topic. Extending the study to include other objects with different geometries such as cones, pyramids, or irregular shapes that could provide a broader understanding on fluid-structure interactions in fluids with different properties. The solid entry can be investigated on fluids with different rheological behaviors,

including shear-thickening and viscoelastic properties. The primary conditions of experiments and surrounding factors can be altered such as temperature variations, fluid turbulence, etc. In addition, developing validated computational models can enhance the capabilities and facilitate the design process in engineering applications. Last but not least, the behavior of bubbles that form due to cavity interaction can help better understanding the solid entry phenomenon.

3.5 Conclusion

A series of detailed laboratory experiments was carried out to investigate the cavity dynamics, crown formation, and energy balance by the entry of solid and annular cylindrical disks into non-Newtonian fluid mixtures. Non-Newtonian fluid mixtures were formed by mixing a wide range of PAM polymer concentrations ranging from 0.01 wt.% to 0.3 wt.% corresponding to apparent viscosity range between 0.013 Pa.s and 0.58 Pa.s which are equivalent to 13 and 580 times of the viscosity of water. Besides the effects of ambient rheology, the impacts of disk relative density and opening diameter of annular disks on cavity formation, crown development, and pinch-off phenomena were investigated. The effect of ambient apparent viscosity was represented with the Reynolds number, the density of disks was normalized with the density of water, and the opening diameter in annular disks was normalized with the disk diameter.

Data analysis indicated that the relative density of disks had the highest impact in variations of pinch-off depth, disk depth at the pinch-off moment, sinking velocity, and impact velocity. The ambient rheology represented by Reynolds number had secondary impact on variations of the mentioned controlling parameters and normalized disk opening had the least effect. Experimental data showed that increasing the opening diameter in annular disks reduced the normalized pinch-off time. A threshold on normalized opening diameter of annular disks was found with a value of $d_h/D = 0.2$. for $d_h/D \leq 0.2$, the effect of opening diameter is negligible, and opening diameter becomes important when opening diameter is larger than 20% of the disk diameter (i.e., $d_h/D > 0.2$).

The size of the curtain wall and height of the through-hole jet had strong correlation with the ambient viscosity and opening diameter. The heights of crown and through-hole jet slightly increased with a small addition of PAM polymer in water. High speed imaging showed that a slight increase in the viscosity of the fluid mixture reduces the instability and turbulence level hence decreases the energy losses. Such phenomena increased the heights of crown and through-hole

jets. However, at higher range of polymer concentration, the addition of viscosity and yield stress overcomes the stability of ambient mixture and the heights of crown and through-hole jet decreases with increasing polymer concentration. The imbalance between turbulence reduction due to surface instability and energy dissipation due to viscosity may explain the variations of normalized sinking velocity with polymer concentration. As polymer concentration increases from 0 (i.e., water) to 0.01 wt.% of PAM, normalized sinking velocity decreases in all experiments. Such reduction in normalized sinking velocity reaches to a local minimum at the polymer concentration of 0.01 wt.%. Subsequently, as polymer concentration increases from 0.01 wt.% to 0.05 wt.%, an intense growth of sinking velocity is observed, contrasting with the previous reduction. In other words, augmentation in mixture's viscosity leads to lower sinking velocity and pinch-off time.

The analysis of time-tracking data for disk displacement, velocity, and acceleration further underscores the role of fluid viscosity in controlling the descent dynamics. In mixtures with higher apparent viscosity, the time required for disks to traverse a specific displacement increases and velocity reduction occurs more gradually. Acceleration profiles demonstrate an initial sharp deceleration due to impact, crown formation and pinch-off followed by stabilization as the disk reaches a constant velocity after the pinch-off moment. Empirical equations were proposed for prediction of pinch-off location and time, sinking velocity, and impact velocity of disks with different densities and opening diameters.

The sloid disk entry in non-Newtonian fluids created narrower cavities and pinch-off occurred later compared to the disk entry into water. The higher viscosity and elasticity resist the cavity collapse. The crown formed upon impact is less pronounced in non-Newtonian fluids, resulting in reduced splash and lower crown height due to dampened upward momentum. Disks deaccelerate more quickly in non-Newtonian fluids because of higher viscous resistance, leading to longer sinking times.

Chapter 4

Energy losses due to entry of disks into water and viscous fluid mixtures

4.1 Introduction

The collision of a solid object with water surface and its immersion, crown formation, and splash have been extensively studied due to the wide applications of the topic in nature and engineering design. Falling of droplets into water surface and falling of lava due to volcanic eruption are some examples that occur in nature. Many applications of object entry exist in industry such as civil engineering, oil and gas, marine, and many others Sarpkaya et al., 1982; Kapsenberg, 2011; Bodily et al., 2014; Sharker et al., 2019; Feng et al., 2020; Guillet et al., 2020; Tavakoli, Khojasteh, et al., 2023). The collision of solid objects with water is a complex phenomenon that needs attention in order to be able to understand the entry of solid object into water and other fluid mixtures. Several phenomena occur in the entry of solid objects in stagnant ambient out of which cavity dynamics, crown formation, and pinch-off have been studied thoroughly. The cavity dynamics is characterized by the pinch-off time, t_p, pinch-off depth, h_p, and the position of the object at the pinch-off moment, h_d. It should be noted that cavity generation and air entrapment do not emerge in all water entry problems. Such phenomenon often occurs when the rigid body is flat or when the water entry occurs in relatively high-speed.

The effects of controlling parameters such as solid object features (i.e., disk geometry, mass, etc.), fluid properties, release condition on the key indicators of cavity dynamics are important. Some research studies identified the impacts of different aspects such as the shape and the relative density of the object on the entry phenomenon of rigid bodies into stagnant ambient. Most research studies in this field focused on the effects of geometry of the rigid bodies such as sphere, disk, and projectile and their aspect ratio on the key dynamic parameters.

A paper based on the content of this chapter is published in the. *International Journal of Heat and Fluid Flow*, Ebrahimi, M., & Azimi, A. H. (2025c). Energy losses due to entry of disks into water and viscous fluid mixtures. *International Journal of Heat and Fluid Flow*

Other controlling parameters are the release height, impact velocity, and the impact angle which control the cavity dynamics and crown formation (M. Wang et al., 2022; Belden et al., 2024; S. B. Li et al., 2024; X. J. Liu et al., 2024; J. J. Wang et al., 2025). Other researchers studied the effects of ambient fluid characteristics such as viscosity and surface tension on cavity dynamics and crown formation (Nigen & Walters, 2001; Akers & Belmonte, 2006; de Goede et al., 2019; Sun et al., 2019).

Ebrahimi and Azimi (2024) studied the effects of aspect ratio and disk density ratio on cavity dynamics of cylindrical disks in water and viscous fluid mixtures. The effects of density ratio, ρ_d/ρ_w, where ρ_d is the disk density and ρ_w is the water density were examined for a density ratio ranging between 1.10 and 2.50. Two aspect ratios of D/h = 1.5 and 3, where D is the disk diameter and h is the disk height were tested. The disks were released at rest and from a specific height on top of the fluid's surface. It was found that the impact Froude number (Fr) plays a major role in cavity formation and crown development which is calculated as $Fr = U/(gD)^{1/2}$, where U is the impact velocity ($U = (2gh_r)^{1/2}$), g is the gravitational acceleration, and h_r is the release height. The viscous fluid mixtures refers to the dynamic viscosity of the polymer-water solutions prepared at varying polymer concentrations and the range of viscosity is between μ = 1.2 and 580 mPa.s. It was found that increasing disk density and mixture's viscosity increased both pinch-off time and depth. The effect of disk aspect ratio on pinch-off features showed an adverse correlation at which the pinch-off time and depth reduced with increasing the disk aspect ratio. A series of experimental tests was conducted to explore the effects of ambient fluid properties on the entry characteristics of solid spheres (Akbarzadeh et al., 2022). Two Newtonian and non-Newtonian fluids were used: glycerin (a Newtonian fluid) and polyacrylamide (a non-Newtonian, Boger fluid). The surface tension, density, and viscosity of the fluids were maintained constant at μ = 120 mPa.s and densities of ρ = 1206 and 1242 kg/m^3. The experiments covered a wide range of Froude numbers from $Fr = U/(gD)^{1/2}$ = 1.2 to 20 where D is the diameter of the spheres. The variations of characteristic length and pinch-off time in both mixtures showed that the pinch-off occurred earlier in Boger fluid and a similar trend was observed in variations of pinch-off length. Their main finding was that the rheological properties of the fluid affect the fluid entry relevant phenomena such as pinch-off features in a way that Boger fluids enhance the damping force of fluid which leads to consequent features.

Besides spheres and projectiles, the entry of thin and thick cylinders in stagnant ambient have been predominantly used to study the motion and cavity dynamics during water entry and pinch-off (Willmarth et al., 1964; Gaudet, 1998; Bergmann et al., 2009; Auguste et al., 2013; Lee et al., 2013; Xu et al., 2021). The entry of cylindrical objects in stagnant ambient was advanced by testing the impact and falling of hollow cylinders in stagnant Newtonian and non-Newtonian ambient fluid mixtures (Hou et al., 2022; Liu et al., 2023; Bi et al., 2018, 2021; Zhou et al., 2021; Janati & Azimi, 2023). Li et al. (2024) conducted a series of experiments to investigate cavity dynamics and its evolution due to the entry of a projectile with a canard wing. It was shown that the canard wing is able to deflect the trajectory of the moving projectile. They proved that any increments in the impact velocity caused the pinch-off depth and cavity to rise. Wang et al. (2024) conducted laboratory experiments on the entry of solid objects in moving ambient with the ambient velocity ranging between 0.50 m/s and 2.85 m/s. A rigid sphere made of carbon chromium steel with a density of ρ = 7778 kg/m^3 and a diameter of D = 14.7 mm was used. It was found that the angle of the tilted cavity (inclination of the cavity's central axis relative to the vertical direction, which is perpendicular to the fluid surface) varies with the ambient flow velocity and increasing the ambient velocity increased the angle of the cavity. Experimental results showed that increasing the impact velocity reduced the angle of the cavity.

Many researchers have developed theoretical and semi-empirical models to predict the unsteady variations of cavity size during the penetration of rigid objects in water (Duclaux et al., (2007); Guo et al., (2012); Liu et al., 2012; Wang et al., (2024). The collision, pinch-off, and sinking of rigid bodies in stagnant ambient fluid have been modeled by employing momentum and energy equations. The momentum and energy of the rigid bodies at different stages of entry were calculated for better estimation of cavity and crown formation, pinch-off, and sinking. Different semi-theoretical and practical correlations have been proposed to evaluate the effects of fluid properties and object's geometry on variations of force imbalance at different stages of evolution (Reseghetti, 2014; Turton and Levenspiel, 1986; Vayig and Rosenberg, 2025). Sharif and Azimi, (2020, 2021)

The entry of rigid bodies into fluids involves the conversion of various forms of energy at different stages of evolution. The focus of this study is to investigate the energy transfer at different stages of evolution known as the collision/immersion, pinch-off, and sinking. This process begins

with the presence of primary kinetic energy, which originates from the initial velocity of the solid object. Such initial velocity is typically acquired by dropping or releasing a rigid body from a distance from the surface of the fluid. At the collision stage, the kinetic energy at the impact is transferred to the ambient and the transferred energy is used for crown formation and splashing. A few studies have directly elaborated on the energy conversions and losses associated with a rigid body entering a fluid (Cointe et al., 2004; Guo et al., 2012; Korkmaz & Güzel, 2017; Lee, 2000; Liu et al., 2020; Wang et al., 2024; Sun, et al., 2021). In different fluid mixture with varying fluid properties and flow condition, different sorts of factors such as the viscous dissipation, turbulence flow condition, and many other elements affect the energy budget (Alharbi et al., 2024; Aparece-Scutariu and Shin, 2022; Barozzi et al., 1984; Islam et al., 2024; M. Wang et al., 2022).

Guleria et al. (2021) performed a series of experiments to study the effect of density on the entry of spheres into water. The density of spheres ranged between 2500 and 7780 kg/m^3 and the diameter of spheres ranged from 3 mm to 5 mm. It was found that more than 80% of the steel sphere's energy is dissipated within 100 milliseconds after the collision while the energy dissipation of glass spheres was around 50%. The energy conversions are imparted with the variations of surface and potential energy of the cavity and kinetic energy of the impact. It was found that the surface energy (i.e., impact kinetic energy) increases with the release height and is abruptly reduced by the collision with the water surface. The reduction continues due to cavity development and as the object sinks into the water cavity. Through a series of numerical simulations, Yang et al. (2020) showed that the kinetic energy of spheres, having the same density as water (988 kg/m^3), reduced by more than 80% in the first 100 milliseconds from the collision. Liu et al. (2023) found that the energy dissipation at the impact is due to formation of wave motion at the water surface and the evolution of the cavity. Panciroli et al. (2015) verified that the impact energy losses vary between 60% to 80% for a rigid body mass of 0.2 kg when the release height ranged from 25 mm to 100 mm. The velocity of the wedges decreased almost linearly while the penetration length advanced in water. On the contrary, the entry angle of 25^o did not change the penetration depth. The current gap based on the literature involves limited comprehensive experimental data and understanding of the energy dissipation processes during the entry of solid and annular disks into non-Newtonian fluid mixtures with varied viscosities and densities.

The current study presents a comprehensive insight into the effects of controlling parameters on variations of energy losses in the entry of solid and annular disks into water and viscous fluid mixtures. The variations of energy losses at different key stages of solid entry are investigated, and such variations are correlated with the rheological characteristics of the fluid mixture and the release conditions of annular disks. In addition, clarifying how energy is transferred to the surrounding fluid helps elucidate the progression and formation of crown, offering valuable insights into splash dynamics. The intricate nature of fluid dynamics and the influence of various factors on the phenomenon of rigid body entry into fluids necessitate further investigation to deepen our understanding of how energy loss relates to the characteristics of the disk and the surrounding fluid. Therefore, an extensive experimental study was carried out to explore the effects of fluid viscosity, density ratio, and normalized disk opening on the energy transfer between the solid and annular disks and the surrounding fluid mixture. The dimensions of the solid to annular disks, the range of density ratio, and normalized disk opening are based on the recent study by the authors (Ebrahimi and Azimi, 2025), where the importance and applications of the entry of the annular disks into water and viscous fluid mixtures have been examined comprehensively. The outcomes of the present study on water are used as a benchmark and the energy transfer in viscous fluid mixtures are applicable in ambient like a swamp or mudflow. A summary of the findings and a discussion of the characteristics of the fluid mixtures and the motion of solid and annular disks were explained in detail in Ebrahimi and Azimi (2024, 2025).

This study depicts valuable insights for real-world challenges in ocean engineering, especially in offshore and subsea operations. The surrounding environment can extend beyond the ocean to include fluids with different properties which can be found in swamps, marine sediments, and drilling muds. The mentioned media required to be investigated, so understanding how solid objects interact with these materials is essential for designing safe systems. The current outcomes enable us to support the operation of the related applications such as oil spills or other pollutants, ship slamming, boat launching in local area, etc.

The current research is followed by our future research where other geometries of the solid objects (e.g., spheres) are experimented to provide a broader understanding of fluid-structure interactions while the applied fluid has different rheological behaviors, including shear-thickening and viscoelastic properties. The goal of our extended studies also includes studying the influence

of primary surrounding factors of fluid turbulence, and solid object impact condition. It should be noted that other measurement techniques such as Particle Image Velocimetry (PIV) and Computational Fluid Dynamics (CFD) can be utilized for further analysis of the phenomenon.

The present paper is organized as follow. In Section 2, a detailed description of the experimental procedures and methodology is explained, and Section 3 presents the results regarding energy losses at three stages of collision, pinch-off, and sinking moments which occur during the entry process. The section 4 is the conclusion remarks and recommendations for future studies.

4.2 Experimental Procedure

A series of laboratory experiments was carried out in the Multiphase Flow Research Laboratory (MFRL) at Lakehead University, Canada, to study the energy transfer from solid and annular cylindrical disks into water and viscous fluid mixtures. Experiments were conducted by employing a square tank of 400 mm × 400 mm × 1000 mm and the tank was filled to a depth of 700 mm with water and viscous fluid mixtures with different viscosities which were prepared by mixing a polymer with different concentrations (see Table 4.1). For consistency and to negate any variability on the initial energy, the release height of the disks was kept constant, and they were released from a fixed height of 500 mm above the liquid's surface. Figure 1 presents the sketch of the experimental setup including the location of the high-speed cameras, source lights, disk geometry, and the coordinate system. In addition, the acting and resistive forces exerting the disk while it is sinking through the ambient are shown in Figure 4.1.

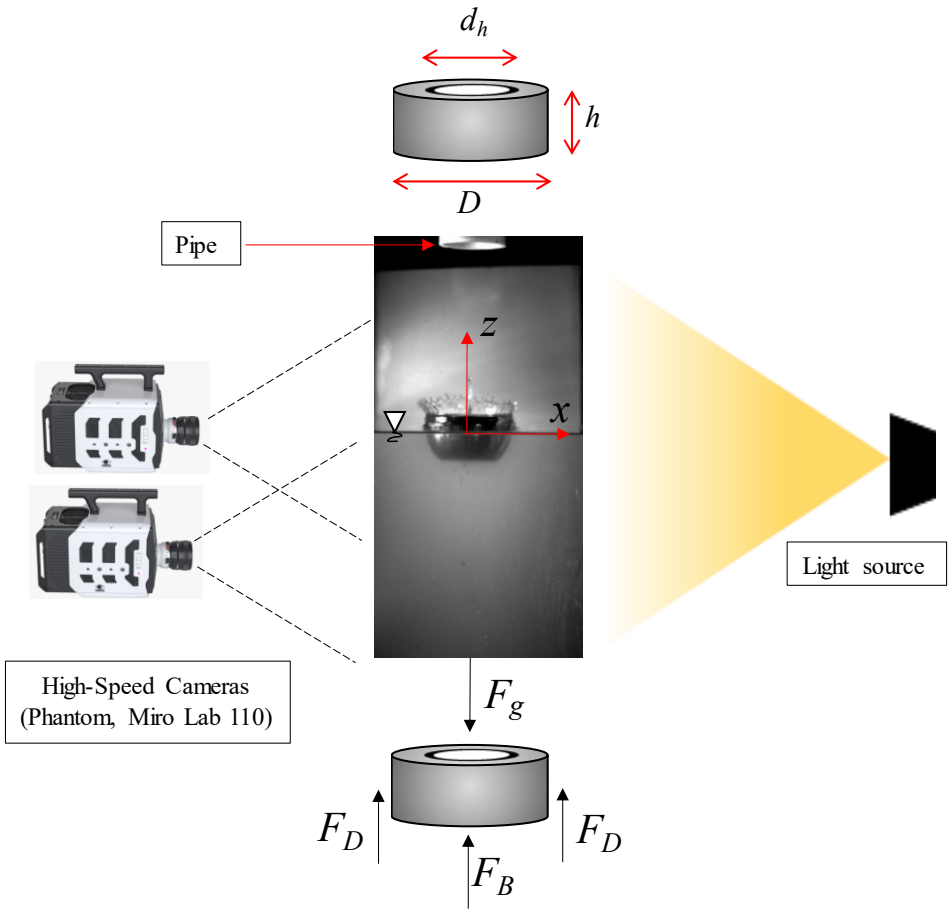

Figure 4.1: Schematic sketch of cylindrical disk entry in stagnant ambient, disk geometry, coordinate system, and acting forces on a sinking annular disk.

Solid rubber disks with a diameter of D = 75 mm, and height of h = 25 mm were used in this study. Using two disks of the same diameter gave an aspect ratio of $D/2h$ = 1.5. Twelve disks with three densities of ρ_d = 1,140, 1,480, 2,500 kg/m^3 and three openings with diameters of d_h = 15, 25, and 40 mm were examined. To study the dynamics of disks entering into water and viscous fluid mixtures, high-speed cameras (Phantom, Miro Lab 110, New Jersey, Wayne, USA) equipped with AF Nikkor 50 mm, f/1.4D lenses (Nikon, Tokyo, Japan) were utilized. The cameras were set to record at a rate of 1000 frames per second, with a resolution of 1280 × 800 pixels. Adequate lighting was crucial for capturing clear images, so telescope work lights with a power of 1000 Watts (Woods, 166 L13, CA, USA) were positioned around the tank to ensure optimal image quality. The reliability of the experimental results was ensured through three repetitions for each experiment. The average, minimum, and maximum values were shown with data points and overbars, respectively.

Viscous fluid mixtures were made by mixing Polyacrylamide (PAM) polymer with water at different polymer concentrations. The PAM polymer was supplied by the SNF Corporation (Rhone-Alpes, France) under the commercial name of FLOPAM AN 934 VHM. This polymer was chosen because of its safety, availability, transparency, and its effectiveness in enhancing the viscosity of liquid mixtures in a controlled manner. The selected polymer has been widely used in many research studies (Mishra et al., 2011; Wong et al., 2006; Yan et al., 2013). The PAM depicts high potential among many other additives as a role model for augmentation of the viscosity of the liquid that has been tested in some industries such as in oil and gas industries (Gao, 2013; Jung et al., 2013; Yan et al., 2013; Hu et al., 2017; Ebrahimi et al., 2020; Lu et al., 2021; Ebrahimi & Sanati, 2021; Ebrahimi et al., 2021).

To make the selected liquid mixtures with relatively wide range of viscosities, a fixed amount of PAM polymer was first dissolved in a small and known volume of water. The concentrated polymer mixture was then diluted with different volumes of water to form the required concentrations. The concentrations of PAM polymer in this study are 0.01%, 0.05%, 0.10%, 0.20%, and 0.30% by weight. An appropriate aging period of 100 hours was allowed for each mixture to ensure complete dispersion and homogeneous distribution of the polymer in the water. The experimental conditions were maintained at an atmospheric pressure with a constant temperature of 25°C. The experimental protocol involved the water entry of twelve different disks into water and viscous fluid mixtures to assess the effects of fluid's viscosity, disk density, and disk opening diameter on energy losses at different stages of evolution. In total, more than seventy distinct experiments were conducted excluding the repetitions of each experiment. Detailed information on the physical parameters and the relative non-dimensional parameters such as Reynolds number are listed in Table 4.2. An in-house MATLAB algorithm (Mathworks, R2018b, Natick, USA) was employed to analyze the images captured during the experiments and to extract data. Detailed information on the extraction of data and the related analysis can be found in Ebrahimi and Azimi (2024, 2025). The experiments were conducted on a laboratory scale, which may not fully replicate the complexities in full-scale or industrial scenarios. The study focused specifically on solid cylindrical disks while the results regarding the entry of flexible structures in water is explained by Tavakoli et al. (2023). Experiments were performed at relatively low velocities (i.e., less than 5 m/s), which limits direct applicability of findings to high-speed water-entry scenarios (i.e., more than 100 m/s) common in certain engineering contexts.

Table 4.1: Correlation between polymer concentrations, C (%), and apparent viscosity of water and non-Newtonian fluid mixtures.

C (%)	0	0.010	0.050	0.10	0.20	0.30
Viscosity (mPa.s)	1	12	54	180	520	580

4.3 Experimental Results

The time series of images on the free falling of an annular disk into stagnant water with a density ratio of $\rho_d/\rho_w = 1.48$ and normalized opening of $d_h/D = 0.20$ is shown in Figure 2. The time interval between each image is 0.01 seconds. The time history of images starts with the time at which the disk collides with the water surface. This event is considered as the initial time of the experiments and all other events such as crown formation, pinch-off, and sinking are referenced to this initial time. Thirty milli-seconds after the collision of the disk with the water surface, the complete immersion of the disk occurs. At this event, part of the kinetic energy of the disk is transferred to the ambient fluid causing water splash and crown formation. As can be seen in Figure 2, droplets are formed at the peak of the crown and such structure was only found in solid entry in water. The crown reached to its maximum height after 40 milli-seconds from the impact while the disk was slightly immersed in water.

Figure 4.3 shows the time history images of a free-falling annular disk into a stagnant viscous fluid mixture with the maximum polymer concentration in this study ($C = 0.30$ wt. % PAM). The opening diameter ratio and the relative density of the disk were similar to the disk presented in Figure 4.2 with the values of $d_h/D = 0.20$ and $\rho_d/\rho_w = 1.48$. Due to faster development of crown and pinch-off, the time interval between each image was selected as 0.005 seconds, which is half of the time step in Figure 4.2. As can be seen in Figure 3, it is evident that the crown height and the size of the Worthington jet are much smaller in the solid entry of disks in a viscous fluid mixture with relatively higher apparent viscosity. This indicates that more energy is required to form a crown in high in viscous fluid mixture and the volume of displaced fluid is much smaller in the presence of a highly viscous fluid mixture. Therefore, the amount of work done by the annular disk to the stagnant ambient fluid was smaller than that of water. This indicates that more energy was dissipated when the disk collides with a fluid with higher viscosity.

Table 4.2: Table of experiments presenting the variations of polymer concentration, C, disk density ratio, ρ_d/ρ_w, disk opening size ratio, d_h/D, collision/immersion, pinch-off, and sinking energy loss ratios, E_c/E_t (%), E_p/E_t (%), E_s/E_t (%), submerged weight, $W_s = mg - \rho_f Vg$, and Reynolds number, Re.

Test No.	C (%)	ρ_d/ρ_w	d_h/D	E_c/E_t (%)	E_p/E_t (%)	E_s/E_t (%)	W_s ($Kg.m/s^2$)	Re
1	0	1.14	0	32.69	11.08	22.75	0.30	1.22E+05
2		1.48		31.75	8.79	17.95	1.01	1.27E+05
3		2.50		26.92	1.10	2.70	3.17	1.47E+05
4		1.14	0.2	21.52	21.30	21.49	1.00	1.67E+05
5		1.48		13.37	27.14	17.27	1.69	1.94E+05
6		2.50		5.37	21.43	1.40	3.80	2.17E+05
7		1.14	0.33	26.92	17.24	23.08	1.22	1.47E+05
8		1.48		16.50	23.78	18.71	1.85	1.84E+05
9		2.50		0.21	26.71	2.94	3.77	2.30E+05
10		1.14	0.53	19.19	24.41	23.54	1.34	1.75E+05
11		1.48		13.37	26.69	16.97	1.86	1.94E+05
12		2.50		0.21	26.13	1.65	3.49	2.30E+05
13	0.01	1.14	0	30.77	13.17	23.39	0.30	5.46E+03
14		1.48		25.41	15.33	18.37	1.01	6.38E+03
15		2.50		23.64	6.71	5.92	3.17	6.66E+03
16		1.14	0.2	23.56	20.41	23.87	1.00	6.67E+03
17		1.48		25.34	15.36	18.74	1.69	6.39E+03
18		2.50		13.37	17.15	6.78	3.79	8.08E+03
19		1.14	0.33	21.52	22.37	23.24	1.21	6.98E+03
20		1.48		16.50	23.93	18.86	1.85	7.67E+03
21		2.50		0.21	29.63	6.84	3.77	9.59E+03
22		1.14	0.53	16.50	27.33	23.83	1.34	7.67E+03

23		1.48		9.70	30.64	18.51	1.86	8.53E+03
24		2.50		0.21	29.72	6.44	3.49	9.59E+03
25	0.05	1.162	0	28.37	14.92	21.85	0.29	2.62E+03
26		1.498		25.41	13.80	15.29	1.01	2.84E+03
27		2.551		19.19	9.33	2.32	3.17	3.25E+03
28		1.137	0.2	16.50	26.66	21.50	1.00	3.41E+03
29		1.466		13.37	25.50	14.79	1.69	3.59E+03
30		2.48		0.21	-2.26	2.00	3.79	4.26E+03
31		1.122	0.33	13.37	30.11	22.83	1.21	3.59E+03
32		1.452		9.70	29.95	16.18	1.85	3.79E+03
33		2.45		6.03	33.62	1.73	3.77	4.55E+03
34		1.162	0.53	16.50	27.09	22.08	1.34	3.41E+03
35		1.498		13.37	26.90	16.30	1.86	3.59E+03
36		2.551		0.21	27.38	1.48	3.49	4.26E+03
37	0.1	1.14	0	28.37	15.28	23.26	0.29	7.87E+02
38		1.48		25.41	14.02	15.70	1.01	8.52E+02
39		2.50		19.21	9.70	3.43	3.17	9.75E+02
40		1.14	0.2	23.56	19.93	22.04	1.00	8.91E+02
41		1.48		19.19	20.77	16.37	1.69	9.75E+02
42		2.50		5.37	23.25	2.86	3.79	1.20E+03
43		1.14	0.33	19.19	24.69	23.12	1.21	9.75E+02
44		1.48		16.50	23.82	17.32	1.85	1.02E+03
45		2.50		5.37	23.15	3.00	3.77	1.20E+03
46		1.14	0.53	19.19	25.16	24.49	1.34	9.75E+02
47		1.48		16.50	25.28	19.76	1.86	1.02E+03
48		2.50		0.21	30.87	6.41	3.49	1.28E+03
49	0.2	1.14	0	30.77	13.63	23.55	0.29	5.05E+02
50		1.48		26.92	14.00	18.50	1.01	5.68E+02
51		2.50		23.64	5.65	3.78	3.17	6.16E+02

52		1.14		21.52	23.08	24.57	1.00	6.45E+02
53		1.48	0.2	19.19	21.65	18.62	1.69	6.76E+02
54		2.50		13.37	15.64	4.13	3.79	7.47E+02
55		1.14		23.56	20.91	24.92	1.21	6.17E+02
56		1.48	0.33	19.19	22.39	20.23	1.85	6.76E+02
57		2.50		13.37	14.00	3.44	3.77	7.47E+02
58		1.14		29.56	15.30	27.19	1.34	5.26E+02
59		1.48	0.53	21.52	21.46	22.76	1.86	6.45E+02
60		2.50		5.37	28.93	8.61	3.49	8.35E+02
61		1.14		13.89	31.04	24.37	0.29	3.32E+02
62		1.48	0	26.92	14.42	18.42	1.01	2.55E+02
63		2.50		21.58	8.34	3.53	3.16	2.89E+02
64		1.14		19.19	25.94	24.55	1.00	3.03E+02
65		1.48	0.2	16.50	25.44	19.22	1.68	3.18E+02
66		2.50		5.37	24.28	3.44	3.79	3.75E+02
67		1.14		21.52	23.61	26.43	1.21	2.90E+02
68	0.3	1.48	0.33	16.50	25.82	20.99	1.85	3.18E+02
69		2.50		5.37	27.21	6.51	3.77	3.75E+02
70		1.14		19.19	26.20	27.26	1.34	3.03E+02
71		1.48	0.53	13.37	29.51	22.45	1.86	3.35E+02
72		2.50		0.21	36.00	10.82	3.49	3.98E+02

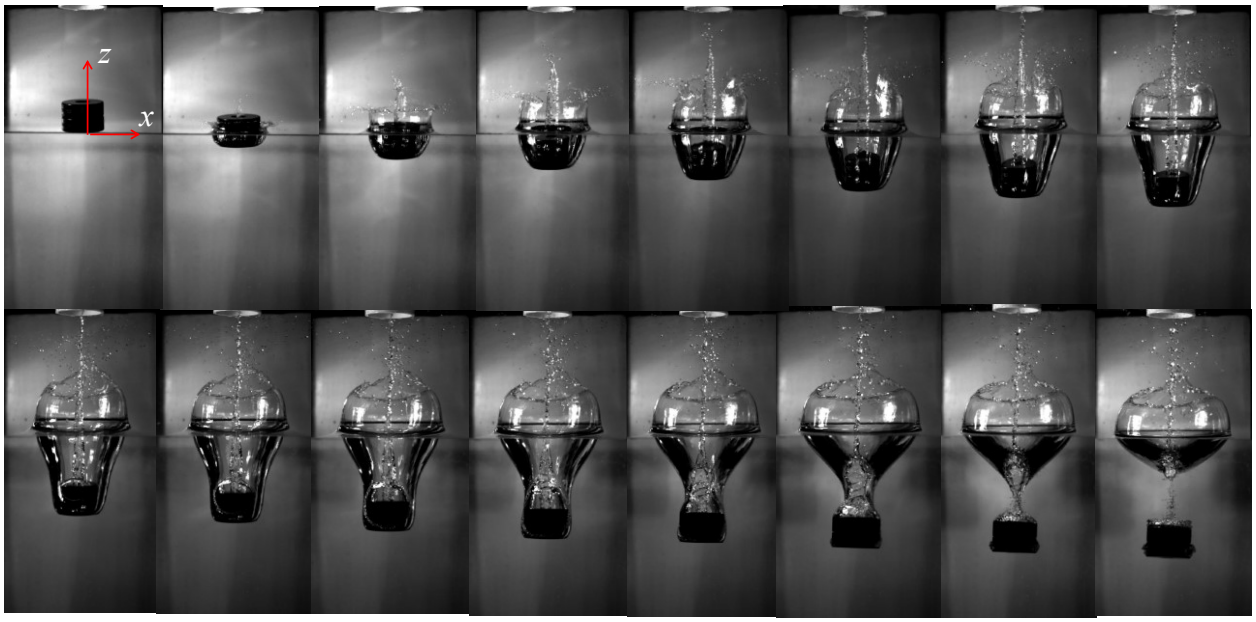

Figure 4.2: Time history images of a free-falling annular disk in stagnant water. The opening diameter ratio of the cylinder is $d_h/D = 0.20$, the density ratio is $\rho_d/\rho_w = 1.48$, and the aspect ratio is $D/h = 1.5$. The time interval between each image is 0.01 seconds.

Figure 4.3: Time history images of a free-falling annular disk with an opening diameter ratio of $d_h/D = 0.20$ in a stagnant fluid mixture with 0.30 wt. % PAM concentration. In this test, the density ratio is $\rho_d/\rho_w = 1.48$. The time interval between each image is 0.005 seconds.

4.3.1 Time variations of disk's position, velocity, and acceleration

The effects of mixture viscosity on the motion of annular disks were studied by measuring the time history of the disk's position, velocity, and acceleration. Figure 4.4 illustrates the variation in the downward travel displacement, velocity, and acceleration of annular disks over time. The density ratio and disk opening size were fixed to $\rho_d/\rho_w = 2.50$ and $d_h/D = 0.33$, respectively. Two polymer concentrations of $C = 0.10$ wt.% and 0.20 wt.% corresponding to apparent viscosities of 180 mPa.s and 520 mPa.s were selected. The experimental data on similar recent studies that were conducted by Akbarzadeh et al. (2022); Jafari & Akbarzadeh, (2022) and Shokri & Akbarzadeh (2022) are added for comparison. The density and viscosity of the fluids were maintained constant at $\mu = 120$ mPa.s and densities of $\rho = 1206$ and 1242 kg/m^3 in the study conducted by Akbarzadeh et al. (2022). The experiments covered a wide range of Froude numbers from $Fr = U/(gD)^{1/2} = 1.2$ to 20. The data generated by Jafari & Akbarzadeh (2022) were on the entry of hollow cylinders with a density of 7700 kg/m^3 and a diameter of $D = 25$ mm and the ambient fluid was water. The data from Shokri & Akbarzadeh (2022) were on the entry of spheres with a density of 7780 kg/m^3 and a diameter of $D = 20$ mm entering water.

Figure 4.4a depicts the time variations of disk position for the selected tests and data from other researchers. Increments in the viscosity of the fluid lead the sphere to travel a specific interval in the shorter period around 20 milliseconds. The results of drowning velocity from Akbarzadeh et al. (2022) were the lowest among all studies due to two key factors of significantly lower density of the rigid body and the properties of the Boger fluid used in their studies. Both solid objects in the study of Shokri & Akbarzadeh (2022) and Jafari & Akbarzadeh, (2022) descended at a faster rate in comparison to our measurements for two reasons of using water and solid objects with relatively higher densities than that of the present study. By comparing the measurements by Shokri & Akbarzadeh (2022) and Jafari & Akbarzadeh, (2022) and our measurements in water, it can be concluded that the differences in velocity and displacement data can be attributed to variations in geometry (sphere, cylinder (hollow and solid), and disk) with different dimensions and the presence of central opening in the cylindrical disks.

Figure 4b shows the effect of ambient viscosity on the time variations of disk velocity and a comparison with the data from the literature. The graph corresponds to the disk with a polymer concentration of 0.20 wt. % PAM. As can be seen, the effect of ambient viscosity on time variations of disk's velocity is noticeable and disk's velocity decreased with increasing ambient viscosity (i.e., polymer concentration from 0.10 wt.% PAM to 0.20 wt.% PAM). The time variation of velocity in presented data from the study of Akbarzadeh et al. (2022) decreased dramatically due to relatively small density of the rigid body and rheological properties of the ambient fluid. In contrast, the velocity of the hollow cylinders from the study by Jafari & Akbarzadeh, (2022) decreased at a much smaller rate due to the lower surface area of the rigid object. Figure 4c illustrates the effect of ambient viscosity on the time-dependent variations in disk deceleration for liquid mixtures containing 0.10 wt.% and 0.20 wt.% PAM polymer. The analysis is conducted for a disk with a density ratio of ρ_d/ρ_w = 2.50 and d_h/D = 0.33. It is evident that acceleration significantly changed in the first 50 milliseconds of the entry. After this initial phase, the variations in acceleration decreased, and approach a near-zero constant value indicating a constant sinking velocity. In Figure 4.4c, the disks exhibit a significant reduction in acceleration, reaching a peak value of approximately $a = -45$ m/s^2. Due to presence of a Boger fluid, the variation of disk's deceleration with time was significant in the study by Akbarzadeh et al. (2022).

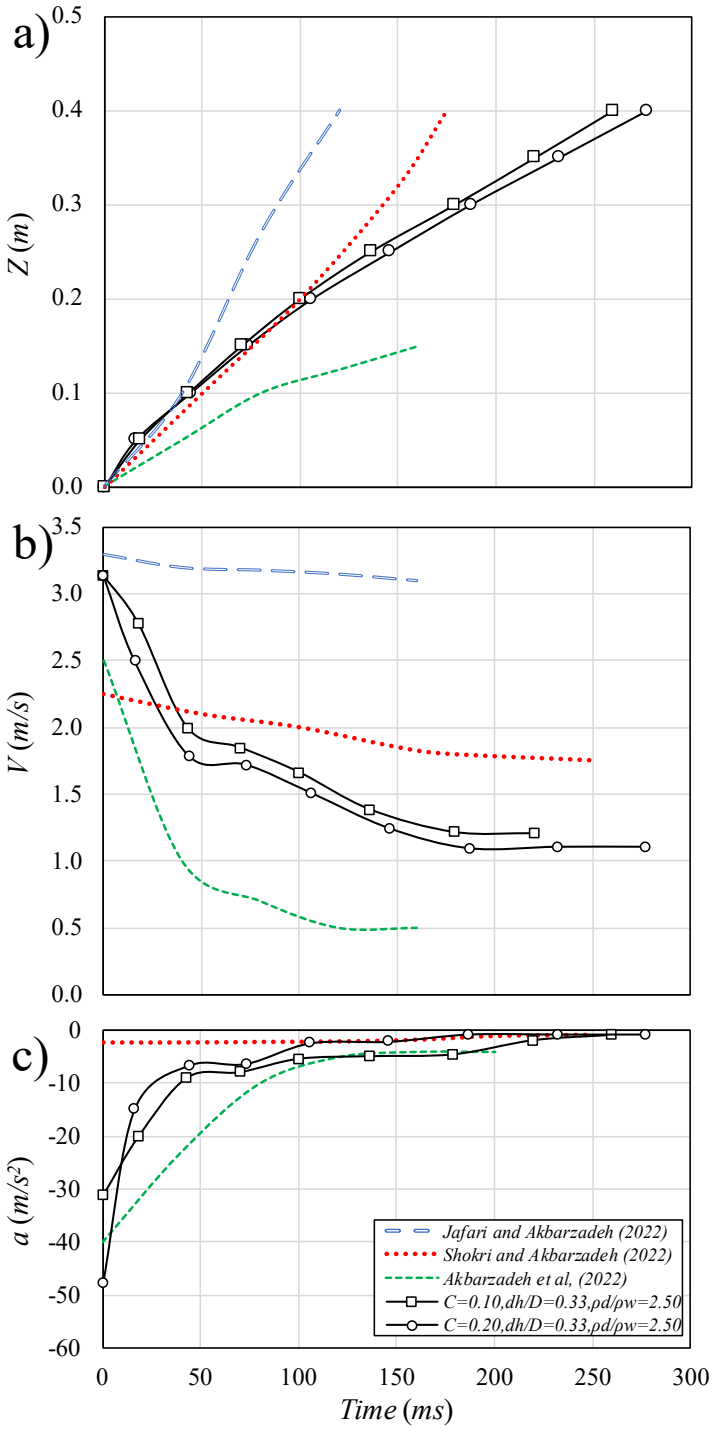

Figure 4.4, Variation of the disk position, velocity, and acceleration with time: a) disk displacement; b) velocity reduction; c) acceleration.

4.3.2 Energy losses

The energy transfer occurs at different stages of evolution upon releasing the disk from a specified distance and colliding with the fluid's surface. To formulate the variations of energy losses with time, four distinct stages of evolution were identified that represent substantial phenomena during the entry of the solid cylindrical disk in the fluid mixture. These stages, which have significant impacts on the energy transfer, are defined as the impact, immersion, pinch-off, and sinking stages. The energy equations between each of the above stages are written and three energy losses were calculated knowing the position and velocity of the disks at those stages. Figure 5 shows the images of a free-falling disk entry into a fluid mixture and the associated energy level at different stages of impact, immersion, pinch-off, and sinking. The total energy losses are calculated by considering the energy balance between the potential energy of the disk at the rest position and the variations of kinetic energy after the collision and during the sinking of a disk. The surface of the fluid mixture is considered as the reference for calculation of potential energy. Figure 5 shows the snap-shot images of a falling disk in four different stages of 1) reaching the disk to the surface of the fluid mixture, this stage is named as the impact/collision stage; 2) immersing the entire disk into the fluid mixture, this stage is named as the immersion stage; 3) position of the disk at the pinch-off, this stage is named as the pinch-off stage; and 4) when the disk reaches at a point where the sinking velocity of the disk is constant, this stage is named as the sinking stage. The potential and kinetic energies at different stages and the reference line are illustrated in Figure 5. The four images in Figure 5 represent the position of the disk and the associated potential and kinetic energies at the defined four stages of evolution. Since the disk was at rest and it was released from a specific height, the kinetic energy at the release point was set equal to zero. When the disk reached the surface of the fluid's mixture, the entire potential energy of the disk was transferred to the impact kinetic energy, E_i, which can be directly determined by measuring the velocity of the disk right before the collision, v_i. The impact energy can be also equated with the potential energy of the disk at rest by assuming that the energy losses due to air resistance is negligible. The impact energy at the collision can be expressed as:

$$E_i = mgh_o = \frac{1}{2}mv_i^2 \tag{4.1}$$

where m is the mass of the disk, g is the gravitational acceleration, h_o is the release height, and v_i is the impact velocity, which is approximated as $v_i = (2gh_o)^{1/2}$. Figure 4.5b shows the moment at

which the disk is fully immersed in the fluid mixture. At this stage, the velocity of the disk significantly reduced due to the energy transfer between the disk and the stagnant ambient fluid. The energy transfer is converted to the work done by the disk to move the surrounding water and to form the crown, water splash, and the cavity. The velocity of the disk at the complete immersion, v_c, was measured from the images taken by the highspeed camera and such velocity was used to calculate the remaining kinetic energy after the impact, E_c. The energy losses due to the impact and immersion of cylindrical disk and formation of cavity and crown are expressed as:

$$E_i = E_c - mgh + \Delta E_c \rightarrow \Delta E_c = mg(h_o + h) - \frac{1}{2}mv_c^2 \tag{4.2}$$

where h is the thickness of one disk. Figure 5c shows the image of a disk at the pinch-off stage. The kinetic energy at the pinch-off was calculated by measuring the velocity of the disk at the pinch-off, v_p, and the position of the disk at the pinch-off stage, y_p. The second stage of energy transfer pertains to the pinch-off stage, where the energy losses occur due to completion of cavity and crown formation. The energy equation at the pinch-off stage is expressed as:

$$E_c - mgh = E_p - mgy_p + \Delta E_p \rightarrow \Delta E_p = mg\left(y_p - h\right) + \frac{1}{2}m\left(v_c - v_p\right)^2 \tag{4.3}$$

Figure 4.5d shows the snap-shot image of a disk after the pinch-off and at a position at which the disk descending with a constant sinking velocity, v_s. As it was shown in Figure 4b, the velocity of the disk becomes constant once a balance is reached between the gravitational, buoyancy, and drag forces. The constant velocity of the disk at this stage is called the sinking velocity, v_s, and the position at which the sinking velocity is reached is y_s. The energy equation at this stage is calculated as:

$$E_p - mgy_p = E_s - mgy_s + \Delta E_s \rightarrow \ \Delta E_s = mg\left(y_s - y_p\right) - \frac{1}{2}m\left(v_p - v_s\right)^2 \tag{4.4}$$

The total energy losses, ΔE_T, can be calculated by the summation of the energy losses at all three stages of evolution as:

$$\Delta E_T = \Delta E_c + \Delta E_p + \Delta E_s = mg(y_s + h_o) - \ E_s \tag{4.5}$$

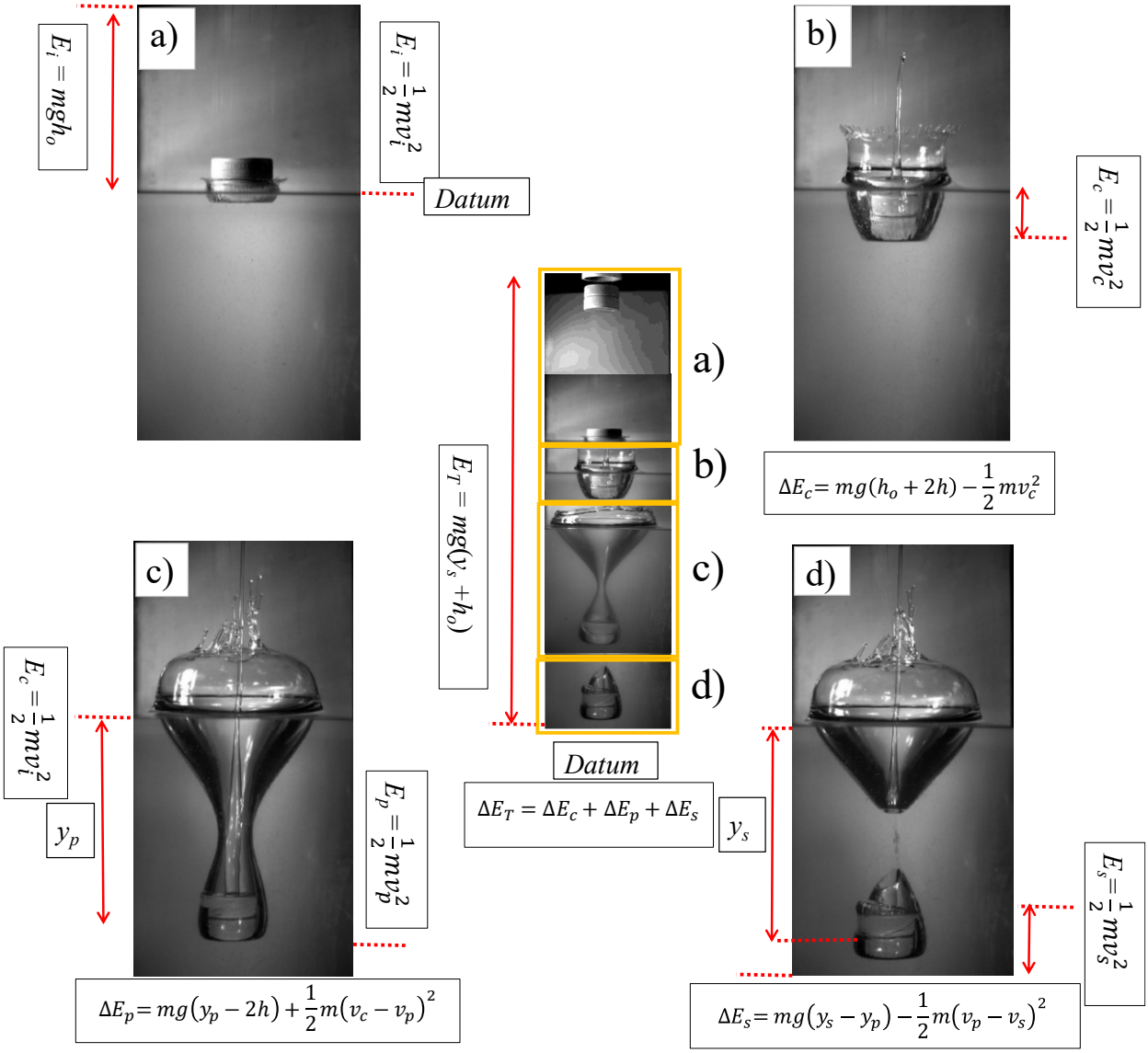

Figure 4.5: Schematic sketch of disk entry in water and non-Newtonian fluid mixtures for estimation of energy losses at different stages of motion: a) impact or collision stage, b) complete immersing stage, c) pinch-off stage, d) disk detachment and gravity sinking stage.

4.3.2.1 Energy losses at the collision and immersion stage

The energy losses due to the collision between the disk and the fluid mixture were calculated for cylindrical disks with different densities and fluid mixtures with different apparent viscosities. The transferred energy from the cylindrical disk caused motion at the surface of the fluid and formed a cavity and a crown. The size and properties of the cavity and crown were highly

dependent on the amount of primary energy imparted to the fluid mixture. The extent and shape of the crown and cavity were directly influenced by the initial impact energy and the magnitude of the transferred energy to the mixture, dictating the dynamics of fluid displacement and surface deformation. Figure 6 shows the effects of disk shape and density on variations of energy losses due to collision in mixtures with different apparent viscosities. The horizontal axis in Figure 6 is the disk opening ratio and the vertical axis is the energy losses due to collision normalized with the potential energy at the position of disk immersion. The subplots in Figure 6 shows the variations of energy losses due to collision for fluid mixtures with different polymer concentrations of C = 0.05%, 0.10%, and 0.20% and each subplot contains three curves corresponding to three different disk density ratios of ρ_d/ρ_w = 1.14, 1.48, and 2.50. The overbars in Figure 4.6a shows the range of measurement uncertainties in calculation of energy losses due to collision. Energy is used to deform the water surface, creating cavities, crowns, and associated waves. Such deformation dissipates the kinetic energy, transitioning it into surface fluctuations and heat.

As can be seen from Figure 4.6, the normalized energy losses decreased with increasing disk density and normalized disk opening diameter. Figure 4.6a shows the variations of normalized energy losses due to collision for disks immersing into a fluid mixture with relatively low polymer concentration. As can be seen, the energy losses significantly dropped for disks with a central opening and the effect of opening diameter was found to be negligible on variations of energy losses due to collision. The minimum energy losses due to impact was found for d_h/D = 0.33 and the impact energy losses slightly increased with increasing the opening diameter. A slight increase on the impact energy losses may be due to formation of boundary layer at the inside wall of the opening that causes disturbance and friction. Although the contact area at the bottom of the disk decreases with increasing the opening diameter, the area of the inner side of the disk increases. Such increase on the overall contact surface leads to a higher friction and consequently greater energy losses. The energy losses due to immersion for the lightest solid disk was approximately 68% of the potential energy and it reduced to approximately 40% due to presence of a central opening in a disk. As the viscosity of the ambient fluid mixture increased, the effect of normalized opening diameter became more evident and the energy losses due to collision reduced with increasing the central opening diameter. This indicated that the energy losses in such collisions are mainly due to the work done by the fluid to move around the cylindrical object.

Increasing disk density elevates its initial kinetic energy, reducing the relative contribution of buoyant force to overall energy losses. While the buoyancy acts as a resistive force during entry, heavier disks possess greater inertia, thus diminishing the relative significance of the buoyancy-induced energy losses. At first, the larger central openings decrease the frontal area exposed to fluid resistance, significantly reducing drag and hence the work done against fluid resistance. However, as the opening size further increases, the wetted surface area along the inner diameter expands as well. Such opening enlargement enhances the interaction between the disk surface and the surrounding fluid, resulting in an increased to drag contribution from the inner surfaces. Consequently, such interplay leads to elevated energy losses despite the initial gains from reduced frontal resistance. Taken together, these factors reduce the fraction of the initial mechanical energy dissipated through pressure work and turbulence, so the normalized energy losses decline as the relative density, ρ_d/ρ_w, increases. The work done by the disk's hydrodynamic resistance (i.e., pressure and viscous drag) is included in drag force. So, the variation of drag with increasing opening size ratio is automatically captured.

Figure 4.6c shows the effect of disk density and opening diameter on the energy losses due to collision and immersion into a more viscous ambient. As can be seen, the energy losses reduced by the existence of a central opening on the cylindrical disk and minimum energy losses due to impact and immersion occurred for $d_h/D = 0.2$. The results indicate that the reduction of the disk's contact surface can significantly reduce the impact energy losses, and such reduction is independent of disk relative density and mixture viscosity. The energy losses due to impact of hollow disks with relatively large opening diameter ratio of $d_h/D = 0.53$ with relatively viscous ambient fluid was highly dependent on the relative density of the disk. The energy losses due to collision and immersion in relatively light disk with large opening diameter was approximately 70% of the potential energy and for heavy disks with the same geometry it was 20%. The significant difference on energy losses due to collision and immersion between the light and heavy disks was due to the impact velocity as the impact velocity in light disk with large opening diameter significantly dropped due to low inertia while the heavy disk penetrates into the ambient fluid mixture with relatively smaller disturbance of the fluid's surface. A portion of energy is dissipated through cross-drag forces exerted on the disk during its entry and sinking stages.

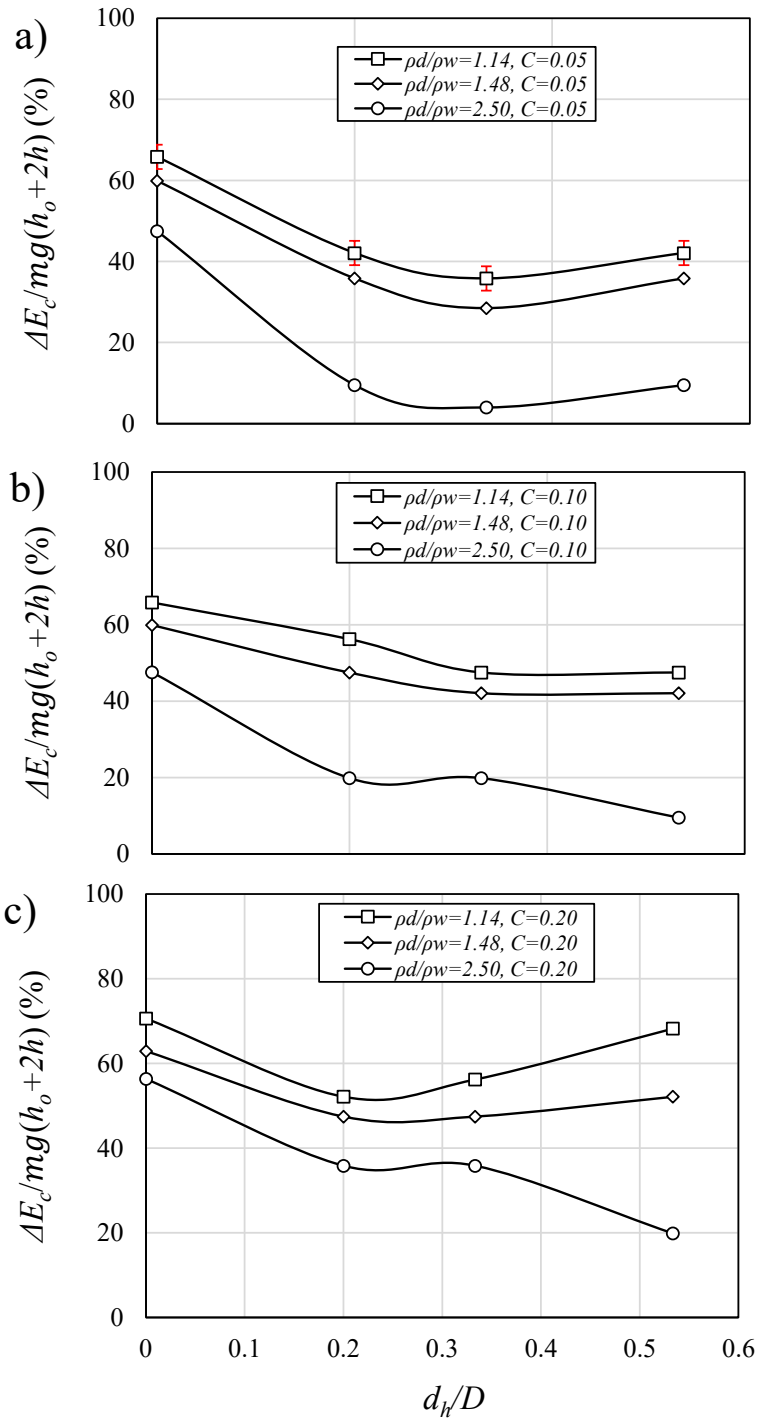

Figure 4.6: Effects of polymer concentration, disk density, and opening diameter on variations of energy losses due to collision in mixtures with different polymer concentrations: a) C = 0.05 % PAM, b) C = 0.10 % PAM, c) C = 0.20 % PAM.

4.3.2.2 Energy losses at the pinch-off stage

Figure 4.7 shows the effects of disk's opening diameter and density on variations of energy losses at the pinch-off stage. The horizontal axis in Figure 4.7 shows the variations of the disk's opening size and the vertical axis is the energy losses at the pinch-off normalized with the summation of total potential energy and kinetic energy prior to the pinch-off. Figure 4.7a, shows the effect of disk density ratio on variation of energy losses at the pinch-off while keeping polymer concentration constant at C = 0.05% PAM. Figure 4.7b depicts the effects of polymer concentration while the disk density ratio is constant with a value of ρ_d/ρ_w = 1.48. As can be seen in Figure 4.7a, disk density significantly affected the variations of energy losses at the pinch-off and it increased with the reduction in disk's density. This trend suggests that lighter disks experienced greater relative resistance and turbulence as they interact with the fluid, resulting in higher dissipation of kinetic energy during the pinch-off.

The opening diameter had a relatively small impact on variations of energy losses and such variations pronounced in disks with higher density. For example, the energy losses due to the pinch-off for a solid disk with a density of 1.48 times of the density of water was 80% and such energy losses increased by 10%, reaching to 88% for a disk with the same density and opening diameter ratio of d_h/D = 0.53. The effect of ambient viscosity on variations of energy losses at the pinch-off indicated that the energy losses increased with increasing ambient viscosity. The normalized energy losses due to the pinch-off by a solid disk in water was 78% and it increased by 9% when the same disk experienced pinch-off in a fluid mixture with a polymer concentration of C = 0.3% PAM. The relative opening diameter increased the energy losses due to pinch-off almost linearly. Overall, an increase in the disk's opening diameter up to d_h/D = 0.53 resulted in approximately 10% increase in the energy losses due to pinch-off. This suggests that larger opening in the disk enhances fluid flow through the disk, increasing the turbulence level which is translated to higher energy dissipation. Increasing polymer concentration leads to higher energy loss for the disks until they reach the pinch-off stage. This is due to the increased viscosity of the fluid, which enhances the resistance to the disk's motion and amplifies viscous dissipation. As a result, more kinetic energy is transferred to the ambient through fluid friction and drag, delaying the pinch-off moment and intensifying the overall energy losses.

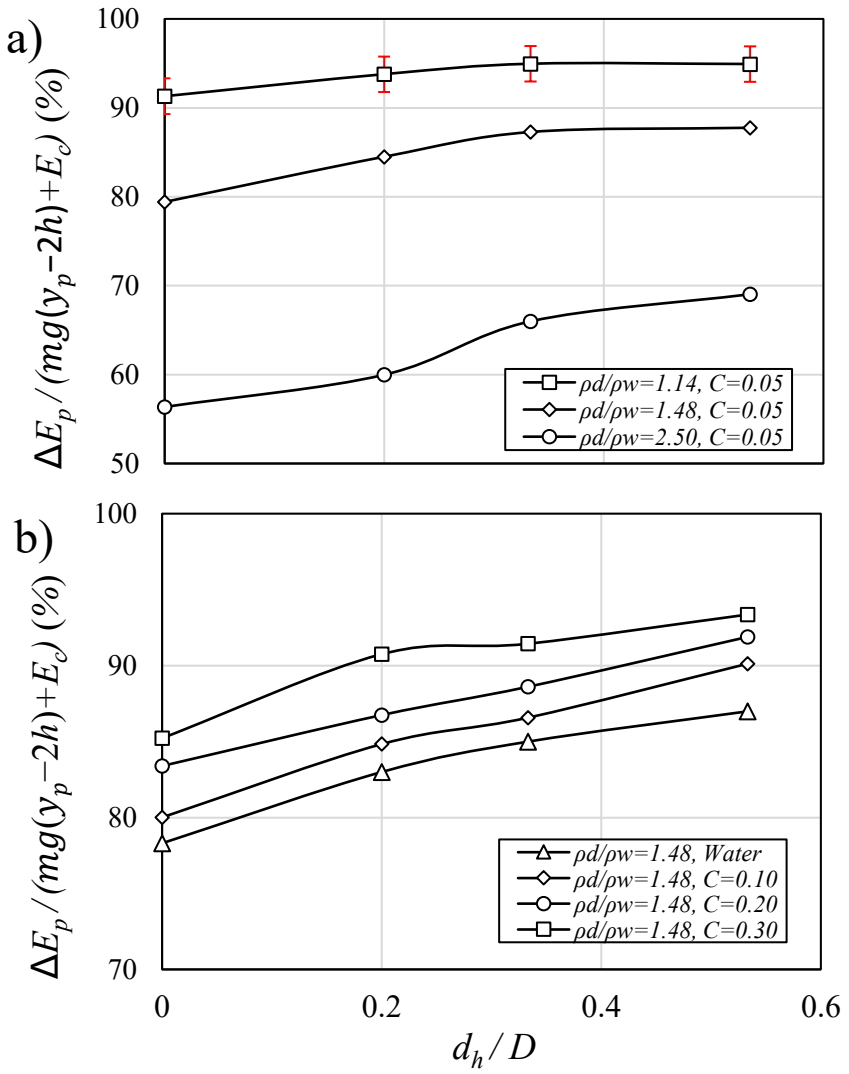

Figure 4.7: Effects of disk density and polymer concentration on variations of pinch-off energy losses relative to the potential energy at the pinch-off stage: a) effect of disk density for constant polymer concentration, C = 0.05 % PAM, b) effect of polymer concentration for disks with constant density ratio of ρ_d/ρ_w = 1.48.

The pressure distribution varies as the disk opening size fluctuates the flow through the disk. The produced vortex impacts the stability of the cavity walls and alters the energy dissipation. The non-Newtonian fluid's elastic properties impart the kinetic energy and cause dampening of the primary energy. Figure 8 shows the effects of disk density ratio, polymer concentration, and disk opening on variations of normalized energy losses at the pinch-off. The horizontal axis in Figure

4.8 is the polymer concentration and the vertical axis is the energy loss due to pinch-off normalized with the summation of potential energy and kinetic energy prior to the pinch-off. The effect of opening diameter ratio is isolated and the effects of disk density ratio with variations of polymer concentration are shown in Figure 4.8a. As can be seen, energy losses due to pinch-off increased with increasing polymer concentration and reduced with increasing disk density ratio. However, the effect of density ratio on variations of energy losses reduced with increasing polymer concentration. The normalized energy losses due to pinch-off of a hollow cylindrical disk in water (i.e., $C = 0\%$) increased from 65% to 95% as the density ratio dropped from 2.5 to 1.14. Whereas the energy losses due to pinch-off of the same hollow disk in a mixture with polymer concentration of $C = 0.3\%$ PAM increased from 84% to nearly 100% as the density ratio dropped from 2.5 to 1.14.

Figure 4.8b shows the effects of polymer concentration and disk opening ratio on variations of normalized energy losses due to pinch-off for a constant disk density ratio of 1.48. Adding a small amount of polymer (i.e., 0.01 wt.% PAM) to water slightly increased the energy losses due to pinch-off. As the polymer concentration increased from 0.01 to 0.05 wt.% of PAM leading to a slight reduction in energy loss of hollow disk with relatively large opening diameter ratio. For polymer concentrations in the range of 0.01 to 0.05 wt.%, the trend of energy losses deviated from the expected correlation with polymer concentration, showing a reduction instead. A comparison between the controlling parameters in Figure 4.8b indicated that both polymer concentration and opening size ratio have the same impact on variations of normalized energy losses at the pinch-off. In addition, larger density ratios amplified the contribution of the gravitational force in comparison to the total energy requirement, while larger opening diameter ratios modified the flow patterns and stress distribution around the disk.

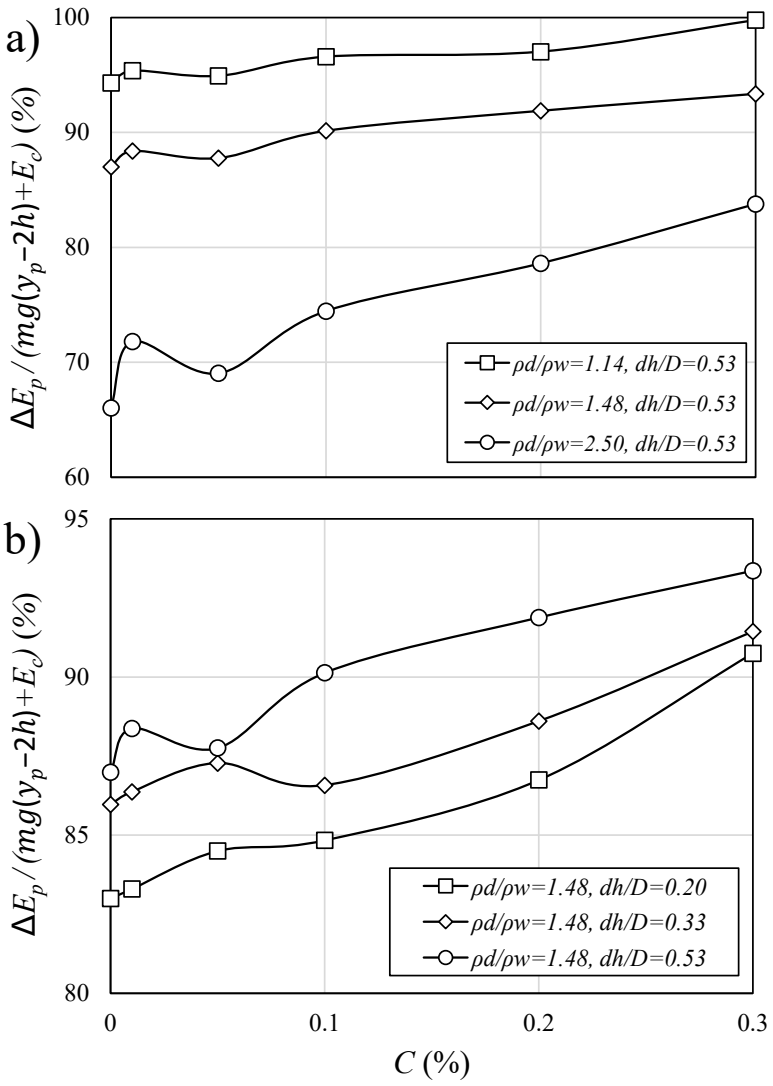

Figure 4.8: Effects of disk density, polymer concentration, and disk opening diameter on variations of normalized energy losses at the pinch-off: a) effect of disk density ratio and polymer concentration on pinch-off energy losses for constant opening diameter ratio of d_h/D = 0.53, b) effect of disk opening diameter ratio and polymer concentration on pinch-off energy losses for constant disk density ratio of ρ_d/ρ_w = 1.48.

To depict the impact of disk's density ratio on energy losses due to pinch-off, the correlation between disk density ratio and normalized energy losses due to pinch-off was plotted in Figure 4.9. This graph provides a quantitative visualization on how disk density correlates with the energy dissipation due to pinch-off. The disks with the same opening diameter ratio of d_h/D =

0.2 were selected and variations on viscosity of the ambient fluid mixture were shown in family of curves. As can be seen, the normalized energy losses due to pinch-off decreased almost linearly with density ratio and increased with increasing the mixture's viscosity. This configuration shows that increasing the mixture's viscosity leads to higher energy losses, with the lines ordered by ascending viscosity levels. A comparison between the disk density increments from 1.14 to 1.48, and 1.48 to 2.5 (i.e., 30% and 70% increase on density), the energy losses of an annular disk in water due to pinch-off reduced by approximately 10% and 40%, respectively.

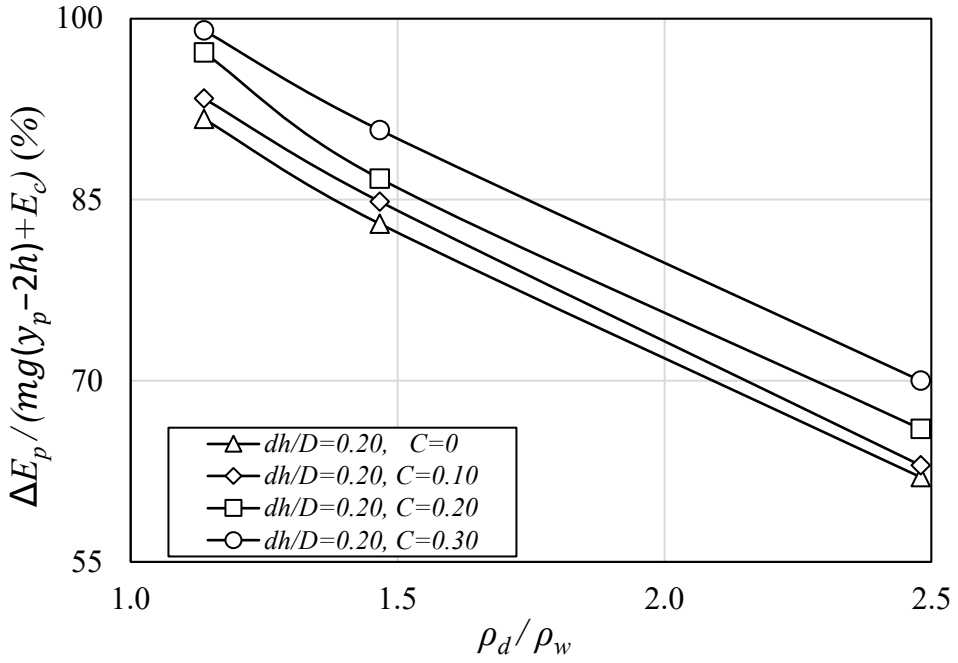

Figure 4.9: Effects of disk density ratio, polymer concentration, and disk opening on variations of normalized energy losses in pinch-off stage. Disk density ratio and polymer concentration are varied, and opening diameter ratio is constant, d_h/D = 0.20.

Higher disk density increases the gravitational force, ending to greater impact momentum and deeper cavities. In non-Newtonian fluids, the interplay between the increased momentum and the fluid's resistance delays in pinch-off moment. The density also affects the rate of energy transfer from the disk to the fluid, influencing deceleration and sinking behavior. It was observed that annular disks entering non-Newtonian fluid mixtures produce through-hole jets whose characteristics depend on the opening size and fluid viscosity, and consequently the amount of the

energy that transfers to the fluid form the solid object. The above figures showed the effects of controlling parameters such as ambient viscosity, disk density ratio, and opening diameter ratio on variations of normalized energy losses at the pinch-off. The mentioned controlling parameters have different impacts on variations of the energy losses and a multi-variable regression correlation model was used to determine the impact of each controlling parameters. The effect of ambient viscosity, varied by the polymer concentration, was shown with the Reynolds number. As it was shown in Figure 4.9, the effect of disk density ratio on energy losses due to pinch-off was more pronounced and the multi-variable regression correlation model found a power of 0.5 for this parameter. The effects of ambient viscosity and normalized opening diameter were found to be the second and third importance level and the powers of 0.05 and 0.005 were chosen by the regression model.

Figure 4.10 shows the variations of normalized energy dissipation due to pinch-off with the combined controlling parameters having the optimized powers of 0.5, 0.05, and 0.005 for disk density ratio, ambient viscosity, and disk opening size ratio, respectively. The ±15% variations from the average are shown with dashed lines in Figure 10. For better visualization of data, the correlation of all data was sorted for different disk density ratio and ambient viscosities. Figure 4.10a shows the correlation between combined controlling parameters having optimized powers with normalized energy losses due to pinch-off. The results were sorted out based on the three disk density ratios of 1.14, 1.48, and 2.50. As can be seen, the effects of other parameters on variations of energy losses due to pinch-off increases with increasing density ratio as data scattered less in disks with small density ratio and more in disks with large density ratio of $\rho_d/\rho_w = 2.5$. The effect of ambient viscosity on correlation between combined controlling parameters and normalized energy losses due to pinch-off is shown in Figure 10b. Same scatter levels are observed in Figure 10b indicating a consistent influence of ambient viscosity (i.e., polymer concentration) on variations of normalized energy losses due to pinch-off, suggesting that while polymer concentration affects the system's behavior, its impact may scale uniformly across different conditions.

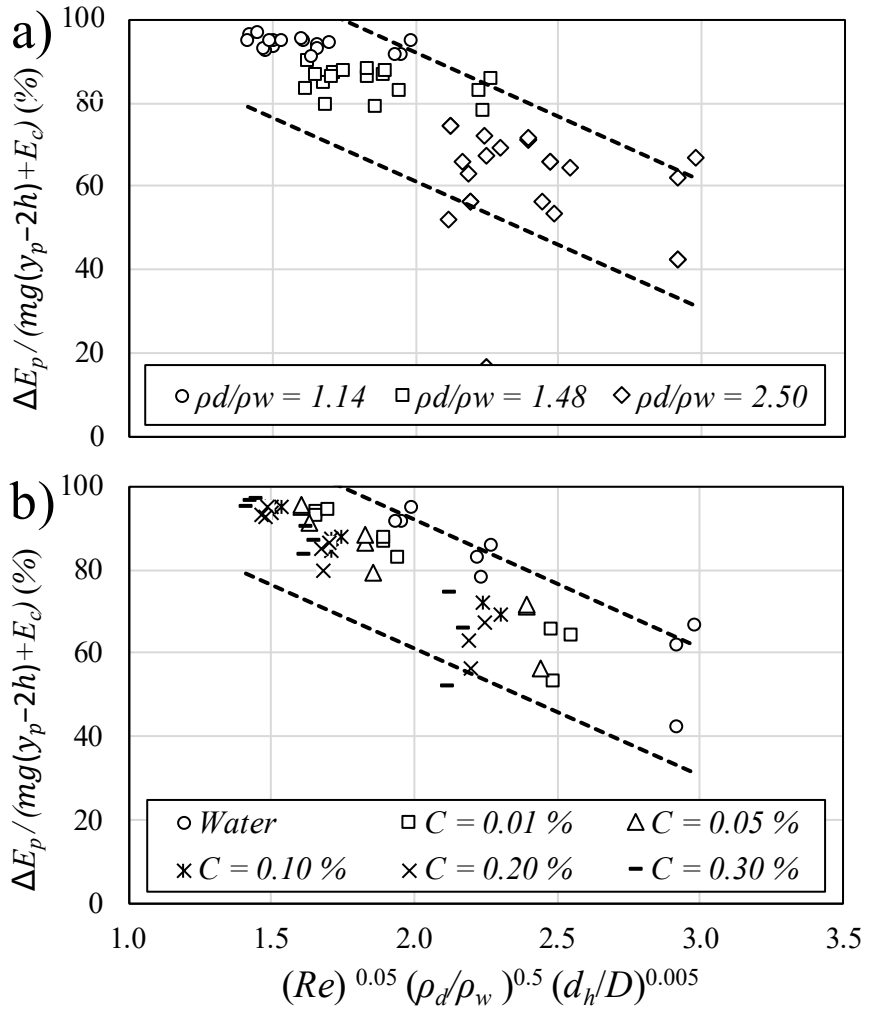

Figure 4.10: Variations of normalized energy losses in pinch-off stage. The energy losses were normalized with the impact energy loss alongside all the under-study factors such as disk density ratio, disk opening size ratio, and Reynolds number: a) effect of disk density ratio, b) effect of polymer concentration.

4.3.2.3 Energy losses at the sinking stage

To compare the magnitude of energy losses at different stages of evolution, the energy losses due to the collision of a cylindrical disk with the fluid's surface, pinch-off, and sinking were combined, and the combined energy losses were compared with the total energy of the disk. The total energy of a disk is calculated by the summation of the potential energy, using a distance between the release position and the settling position at the end of the Region of Interest (ROI),

and the kinetic energy based on the sinking velocity. The effects of controlling parameters on energy losses for solid cylindrical disks, without an opening at the center ($d_h/D = 0$), are shown in Figure 4.11. This figure comprises of six subplots for different polymer concentrations and each subplot displaying three energy loss graphs corresponding to different disk density ratios. Within each subplot, the column graphs illustrate three types of energy losses as a percentage of the total energy, E_T. Each bar plot represents three sections. First, the energy losses during the collision and immersion as a fraction of the total energy, $(\Delta E_c)/E_T$. The second section in each column bar represents the energy losses due to pinch-off as a percentage of the total energy, $(\Delta E_p)/E_T$. The third section in each column bar illustrates the energy losses associated with the sinking phase, $(\Delta E_s)/E_T$.

Figure 4.11a shows the energy balance of a solid cylindrical disk in water. As can be seen, the normalized energy losses due to collision were almost independent of disk's density and the energy losses in pinch-off stage adversely correlated with the density ratio. The most impact of the density ratio was in the sinking stage at which the sinking energy losses in relatively dense disks was found to be much smaller than that of relatively lighter disks. This can be due to the stability of heavy disks in sinking stage which can reduce the energy losses significantly. As can be seen, the sinking energy losses in solid disks with a density ratio of 1.14 was equal to 21.85% of the total energy whereas such energy losses in relatively heavier disk was only 2.32% of the total energy. This indicated that relatively dense disks can preserve the total energy much better than that of lighter disks. Such observations were found to be consistent regardless of ambient viscosity and the sinking energy losses in heavy and solid disks varied between 3% to 6% of the total energy. Based on the findings of Guleria et al., (2021), it was shown that approximately 90% of the primary kinetic energy is lost for a sphere with a density of 2500 kg/m³, whereas around 50% is lost for a sphere with a density of 7780 kg/m³. These results align with the current study, confirming that the density of a rigid body significantly influences the energy losses. Specifically, an increase in the rigid body's density reduces the primary kinetic energy losses.

A slight increase on the ambient viscosity altered the composition of energy losses at the three mentioned stages and such transfer of energy losses was more pronounced in relatively heavier disks. For example, for a disk with a density ratio of 2.5, a slight change on polymer concentration from water (i.e., $C = 0\%$ PAM) to $C = 0.01\%$ PAM (comparing Figures 4.11a and

4.11b) reduced the energy losses due to collision from 31.47% to 28.18% indicating that the slight increase in the ambient viscosity reduced the water movement and formation of large crown and fluid's splash. The energy losses due to pinch-off slightly increased with the addition of ambient viscosity from 12.78% to 17.51%, which can be due to formation of cavity and additional work done by the disk to create and hold the cavity. The small addition of ambient viscosity continuously reduced the sinking velocity of the disk due to formation of larger skin friction drag force resulted in almost doubling the energy losses due to sinking, a change from 2.7% to 5.92%. As it was expected, the addition in ambient viscosity increased the total energy losses. The total energy losses by a solid disk entry in water and in a fluid mixture with 0.01% PAM were 47%, and 51.6% of the total energy, respectively. The drag force promotes the total energy dissipation. In addition, increasing the disk opening reduces the frontal area which reduces the drag force and consequently the energy dissipation related to cross-drag flows. The viscosity of the fluid further enhances the drag-induced energy losses through viscous dissipation and turbulence modulation.

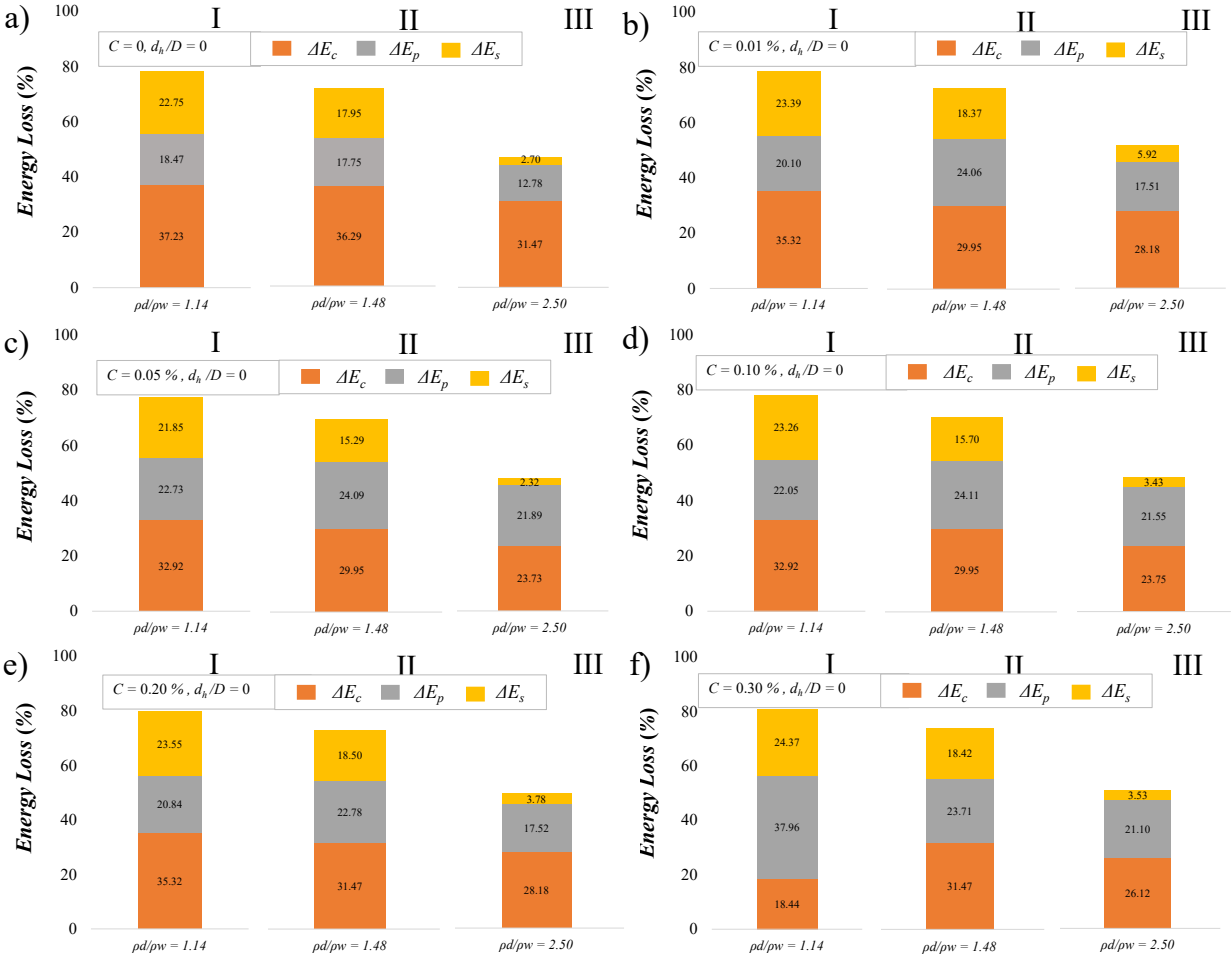

Figure 4.11: Effects of polymer concentration and disk density ratio of solid disks on variations of energy losses in collision, pinch-off, and sinking stages. The disks in this figure were solid without an opening at the center of the disk (i.e., $d_h/D = 0$): a) $C = 0\%$ PAM (Water), b) $C = 0.01\%$ PAM, c) $C = 0.05\%$ PAM, d) $C = 0.10\%$ PAM, e) $C = 0.20\%$ PAM, f) $C = 0.30\%$ PAM.

Figure 4.12 presents the effects of disk opening diameter on variations of collision and immersion, pinch-off, and sinking energy losses for a constant polymer concentration and density ratio of $C = 0.30$ wt.% and $\rho_d/\rho_w = 1.14$, respectively. The disk opening diameter ratio varies from zero to 0.53 which are presented in columns I, II, III, and IV, respectively. As can be seen, the energy losses due to collision significantly dropped from 31.47% of the total energy for solid disks to approximately 20% by annular disks. The sudden drop in reduction of energy losses due to collision is due to reduction of contact surface of the disks. Further reduction of the disk's contact surface reduced the energy losses due to collision from 21% to approximately 18% of the total energy of the disk. The reduction on the energy losses due to collision was compensated by the energy losses due to pinch-off.

As can be seen from Figure 4.12, the percentage of energy losses due to pinch-off increased from 23.71% in solid disk to 36.3% in an annular disk with $d_h/D = 0.53$. Such growth in energy losses due to pinch-off may be due to formation of Worthington jet in annular disks (see Figure 4.2). The energy that is required to develop the Worthington jet is taken from the disk's kinetic energy and such phenomenon increases the energy losses due pinch-off. Figure 4.12 shows the steady growth of energy losses due to skinning with the central opening on the disk. This indicated a steady growth on the percentage of sinking energy losses from 18.42% in solid disk to 22.45% in an annular disk with $d_h/D = 0.53$. The steady growth of energy losses due to sinking may be correlated with the increase on the contact surface in annular disks. The higher opening diameter increases the contact surface area which increases the friction between the disk and the ambient fluid. The total energy losses in solid and annular disks with different opening diameter ratios of 0.2, 0.33, 0.53 were 73.6%, 74.79%, 75.54%, and 76.66%, respectively. This indicates that the total energy losses increased with the existence of the central opening and increased with increasing the opening diameter. The kinetic energy variation results from the balance between gravitational forces and resistive forces from the fluid (i.e., viscous drag and elastic stresses in

non-Newtonian fluid mixtures). The disk imparts momentum to the fluid and initiate cavity formation. The rate of momentum transfer depends on disk mass, impact velocity, and fluid properties. The present non-Newtonian fluid mixtures exhibit shear-dependent viscosity and elasticity, affecting how the fluid alter the behavior of the sinking disk which influence drag forces (Ebrahimi and Azimi, 2024, 2025).

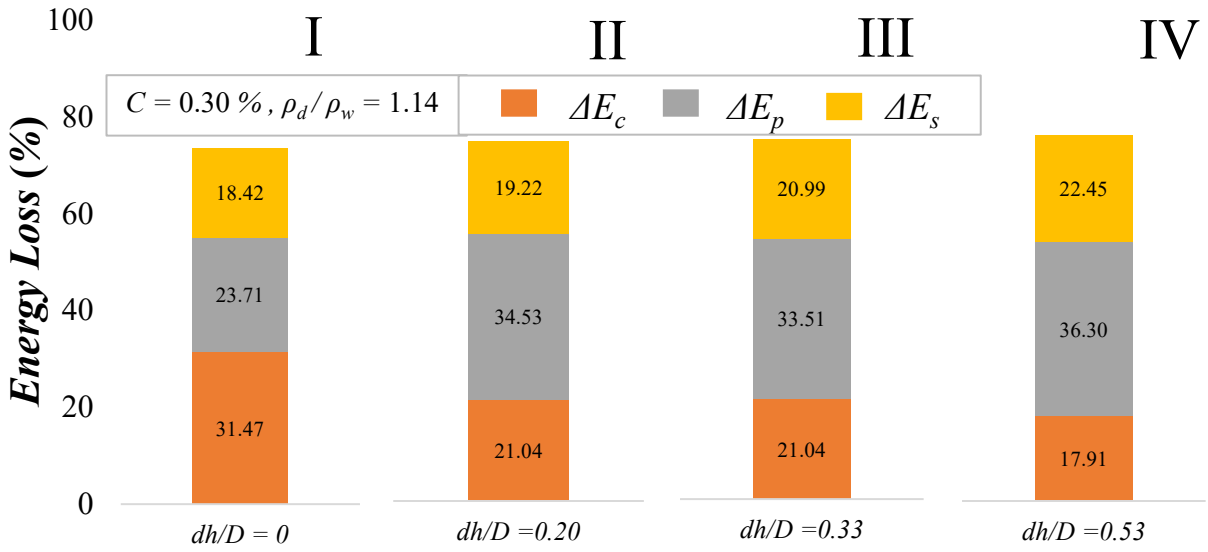

Figure 4.12: Effects of disk opening size ratio on variations of energy losses in collision, pinch-off, and sinking stages. Polymer concentration and density ratio were kept constant with values of C = 0.30 wt.% and ρ_s/ρ_w = 1.14, respectively.

4.5 Conclusions

The present study elucidates the dominant mechanisms governing energy dissipation during the entry of solid and annular disks into water and viscous fluid mixtures and the subsequent cavity formation processes. Our results demonstrate that collision with the liquid surface is the critical stage where most of the initial kinetic energy is lost, establishing a strong link between disk density, ambient viscosity, and geometric configuration. Four distinct stages of evolution, named as collision, immersion, pinch-off, and sinking, were identified that represent substantial phenomena during the entry of the solid cylindrical disk in the fluid mixture. The energy losses due to collision and immersion significantly dropped for disks with a central opening while the

effect of opening diameter was found to be negligible on variations of energy losses due to collision. The energy losses due to immersion of the disk in fluids mixture was approximately 68% of the potential energy for the lightest solid disk and it reduced to approximately 40% due to presence of a central opening in a disk.

The relative density of solid and annular disks significantly affected the variations of energy losses at the pinch-off and an adverse correlation was found between disk density and energy losses at the pinch-off. The effect of ambient viscosity on variations of energy losses at the pinch-off indicated that the energy losses increased with increasing ambient viscosity while opening diameter had a relatively small impact on variations of energy losses. The multi-variable regression analysis determined the importance of the controlling parameters and found that the density has the highest impact on energy losses due to pinch-off followed by the ambient viscosity and opening diameter.

The percentages of energy losses at different stages of evolution with respect to the total energy of the disk were calculated for all tests. The most impact of the density ratio was found to be in the sinking stage. The normalized sinking energy losses in relatively dense disks was found to be much smaller than that of relatively lighter disks. It can be concluded that relatively dense disks can preserve the total energy much better than that of lighter disks. Experimental data indicated that the ambient viscosity altered the composition of energy losses at the three mentioned stages and such transfer of energy losses was more pronounced in relatively heavier disks. Overall, the total energy losses increased with the existence of opening and a direct correlation was found between total energy losses and opening diameter.

A significant portion of the disk's kinetic energy is converted into surface energy, which results in splash formation. Pressure at the fluid-solid interface induce abrupt fluid acceleration in outward direction, overcoming surface tension and gravity, and subsequently generating droplets and splash. The splash is influenced by elements such as impact velocity, fluid viscosity, and the geometry of the disk. Overall, the present experimental data indicated that higher impact velocities and lower viscosities resulted in more splash generation.

Chapter 5

Effects of impact geometry and orientation on water entry of cylindrical disks

5.1 Introduction

Water entry of rigid bodies has come to great consideration due to their numerous applications in many fields of engineering such as marine engineering, offshore, and oil and gas industries (Faltinsen et al., 2004; Seddon and Moatamedi, 2006; Kapsenberg, 2011; Ebrahimi et al., 2020; Ebrahimi and Sanati, 2021). Entry of rigid bodies into water is accompanied by the generation of different phenomena such as splash formation at the water surface due to momentum transfer from the rigid bodies to the water. Cavity formation occurs beneath the contact surface due to pressure difference and air entrainment followed by the pinch-off. The location and time of pinch-off and the associated parameters in addition to formation of crown and splash curtain have been studied through detailed experimental studies (Aristoff et al., 2010; Bodily et al., 2014; Shi et al., 2019; Zhang et al., 2021 Huang et al., 2024; Wang et al., 2024 ; Akbarzadeh et al., 2022; Ebrahimi and Azimi., 2024, 2025a, 2025b). Many underlying parameters have been recognized in the past that affect the entry of rigid bodies into stagnant ambient and that control the momentum and energy transfer from the moving object into the surrounding ambient. Such factors are categorized by 1) the rigid body features, 2) the properties of the surrounding fluid, and 3) the release conditions. Many research studies have focused on the characteristics of rigid bodies such as geometry, density, shape, etc. (Willmarth et al., 1964; Guleria et al., 2021; Zhou et al., 2021; Zhang et al., 2022; Akbarzadeh et al., 2023; Alif et al., 2023; Li et al., 2024). Other studies have focused on release conditions, such as release direction and release orientation of the object, which affect the impact velocity and the contact angle.

A paper based on the content of this chapter is published in the *Physics of Fluids, Ebrahimi, M., & Azimi, A. H. (2025b).* Effects of impact geometry and orientation on water entry of cylindrical disks. Physics of Fluids

Shokri and Akbarzadeh (2022) studied the effects of sphere geometry and release height on the water entry of dimpled spheres. The selected release heights resulted in different impact velocities varied between 0.30 to 4.30 m/s and the number of dimples ranged from 0 (i.e., smooth surface) to more than 50 dimples for a constant sphere diameter, D = 20 mm, and density of ρ = 7780 kg/m^3. The existence of dimples on the sphere's surface imposes instabilities due to wave-like disturbances on splash formation and cavity surface in comparison to the corresponding smooth sphere. It was found that an increase in the impact Froude number increases the pinch-off characteristics such as pinch-off depth and time. In addition, the air entrainment volume increased with the number of dimples and led the cavity regime to transit from shallow-seal to deep-seal. Tveitnes et al. (2008) conducted a series of experimental studies on the water entry of rigid wedge-shaped bodies in water. The wedge-shaped bodies had different deadrise angles with the masses varying from 2.5 to 7.1 kg, and the impact velocity ranged from 0.24 to 1.20 m/s. It was found that increasing the deadrise angle leads to a reduction in the drag coefficient. A similar trend was observed for the added mass coefficient in response to the increments in the deadrise angles. The release angle plays an important role in momentum transfer from the moving object to the ambient water. Song et al. (2020) performed an experimental study on the oblique water entry of projectiles while the entry angle was adjusted between 30^o and 90^o. The diameter of the projectiles was constant, D = 8 mm, and the mass and impact velocity of the projectiles varied from 0.01 to 0.02 kg and 80 to 130 m/s, respectively. It was found that the oblique water entry formed the second and third cavities, which affect the deceleration of projectiles over time. The influence of the entry angle was shown with two parameters of axial and horizontal velocities, where the horizontal velocity stands in the descending order through the increments in the entry angle, and it was opposite to the axial velocity.

Many research studies focused on the entry dynamics of hollow cylinders in water (Hou et al., 2019, 2021, 2022). The diameter of the exerted cylinder was constant with a value of D = 30 mm while the impact Froude number varied in the range of $Fr = v/(gL)^{1/2}$ = 5 to 10, where g is the gravitational acceleration, L is the characteristics length of the cylinder, and m is the mass of the cylinder ranged from m = 0.13 to 0.33 kg. A strong correlation was found between the hole diameter and the water entry parameters such as the diameter and height of the through-hole jet. It was found that both mass and impact velocity of the cylinders increased the pinch-off depth and sinking velocity of the cylinders. Jafari and Akbarzadeh (2022) investigated the entry dynamics of

annular cylinders. The density and the diameter of the cylindrical disks were constant with the values of ρ_d = 7700 kg/m^3 and D = 25 mm, while the impact velocities varied from 0.30 to 4.30 m/s. Strong correlations were observed between the impact velocity of the disks and the pinch-off time and depth. In addition, the impact velocity increased the dimensions of the through-hole jet. The conical hole geometry exhibited a larger impact cross-section compared to the other two projectiles tested by Jafari and Akbarzadeh (2022)

The effects of geometry and release conditions on the water entry of cylindrical disks were investigated by Janati and Azimi (2023). The density of the disks varied from 1140 to 2500 kg/m^3 and the entry dynamics of annular disks were compared with the corresponding solid disks having the same diameter of D = 75 mm and opening size of d_h = 38 mm. The impact Froude number varied between $Fr = v/(gD)^{1/2} = 1$ and 3.5 to examine the momentum transfer impacts. It was found that the splash diameter was correlated with the collision surface area of the disks and the splash diameter of the solid disks was larger than that of annular disks by 15 %.

The ambient fluid properties significantly affect the entry phenomenon and formation of the cavity and splash curtain. Ebrahimi and Azimi, (2024, 2025a, 2025b) performed a series of detailed laboratory experiments on the entry of a solid disk in a non-Newtonian ambient to investigate the effects of fluid viscosity, ranging from 12 to 580 mPa.s, on solid entry, cavity formation, and energy transfer between the disks and the ambient fluid mixtures. Ebrahimi and Azimi (2024) examined the entry dynamics of solid disks with densities varied between ρ_d = 1140 and 2500 kg/m^3 and disks aspect ratios of D/h = 1.5 and 3.0, where D and h are the diameter and thickness of the disks, respectively. The release height of disks was constant (h_r = 0.50 m) and the disk diameter was D = 0.075 m. All disks were released in a way that the flat surface of the disks was parallel to the fluid's surface. Such disk orientation is called the face-on release condition. Experimental results indicated that increasing the disk density increases the pinch-off time and depth. In addition, the aspect ratio of disks reduced the overall sinking velocity and prolonged the pinch-off depth.

The solid entry of annular disks with different hole diameters in water and non-Newtonian ambient was investigated by Ebrahimi and Azimi (2025a). The hole size ratio varied between d_h/D = 0.20 and 0.53 while the disk aspect ratio was kept constant at D/h = 1.5. The results demonstrated that increasing the hole size ratio significantly reduced sinking velocities, achieving

approximately 50% to 70% of the velocities observed for solid disks. In addition, pinch-off by annular disks occurred closer to the fluid's surface. Ebrahimi and Azimi (2025b)studied the energy loss variations in different stages of collision, pinch-off, and sinking. The effects of disk density, disk opening size, and fluid viscosity on energy losses were investigated. It was found that increasing the fluid viscosity leads the damping force to increments, which increases the energy losses. The total energy losses were found to be varied between 50% and 80% where the main energy losses happen during the collision stage.

The recent research studies have focused on the entry of solid disks in the face-on orientation (Ebrahimi and Azimi, 2024, 2025a, 2025b). In such a disk orientation, the surface of the disk is parallel to the fluid surface, the collision and the resulting crown and splash curtain are symmetrical. The current study aims to investigate the geometrical characteristics of the entry of solid disks such as crown dimensions and pinch-off and the dynamic features of the cylindrical disks such as impact velocity and settling in the edge-on orientation (see Figure 1). Preliminary experiments indicated that the crown formation in edge-on release conditions is asymmetric and such asymmetry significantly impacts the cavity dynamics and pinch-off. Experimental observations indicated that the curved lateral surface collides with the water, leading to fundamentally different impact dynamics compared to the face-on release orientation.

The new orientation reduces the initial contact surface (i.e., wetted area) and geometric asymmetry influences the entry hydrodynamics and subsequent cavity formation. Therefore, such orientation adjustment enables a comparative assessment on how initial contact area and impact geometry can influence cavity formation and hydrodynamic response. In such orientation, the crown is asymmetric, and the splash curtain is three-dimensional due to the curved contact surface of the disk and such asymmetric and three-dimensional impact may result in a significant change in velocity retardation and energy transfer. As a result, visual observations are conducted in the frontal, lateral (side), and oblique (45º) views to determine the asymmetry effect (see Figure 1a). The current study examined the effects of edge-on entry of both solid and annular disks with different densities, aspect ratios, and hole diameters. Such systematic variation enables a comprehensive analysis of the geometry-dependent behavior during the water entry process.

Previous research studies have examined the effects of some controlling parameters on the water entry of spheres and cylindrical disks. The release orientation of all disks in previous studies

was in face-on orientation, there remains a lack of a systematic, side-by-side comparison of other release orientation for solid and annular disks under identical geometric (i.e., diameter, thickness, opening ratio) and release (i.e., height, entry angle) conditions. Preliminary observations indicated asymmetry crown formation which the initial collision area and opening ratio can be the main source of such asymmetry growth. The spatiotemporal evolution of cavity pinch-off, and the partitioning of energy losses at different stages of collision, pinch-off, and sinking have not been quantified in previous studies which requires more attention. The present study fills the gap of knowledge by mapping the influence of disk impact orientation (edge-on versus face-on) on crown asymmetry, pinch-off time and depth, and sinking velocity for solid and annular disks. In addition, the effects of disk aspect ratio, disk opening and density on splash and cavity evolution are considered.

In the following, the experimental procedure and measurement techniques are presented. To introduce the results, the consecutive images of different experiments are illustrated to understand the effects of edge-on entry on dynamics and energy transfer. To present the quantitative outcomes, the phenomena related to the under water surface such as pinch-off time and depth and sinking velocity are illustrated before the upper water surface phenomena (i.e., splash curtail and crown formation). Detailed information on the splash formation and the related parameters such as splash diameter and height are presented as well. More importantly, the effects of release orientation on energy losses at different stages of collision, pinch-off, and sinking are studied, and the results are compared with the corresponding face-on release orientation of the disks.

5.2 Experimental setup

A glass-walled tank with dimensions of 400 mm × 400 mm × 1000 mm was used to perform the experiments. The tank was filled up to a height of 700 mm, and the 300 mm height above the water surface was empty for splash observation after the disk entry. It was ensured that the water surface height remains constant and stable after each test to reduce experimental uncertainty. All 24 disks had a constant diameter of $D = 75$ mm with two thicknesses of $h = 50$ and 25 mm giving two aspect ratios of $D/h = 1.5$ and 3, respectively. The disks were homogeneous and made of compressed rubber with densities of $\rho_d = 1140$, 1480, and 2500 kg/m^3. The disks included a rounded rim on the side edge with a roughness height of 1 ± 0.1 mm. The solid and annular disks used in this study are classified into four groups with inner diameters of $d_h = 0$, 15, 25, 40 mm

giving the opening diameter ratio of d_h/D = 0, 0.20, 0.33, 0.53, respectively. The release height was kept constant with h_r = 500 mm from the water surface. All disks were released from the rest, and they accelerated due to the gravitational force. The gravity-driven release of disks ensures that the disks enter the water surface perpendicularly, which makes the entry angle equal to 90°. Disks were positioned at the center of the tank to eliminate the wall effect. The fluid used in this study was water with the density and viscosity of ρ_w = 998 kg/m^3 and μ = 1 mPa.s.

To assess the behavior of a free-falling disk into water, two high-speed cameras (Phantom, Miro Lab 110, New Jersey, Wayne, USA) with the camera lens AF Nikkor 50 mm, f/1.4D (Nikon, Tokyo, Japan) were employed. The productivity of the cameras is dependent on providing sufficient brightness, which is supplied by six source lights (Woods 166 L13, 1000-W telescope work light, CA). Each experiment was repeated three times to ensure the credibility of the experiments and to determine measurement uncertainty. The high-speed cameras were set to capture images with a frequency of 1000 fps and a resolution of 1280 × 800 pixels. A sufficient relaxation time of more than 20 minutes between each experiment was given to eliminate water surface fluctuations. All experiments were carried out in the Multiphase Flow Research Laboratory (MFRL) at Lakehead University, Canada.

The experiments were conducted at atmospheric pressure, and the water temperature was kept constant at 25 °C. The experiments commenced with the water entry of 24 disks, followed by two other trials using the exact same disk to investigate the impacts of disk aspect ratio, disk density, and opening diameter through all perspectives. Overall, 72 experiments, excluding the repetition tests, were conducted.

An in-house MATLAB (Mathworks, R2018b, Natick, USA) algorithm was used for image analysis and to extract the required information from the images. In the following, the results of the conducted experiments are presented by identifying features such as pinch-off characteristics, splash properties, disk position, etc. The details of experimental data are presented in Table 1, which shows the variations of pinch-off and splash characteristics with the geometry of the disk, disk density ratio, and disk aspect ratio.

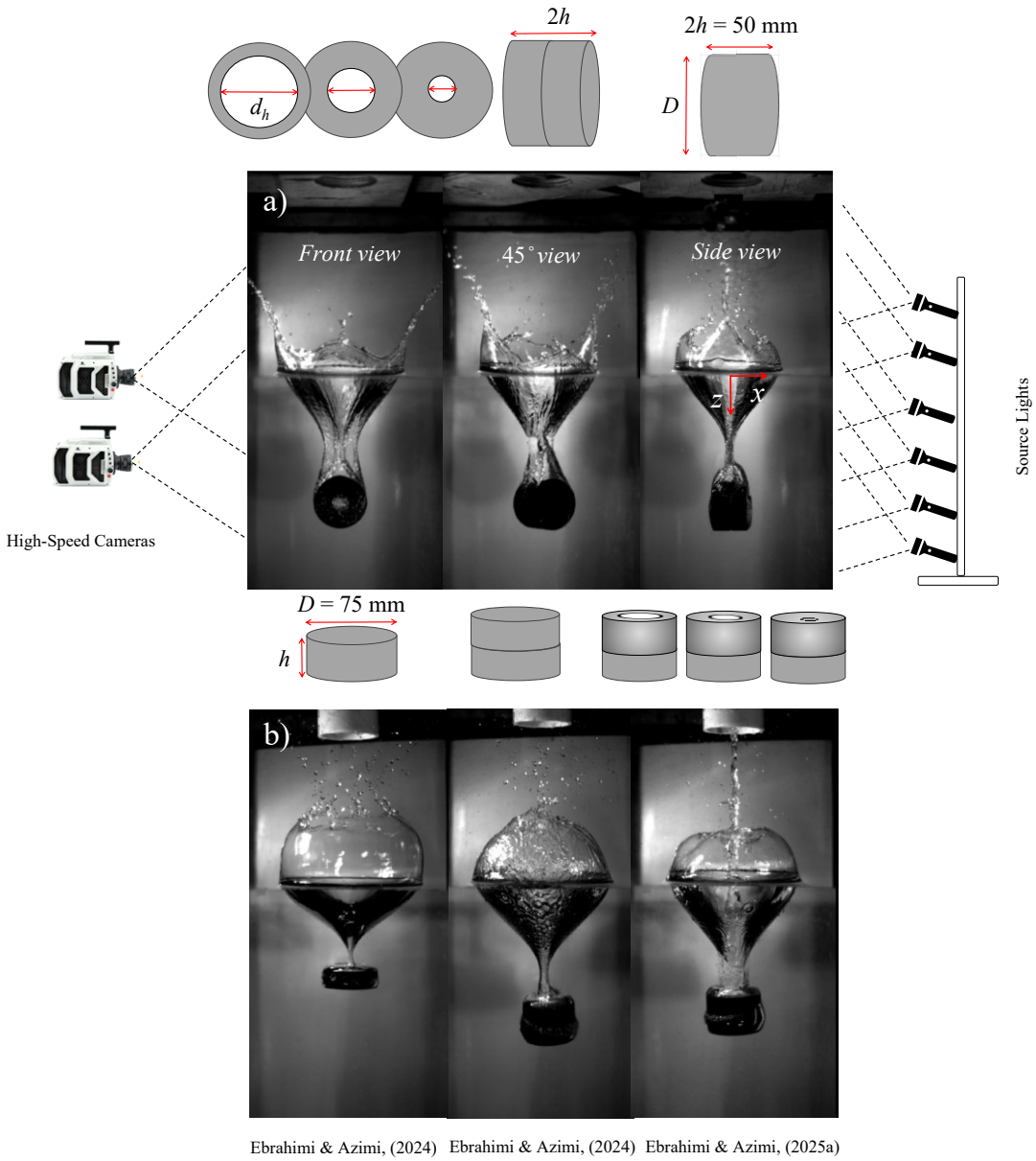

Figure 5.1: Experimental setup of the cylindrical disk entry in water, disk geometry, impact orientation, and the coordinate system: a) the edge-on impact orientation configuration for the three perspectives of the front view (left image), 45˚view (middle image), and side view (right image), b) face-on impact orientation configuration from the experimental study of Ebrahimi & Azimi (2024, 2025a)

Table 5.1: Variations of pinch-off and crown characteristics with the geometry of the disk, and density ratio.

Test No.	*D/h*	ρ_d/ρ_w	d_h/D	t_p/T	h_p/D	h_d/D	v_s/v_e	h_c/D *frontal view*	d_c/D *frontal view*	h_c/D *Side view*	d_c/D *Side view*
1	1.5	1.14	0	1.42	1.37	1.84	0.75	1.60	2.43	0.81	2.08
2		1.48		1.44	1.48	2.11	2.20	1.61	2.49	0.87	2.12
3		2.50		1.48	1.65	2.80	3.80	1.65	2.51	0.87	2.15
4		1.14	0.20	1.41	1.35	1.79	1.45	1.09	2.44	0.95	2.09
5		1.48		1.43	1.41	2.07	2.41	1.36	2.51	0.96	2.13
6		2.50		1.46	1.61	2.76	4.72	1.57	2.51	1.05	2.15
7		1.14	0.33	1.37	1.33	1.76	1.04	1.07	2.43	1.00	2.07
8		1.48		1.42	1.38	1.85	2.01	1.30	2.49	1.01	2.11
9		2.50		1.46	1.60	2.63	4.17	1.57	2.55	1.07	2.15
10		1.14	0.53	1.34	1.15	1.50	0.68	1.10	2.42	0.97	2.09
11		1.48		1.41	1.35	1.59	1.29	1.50	2.51	1.00	2.12
12		2.50		1.45	1.59	2.53	2.68	1.70	2.58	1.10	2.16
13	3.0	1.14	0	1.18	1.30	1.54	0.78	0.20	1.60	0.40	1.50
14		1.48		1.20	1.41	2.00	2.40	0.22	1.66	0.49	1.57
15		2.50		1.25	1.48	2.40	3.80	0.25	1.71	0.55	1.80
16		1.14	0.20	1.14	1.27	1.51	1.52	0.29	1.83	0.65	1.45
17		1.48		1.18	1.37	1.80	2.53	0.56	1.85	0.67	1.46
18		2.50		1.24	1.45	2.34	4.00	0.80	1.93	0.69	1.55
19		1.14	0.33	1.14	1.06	1.48	1.17	0.50	1.84	0.70	1.46
20		1.48		1.17	1.29	1.72	2.24	0.60	1.85	0.73	1.54
21		2.50		1.21	1.38	2.31	3.80	0.62	1.96	0.80	1.56
22		1.14	0.53	1.12	1.02	1.23	0.77	0.20	1.83	0.23	1.51
23		1.48		1.17	1.15	1.55	1.57	0.23	1.88	0.30	1.55
24		2.50		1.20	1.35	2.16	3.52	0.40	1.97	0.45	1.57

5.3 Results and Discussion

Figure 5.1 shows the experimental setup of the cylindrical disk entry in a stagnant ambient water, disk geometry, coordinate system, and impact orientations. The figure consists of the disks with the two mentioned aspect ratios in addition to the disk opening diameter, d_h. To present the three understudy perspectives, three images were taken to show the front, 45^o (oblique), and lateral views. Figure 1a shows the snapshot images of the edge-on disk entry at the pinch-off moment. Figure 5.1b shows the images of the face-on disk entry from the experimental studies of Ebrahimi and Azimi (2024, 2025a). As can be seen, the splash curtains in edge-on release orientation are asymmetric while the face-on release orientation forms a symmetrical dome-shaped splash curtain.

Figure 5.2 presents the process of image analysis, thresholding, and boundary detection algorithms. The original images were converted to grayscale for edge detection process. Then, a background subtraction algorithm was performed using a morphological opening process. All background noises were removed by implementing a Gaussian filtering, which aids in improving the precision of subsequent edge detection process. To perform the edge detection algorithm, the images were transformed to binary format using automatic thresholding. Some algorithms such as the Sobel and Canny operator edge detection were performed to detect the edge of the disk (Lynn et al., 2021; Shihab Ahmed, 2018).

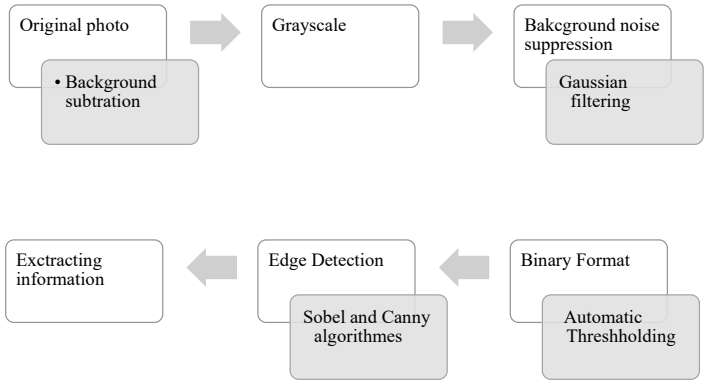

Figure 5.2: The process of image analysis, thresholding, and boundary detection algorithms.

5.3.1 Splash and cavity evolution

Figures 5.3 to 5.5 show the time series images of free-falling disks into the water as a sample in three different views of frontal, oblique, and lateral, for a constant disk aspect ratio of $D/h = 1.5$ while the opening size and density ratios vary. The time interval between each image in all three figures is $\Delta t = 10$ milliseconds. Each time-history sequence links to a specific viewing angle leading to a comprehensive 360° visualization of the water entry event. This provides a helpful perspective on the splash and other related phenomena.

Figure 5.3 presents the time history images of the frontal view of a free-falling solid disk (i.e., $d_h/D = 0$) in stagnant water colliding in its edge-on orientation (Test No: 2). The density ratio of the disk is $\rho_d/\rho_w = 1.48$. The chronophotographic photos start from the impact moment which counts as the reference time (i.e., $t_o = 0$). It takes approximately 35 milliseconds for the disk to become fully submerged in water and within the next 120 milliseconds the pinch-off of the disk occurs. Unlike the previous studies in the literature where the pinch-off detached at only one point, the pinch-off is not confined to a single point in the current study. Instead, it initiates at three distinct points, one at the center and two at the lateral edges of the disk. Such a pinch-off indicates a spatially distributed pinching mechanism. In addition to pinch-off geometry, there are two symmetrical gaps between the central pinch-off point and the lateral ones which may be due to the curved contact surface of the disk at the impact moment.

The splash evolution in edge-on disk entry is not symmetrical and the curtain walls vary distinctly depending on the orientation of the disk. As can be seen from the frontal view, the splash height on the sides is higher than that of the center. Two prominent splash peaks are observed at the sides while the two central peaks of similar heights can be seen with lower heights than the lateral splash heights. Positioned between the central and side splash are two smaller structures, forming concave sections that serve as transitional connections between the middle and lateral splash regions. In addition, many droplets are generated on top of the middle and the side sections of the splash, which may impact the energy dissipation due to impact and pinch-off.

Figure 5.3: Time history images of frontal view for a free-falling solid disk in stagnant water. The density ratio and aspect ratio of the disk is $\rho_d/\rho_w = 1.48$, $D/h = 1.5$. The time interval between each image is $\Delta t = 0.01$ s.

To provide a 360° visualization of the disk entry phenomenon, the oblique and lateral views are presented in Figures 5.4 and 5.5. In Figure 5.4 (Test No: 7), the disk hole diameter, density, and aspect ratios of the test are equal to $d_h/D = 0.33$, $\rho_d/\rho_w = 1.14$, and $D/h = 1.5$, respectively. Similar to Figure 5.3, the time interval between each image is $\Delta t = 10$ milliseconds. It takes more than 40 milliseconds for the disk to immerse thoroughly. The pinch-off happened at around 130 milliseconds after the impact moment and the asymmetrical splash curtain is evident in 45° orientation. Figure 5.5 (Test No: 7) shows the 90° side view of the same disk as shown in Figure 5.4. A comparison between the time series images and the images shown in Figure 3, where the disk density ratio is $\rho_d/\rho_w = 1.48$, indicates a longer immersion time in the current case which is attributed to the lower disk density ratio ($\rho_d/\rho_w = 1.14$) in Figures 5.4 and 5.5. Furthermore, the opening diameter ratio of the disk is $d_h/D = 0.33$ compared to the solid disk in Figure 3. The existence of a hole in the disk generates flow-induced forces that act as a resistance force that causing the disk to sink more slowly. The splash generated by the annular disk (see Figure 5.5) follows the same pattern as the solid disk in Figure 3 with the switch in the position of the side and middle section of the splash where the middle splash observed in the lateral view resembles the

side splash in the frontal view, indicating a rotated symmetry due to the disk's geometry and impact orientation. All disks included a rounded rim on the side edge with a roughness height of 1 ± 0.1 mm. Therefore, across all perspectives, the cavity dynamics are not smooth, and it presents a wavy-like cavity regime.

Figure 5.4: Time history images of oblique 45˚ view of a free-falling annular disk in stagnant water. The hole diameter ratio, density ratio, and aspect ratio of the test are $d_h/D = 0.33$, $\rho_d/\rho_w = 1.14$, $D/h = 1.5$, respectively. The time interval between each image is $\Delta t = 0.01$ s.

Figure 5.5: Time history images of side view of a free-falling annular disk in stagnant water. The hole diameter ratio, density ratio, and aspect ratio of the test are $d_h/D = 0.33$, $\rho_d/\rho_w = 1.14$, $D/h = 1.5$, respectively. The time interval between each image is $\Delta t = 0.01$ s.

Figure 5.6 illustrates the snapshot images of fluid entry of disks with different densities, disk aspect ratios, and disk hole sizes into water and at the pinch-off moment. There are four subplots where each includes three photos representing different views of frontal, 45° oblique, and side views of the same disk. Twelve distinct experiments with four different disk features were chosen as a sample to depict the difference between the three main views that present the difference between the water entry phenomenon, especially with the splash evolution. Figure 6a shows the splash formation by a disk with a density ratio, aspect ratio, and hole size ratio of $\rho_d/\rho_w = 1.14$, $D/h = 1.5$, and $d_h/D = 0.33$ (Test No: 7). For different perspective views of frontal, oblique, and side from left to right, the key parameters of pinch-off depth, h_p, splash diameter at the pinch-off moment, d_s, and splash height, h_s, were obtained by image analysis.

In Figure 5.6b, the disk density ratio, disk aspect ratio, and disk hole size ratio are $\rho_d/\rho_w = 2.50$, $D/h = 1.5$, and $d_h/D = 0$ (Test No: 3). A comparison between Figure 5.6a and 5.6b indicates that increasing the density ratio from $\rho_d/\rho_w = 1.14$ to 2.50 increased the pinch-off depth and splash height. Figure 5.6c shows the images of solid disk ($d_h/D = 0$) entry with $\rho_d/\rho_w = 2.50$, and $D/h = 3.0$ (Test No: 15). The disk aspect ratio has a considerable impact on splash and pinch-

off evolution properties, where for the disk with the aspect ratio of D/h = 3.0, the splash diameter and height beside the related pinch-off features declined dramatically. Figure 6d shows the images of pinch-off and splash curtain for an annular disk with ρ_d/ρ_w = 1.14, D/h = 3.0, and d_h/D = 0.53 (Test No: 22). A comparison between Figures 5.6d and 5.6c indicates that reducing the density and existence of a hole introduces air into the fluid and imposes extra resistance to the downward movement. Therefore, pinch-off depth, splash height, and splash diameter are expected to reduce significantly. For D/h = 3.0, the middle splash height is higher than that of the side view. This contrasts with the same observation with a smaller aspect ratio of D/h = 1.5.

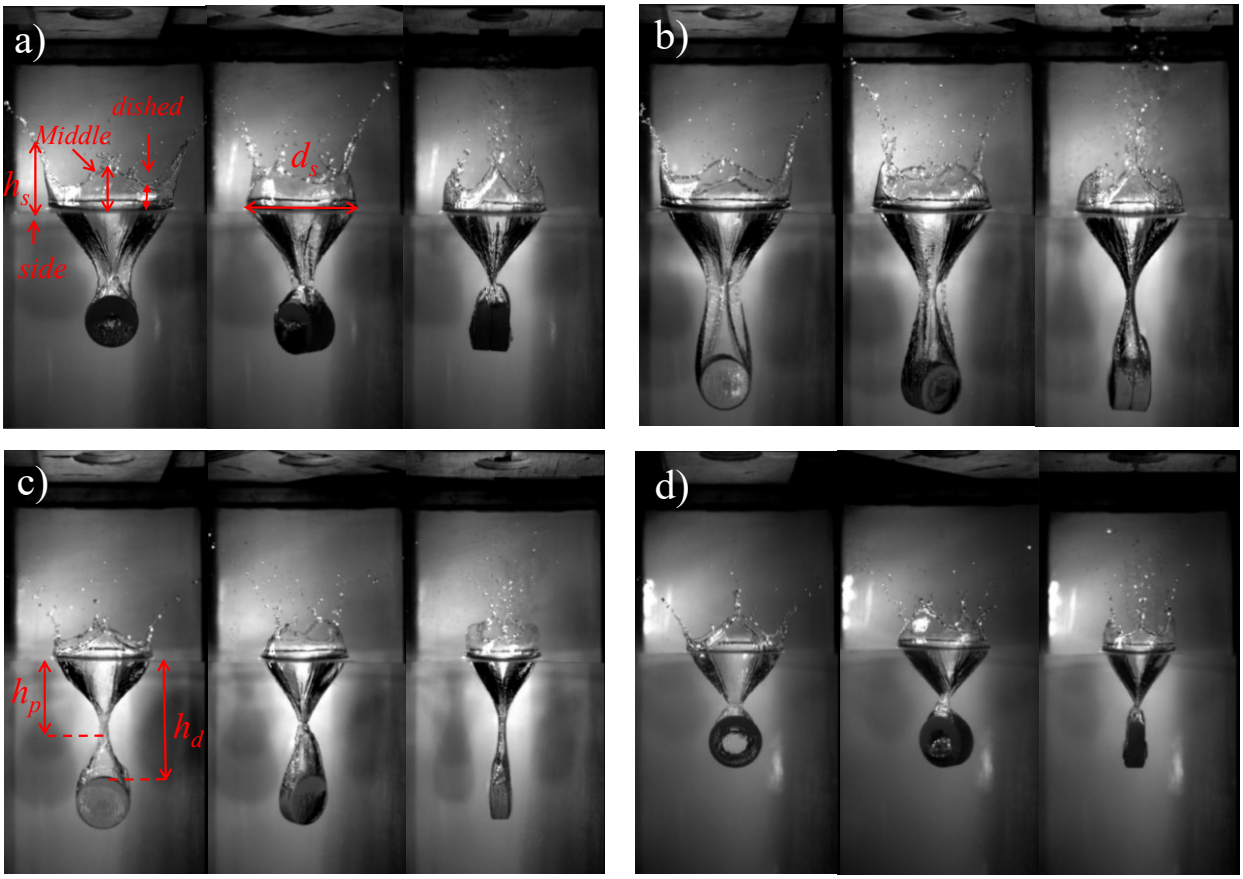

Figure 5.6: Images of water entry of disks with different densities, aspect ratio, and opening diameters at the pinch-off time: a) ρ_d/ρ_w = 1.14, D/h = 1.5, and d_h/D = 0.33, b) ρ_d/ρ_w = 2.50, D/h = 1.5, and d_h/D = 0, c) ρ_d/ρ_w = 2.50, D/h = 3.0, and d_h/D = 0.00, d) ρ_d/ρ_w = 1.14, D/h = 3.0, and d_h/D = 0.53. The left image in each subplot is the frontal, the middle image is the 45° oblique, and right image is the side views, respectively.

To study the effects of release orientation and the corresponding surface area of the solid object at the collision, the splash formation and cavity formation by a solid disk in face-on and edge-on orientations were compared while all other parameters such as disk density, opening size, and aspect ratio were kept constant. The time series images of the edge-on impact orientation were taken from the present study, and the results were compared with the experimental results of Ebrahimi and Azimi (2024, 2025a, 2025b) for face-on impact orientation. Figure 5.7 shows the time history images of the free-falling solid disk collision and immersion from the impact up to 150 milliseconds after the impact. The disks had a density ratio of $\rho_d/\rho_w = 1.14$ and an aspect ratio of $D/h = 1.5$, in both face-on and edge-on release orientations. The time interval between the consecutive images was $\Delta t = 10$ milliseconds and the collision surface varies in edge-on impact orientation (Figure 5.7a) (Test No: 1) and face-on impact orientation (Figure 5.7b). As can be seen in the edge-on release orientation, the pinch-off occurred at around $t_p = 130$ milliseconds, while in face-on release orientation, the pinch-off was extended to the approximate pinch-off time of $t_p = 145$ milliseconds.

The fundamental appearance alteration can be seen in the splash evolution where the formed splash for the face-on impact orientation establishes the splash, dome, and splash curtain sealed after presenting the inward movement which is all symmetrical in the splash evolution progress. On the contrary, the splash evolved asymmetrically where no inward motion was seen during the evolution of the splash. The splash evolved in an intense outward motion where no splash sealing occurred.

Figure 5.7: A comparison between the edge-on and face-on entry of solid disk impacting in stagnant water. Both disks have a density ratio of $\rho_d/\rho_w = 1.14$ and an aspect ratio of $D/h = 1.5$. The

time interval between consecutive images is Δt = 0.01 s: a) edge-on impact orientation, b) face-one impact orientation.

5.3.2 Pinch-off time

Figure 5.8 shows the effects of controlling parameters such as relative hole diameter, d_h/D, disk density ratio, ρ_d/ρ_w, and disk aspect ratio, D/h, on variations of normalized pinch-off time. The pinch-off time, t_p, was normalized with a characteristic time scale, $T = (D/g)^{0.5}$ where g is the gravitational acceleration (i.e., g = 9.81 m/s^2) and D is the disk diameter. Figure 8a shows the variation of dimensionless pinch-off time, t_p/T, with the disk hole size ratio and disk density ratio. The presented results are limited to the disks with the aspect ratio of D/h = 1.5. Based on the results presented in Figure 8a, an adverse correlation was found between the disk hole size and the pinch-off time. Such a reduction of normalized pinch-off time with hole size ratio is more considerable when the density ratio is smaller. To address the accuracy of the obtained pinch-off time for the conducted experiments, the overbars are plotted as a sample in Figures 8a and 8b for the experiments with the disk density ratio of ρ_d/ρ_w = 2.50 and disk hole size ratio of d_h/D = 0.53, respectively.

Overall, the dimensionless pinch-off time, t_p/T, varies between t_p/T =1.32 and 1.48. For the disk with the density ratio of ρ_d/ρ_w = 1.14, the pinch-off time declined from t_p/T =1.42 to 1.32 while the disk opening ratio increased from zero to d_h/D = 0.53. Such 7% reduction in the pinch-off time represents the effects of the disk opening ratio in relatively lighter disks. However, shortening the pinch-off time for the disk with a higher density is not as sharp as the tests with the density ratio of ρ_d/ρ_w = 1.14, where the normalized pinch-off dropped from t_p/T = 1.44 to 1.41 for the disk with the density ratio of ρ_d/ρ_w = 1.48 and t_p/T = 1.47 to 1.45 for the disk with the density ratio of ρ_d/ρ_w = 2.50. As can be seen, increasing the disk opening ratio to d_h/D = 0.53, slightly reduced the normalized pinch-off time for disks with the density ratios of ρ_d/ρ_w = 1.48 and ρ_d/ρ_w = 2.50 by 2.1% and 1.3%, respectively.

Figure 5.8b depicts the variations of normalized pinch-off time, t_p/T, alongside the disk density ratio, ρ_d/ρ_w, and with respect to the disk opening ratio, d_h/D, for the disks with the aspect ratio of D/h = 1.5. The overall trend shows that increasing the disk density ratio, ρ_d/ρ_w, results in a rise in the pinch-off time, t_p/T. Such variations are due to a higher air entrainment by the annular

disk into the water, which extends the pinch-off time for the annular disks with higher relative density. Moreover, the increments on the disk opening led to a reduction in the pinch-off time. At higher disk opening ratios, the delay in pinch-off time becomes more pronounced compared to that observed for solid disks. For disks with an opening ratio of $d_h/D = 0.53$, increasing the disk density ratio from $\rho_d/\rho_w = 1.14$ to 2.50 leads the pinch-off time to increase by approximately 9%. The intensity of such increment on the pinch-off time varies with the disk hole size ratio, where any rise in the inner diameter of the hole leads to further reduction of the normalized pinch-off time. For instance, the increments over the pinch-off time for the solid disk with a rise in the disk density ratio of $\rho_d/\rho_w = 1.14$ to 2.50 are around 3.5%, which is approximately half of the increase in the pinch-off time for the disk with a hole size ratio of $d_h/D = 0.53$.

Figure 5.8c illustrates the effects of all controlling parameters on variations of the pinch-off time in both face-on and edge-on orientations. The experimental results on the entry of face-on solid and annular disks were also added from the studies by Ebrahimi and Azimi, (2024, 2025a). All data belong to the current study are sorted out based on the controlling parameters of disk opening ratio, d_h/D, disk density ratio, ρ_d/ρ_w, and disk aspect ratio, D/h. Ebrahimi and Azimi, (2024) conducted their experiments with the solid disk owning the density ratios of $\rho_d/\rho_w = 1.14$, 1.48, and 2.50 while the disks are categorized into two groups with the disk aspect ratios of $D/h =$ 1.5 and 3.0. On the other hand, Ebrahimi and Azimi, (2025a) applied the annular disks with the same disk density ratios but the constant disk aspect ratio of $D/h = 1.5$. The disk hole size varied between $d_h/D = 0.20$ and 0.53. The horizontal axis in Figure 8c is the combined products of the disk density ratio and the area ratio between the disk's flat side and the solid disk, which is represented as $(\rho_d/\rho_w)(A_d/A_{solid\ disk})$, where A_d depicts the area of the flat side of the disk (i.e., face-on) as $A_d = \pi (D^2 - d_h^2)/4$ and $A_{solid\ disk}$ is the area of the side of the solid disk, $A_{solid\ disk} = \pi D^2/4$.

The result of the current study is categorized into six groups considering the disk density ratio, ρ_d/ρ_w, and disk aspect ratio, D/h. Increasing the combined disk density ratio and side surface area of the disk increased the pinch-off time which is also valid for both the studies conducted by Ebrahimi and Azimi, (2024, 2025a). The outcomes imply that the disks with a higher aspect ratio of $D/h = 3.0$ have a shorter pinch-off time where the results considering the disk with such an aspect ratio vary from $t_p/T = 1.10$ to 1.25. On the contrary, for disks with an aspect ratio of $D/h =$ 1.5, the normalized pinch-off time varies from $t_p/T = 1.33$ to 1.48, which shows a 20% increase

due to the effect of aspect ratio. In addition, increments in the disk density ratio, ρ_d/ρ_w, increased the pinch-off time. By comparing the results of the current study with the results obtained by Ebrahimi and Azimi, (2024, 2025a) on face-on release orientation, it can be concluded that the density ratio in face-on orientation also leads to a higher pinch-off time (i.e., t_p/T = 1.40 to 1.75) which is to the results from the edge-on release orientation. The mean relative pinch-off time in the studies by Ebrahimi and Azimi, (2024, 2025a) was around t_p/T = 1.575 while in the present study, they were equal to t_p/T = 1.175 and t_p/T = 1.405 for disks with aspect ratios of D/h = 3.0 and D/h = 1.5, respectively. As a result, the normalized pinch-off time in face-on release orientation increased by 34% and 12% to that of the edge-on orientation impact for D/h = 3.0 and D/h = 1.5, respectively. The mentioned behavior is sourced from the fact that the disks with a lower aspect ratio and higher density entrap more air into the ambient fluid and cause a larger cavity which directly affects the pinch-off time.

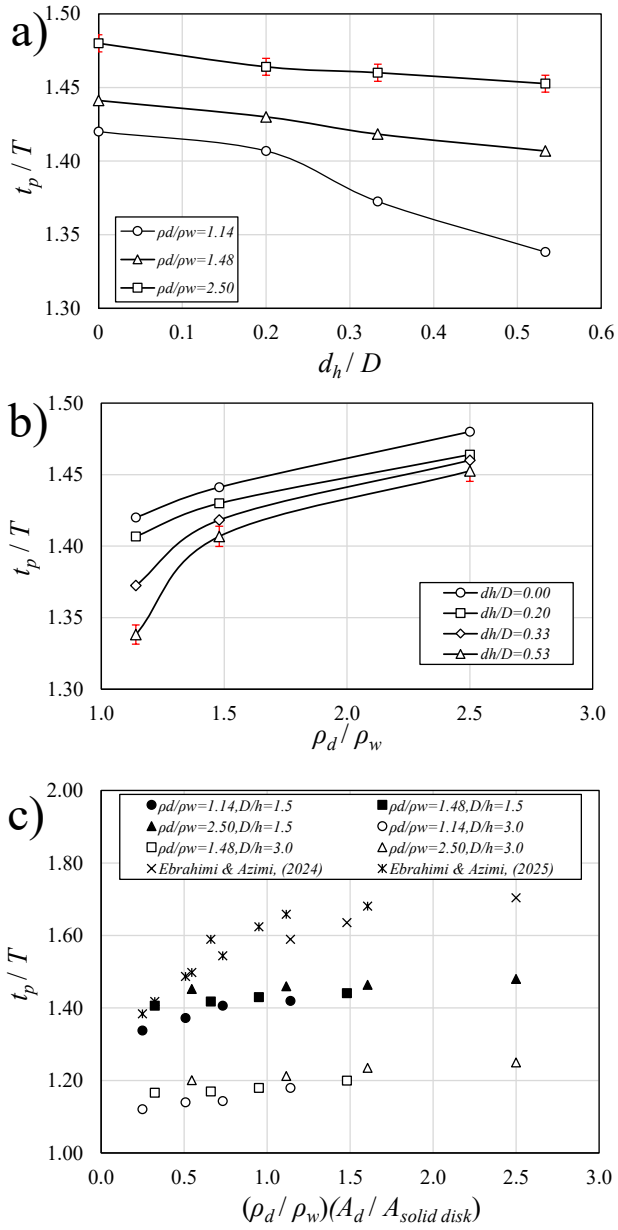

Figure 5.8: Effects of controlling parameters of on variation of normalized pinch-off time entering into ambient water: a) effect of disk hole size ratio, d_h/D, with respect to the disk density ratio, ρ_d/ρ_w, b) effect of disk density ratio, ρ_d/ρ_w, with respect to the disk hole size ratio, d_h/D, c) effect of combination of disk density ratio and disk area ratio, $(\rho_d/\rho_w)(A_d/A_{solid\ disk})$, considering the disk hole size ratio, d_h/D.

5.3.3 Pinch-off depth

Effects of controlling parameters on variations of pinch-off depth were studied and the results were plotted in Figure 5.9. Figure 5.9 consists of four subplots that in each subplot shows the effects of two parameters while the other parameters were kept constant. The pinch-off depth was normalized by the disk diameter, h_p/D. Figures 5.8a and 5.8b show the relationship between the normalized pinch-off depth and disk opening ratio across different disk density ratios while the disk aspect ratios are D/h = 1.5 and 3.0, respectively. The uncertainty variations of the measured pinch-off depths are included in Figure 5.9a. A comparison between the two subplots provides some information on the effects of aspect ratio on variations of normalized pinch-off depth. The overall trend based on the disk opening ratio shows that the pinch-off depth decreases while the disk opening ratio increases for the disks with both aspect ratios of D/h = 1.5 and 3.0. In addition, the higher disk density caused a higher pinch-off depth.

The normalized pinch-off depth, h_p/D varies from 1.1 to 1.7 in tests with the disk aspect ratio of D/h = 1.5 and it varies from 1.0 to 1.45 in tests with the aspect ratio of D/h = 3.0. As can be seen, for the disks with the aspect ratio of D/h = 1.5, the pinch-off depth reduced by approximately 14%, 9.3%, and 4.2% for density ratios of ρ_d/ρ_w = 1.14, 1.48, and 2.50 while the disk opening ratio, d_h/D, increased from 0 (i.e., solid disk) to 0.53. For D/h = 3.0, the pinch-off depth decreased by approximately 23%, 17%, and 6.8% for density ratios of ρ_d/ρ_w = 1.14, 1.48, and 2.50 while the disk opening ratio, d_h/D, increases from 0 (i.e., solid disk) to 0.53. Such a common trend in both figures indicates the effect of hole size and density ratio on variations of pinch-off depth in solid and annular disks. Such behavior indicates that the disk aspect ratio has an inverse relationship with pinch-off depth which is contrary to the effect of disk density.

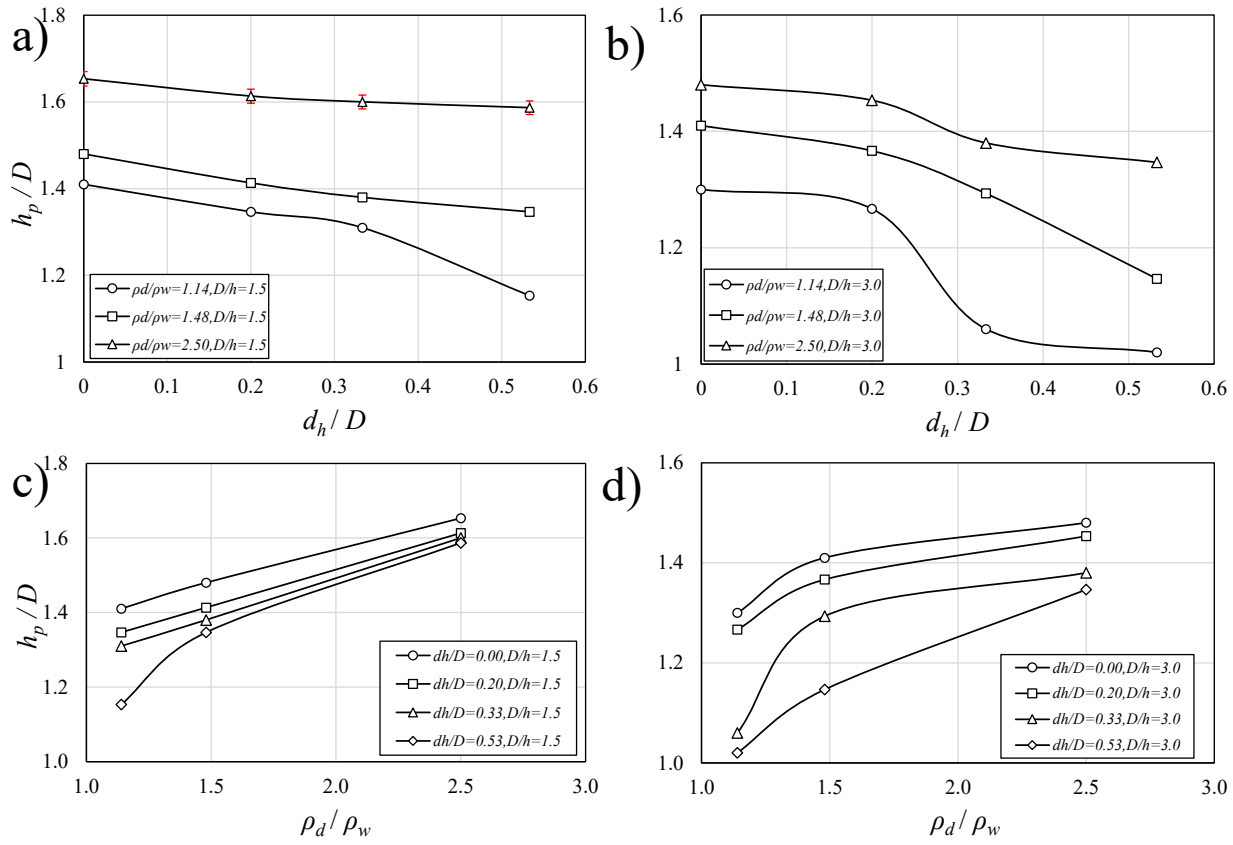

Figure 5.9: Effects of controlling parameters on variations of the normalized pinch-off depth for disk entry into a stagnant water: a) effect of normalized hole diameter, d_h/D, for D/h = 1.5, b) effect of normalized hole diameter, d_h/D, for D/h = 3, c) effect of density ratio, ρ_d/ρ_w, for D/h = 1.5, d) effect of density ratio, ρ_d/ρ_w, for D/h = 3.

Figure 5.10 shows the variations of normalized pinch-off depth, h_p/D, in edge-on released orientation versus the combined disk density and surface side area ratios $(\rho_d/\rho_w)(A_d/A_{solid\ disk})$. The variations of the presented combined normalized parameter with the corresponding pinch-off depth in face-on release orientation were also added from the studies by Ebrahimi and Azimi (2024, 2025a). As can be seen, increasing the disk aspect ratio shows a reduction in the corresponding pinch-off depth. Such observations are supported in both face-on release orientation from the previous studies and the edge-on release orientation from the present study. In all tests, increasing the combined parameters of $(\rho_d/\rho_w)(A_d/A_{solid\ disk})$ increased the normalized pinch-off depth almost linearly. Figure 10 shows that the pinch-off depths in solid disks with face-on orientation (Ebrahimi and Azimi, 2024) and with an aspect ratio of D/h = 3.0 have some overlaps with the outcomes of the current study with edge-on release orientation. However, the face-on release for solid disks

with the aspect ratio of D/h = 1.5 (Ebrahimi and Azimi, 2024) stands in the range of h_p/D between 1.75 and 2.51 while the results on the face-on release of annular disks with the aspect ratio of D/h = 1.5 (Ebrahimi and Azimi, 2025a) stand in the range of h_p/D between 1.60 and 2.50. This indicates that the disk impact in face-on orientation has higher pinch-off depths than those of the corresponding edge-on release orientation. Such differences in variations of pinch-off depth may be due to the fact that the face-on impact orientation drags more air into the fluid than that of the edge-on impact orientation, which leads to a larger cavity and deeper pinch-off depth.

The ratio of pinch-off depth, h_p, to the solid object depth at the pinch-off moment, h_d, is called the pinch-off depth ratio and it has been utilized as a key parameter to describe the solid entry of free-falling objects with different geometries in water and in non-Newtonian fluid mixtures (Duclaux et al., 2007; Mansoor et al., 2014; Ebrahimi and Azimi, 2024, 2025a). Figure 5.10 shows the correlation between normalized pinch-off depth with the disk depth at the pinch-off moment, h_d, normalized by the disk diameter, D. To conduct a comparison considering the geometry of the solid spherical object, the results obtained by Duclaux et al. (2007) and Mansoor et al. (2014) are added in Figure 5.11. The study by Duclaux et al. (2007) belongs to spheres with diameters ranging between D = 12 mm and 40 mm, and Froude numbers ranging from Fr = 10 to 330. The results presented by Mansoor et al. (2014) also belong to solid spheres with different diameters ranging from 15 mm to 25 mm and different impact velocities varied between 1.5 m/s and 8.5 m/s. Moreover, the applied sphere density, ρ_s, ranged between 980 and 1020 kg/m^3.

To enable conducting a comparison between identical solid objects in different configurations (solid versus annular disks), the results from the study by Ebrahimi and Azimi (2024, 2025a) were included as well. The results show the correlation between pinch-off depth and disk depth at the pinch-off for solid and annular disks with face-on release orientation. As it was mentioned in the experimental setup section, the results of the present study belong to the free-falling of solid and annular disks with edge-on release orientation. Although the impacting body is a disk in both face-on and edge-on release orientations, the edge-on collision produces dynamics resembling a hybrid between a hemisphere and a disk, due to the curved surface interacting with the fluid upon entry.

The pinch-off depth ratio, h_p/h_d, for spheres (from the studies by Duclaux et al. (2007) and Mansoor et al., 2014) varied in the range of h_p/h_d = 0.45 to 0.50 while such ratio for solid and

annular disks in face-on release orientation (i.e., from the studies by Ebrahimi and Azimi., 2024, 2025a) was higher and varied from h_p/h_d = 0.48 to 0.78. However, the pinch-off ratio for the edge-on release orientation varies from h_p/h_d = 0.58 to 0.90. The values of pinch-off ratio in edge-on release orientation are significantly higher than those of spheres and on average, they were 28% and 68% higher than predictions by Duclaux et al. (2007) and Mansoor et al. (2014), respectively. Such differences are due to the geometry of the solid object (i.e., cylindrical disk in this study versus the sphere in the studies by Duclaux et al. (2007) and Mansoor et al. (2014). Accordingly, the disk geometry introduces a higher pinch-off ratio, h_p/h_d, than that of spherical geometry. On the other hand, the pinch-off ratios, h_p/h_d, were between 7% and 20% larger in edge-on release orientation than those of corresponding tests with face-on release orientation. It should be noted that the central hole aligns perpendicularly to the direction of motion, exhibiting additional resistance during descent. Such a configuration also enhanced the cohesion between the disk and the formed cavity, sponsoring the observed variations.

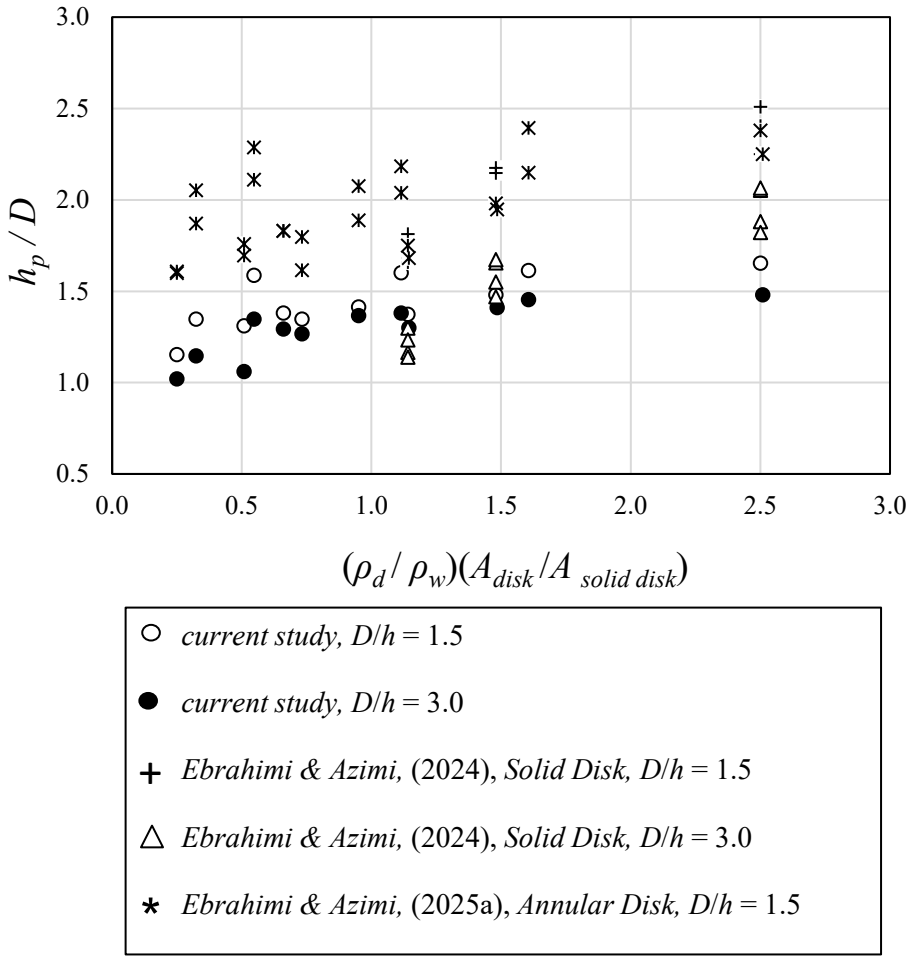

Figure 5.10: Effects of disk orientation (i.e., edge-on versus face-on) on variations of normalized pinch-off depth with the disk density and side area ratio.

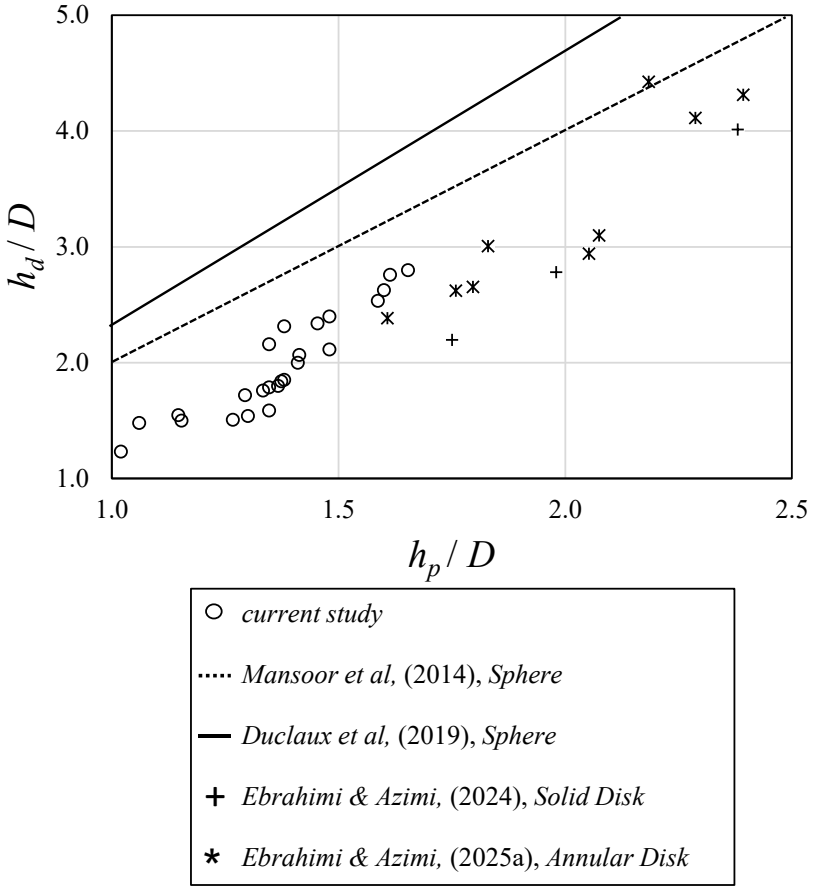

Figure 5.11: Effects of disk orientation (i.e., edge-on versus face-on) on variations of normalized pinch-off depth with disk depth at the pinch-off moment.

5.3.4 Sinking velocity

The velocity of a sinking cylindrical disk in the fluid is a considerable criterion that can elucidate the behavior of solid objects and their interactions with the ambient fluid. The velocity of solid objects after the pinch-off was measured until the object reached the bottom of the tank and the results were averaged to calculate the sinking velocity. The calculated sinking velocity was normalized with a characteristic disk velocity, which is presented as $v_e = (\rho_d A_d / 2mg)^{1/2}$. The effects of controlling parameters such as disk density ratio, ρ_d/ρ_w, disk aspect ratio, D/h, and disk opening ratio, d_h/D, on variations of sinking velocity were studied and the results are shown in Figure 5.12. Figures 5.12a and 5.12b show the variations of normalized sinking velocity versus disk density

ratio and disk opening ratio for disk aspect ratios of D/h = 1.5 and 3, respectively. As can be seen, normalized sinking velocity increased with increasing disk density ratio and an adverse correlation was found between disk opening and normalized sinking velocity. The effect of disk aspect ratio can be analyzed by comparing the results presented in Figures 5.11a and 5.11b. A comparison between Figures 11a and 11b indicated that the normalized sinking velocity decreases with increasing disk aspect ratio. For both aspect ratios of D/h = 1.5, and 3.0, increasing disk density ratio from ρ_d/ρ_w = 1.14 to 2.50, increased the dimensionless sinking velocity, v_s/v_e, by almost 3 times. The maximum normalized sinking velocity for D/h = 3.0 is v_s/v_e = 4.0, whereas the same value for D/h = 1.5 is v_s/v_e = 4.7.

Figures 5.12c and 5.12d show the effects of disk hole diameter and density ratio on variations of normalized sinking velocity for D/h = 1.5 and 3.0, respectively. The variations of normalized sinking velocity with disk hole size were complex. Overall, all data show a peak value for d_h/D = 0.2, indicating that normalized sinking velocity increases in annular disks with relatively small opening but further increasing the hole size reduces the sinking velocity due to formation of vortices at the wake of the cylinder. Initially, the sinking velocity rises while the disk hole size increases from d_h/D = 0 to 0.20, suggesting that the introduction of a central opening reduces hydrodynamic resistance during descent. As the disk hole size ratio increases more than d_h/D = 0.20, the sinking velocity declines with disk hole diameter almost linearly. As can be seen, for disks with the highest hole size ratio of d_h/D = 0.53, normalized sinking velocities were equal to or less than that of the sinking velocity of the corresponding solid disks (i.e., $(v_s/v_e)_{dh/D\,=\,0.53} \leq (v_s/v_e)_{Solid\ disk}$). It can be concluded that the disk aspect ratio does not have a noticeable impact on the sinking velocity in disks with edge-on release orientation.

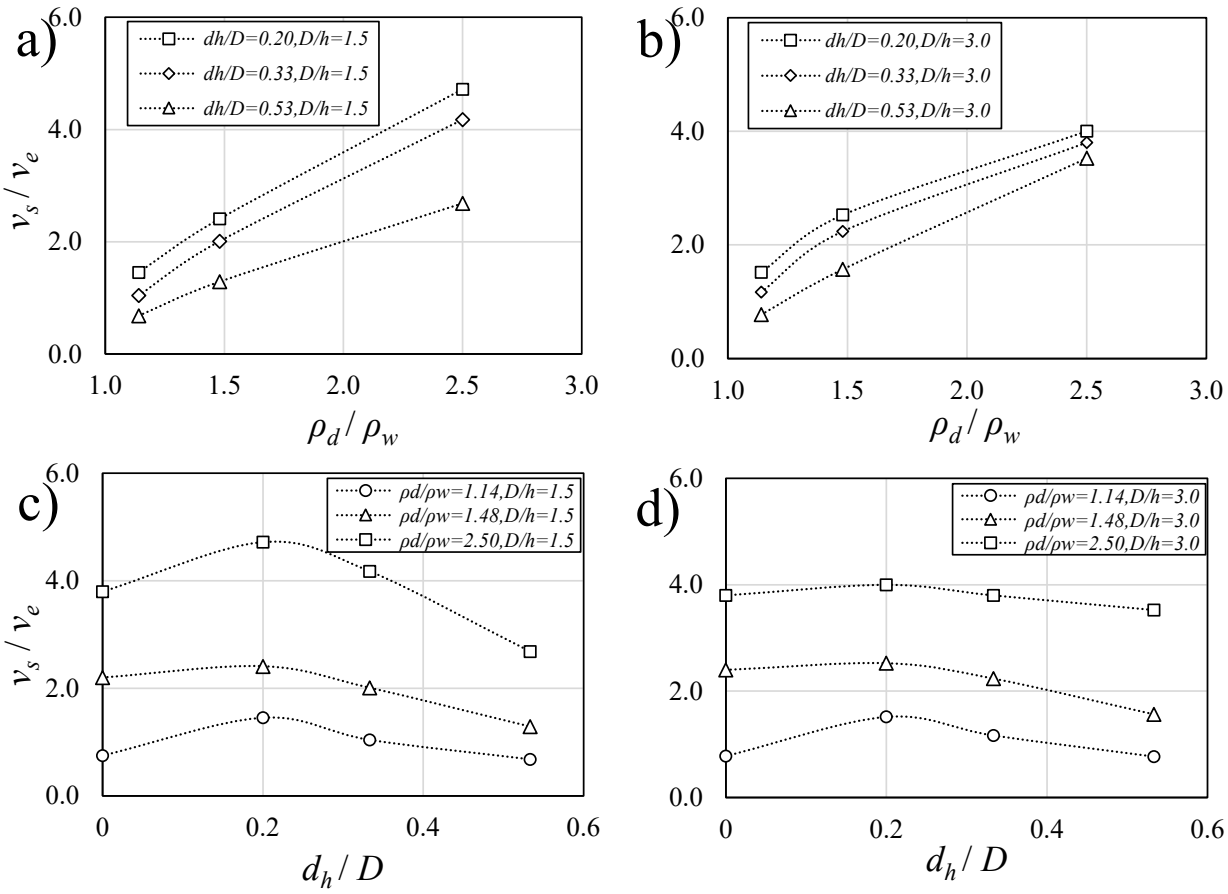

Figure 5.12: Effects of controlling parameters on variations of dimensionless sinking velocity: a) effect of disk density ratio for D/h = 1.5, b) effect of disk density ratio for D/h = 3.0, c) effect of disk opening size for D/h = 1.5, and d) effect of disk opening size for D/h = 3.

Figure 5.13 shows the effect of release orientation and density ratio on variations of normalized sinking velocity. The current study shows the effects of disk area and density on variations of sinking velocity of edge-on release orientation and the results reported by Ebrahimi and Azimi (2024, 2025a) belong to face-on release orientation of solid and annular disks. The horizontal axis in Figure 5.13 shows a product of disk density ratio and disk hole size ratio besides the disk area in the form of $(\rho_d /\rho_w)(A_d /A_{solid\ disk})$. The normalized sinking velocity in edge-on release orientation varied between v_s/v_e = 0.5 to 5.0, which were much lower than the normalized sinking velocity in face-on release orientation (i.e., from Ebrahimi and Azimi, 2024, 2025a) ranged from v_s/v_e = 5 to 20. The differences in normalized sinking velocities were mainly due to release orientation. In face-on release orientation of solid disks (i.e., Ebrahimi and Azimi, 2024), the disk

aspect ratio has a notable impact on sinking velocity. For D/h = 1.5, the sinking occurred at nearly twice the velocity of those with an aspect ratio of D/h = 3. This indicates the sensitivity of sinking velocity to the mass of the solid disk where the disk with higher mass descends faster. However, less sensitivity was observed in tests with edge-on release orientation despite validation of the reduction in the sinking velocity as the disk aspect ratio increases.

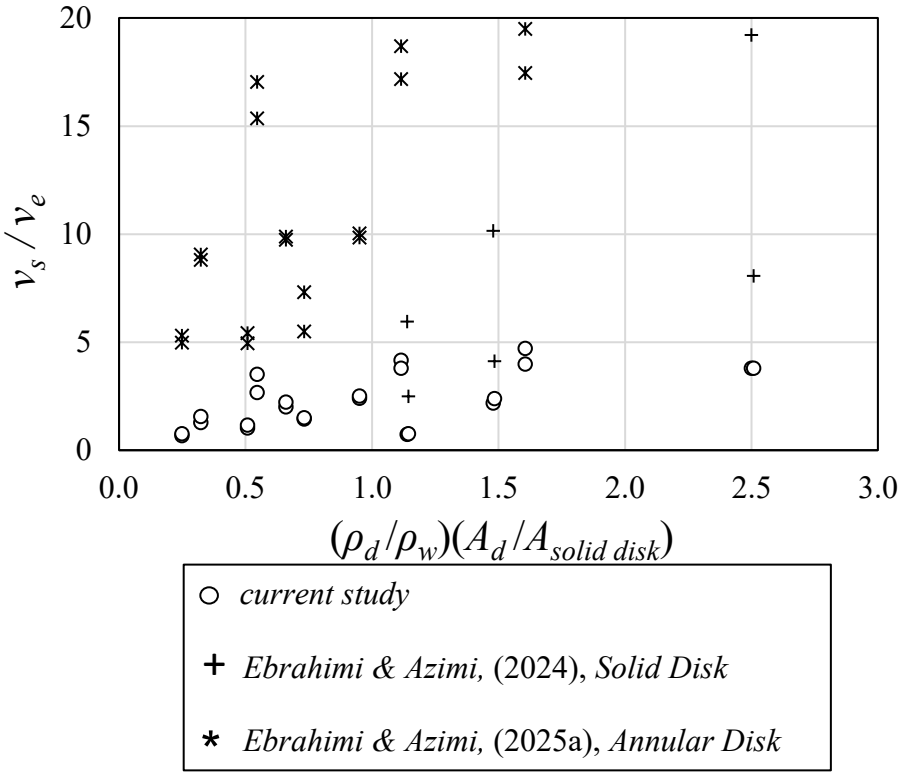

Figure 5.13: Effects of disk orientation (i.e., edge-on versus face-on) on variation of normalized disk sinking velocity versus the combined disk density and side area ratio.

5.3.5 Splash evolution

The splash evolution by insertion of edge-on solid and annular disks was studied by measuring splash diameter, d_s, and splash height, h_s. Unlike most previous studies from the literature where the applied solid object formed a symmetrical splash, the splash by edge-on release orientation was not symmetrical. Therefore, the splash gestures in front and side views were investigated. The splash dimensions were affected by the disk impact area and the splash diameter differed in different perspectives.

The effects of disk opening and density ratio on variations of normalized splash diameter, d_s/D, for $D/h = 1.5$ and $D/h = 3$ are shown in Figures 5.14a and 5.14b, respectively. The horizontal axis is the combination of release orientation and density ratio in the form of $(\rho_d/\rho_w)(A_d/A_{solid\ disk})$. Each shows the frontal and side views to indicate the differences between the values regarding each perspective. The splash diameter in the frontal view was found to be much larger than that of the side view (see Figure 5.1a). Additionally, the data in each figure are grouped according to disk opening ratio, revealing that splash diameter increases with increasing hole size. Figure 5.14a shows data for the disk aspect ratio of $D/h = 1.5$. The splash diameter varies between $d_s/D = 2.4$ and 2.6 while the side view shows the splash diameter that varies between $d_s/D = 2.0$ and 2.2. The splash diameter diminishes in a relatively higher aspect ratio for a disk with $D/h = 3$. As can be seen in Figure 5.14b, the normalized splash diameters for the frontal and side views vary from $d_s/D = 1.8$ to 2 and $d_s/D = 1.4$ to 1.6, respectively. On average, the splash diameter for the frontal view is higher than that of the side view and such increments for $D/h = 1.5$ and 3 were 16% and 21%, respectively. In addition, by increasing the disk aspect ratio from $D/h = 1.5$ to 3, the frontal splash diameter diminishes by around 24% and such a reduction is equal to 28% while observing through the side perspective.

The splash diameter variation considering the disk opening ratio shows that increasing the disk opening size leads the splash diameter to increase as well. For disks with the aspect ratio of $D/h = 1.5$, increasing the disk hole size ratio from $d_h/D = 0$ to 0.53 increased the splash diameter in the front and side views by approximately 3% and 1.5%, respectively. It should be noted that the variation of splash diameter is more considerable for $D/h = 3$. For the disks with the aspect ratio of $D/h = 3$, by imposing the central hole in the solid disks ($d_h/D = 0$) and enlarging the hole dimension to $d_h/D = 0.53$, the frontal and side splash diameters increased by approximately 5% and 4.5%, respectively.

The effects of impact orientation on the formation of the splash curtain are shown in Figure 5.14c. In this figure, data regarding the edge-on release orientation configuration (i.e., the current study), which are categorized into the two perspectives of frontal and side views, and data for the face-on release orientation from the studies by Ebrahimi and Azimi, (2024, 2025a) are compared. Figure 5.13c vividly shows that an increase in the disk density and disk hole size increases the splash diameter. In addition, it can be inferred from the results that the face-on impact orientation

of the disk with the fluid surface leads to a higher splash diameter in comparison to the edge-on release orientation. The maximum normalized splash diameter by a solid disk in its face-on orientation is equal to $d_s/D = 3.85$ for the highest disk density and hole size. Whereas the maximum normalized splash diameter in edge-on release orientation is around $d_s/D = 2.60$, which is approximately 69% of the maximum normalized splash diameter in face-on impact orientation. While the collision surface area of the disk with the water surface changes from face-on to edge-on release orientations, the disk's opening impact on the splash diameter reduced drastically. Therefore, it can be concluded that the splash diameter is highly dependent on the collision surface area of the solid object and the fluid surface.

The effects of release orientation and other controlling parameters on variations of splash height were assessed. The analysis was conducted through the frontal view where the middle splash and the two side splash sections were shorter than those formed on the sides. A similar formation can be seen at 180˚ in the current view. The labeling of the side and middle sections of the splash, excluding the concave regions, depends on the viewer's perspective. The splash height variations in each section follow a consistent proportional relationship where an increase in one region is typically accompanied by subsequent growth in the others. Therefore, inspection of one section of the splash height reflects the overall variation of the other sections.

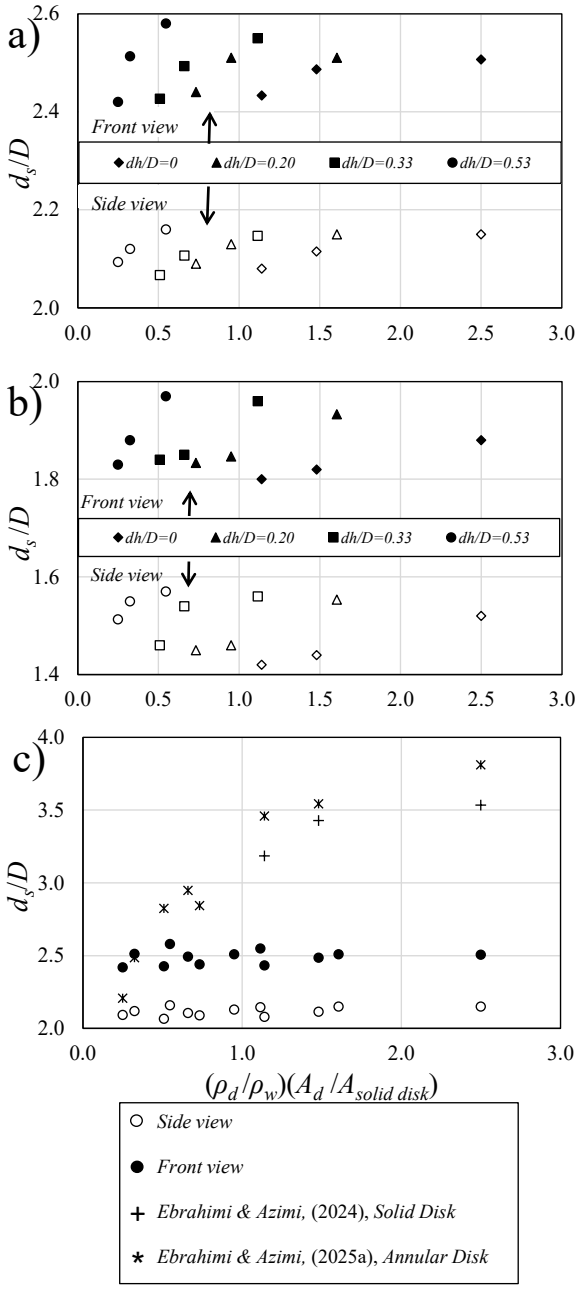

Figure 5.14: Effects of disk opening and density ratio on variations of dimensionless splash diameter, d_s/D: a) edge-on, $D/h = 1.5$, b) edge-on $D/h = 3$, c) face-on from the experimental studies of Ebrahimi & Azimi, (2024, 2025a).

Figure 5.15 shows the variations of normalized splash height, h_s/D, with the combined understudy elements of disk hole size and disk density ratio in the form of $(\rho_d/\rho_w)/(d_h/D)$. Figure 14a shows the splash height for $D/h = 1.5$. Accordingly, the side splash is higher than that of the

middle splash by around 1.5 times. As can be seen, increasing the hole diameter increased the splash height as well. The side splash height varied from h_s/D = 1.0 to 1.8 while the variations of the normalized splash height in the middle section varied from h_s/D = 0.9 to 1.1.

Figure 5.15b shows the correlation between normalized splash height and the combined function of disk density and hole diameter for D/h = 1.5 (i.e., solid circles) and D/h = 3.0 (i.e., open circles). In agreement with the finding presented in Figure 15a, increasing the magnitude of $(\rho_d/\rho_w)/(d_h/D)$ slightly reduced the normalized splash height. There is a considerable difference between the formed splashes by the disks with the aspect ratios of D/h = 1.5 and 3, as the splash heights for D/h = 1.5 were higher than those of D/h = 3. Such behavior may be correlated to the surface area of the disks colliding with the water surface, where disks with a smaller aspect ratio, D/h = 1.5, have higher interface area and impart more energy to the water. Such energy transfer leads to the formation of a higher splash. As can be seen, the splash height on the side sections for D/h = 1.5 varied from h_s/D = 0.9 to 1.8, while for D/h = 3 it was between h_s/D = 0.2 and 0.8. The best linear fit through each group of data for the prediction of splash height based on the given disk aspect ratio, disk density, and hole diameter is expressed as:

$$\frac{h_s}{D} = -0.508\left(\frac{d_h}{D}/\frac{\rho_d}{\rho_w}\right) + 1.304 \qquad \text{For} \qquad D/h = 1.5 \tag{5.1a}$$

$$\frac{h_s}{D} = -1.3157\left(\frac{d_h}{D}/\frac{\rho_d}{\rho_w}\right) + 0.826 \qquad \text{For} \qquad D/h = 3.0 \tag{5.1b}$$

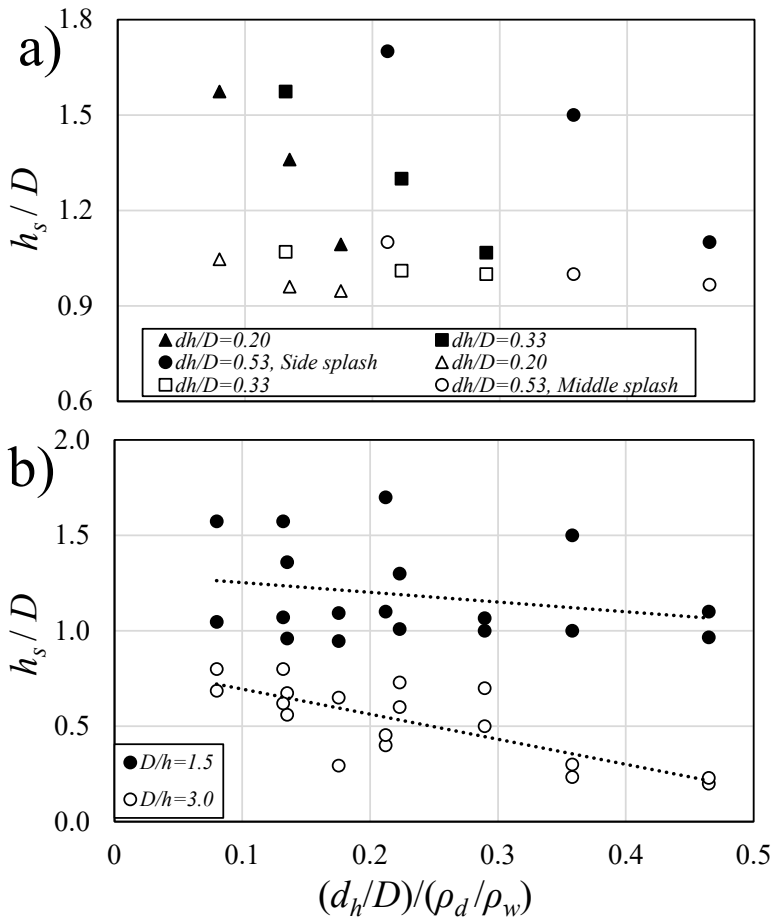

Figure 5.15: Effects of disk opening and density ratio on variations of dimensionless splash height, h_s/D, a) effect of disk opening for the disks with the aspect ratio of D/h = 1.5, and b) effect of disk aspect ratio, D/h.

5.3.6 Energy losses

The properties of the formed splash such as splash height and droplets are undoubtedly dependent on the magnitude of the energy transfer from the disk's kinetic energy to the ambient water. The energy transfer between the disk and water is highly contingent on the solid object features and the rheological characteristics of the ambient fluid. Therefore, it is expected to obtain different energy losses by altering the disk density and its geometry. The geometry of the disk affects the collision surface area, and the central hole increases the contact surface between the solid object and the ambient fluid. To study the effect of disk geometry and release condition on energy transfer, the energy losses due to the collision of the disks with the water surface were calculated for disks with edge-on release orientation. The data were compared with the energy losses of the same disks with face-on release orientation from the studies by Ebrahimi and Azimi,

(2024, 2025b). The energy transmissions between the disk and the surrounding water commence with the collision of the disk with the water surface, and it continue till the disk reaches the bottom of the tank. Table 5.2 illustrates the variations of disk density ratio, ρ_d/ρ_w, disk opening size ratio, d_h/D, disk aspect ratio, h/D, at three identified stages of collision/immersion, pinch-off, sinking, and the remaining energy left at the time close to the bottom of the tank, which are represented by E_c/E_t (%), E_p/E_t (%), E_s/E_t (%), and $\Delta E_t/E_t$ (%), respectively.

Table 5.2: Table of experiments presenting the variations, disk density ratio, ρ_d/ρ_w, disk opening size ratio, d_h/D, disk aspect ratio, D/h, collision/immersion, pinch-off, and sinking energy loss ratios, E_c/E_t (%), E_p/E_t (%), E_s/E_t (%), $\Delta E_t/E_t$ (%)

Test No.	*D/h*	ρ_d/ρ_w	d_h/D	E_c/E_t (%)	E_p/E_t (%)	E_s/E_t (%)	$\Delta Et/Et$ (%)
1	1.5	1.14	0	34.22	18.66	18.04	70.93
2		1.48		33.23	9.89	16.33	59.45
3		2.50		26.82	3.43	8.73	38.98
4		1.14	0.20	35.14	13.70	19.14	67.97
5		1.48		34.22	8.69	17.77	60.69
6		2.50		31.00	2.47	13.18	46.64
7		1.14	0.33	35.98	15.01	20.23	71.23
8		1.48		35.14	10.27	18.91	64.32
9		2.50		31.00	2.00	13.27	45.02
10		1.14	0.53	36.77	14.99	22.09	73.84
11		1.48		33.23	16.62	17.23	67.09
12		2.50		29.73	11.44	12.09	53.26
13	3.0	1.14	0	35.14	17.51	19.46	72.11
14		1.48		33.23	8.44	16.80	58.48
15		2.50		31.00	3.13	14.09	48.21
16		1.14	0.20	34.22	13.25	18.77	66.24

17		1.48		32.16	8.00	16.03	56.18
18		2.50		31.00	0.71	14.27	45.97
19		1.14	0.33	35.14	13.47	21.09	69.70
20		1.48		33.23	0.67	17.60	51.50
21		2.50		29.73	0.77	13.50	44.00
22		1.14	0.53	35.98	14.48	22.21	72.67
23		1.48		33.23	13.30	18.60	65.13
24		2.50		28.34	3.80	12.34	44.48

To investigate the energy transfer, the three different stages with the most hydrodynamic signatures were identified as the collision, pinch-off, and sinking stages. Additionally, the total energy losses were calculated to provide a comparison between the impacts of the understudy parameters. Moreover, a comparison between the outcomes of the edge-on impact orientation (i. e., the current study) and the face-on impact orientation from the studies by Ebrahimi and Azimi, (2024, 2025b) was made. All the energy losses were converted to a dimensionless format and represented as a percentage of the total potential energy from the release moment to the bottom of the tank. The potential and kinetic energies through the disk movement were calculated to determine the energy losses at each stage. The disk impacts the water surface with a specific energy that can be evaluated either as a potential energy based on the release height, or as kinetic energy just before the impact as:

$$E_i = mgh_r = \frac{1}{2}mv_i^2 \tag{5.2}$$

where, m is the mass of the disk, g is the gravitational acceleration, h_r is the release height, and v_i is the impact velocity, which is calculated as $v_i = (2gh_r)^{1/2}$ by assuming negligible energy losses due to air friction above water surface. The collision of the disk with the water surface influences the primary energy considerably; therefore, the kinetic energy is computed after the complete immersion to determine the energy losses due to impact. The kinetic energy after the collision stage is represented as E_c and it is calculated as:

$$E_c = \frac{1}{2}mv_c^2 \tag{5.3}$$

$$\Delta E_c = mg(h_r - D) - E_c \tag{5.4}$$

where v_c is the velocity of the disk at the collision, where the entire disk is submerged in water. The energy losses due to collision can be calculated by subtracting the available potential energy from the available kinetic energy.

Most of impact energy was imparted to water after the collision stage, which caused splash and cavity formation. The energy dissipated during such initial interaction plays a significant role not only in reducing the disk's primary kinetic energy but also it substantially contributes to the overall energy losses throughout the entry process. Therefore, the imparted energy at the collision stage was calculated based on the available potential energy at the complete disk immersion. Notably, the collision of the disk with the water surface causes the disk to dissipate most of its energy to the ambient water as $\Delta E_c/(mg(h_r + D) > 50\%$. Such normalized energy losses based on the potential energy to the depth of the complete immersion varied between 50% and 70% depending on the disk geometry and release conditions. Overall, increasing the disk density ratio and the side surface area ratio of the disk reduced the energy losses at the collision stage.

To investigate the variations of energy losses in different stages of collision, pinch-off, and sinking as a fraction of the total energy, the energy losses for solid and annular disks with different densities and release orientations were calculated and the results are shown in Figure 16. The left column in Figure 16 shows the variations of energy losses in edge-on release orientation and the right column shows the energy losses of the corresponding disks in face-on release orientation, which were extracted from experimental studies by Ebrahimi and Azimi, (2024, 2025b). The effect of opening diameter on energy losses for d_h/D = 0, 0.20, 0.33, and 0.53 are shown in Figures 16a to 16d, respectively. The total energy is introduced as the summation of all the potential energies referenced from the release height to the bottom of the tank as:

$$E_T = mgh_T \tag{5.5}$$

Each bar plot in Figure 5.16 shows the energy losses in three stages of collision (in blue color), pinch-off (in green color), and sinking (in grey color) and the energy losses were normalized by the total energy in form of $(\Delta E_c)/E_T$, $(\Delta E_p)/E_T$, and $(\Delta E_s)/E_T$, respectively. Overall, increasing the disk density ratios, ρ_d/ρ_w, reduces the total energy losses. For the edge-on release orientation, most of the energy losses occurred in the collision stage, which is followed by the sinking and

pinch-off moment, respectively. However, for the face-on impact orientation, such a trend is only valid for the solid disk. For annular disks, most of the energy losses in the system correspond to the pinch-off moment.

Under edge-on release orientation, approximately 70% of the total energy is transferred to water for the solid disk with an aspect ratio of D/h = 1.5 and a density ratio of ρ_d/ρ_w = 1.14. In contrast, for the disk with a higher density ratio of ρ_d/ρ_w = 2.50, the energy losses were reduced to around 40%, which represents the inverse relationship between disk density and the proportion of energy dissipated to the surrounding fluid. As can be seen in Figure 16, more than 50% of the impact energy losses correspond to the collision stage, which is valid for the annular disks with different opening ratios. Remarkably, it was observed that while the solid disk collides with the fluid surface in its face-on orientation, more energy is imparted to the system than in the edge-on release orientation. However, such a trend reversed in annular disks, where the energy losses due to collision were higher in edge-on release orientation. Such behavior reflects the additional resistive force that was introduced by the presence of the central hole in the edge-on release orientation, which impedes the disk's downward motion. In contrast to edge-on release, the hole reduces the frontal area that was exposed to resistance in face-on release. Therefore, the initial resistive force reduces in annular face-on cases and allows for more efficient penetration of the object into water. For instance, the total energy losses in edge-on release of solid disks with the density ratio of ρ_d/ρ_w = 1.14 and ρ_d/ρ_w = 2.50 were almost 80% and 45%, respectively. The energy losses of the corresponding disks in face-on release orientation were approximately 70% and 40%, respectively.

The average energy losses in the pinch-off stage for both solid and annular disks in edge-on and face-on release orientations were approximately 11% and 28%, respectively. On the other hand, the average energy losses at the collision stage for disks in edge-on and face-on release orientations were 33% and 22%, respectively. The average energy losses at the sinking stage for disks with edge-on and face-on release orientations were 16% and 14%, respectively. Such noticeable differences in the effect of release orientation at the pinch-off stage may be due to the cohesion between water and solid objects at the pinch-off stage since a larger solid object area engages in the pinching process while the disk enters the water on its face-on impact orientation.

The engaged area of the disk with water in the pinch-off point for the face-on release orientation was almost 5 times larger than that of the edge-on impact orientation.

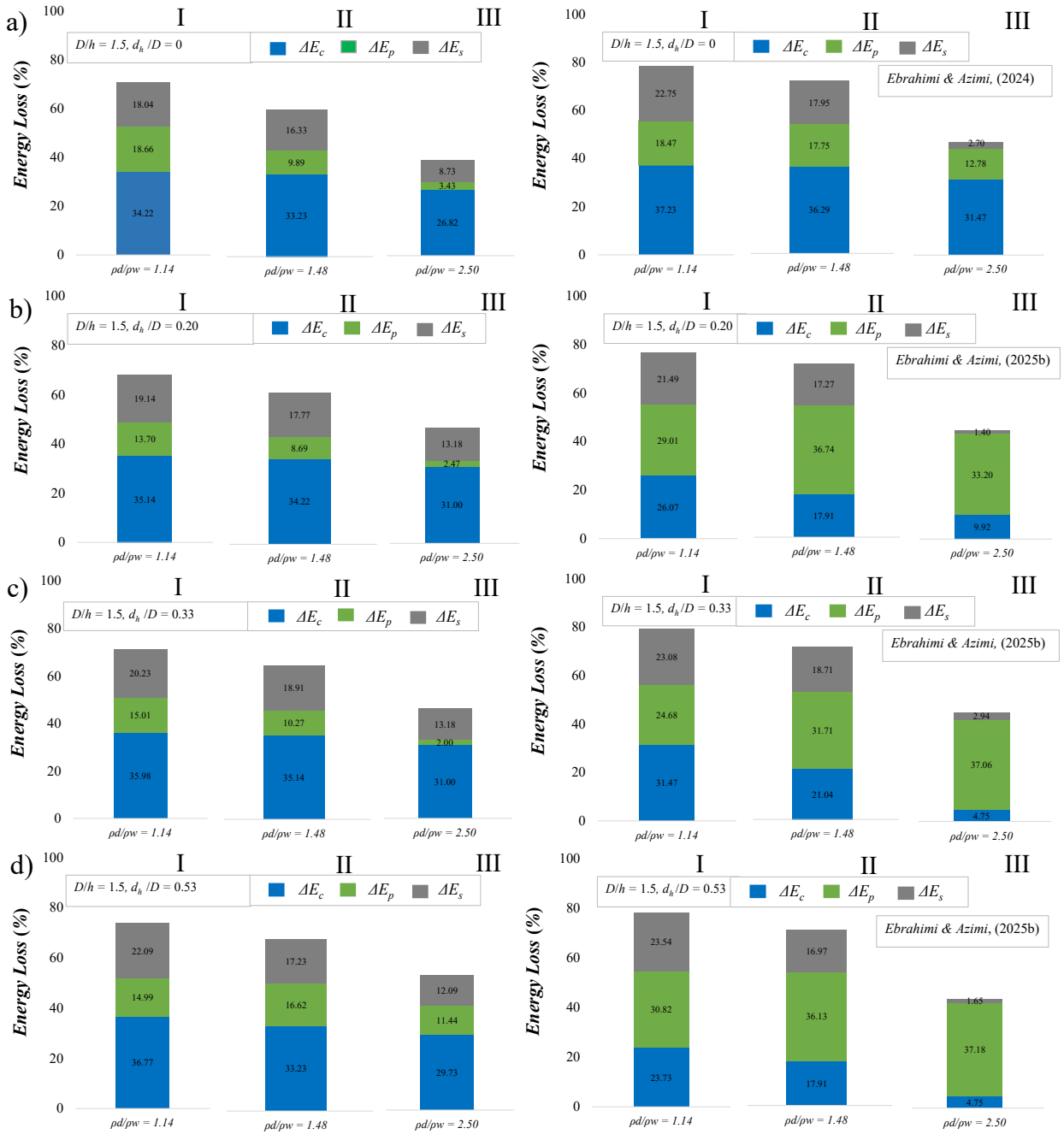

Figure 5.16: Effects impact orientation (edge-on in the left versus face-on in the right) and controlling parameters such as disk density ratio and disk aspect ratio on variations of energy losses in collision, pinch-off, and sinking stages. The disks aspect ratio is $D/h = 1.5$: a) $d_h/D = 0$, b) $d_h/D = 0.20$, c) $d_h/D = 0.33$, d) $d_h/D = 0.53$.

Figure 5.17 shows the effects of controlling parameters such as disk density ratio and disk aspect ratio on variations of total energy losses and energy losses due to collision, pinch-off, and sinking stages for disks with the edge-on impact orientation. The effect of disk density ratio and opening are combined in form of a non-dimensional parameter. As can be seen, an increase in the combined disk density ratio and opening leads the energy loss to diminish unanimously in different stages of collision, pinch-off, and sinking. However, lessening the total energy losses is more intense in comparison to individual stages. Empirical equations were best-fitted from data of energy losses at different stages of evolution. It was found that a logarithmic model is best describing the energy losses at different stages. The derived correlations regarding the total, collision, pinch-off and sinking energy losses are presented in equations 6a to 6b, respectively. Increasing the $(\rho_d/\rho_w)(A_d/A_{solid\ disk})$ from 0.5 to 2.5, leads the total energy loss decreasing by an average value of 20%.

$$\Delta E_T = -10.43 \ln((\rho_d/\rho_w)(A_d\ /A_{solid\ disk})) + 56.89 \quad (5.6a)$$

$$\Delta E_c = -2.06 \ln((\rho_d/\rho_w)(A_d\ /A_{solid\ disk})) + 32.43 \quad (5.6b)$$

$$\Delta E_p = -4.78 \ln((\rho_d/\rho_w)(A_d\ /A_{solid\ disk})) + 8.51 \quad (5.6c)$$

$$\Delta E_s = -3.31 \ln((\rho_d/\rho_w)(A_d\ /A_{solid\ disk})) + 16.03 \quad (5.6d)$$

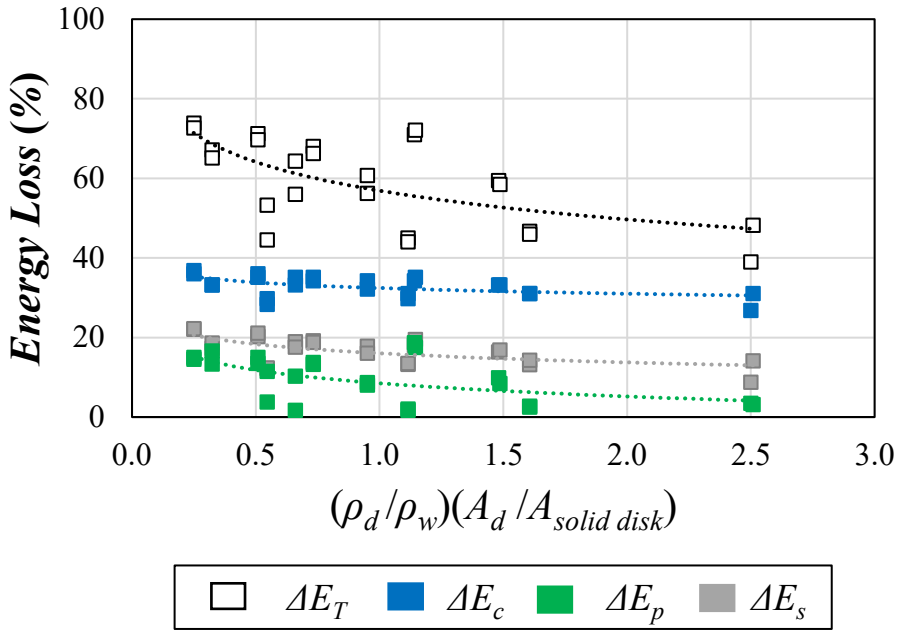

Figure 5.17: Effects of controlling parameters such as disk density ratio and disk aspect ratio on variations of energy losses in total, collision, pinch-off, and sinking stages for the edge on impact orientation.

5.5 Conclusions

A series of laboratory experiments were carried out to study the effects of disk geometry and release orientation in solid and annular disks. To highlight the impact surface, edge-on releases orientation were tested and the results benchmarked with the face-on release orientation results that were reported by Ebrahimi and Azimi (2024, 2025a, 2025b). The splash and cavity formation due to release orientation were investigated in three different perspectives of frontal, oblique, and lateral views due to the inherent asymmetry introduced by the disk geometry. Experimental results indicated that increasing the disk–fluid density ratio raises both splash height and normalized splash diameter, while increasing the disk aspect ratio reduces the splash and cavity size. The maximum normalized splash diameter for edge-on release was approximately 70% of the corresponding case with face-on release orientation. The pinch-off time prolonged with the disk–fluid density ratio but modestly decreased, by 1.7% on average across densities, as the opening ratio grows. It was found that the projection area played an important role and the face-on impacts took longer to pinch off than the edge-on release and such difference were approximately 34% for $D/h = 3.0$ and approximately 12% for $D/h = 1.5$.

The pinch-off occurred at deeper location in face-on impacts in comparison with the corresponding case with edge-on impact. For annular disks released with edge-on orientation, the central hole remained perpendicular to the trajectory, presenting an additional hydrodynamic resistance; in contrast, the face-on orientation enhanced disk–cavity cohesion. The pinch-off depth grew with the density ratio but decreased with the aspect ratio of the disks. On average, the pinching ratio (h_p/h_d) was approximately 13% higher in edge-on release orientation in comparison with the face-on impact.

The splash diameters were found to be higher in the front view than the side view by an average value of 18% in edge-on release orientation indicating the asymmetry in formation of splash curtain. However, the maximum splash diameter on the edge-on release orientation was approximately 70% of the corresponding disks with face-on impact. In disks with face-on impact, increasing the opening ratio reduced the splash diameter, while in edge-on impact, the effect of opening ratio was minimal. Raising the aspect ratio from D/h = 1.5 to 3.0 also reduced the splash diameter by approximately 26% in both views.

The impact stage dominated the energy budget where more than half of the available energy was transferred from the disk to the water at collision, $\Delta E_c /(mg(hr + D) > 50\%$. Higher density ratio and larger projected area at the impact (face-on) reduced the fraction of energy losses at the collision stage. Averaged by stage and orientation, the energy losses at the pinch-off stage were 11% for the edge-on impact while it was 28% for the face-on impact. At the collision stage, the averaged energy losses was 33% on edge-on impact versus 22% in face-on impact. Finally, at the sinking stage, the energy losses were 16% in edge-on release orientation versus 14% for face-on impact. The higher values of energy losses in pinch-off stage and in face-on impact likely reflected the stronger disk–cavity cohesion, as more solid area engaged in the pinching process.

Chapter 6

Bubble plume dynamics in non-Newtonian ambient fluid mixture

6.1 Introduction

Bubble plumes have been employed in many civil, mechanical, chemical, and environmental engineering projects, and they are applicable in many industries such as wastewater treatment, gas mixing, and biochemical processes. Their applications extend to improve water quality in lakes and natural water streams by employing artificial aeration, reducing wave-induced damage, and mitigating pollution from offshore oil and gas extraction activities (Abdulmouti, 2022). Artificial aeration has proven to be a very effective technique, mainly due to its ability to achieve high oxygen transfer rates, to extend retention times, and to create a large surface area for gas exchange. Consequently, enhancing aeration efficiency has been one of the most significant advancements in water treatment and the related processes (Cao et al., 2020; Chen et al., 2022; Shi et al., 2022). Many experimental studies on bubble plume dynamics have been carried out in bubble columns due to their ease of construction and affordability in comparison to other experimental methodologies. Bubble columns have been designed with different controlling factors such as injection conditions, column dimensions, injection rate, and fluid properties (Clift et al., 2013; Sato et al., 2015; Niida and Watanabe, 2018; Besagni and Deen, 2020; Behzadipour et al., 2022; Feng and Zhang, 2023).

Beside hydrodynamic parameters, recent laboratory experiments employed mechanical devices such as diffusers, grid screens, natural barriers, etc., to reduce bubble size and velocity to improve oxygen transfer. Behzadipour et al. (2022) studied the effect of grid screens on changing bubble characteristics for oxygen transfer improvement. The effects of air discharge, ranging from Q_a = 4 to 8 L/min, on variations of bubble size and rising velocity were evaluated. The nozzle size ranged between d_o = 1 mm and 3 mm, and the grid screens ranged between 0.84 mm and 2.38 mm.

A paper based on the content of this chapter is published in the *Chemical Engineering Science, Ebrahimi, M., & Azimi, A. H. (2026).* Bubble plume dynamics in non-Newtonian ambient fluid mixture. Chemical Engineering Science,

The results demonstrated that the presence of a grid screen significantly reduced bubble size, increasing its effectiveness in modifying bubble dynamics within the system, and increasing the total number of bubbles by approximately 20%. Experimental results showed that the bubble size decreased while bubbles moved upward, and the bubble rising velocity dropped by approximately 30% due to momentum exchange with the grid screens. The experimental results obtained by Behzadipour et al. (2023) indicated that increasing air discharge augmented both bubble velocity and bubble concentration. Li et al., (2020) conducted a series of laboratory experiments to investigate the impacts of diffusers on bubble size. Two different diffusers with a nozzle diameter of 0.8 mm and two air discharges of 0.25 L/min and 1.2 L/min were tested. The size of bubbles was quantified by image processing techniques, and the results indicated that by increasing the air discharge, bubble diameter and slip velocity increased as well.

The gas phase such as air, can be released from a variety of sources, each yielding different bubble plume characteristics. Several experimental studies have been conducted to explore the impact of nozzle size on variations of centerline bubble velocity along the distance from the nozzle, and non-linear correlations were observed between the tested variables (Bombardelli et al., 2007; Lima Neto et al., 2008; Lima and Lima Neto, 2018; Lai and Socolofsky, 2019; Bohne et al., 2020; Behzadipour et al., 2022). Milgram. (1983) carried out a series of laboratory experiments with different air discharges to investigate the variations in bubbles' centerline velocity. The results revealed that the centerline velocity decreased by approximately 45% at 1.5 m above the release point. Ziegenhein and Lucas (2017) used different nozzle sizes in the range of d_o = 0.12 mm to 1.5 mm while the air discharge varied between 0.5 L/min to 6 L/min. The correlations between the tested parameters were reported by employing the well-known Reynolds, *Re*, and Eötvös numbers, *Eo*. The results revealed that by increasing the Eötvös number, *Eo*, from 0.2 to 5, the bubble aspect ratio declined from 0.95 to 0.5. Such a reduction is more noticeable in relatively small discharges (i.e., $Q_a \approx 0.6$ L/min).

Many experimental studies have been conducted to evaluate the effects of ambient viscosity on bubble characteristics and bubble plume dynamics. Ruzicka et al. (2003) investigated the effects of ambient viscosity on variations of gas hold-up and discharge regime transitions. The study demonstrated that the low-viscosity fluids (i.e., $\mu < 5$ mPa.s) facilitated stable discharge conditions, enhanced flow uniformity, and reduced turbulence during the release process. In

contrast, fluids with higher viscosities (i.e., 5 mPa.s $\leq \mu \leq$ 20 mPa.s) facilitated the transition between discharge regimes by destabilizing the homogeneous regime. A mixture of glycerin and water (i.e., Glycerol), with different glycerin concentrations, was used to prepare seven fluid mixtures to study the effect of ambient viscosity on bubble dynamics issued from a nozzle. The results indicated a direct correlation between the air discharge and gas hold-up. Additionally, the data revealed that higher viscosity reduced the gas hold-up. Zahradnick et al. (1999) examined the impacts of ambient viscosity on bubble dynamics by adding alcohol to water. The viscosity of the fluid mixture was in the range of 1.4 to 120 mPa.s, and represented that by increasing the alcohol concentration. It was found that the gas hold-up increased with increasing ambient viscosity.

Besagni and Inzoli (2017) studied the effects of fluid properties on some bubble dynamics parameters such as discharge regime, bubble size distribution, bubble shapes, and bubble concentration. The type of fluids used in their study was tap water, a mixture of salt (i.e., NaCl) and water, water-monoethylene glycol, and water-ethanol mixtures. Spargers with different diameters, ranging between d_o = 2 mm and 4 mm, were utilized. The results demonstrated that increasing salt concentration significantly raised bubble concentration by approximately 30% which complemented the observations by Zahradnick et al. (1999) in correlation between ambient viscosity and gas hold-up. Additionally, the gas hold-up increased with higher superficial gas velocities. Olivieri et al. (2013) used sodium chloride and sodium monoacid alginate as the two additives to change the viscosity in the ambient fluid in a range from 0.9 to 20 mPa.s. The results confirmed that the trend of superficial bubble velocity is consistent with the behavior of gas hold-up. In contrast, viscosity did not exhibit a clear correlation with either the number of bubbles or the superficial gas velocity. The superficial gas velocity showed an initial increase followed by a subsequent decline.

Recent experimental studies emphasised the importance of ambient fluid viscosity on bubble characteristics (Laupsien et al., 2017, 2022). Polyalkylene glycol lubricant (Breox) solution was utilized to prepare fluid mixtures with different viscosities ranging from 1 to 100 mPa.s. At a constant air discharge of Q_a = 0.85 L/min, the superficial bubble velocity was found to be approximately 0.65 m/s. Two distinct spargers were utilized to generate two types of bubbles: ellipsoidal bubbles and spherical cap bubbles. The vertical mean velocities were compared with the horizontal mean velocities and found that the maximum vertical velocity was approximately

0.4 m/s, whereas the maximum horizontal velocity was around 0.15 m/s. At high mixture viscosities, the oscillation of the bubble plume was easily suppressed, and both the plume expansion and oscillation period occurred at a faster rate. The tested mixtures had Newtonian behaviour, and it was suggested to test mixtures with non-Newtonian fluid properties. Lee et al. (2021) used the glycerine-water mixture to examine the effect of ambient viscosity on bubble characteristics. The ambient viscosity varied between 5 and 800 mPa.s, and air discharge ranged from 0.3 to 1.5 L/min. It was concluded that while the ambient viscosity increased, the bound expansion stage and acceleration expansion stage in bubbles increased as well. It was found that the bubble rising velocity decreased with increasing viscosity of the mixture. Moreover, increasing the Reynolds number in bubbles increased the volume of bubbles in addition to rise the probability of bubble coalescence.

Many laboratory experiments investigated the effects of non-Newtonian fluid mixtures on bubble characteristics and the formation of bubbles issued from single and multiple nozzles. (Xu et al. (2017) utilized carboxymethyl cellulose (CMC) to develop a non-Newtonian fluid mixture with viscosities ranging from 1 to 230 mPa.s. The rise of the single bubble was studied to elucidate the behavior of the bubble dynamics and the trajectory of the rising bubble. Digital image processing techniques were employed to analyze data for bubbles released from nozzles with different nozzle diameters of d_o = 1.1 mm, 1.5 mm, and 2 mm. It was found that the equivalent bubble diameter increased with increasing ambient viscosity, while bubble velocity decreased. Liu et al., (2015) performed a series of experimental studies to assess the shape and motion of air bubbles in a viscous ambient. The density and viscosity of the ambient fluid ranged between ρ_f = 999 to 1246 kg/m^3 and ambient viscosity ranged from μ = 0.8 to 620 mPa.s, respectively. It was found that the terminal velocity of bubbles, ranging between V_T = 0.10 m/s and 0.20 m/s, increased with bubble diameter ($0.4 \leq d_b \leq 1$), contrary to the trend observed between bubble aspect ratio, where it declined with increasing bubble diameter. Moreover, the bubble aspect ratio declined from 1 to almost 0.3 while the Weber number increased from We = 0.001 to approximately 10. Table 1 shows a summary of the experimental studies in the literature and the related parameters for bubble plumes discharged in Newtonian and non-Newtonian fluid mixtures.

Despite numerous experimental studies on bubble dynamics in viscous ambient, less information is available on bubble characteristics and the motion of bubbles in non-Newtonian

fluid mixtures. While the range of viscosity in non-Newtonian fluid mixtures may be similar to Newtonian viscous ambient, the yield stress and the nonlinear correlation between shear stress and shear rate may significantly affect the size and motion of bubbles. The present study investigates the effects of non-Newtonian ambient fluid on bubble characteristics and bubble dynamics. Due to non-linearity in fluid dynamics of non-Newtonian fluid, the effect of other controlling parameters such as nozzle size and air discharge on bubble plume dynamics is studied. Four non-Newtonian fluid mixtures with different apparent viscosities and yield stresses were prepared to explore bubble dynamics and to provide detailed analysis on the effect of ambient rheology on the size and dynamics of bubbles. Additionally, different nozzle sizes and air dischargers were employed to assess the role of nozzle diameter and initial air velocity on bubble dynamics. Image processing algorithms were developed by utilizing MATLAB software to process the primary data, where multiple algorithms were integrated to extract accurate data from high-speed imaging. The present approach enabled detailed examination of bubble velocity patterns, alongside the analysis of bubble size variations. Additionally, the bubble rising velocity variation according to the understudy factors and a regime plot of the bubble shape under new conditions were examined. The current study is complemented by validated numerical simulation which can provide many detailed information on different aspects of bubble formation, wake-induced interaction, and bubble coalescence. It is important to study the effect of nozzle tips geometry (e.g., beveled versus flat) in formation of bubbles which can be the topic of future study.

Table 6.1: Flow and bubble characteristics of bubble column experiments in the literature.

Researcher	Ambient	Q_a (L/min)	d_o (mm)	μ (mPa.s)	ρ_f/ρ_w	Tank Dimensions (mm)
(Rensen and Roig, 2001)	Water	1.2	Capillary tube	1	1	150 × 150 × 670
(Roig and De Tournemine, 2007)	Water	0.4-5	Capillary tube	1	1	300 × 150 × 3100
(Seol et al., 2007)	Water	1-7	Air stone	1	1	380 × 380 × 800
(Seol et al., 2009)	Water	0.1	Air stone	1	1	380 × 380 × 800
(Riboux et al., 2010)	Water	-	0.1	1	1	150 × 150 × 1000
(Bryant et al., 2009)	Water	0.5-1.5	Air stone	1	1	1000 × 2000 × 1500
(Ziegenhein and Lucas, 2017)	Water	0.6	0.7-0.9	1	1	50 × 250 × 600
(Lima and Lima Neto, 2018)	Water	1-9	3.5-30	1	1	500 × 500 × 1000

(Niida and Watanabe, 2018)	Water	0.015	0.26	1	1	150 × 170 × 200
(Lai and Socolofsky, 2019b)	Water	0.5-1.5	Air stone	1	1	1000 × 1000 × 1000
(Wang et al., 2019)	Water	0.25	0.4	1	1	9100 × 4600 × 1680
(Behzadipour et al., 2022b)	Water	1-3	4-8	1	1	850 × 1600 × 800
(Behzadipour et al., 2023a)	Water	3	3-12	1	4	850 × 1600 × 800
(Gao et al., 2022)	Aqueous glycerol	0.36-3.6	4	308-4174	1.235-1.267	400 × 120 × 1200
(Jiang et al., 2017)	Water, SDS, PAAM	-	0.5	1-1400	1-1.23	50 × 50 × 65
(Aoyama et al., 2017)	Water + glycerol	-	-	9-45	1.1-1.2	1500 × 1500 × 2100
(Dijkhuizen et al., 2010)	Glycerol + water–air	-	Air syringe	0.9-153	1-1.2	200 × 200 × 1400
(Zhang et al., 2008)	Glycerin solution	-	-	0.6-775	1.1-1.3	-
(Feng et al., 2016a)	Glycerol + water	-	-	580-2300	1.2	250 × 250 × 600
(Feng et al., 2016c)	Glycerin, Polyacrylamide	-	-	580-2300	1.2	250 × 250 × 600
Current study	Water + Polyacrylamide	1-12	2-12.7	1-580	1-1.1	400 400 × 1000

6.2 Regime classification

A regime plot based on the correlation between non-dimensional parameters and bubble shape was first introduced by Grace (1973). The proposed regime plot shows the correlation between the Reynolds number $Re = \rho_f d_e u_b/\mu_f$ versus the Eötvös number $Eo = \rho_f g Re^2/\sigma$, where ρ_f, is the density of the fluid, d_e, is the equivalent bubble diameter, u_b, is the bubble velocity, μ_f, is the viscosity of the fluid, σ, is the surface tension, and g is the gravitational acceleration. Figure 6.1 shows the four primary regions corresponding to distinct bubble shapes of spherical, ellipsoidal, conical, and spherical cap. The conical regime is new, and it was added based on bubble observations in this study. The identified regions help to classify bubble morphology under varying fluid dynamic conditions. The markers corresponding to the apparent viscosities of $\mu_m/\mu_w = 180$ (i.e., polymer concentration of 0.10 wt.%) are positioned above those representing $\mu_m/\mu_w = 520$,

and 580 (i.e., polymer concentrations of 0.20 wt.% and 0.30 wt.%). The bubbles generally exhibit a conical shape, except for those formed at air discharge of Q_a = 1 L/min, which are categorized as ellipsoidal bubbles. The correlations between the Reynolds and Eötvös numbers for different ambient viscosities are described by different equations as:

$$Re = 8.1961Eo^{0.9598} \quad \text{for } \mu_m/\mu_w = 180 \tag{6.1a}$$

$$Re = 4.3891Eo^{1.0482} \quad \text{for } \mu_m/\mu_w = 520 \tag{6.1b}$$

$$Re = 0.7033Eo^{1.2514} \quad \text{for } \mu_m/\mu_w = 580 \tag{6.1c}$$

As can be seen, different exponential formulas are proposed to describe the correlation between *Re* and *Eo*, which is because of the yield stress and the non-linear correlation between shear stress and shear rate of the selected materials. As air discharge increases, all data shift toward the spherical cap region. However, as ambient viscosity increases, data deviate further from the spherical cap region. Figure 6.1 illustrates that increasing fluid viscosity causes a transition toward more conical or ellipsoidal geometries. At high viscosity levels such as a viscosity ratio of μ_m/μ_w = 580, the formation of a spherical cap becomes highly unlikely. Bubble formation characteristics are characterized by dimensionless numbers such as the Reynolds, Galilei, and Eötvös numbers, which are expressed as:

$$Re = \frac{\rho_m d_e u_b}{\mu_m} \tag{6.2}$$

$$Eo = \frac{\rho_m g d_e^2}{4\sigma} \tag{6.3}$$

$$Ga = \frac{\rho_m g^{1/2} d_e^{3/2}}{2^{3/2}\mu_m} \tag{6.4}$$

where ρ_m is the mixture's density, d_e is the equivalent bubble diameter, u_b is the bubble terminal velocity, μ_m is the mixture's viscosity, and g is the gravitational acceleration. The apparent viscosity in non-Newtonian fluids vary with shear rate and in shear thinning non-Newtonian fluid mixtures, the apparent viscosity decreases with increasing the shear rate. The values of apparent viscosities in relatively small (i.e., near zero) shear rate were used in calculation of non-dimensional numbers to be consistent with all other fluid mixtures. These three dimensionless numbers serve as the best representatives of the case since they encompass all three controlling parameters. Figure 6.2 shows the correlations between the selected non-dimensional parameters. The effects of ambient viscosity

on the correlation between the selected non-dimensional numbers are shown in Figure 6.2. As can be seen, by increasing the Galilei number, which is representative of the fluid properties, both Reynolds and Eötvös numbers rise. Figure 6.2a shows a non-linear correlation between Reynolds and Galilei numbers in this study, which can be formulated as:

$$Re = 2.643Ga^{1.317} \tag{6.5}$$

Figure 6.2b shows the correlation between Eötvös number and Galilei number for bubble plumes with different ambient viscosities. The correlation between the selected non-dimensional numbers are expressed as:

$$Eo = 0.3122Ga^{1.333} \quad \text{for } \mu_m/\mu_w = 180 \tag{6a}$$

$$Eo = 0.5096Ga^{1.333} \quad \text{for } \mu_m/\mu_w = 520 \tag{6b}$$

$$Eo = 1.4848Ga^{1.333} \quad \text{for } \mu_m/\mu_w = 580 \tag{6c}$$

The results were compared with the outcomes of the experimental study by Lee et al., (2021) and Tripathi et al. (2015). The results obtained by Tripathi et al. (2015) fall below all other studies, as the associated Eötvös numbers are lower. This discrepancy arises due to the use of water as the ambient fluid, which has much lower viscosity than that of the other fluids in the two studies. As explained in the literature, Lee et al., (2021) performed their experiments in fluids with different viscosities ranging from 5 to 800 mPa.s and discharge rates of Q_a = 0.3 to 1.5 L/min. Based on the results, the Galilei number experienced an increment by rising the Eötvös number. However, the Eötvös number in the study by Lee et al. (2021) is lower than that of the current study due to the noticeable difference in air discharge which is 8 times smaller than the discharge in the present study. Such variations elucidate the impacts of air discharge in regime classification. Conical bubbles observed in our experiments arise due to the rheological characteristics of the non-Newtonian fluids employed (i.e., strong shear-thinning behavior). Damping forces due to the fluid viscosity inhibit bubble deformation and stabilize elongated or pointed shapes by resisting fluid rearrangement around the bubble. At higher viscosities and flowrates, the interaction between buoyancy-driven forces and viscous resistance further promotes such distinct conical geometry.

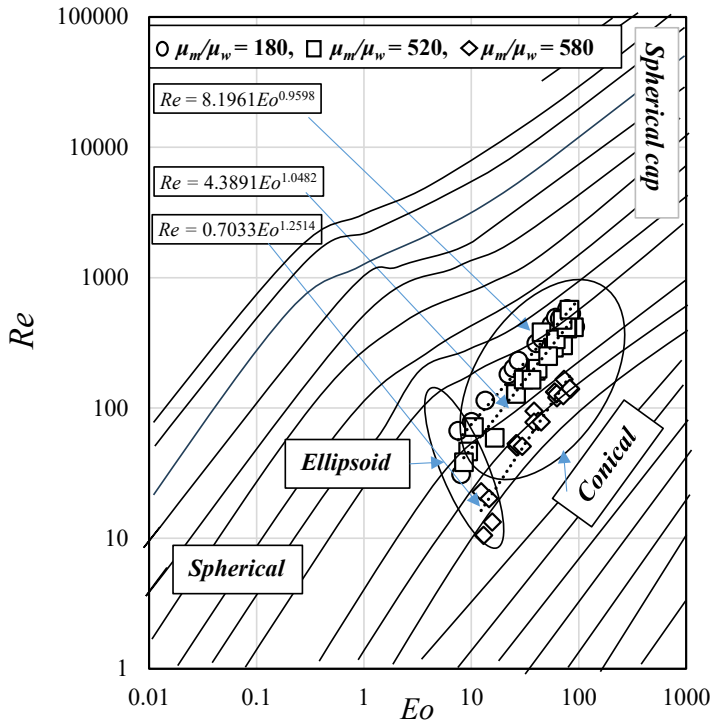

Figure 6.1: The position of the present experimental data in the bubble regime plot of the Reynolds number, *Re*, versus the Eötvös number, *Eo*.

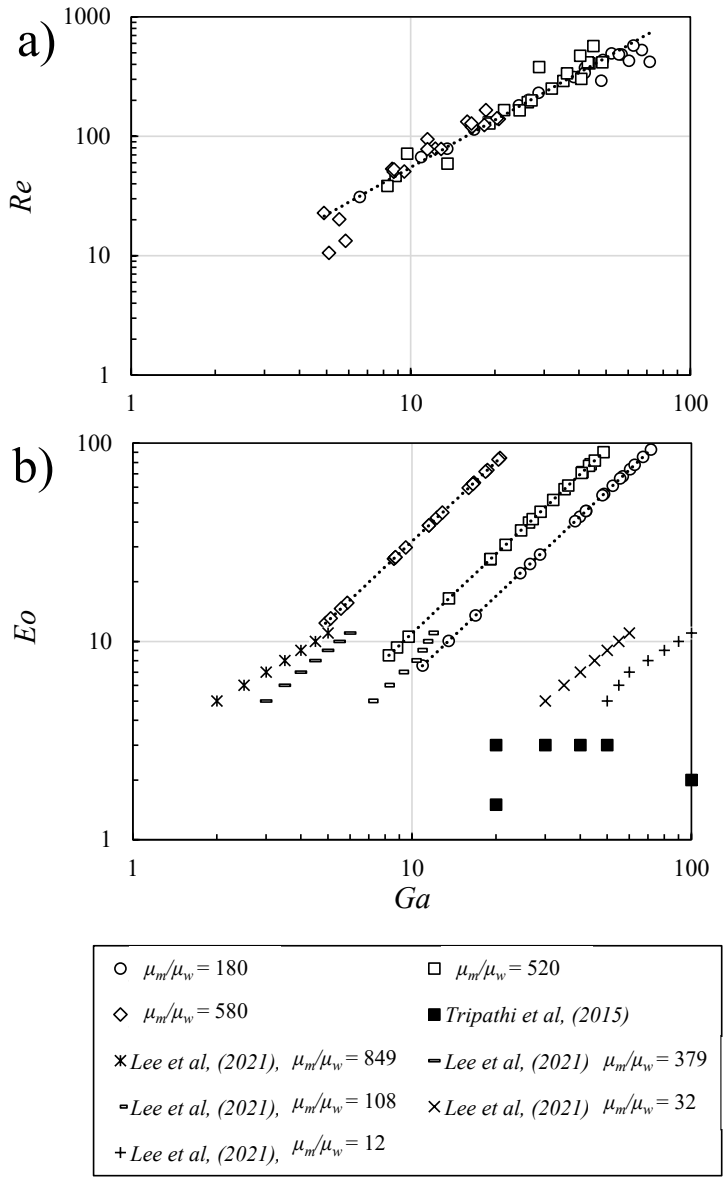

Figure 6.2: Effect of ambient viscosity on the positioning of the present experimental data in the regime plots of the non-dimensional parameters and comparison with other data from the literature: a) a correlation between the Galilei number, *Ga*, versus the Reynolds number, *Re*, b) a correlation between the Galilei number, *Ga*, versus the Eötvös number, *Eo*.

6.3 Methodology

6.3.1 Experimental setup

A series of laboratory experiments was carried out in the Multiphase Flow Research Laboratory (MFRL) at Lakehead University, Canada. A tempered glass tank with dimensions of 400 mm × 400 mm × 1000 mm was used to investigate the effects of fluid properties, nozzle size, and air discharge on bubble characteristics and dynamics of bubbles in bubble plumes. Four nozzle diameters of d_o = 2 mm, 3 mm, 5 mm, and 12.7 mm and five air discharges of Q_a = 1, 3, 6, 9, and 12 L/min were utilized to develop a wide range of Reynolds numbers, to properly scale with tank dimensions, and to align with industrial application requirements. Overall, 60 experiments with a wide range of air discharges, nozzle sizes, and fluid mixtures with different apparent viscosities were tested in this study. The experimental parameters and the associated experimental results such as horizontal and vertical bubble sizes, bubble equivalent diameter, bubble rising velocity, and the related non-dimensional numbers such as Eotvos, Reynolds, and Galilei numbers are listed in Table 6.2.

Figure 6.3 shows the schematic of the experimental setup and the coordinate system. A circular nozzle was installed at the bottom of the tank, and a series of pipes was used to facilitate the passage of air flow. Air passes through the pipes and nozzles and is then released into the fluid mixture from the bottom of the tank with different nozzle sizes and discharges. A gas flowmeter was utilized to control and measure the output discharge. Six light sources (Woods 166 L13, 1,000-W telescope work light, CA) were applied to generate sufficient light and uniform brightness over the tank and to support capturing high-quality images while two high-speed cameras (Phantom, Miro Lab 110, New Jersey, Wayne, USA) were exerted to capture time-series images. The high-speed cameras captured images with a frequency of 1000 fps and a resolution of 1280 × 800 pixels (Phantom, Miro Lab 110, New Jersey, Wayne, USA) using a proper camera lens (AF Nikkor 50 mm, f/1.4D, Nikon, Tokyo, Japan). The spatial resolution were 4.3 pixel/mm horizontally and 2.7 pixel/mm vertically. The camera system was calibrated using a precision calibration grid placed inside the experimental tank, enabling pixel-to-physical unit conversions. In addition, the applied software for image capturing by the high-speed cameras can perform automatic calibration of the Region of Interest (ROI). Regular calibration checks were performed before and after sets of experiments to maintain consistent accuracy. A sufficient relaxation time of at least 24 hours was allotted between each experiment and to ensure system stabilization while maintaining a constant

fluid level. After each test, the fluid was remixed to ensure homogeneity and to maintain consistent experimental conditions. Uniformity of airflow across all nozzle diameters, particularly the largest (d_o = 12.7 mm), was maintained using an accurate gas flowmeter, pressure regulators, and straight tubing lengths exceeding 50 times the nozzle diameter to minimize entrance turbulence. Preliminary flow visualization experiments confirmed stable conditions at the nozzle exits.

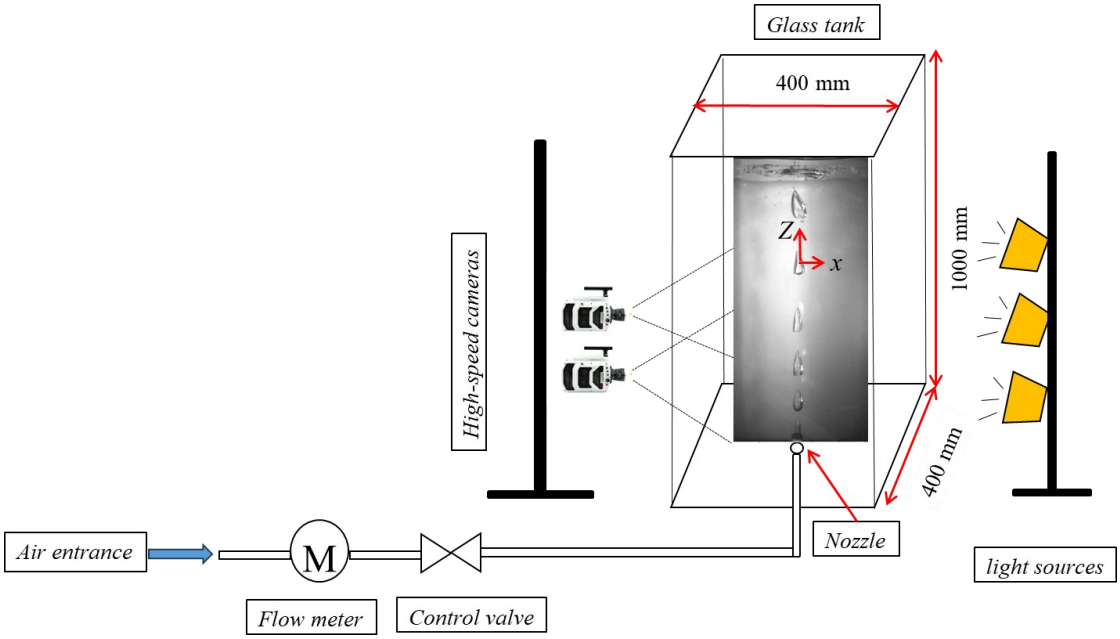

Figure 6.3: Schematic diagram of the experimental setup, coordinate system, and the positioning of the highspeed cameras.

6.3.2 Fluid properties

A chemical additive is required to enhance the viscosity of the fluid mixture while the final mixture should remain sufficiently transparent to allow clear image capturing by the high-speed cameras. A mixture of Polyacrylamide (PAM) and water was selected for the ambient fluid to form a non-Newtonian fluid mixture which is environmentally friendly and economical. The PAM and water mixture met the critical balance between increasing viscosity, maintaining transparency, environmental safety, and cost-effectiveness, and has been utilized in many research studies (Gao, 2013; Jung et al., 2013; Pei et al., 2016; Hu et al., 2017; Kumar et al., 2020; Lu et al., 2021;Ebrahimi et al., 2020; Ebrahimi and Sanati, 2021). The polyacrylamide (PAM) and water mixture that was used for this study was supplied by the SNF (France) corporation, and its

commercial name is FLOPAM AN 934 VHM. The procedure of preparing the fluid mixtures was explained in detail in recent publications by the authors (Ebrahimi and Azimi, 2025a, 2025b, 2024).

To prepare fluid mixtures with varying viscosities, different concentrations of the PAM polymer were added to ionized water. The polymer concentrations were set at 0.10 wt.%, 0.20 wt.%, and 0.30 wt.% to achieve a broad range of viscosities, measured at 180, 520, and 580 mPa.s, respectively. After preparation, the viscosities of the fluid mixtures were measured by a Brookfield viscometer (DVPlus viscometer, Massachusetts, USA). The minimum aging time of all the acquired mixtures was seven days, and the aging time was long enough to ensure that all polymers were homogeneously dissolved in water. The minimum 7-day aging period for PAM mixtures effectively mitigated thixotropic effects, which is confirmed through rheological tests. The results showed consistent viscosity values in the undergo dominating conditions which ensures stable rheological conditions throughout experiments. A mechanical stirring unit was continuously used between experiments to ensure fluid mixture homogeneity. Homogeneity was also verified before each experiment by sampling the fluid mixtures at different depths and perform rheological measurements. All rheological measurements were conducted under identical temperature conditions (25°C) and atmospheric pressure as those used in experiments. Figure 4 displays the effect of polymer concentration on the correlation between the viscosity of the mixture at different values of shear rate. As can be seen, the selected fluid mixture is non-Newtonian shear thinning as the viscosity of the mixtures decreased non-linearly with the shear rate.

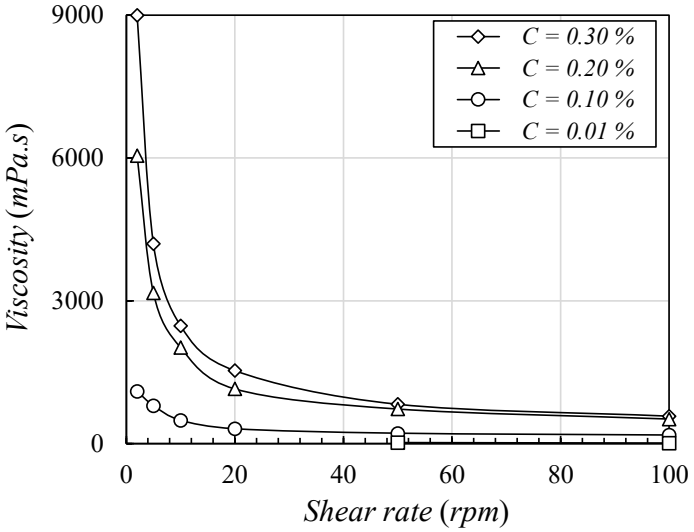

Figure 6.4: Effect of polymer concentration on variations of mixture viscosity with the shear rate. The above plot indicates the shear-thinning behaviour in the proposed water-based mixtures.

Table 6.2: Experimental parameters including flow rate, nozzle size, polymer concentration, and experimental results including horizontal and vertical bubble size, bubble equivalent diameter, rising velocity, Eotvos, Reynolds, and Galileo numbers.

Test No.	Q_a (*L/min*)	d_o (*mm*)	C (%)	w (*mm*)	h (*mm*)	d_b (*mm*)	V (*m/s*)	*Eo*	*Re*	*Ga*
1	1	2	0.10	12.56	9.70	10.57	0.70	8	31	7
2	3			15.44	32.44	25.33	1.32	22	182	24
3	6			17.75	49.44	35.14	1.65	42	316	40
4	9			22.50	62.56	44.49	1.90	68	485	57
5	12			23.94	71.69	49.73	1.99	85	530	67
6	1	3		14.68	14.87	14.81	0.83	8	67	11
7	3			18.00	32.56	26.72	1.39	25	202	26
8	6			20.31	44.44	34.23	1.68	40	315	38
9	9			21.63	54.75	40.17	1.99	56	437	49
10	12			22.81	66.00	46.32	2.05	74	430	60
11	1	5		14.56	18.50	17.08	0.95	10	79	14
12	3			18.38	35.00	28.24	1.50	27	232	29
13	6			20.00	49.06	36.38	1.88	46	374	42
14	9			20.81	59.88	42.10	2.16	61	497	52
15	12			23.19	68.00	47.51	2.23	78	578	63
16	1	12.7		16.80	21.50	19.80	1.06	13	114	17
17	3			27.19	42.00	36.33	1.50	45	340	42
18	6			24.25	51.00	39.81	1.70	55	293	48
19	9			22.00	62.00	43.89	1.90	66	485	56
20	12			28.63	70.00	51.96	2.10	93	421	72
21	1	2	0.20	15.55	16.90	16.44	0.75	9	46	9
22	3			18.60	33.31	27.43	1.26	26	131	19
23	6			20.00	44.25	33.96	1.50	40	193	26
24	9			25.50	60.81	45.52	1.76	71	303	41
25	12			29.88	66.88	51.12	1.94	90	416	48
26	1	3		15.18	16.00	15.72	0.65	9	38	8
27	3			19.44	32.69	27.49	1.23	26	128	19
28	6			21.30	44.19	34.65	1.53	41	200	27
29	9			23.38	54.81	41.26	1.86	59	291	35
30	12			26.48	63.94	47.66	2.00	78	409	44
31	1	5		15.88	18.38	17.50	0.85	11	72	10
32	3			20.00	36.44	29.83	1.47	31	166	22
33	6			21.00	47.44	36.15	2.00	45	382	29
34	9			21.50	59.00	42.14	2.11	61	337	36
35	12			24.00	66.25	47.23	2.33	77	416	43

36	1	12.7	0.30	20.63	22.50	21.86	0.72	16	59	14
37	3			22.81	38.75	32.48	1.34	36	165	25
38	6			24.25	49.00	38.76	1.71	52	251	32
39	9			25.00	61.00	45.31	2.77	71	474	40
40	12			25.75	67.00	48.71	3.10	82	571	45
41	1	2		16.44	20.31	18.93	0.71	12	23	5
42	3			19.83	32.44	27.53	1.10	26	53	9
43	6			20.18	42.94	33.38	1.40	38	95	11
44	9			20.75	58.78	41.54	1.88	59	133	16
45	12			21.94	59.81	42.81	1.68	63	122	17
46	1	3		16.70	21.00	19.46	0.32	13	11	5
47	3			21.95	31.19	27.75	1.07	27	50	9
48	6			23.70	42.36	34.90	1.33	42	79	12
49	9			24.00	56.82	42.63	1.62	63	120	17
50	12			24.29	70.48	49.41	1.69	84	140	21
51	1	5		20.00	22.00	21.31	0.37	16	13	6
52	3			22.50	30.88	27.78	1.12	27	53	9
53	6			23.56	39.75	33.39	1.37	38	78	11
54	9			24.40	56.13	42.52	1.78	62	128	16
55	12			26.66	60.54	46.06	2.12	73	166	19
56	1	12.7		16.50	23.00	20.59	0.58	15	20	6
57	3			20.81	34.94	29.40	1.02	30	51	9
58	6			23.19	44.83	35.98	1.28	45	78	13
59	9			27.88	58.38	45.63	1.60	72	124	18
60	12			31.13	61.38	48.94	1.71	83	142	20

6.3.3 Image analysis & data processing

Image analysis was implemented in this study by employing in-house algorithms and using MATLAB software (Mathworks, R2018b) to detect bubbles and extract meaningful data on the size and dynamic features of bubbles. Such image analysis methodology has been exerted by many researchers in the past such as by Liu et al., (2015); Sato et al., (2015); Besagni et al., (2016); Besagni and Deen, (2020); and Laupsien et al., (2019, 2021); Mohammadkhani et al., (2025). The image analysis algorithms have been developed to derive the required information on bubble parameters and multiple steps were required to achieve such goals. Figure 5 shows the procedure of image processing for bubble boundary detection. The original image of bubbles is shown in Figure 5a, and it was then converted to a grayscale image. The background subtraction algorithm was performed using a morphological opening method, and the outcome of such background removal is shown in Figure 6.5b.

The Gaussian filtering method was exerted to reduce the remaining background noise, which helped to improve the accuracy of subsequent edge detection. The prepared image was then adapted to a binary format using automatic thresholding to separate the bubbles (i.e., white color) from the background (black color), and the resulting image is shown in Figure 6.5c. In the next step, any holes within the detected bubbles were filled with white pixels to ensure that the bubbles are unified in the binary image. The Sobel operator edge detection algorithm was then performed to detect the edge of bubbles. To improve the robustness of the proposed image processing process, an additional edge detection approach, named as the Canny method, was conducted (Shihab Ahmed, 2018; Lynn et al., 2021). Both methods were combined and implemented to the images (see Figure 5d). To provide a visual representation of the detected bubble boundaries, the dilated edges were overlaid on the original grayscale image. Figure 6.5e shows the rising bubbles after conducting the mentioned procedures, and the images at this stage are ready for the extraction of bubble characteristics. The obtained results indicate that boundary detection accuracy exceeds 95%.

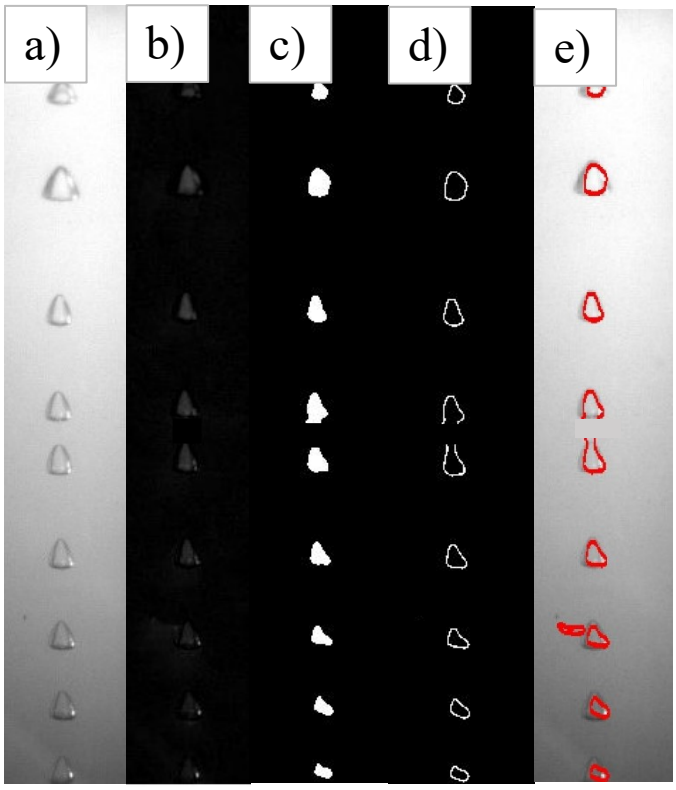

Figure 6.5: The procedure of image processing for bubble boundary detection: a) the raw image, b) the raw image is converted to the grayscale, c) the Gaussian-filter is applied, and the image is binarized, d) edge detection algorithm is applied, e) boundary detection algorithm is employed.

6.3 Results and Discussion

Figure 6.6 shows the effect of ambient fluid viscosity on bubble formation by two snapshot images of bubble plumes in water and a non-Newtonian fluid mixture with the viscosity ratio of $\mu_m/\mu_w = 180$. The nozzle diameter and air discharge in both tests are $d_o = 2$ mm and $Q_a = 3$ L/min, respectively. The ambient fluid mixture with the viscosity ratio of $\mu_m/\mu_w = 180$ was made by adding PAM polymer with a concentration of $C = 0.10$ wt.%. As can be seen, the viscous ambient prevents the formation of small bubbles and enlarges the size of the relatively large bubbles. The spreading of bubble plume in water is significantly reduced due to higher viscosity and the existence of yield stress in the non-Newtonian ambient, which reduces the contact surface area between bubbles and the ambient fluid. In addition, bubble dynamics in the ambient water appear to be more random, disordered, and non-uniform, whereas in the same discharge condition, the generated bubbles in an ambient with higher viscosity and yield stress exhibit structured and organized upward motion with a minimum distortion in the shape and path of bubbles. Bubbles in highly viscous ambient rise in a straight path while maintaining nearly constant dimensions both with time and space. In contrast, the size of bubbles rising in water significantly fluctuates both with time and space. Additionally, bubbles rising in water do not follow a path and exhibit random lateral motion as bubbles move upward.

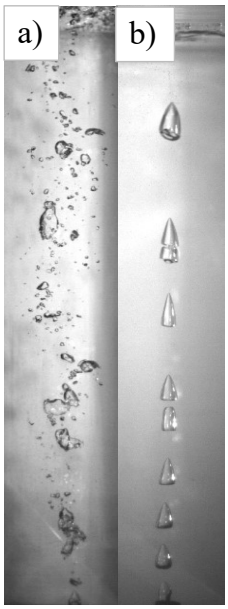

Figure 6.6: Effect of ambient fluid viscosity on bubble formation. The nozzle diameter is d_o = 2 mm and air discharge is Q_a = 3 L/min: a) Newtonian ambient fluid, water, b) non-Newtonian ambient fluid, water and PAM mixture with an ambient viscosity of μ_m/μ_w = 180, which is made by the addition of C = 0.10 wt.% PAM.

The effects of air discharge on the formation of bubbles in a non-Newtonian ambient fluid with a constant viscosity ratio of μ_m/μ_w = 180 are studied. The air discharge systematically increased from Q_a = 3 L/min by two, three, and four times to reach the maximum air discharge of 12 L/min. Figure 6.7 shows the snapshot images of bubbles discharging from a d_o = 2 mm diameter nozzle and rising through a non-Newtonian ambient fluid mixture with a viscosity ratio of μ_m/μ_w = 180. Each subplot in Figure 6.7 shows a snapshot image of bubbles with different air discharges. As can be seen, both horizontal and vertical dimensions of bubbles increased with increasing air discharge. Such change in bubble size affected other geometrical characteristics of bubbles including bubble aspect ratio and the total number of bubbles within the column.

The viscous force in the ambient suppresses the formation of numerous smaller bubbles and controls the shape of irregular bubbles to promote the formation of fewer bubbles with regular and larger sizes. As air discharge increased, the total number of bubbles within the bubble column reduced and reached a limit in relatively higher air discharges. As can be seen in Figures 6.7c and 6.7d, the total number of bubbles is equal even though the air discharge increased from 9 L/min to 12 L/min. Such a 33% increase in air discharge slightly increased the size of bubbles. A closer look

at the snapshot images in Figures 6.7c and 6.7d indicates that the aspect ratio of bubbles slightly increased with increasing air discharge from Q_a = 9 L/min to 12 L/min.

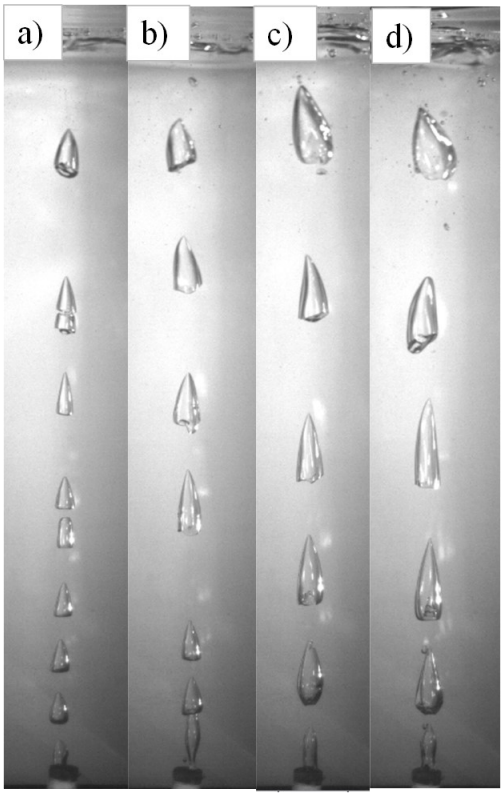

Figure 6.7: Effect of air discharge on formation of bubbles in a non-Newtonian fluid mixture with an ambient viscosity of μ_m/μ_w = 180, which is made by the addition of C = 0.10 wt.% PAM. The nozzle diameter is d_o = 2 mm: a) Q_a = 3 L/min, b) Q_a = 6 L/min, c) Q_a = 9 L/min, d) Q_a = 12 L/min.

6.3.1 Bubble dimensions

The effects of controlling parameters on bubble size can be characterized by measuring bubble aspect ratio, which is defined as the ratio of the bubble's width, w, to its height, h. The variations in bubble width and height with the controlling parameters were plotted in Figure 6.8 to analyze their effects on bubble morphology. Since the ambient fluid mixture is non-Newtonian with a yield stress, it is not possible to combine the effects of controlling parameters such as nozzle size, air discharge, and ambient viscosity into a single non-dimensional number such as the Reynolds number due to the non-linearity of the ambient viscosity, and the presence of yield stress. Therefore, in the following figures, one parameter was kept constant in each subplot and the correlations between the controlling parameters and the dependent variables were plotted as a

family of curves. Data presented in Figures 6.8–6.10 correspond to the equilibrium stage of bubble formation when bubbles reached stable dimensions. Figure 6.8 illustrates the variations of dimensionless bubble width with air discharge for different nozzle diameters and polymer concentrations. Figures 6.8a and 6.8b show the effects of nozzle size and ambient viscosity on the relationship between the normalized bubble width as a ratio of the nozzle diameter with air discharge Q_a. As can be seen in Figure 6.8a, an increase in air discharge gradually increases the dimensionless bubble width, but it is significantly affected by the nozzle size. The represented graphs in Figure 6.8a pertain only to experiments conducted with the highest mixture viscosity with a value of $\mu_m/\mu_w = 580$.

Each graph illustrates the variations according to the discharge while keeping the nozzle size constant. The set includes four graphs representing different nozzle sizes, with the graphs corresponding to smaller nozzle sizes positioned above those with larger nozzle sizes. As the nozzle size increases, the graphs are displayed in descending order. Within Figure 6.8a, the graph corresponding to the nozzle size of d_o = 12.7 mm is plotted on the right side to present the correlation with more detail. The dimensionless bubble width varies with both air discharge and nozzle size. For d_o = 2 mm, the bubble width ratio ranges from 8 to 12, while for d_o = 12.7 mm, the bubble width ratio ranges from 1 to 2.5. A comparison between the bubble width ratios for air discharge of Q_a = 12 L/min indicates that for d_o = 2 mm, the bubble width is nearly six times that of the bubbles discharged from d_o = 12.7 mm. However, for smaller air discharge (Q_a = 1 L/min) such a difference in bubble width discharged from large and small nozzles reduces from 6 times to 4 times of the nozzle diameter. This indicates that while the air discharge increases from Q_a = 1 L/min to 12 L/min, the bubble width ratio increases by approximately 50%.

Figure 6.8b shows the effect of ambient viscosity on variations of bubble width ratio with air discharge for a constant nozzle diameter of d_o = 5 mm. As can be seen in all data, the bubble width ratio increases with increasing air discharge. Increasing the air discharge from 1 to 12 L/min, increases the bubble width ratio by approximately 50% in ambient viscosity ratios of $\mu_m/\mu_w = 180$, and $\mu_m/\mu_w = 520$, while for the same increment in air discharge and in the ambient viscosity ratio of $\mu_m/\mu_w = 580$, the bubble width ratio increases by 37%. Figure 6.8c shows the correlation between ambient viscosity and bubble width ratio in constant air discharge of Q_a = 6 L/min. As can be seen, the bubble width ratio increases with the ambient viscosity; however, the effect of ambient

viscosity in comparison to nozzle diameter is negligible. Therefore, the effect of nozzle diameter on variations of bubble width may be dominant. To study the effect of nozzle diameter on bubble size, the correlation between bubble width and nozzle diameter was plotted in Figure 8d. Figure 8d shows the correlation between normalized bubble width and nozzle diameter for different air discharges of Q_a = 3 to 12 L/min and for constant ambient fluid with a viscosity ratio of μ_m/μ_w = 520. Increasing nozzle size reduces the relative bubble width, and the effect of air discharge on variations of bubble width diminishes in relatively large nozzles.

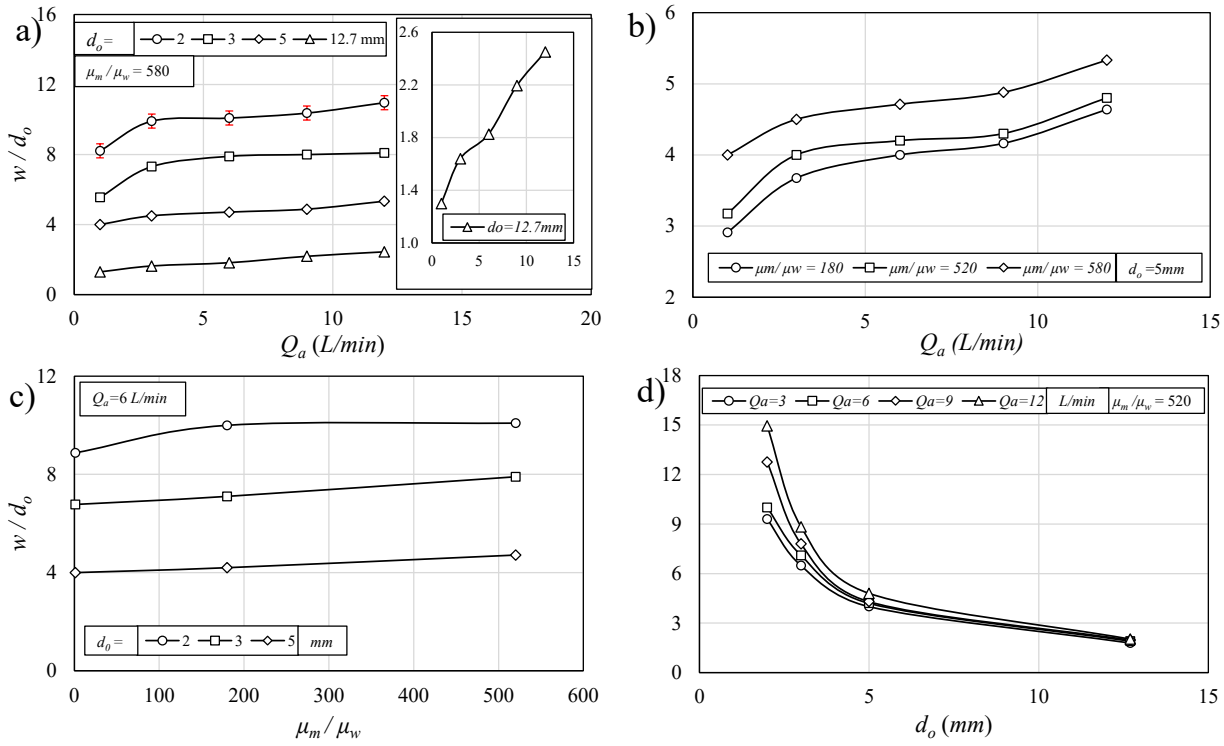

Figure 6.8: Effects of controlling parameters on variations of normalized bubble width: a) effect of nozzle diameter with different air discharges, b) effect of ambient viscosity with different air discharges, c) effect of nozzle diameter with different ambient viscosity, d) effect of air discharge with different nozzle diameters.

Figure 6.9 shows the effects of controlling parameters such as air discharge, nozzle size, and fluid viscosity on variations of dimensionless bubble height, h/d_o. Figure 6.9a shows the effect of air discharge and nozzle size on variations of bubble height normalized by the nozzle diameter. This figure allows for comparative analysis across different nozzle diameters and discharges for a

constant ambient viscosity of μ_m/μ_w = 180. As can be seen, the normalized bubble height non-linearly increases with air discharge. In terms of nozzle size, the graphs follow a descending arrangement, with the bottom curve corresponding to d_o = 12.7 mm and the top curve representing d_o = 2 mm. However, the rate at which the bubble height increases with rising air discharge depends on the nozzle size, and the highest rise is observed for d_o = 2 mm. As the nozzle size increases, the rate of increase in bubble height diminishes. The curve regarding the nozzle size of d_o = 12.7 mm is plotted as a subplot in Figure 6.9a to present the variation in more detail. The normalized bubble height ranges between 1 and 6 in relatively low air discharge of Q_a = 1 L/min, while the range of normalized bubble height is between 5 and 37 in relatively high air discharge of Q_a = 12 L/min.

In Figure 6.9b, the air discharge was isolated by selecting a constant value of air discharge (i.e., Q_a = 6 L/min), and the effects of ambient viscosity on variations of bubble height, h, for different nozzle sizes are investigated. The apparent viscosity of the ambient fluid mixture was normalized with the viscosity of water, and bubble height was normalized with the nozzle diameter. As can be seen, increasing the apparent viscosity of the fluid mixture reduces the bubble height, which is contrary to the effect of ambient viscosity on bubble width. This indicates that in presence of the same nozzle size and air discharge, bubbles become shorter and wider while passing through a fluid with higher viscosity. However, the variation in normalized bubble height, h/d_o, by the fluid viscosity is not as considerable as air discharge and nozzle diameter. Figure 6.9c illustrates the variations of dimensionless bubble height with nozzle size across different air discharges for a constant ambient viscosity ratio of μ_m/μ_w = 520. Such correlations follow the same pattern as observed on bubble width (see Figure 6.8d) indicating that both bubble height and width decrease non-linearly with nozzle size, but increase with increasing air discharge.

Figure 6.9d shows a comparison between the growth rates of bubble height and width due to increasing air discharge. The nozzle size and ambient viscosity were kept constant with the values of d_o = 2 mm and μ_m/μ_w = 520, respectively. The plot demonstrates that an increase in air discharge increases both bubble width and height almost linearly. However, it is evident that the bubble height exhibits significantly greater variation compared to the bubble width, and such a difference in growth rate becomes more pronounced as air discharge increases. At relatively low air discharge of Q_a = 2 L/min, the width and height of bubbles were nearly identical, resulting in a width-to-height ratio, w/h, of unity. In contrast, at a relatively high air discharge of Q_a = 12 L/min, the w/h

ratio decreases to approximately 0.5, indicating that the bubbles become significantly elongated in the vertical direction. The reduction in bubble aspect ratio at high air discharge is predominantly influenced by inertial forces overcoming surface tension and viscous resistance which induces the significant vertical elongation. Additionally, increased wake instabilities further amplify bubble deformation at elevated discharge rates.

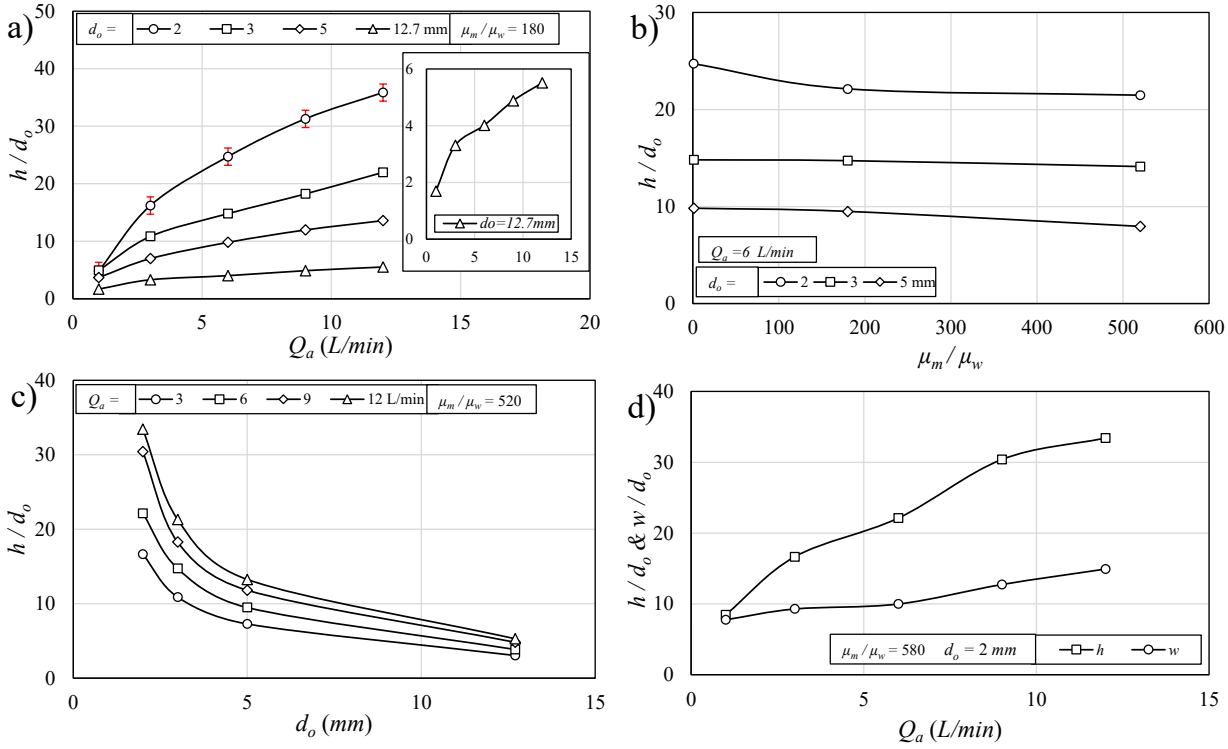

Figure 6.9: Effects of controlling parameters on variations of normalized bubble height: a) effect of nozzle diameter with different air discharges, b) effect of nozzle diameter with different ambient viscosity, c) effect of air discharge with different nozzle diameters, d) a comparison of normalized bubble height and width for nozzle diameter of d_o = 2 mm and ambient viscosity of μ_m/μ_w = 520.

Figure 6.10 shows the effect of ambient viscosity and air discharge on variations of bubble height at the pinch-off, h_p. The normalized bubble height at the pinch-off is compared with the bubble height after the pinch-off, h, to highlight the differences. Figure 6.10a shows the correlation between air discharge and normalized bubble height passing through a mixture with a viscosity ratio of μ_m/μ_w = 580, and Figure 6.10b shows the same correlations passing through a fluid mixture with a smaller apparent viscosity ratio of μ_m/μ_w = 180. The nozzle size in Figure 6.10 is constant

for all tests with a value of d_o = 5 mm. Figure 6.10 shows the impacts of fluid viscosity and air discharge on the difference between bubble height before and after the pinch-off. As can be seen, both bubble heights at the pinch-off and after it follow a linear trend with air discharge, and bubble height at the pinch-off is always higher than that of bubble height after the pinch-off. The nearly parallel linear correlations of the two trends suggest that air discharge affects both variables similarly at a relatively small viscosity ratio. Overall, decreasing the fluid viscosity reduces the disparity between the two trend lines, indicating less complexity in the effects of air discharge and less sensitivity to air discharge variations. As the mixture viscosity ratio increases from 180 to 580, the difference between h_p and h becomes more evident, indicating that the higher ambient viscosity suppresses air bubbles and reduces bubble heights after the pinch-off. Such correlations are independent of air discharge variations. Overall, the height of bubbles in low viscous ambient reduces by 15%, while in the presence of high ambient viscosity, the suppression of bubble height after the pinch-off increases to 28%. Bubble geometry measurements were validated and demonstrated a maximum uncertainty of less than ± 0.2 mm. Moreover, the accuracy was verified through three times repeated conducting experiments, coupled with manual validation checks, and applying robust image analysis.

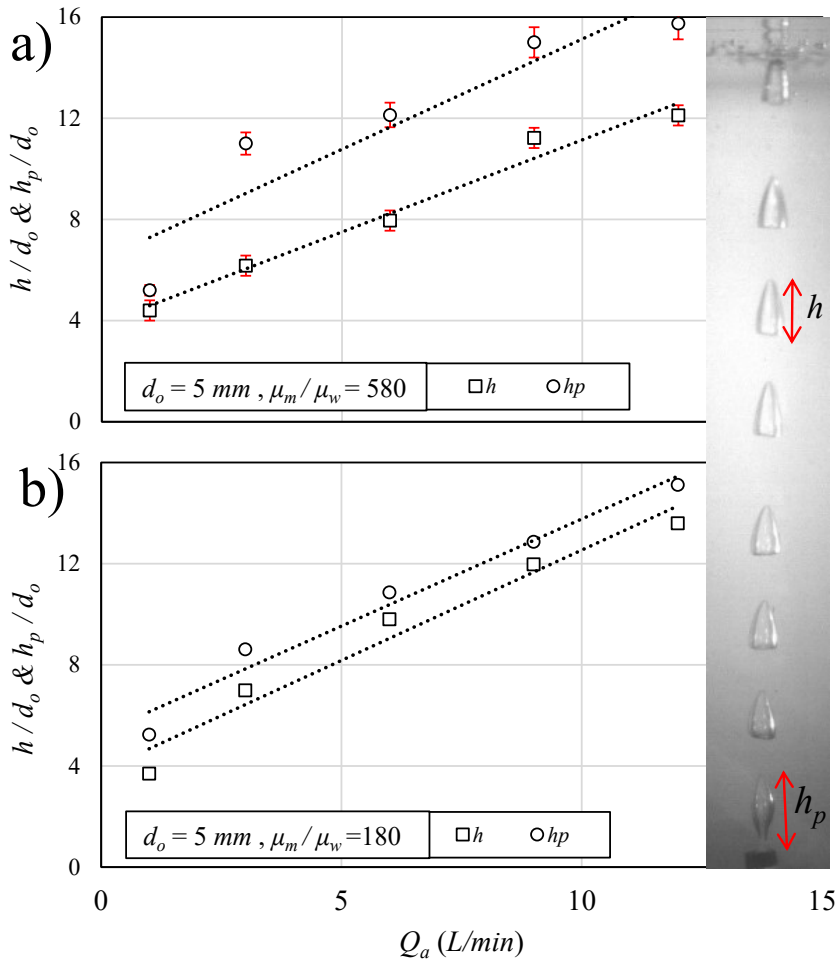

Figure 6.10: Effects of air discharge and ambient viscosity on variations of normalized bubble height, h, and bubble height at the pinch off from the nozzle, h_p: a) μ_m/μ_w = 580 b) μ_m/μ_w = 180. The nozzle diameter is d_o = 5 mm.

6.3.2 Bubble rising velocity

The time variation in bubble velocity is an important factor in evaluating effective mixing and gas exchange rate in bubble columns. Both the instantaneous and the average bubble rising velocities, as each offers distinct insights into the bubble dynamics are calculated. Bubble rising velocity was calculated by tracking the vertical displacement of bubble centroids between consecutive high-speed image frames, divided by the known inter-frame time. The average rising velocity was calculated by tracking the full trajectory of individual bubbles from the moment of their release at the nozzle exit until they reached the liquid surface along the bubble column. This approach captures the overall ascent behavior and complements the time-resolved information

provided by the instantaneous velocity data. Experimental results indicate a relatively sharp change in bubble velocity during the growth of bubbles and a gradual decline in bubble velocity after reaching the peak rising velocity. Several factors affect the peak and time-variant velocity in bubbles such as the initial bubble velocity, ambient fluid properties, nozzle size, and the density difference between the gas (i.e., air) and the ambient fluid. Figure 6.11 illustrates the effect of air discharge on the time history of bubble rising velocity, V_b. The nozzle size and the ambient fluid characteristics were kept constant to d_o = 5 mm and μ_m/μ_w = 580, respectively. The time-variant bubble velocity passing through pure glycerine with a viscosity ratio of μ_m/μ_w = 849 and an orifice diameter of d_o = 10 mm from the study of Lee et al. (2021) was added for comparison. The air discharges in the study by Lee et al. (2021) ranged between Q_a = 0.3 and 1.5 L/min, which are much smaller than the range of air discharge in this study. As can be seen in Figure 11, bubble velocity increases sharply from the release moment and reaches a peak bubble velocity relatively shortly after the release. After the bubble rising velocity reaches its maximum value, the bubble velocity reduces due to the diminishing driving force caused by the progressive equalization of pressure between the initially entrapped air, which expands and loses internal pressure over time, and the surrounding ambient fluid. A comparison between the present data and the results from Lee et al. (2021) indicates that the time history of bubble rising velocities follows the same trend, and air discharge significantly affects the magnitude of bubble rising velocity. However, the peak bubble velocity in Lee et al. (2021) is significantly smaller than that of the peak bubble velocity in the present study due to lower air discharge, which is approximately 10 times smaller.

It is obvious that in the presence of relatively small air discharges, bubbles require more time to reach the surface of the fluid mixture. This is the reason for the elongation of time-variant velocity profiles in relatively low air discharges. Figure 6.11 shows an ascending order in peak rising velocity with air discharge indicating a direct correlation between bubble rising velocity and air discharge. The maximum rising velocity occurs shortly after the pinch-off, followed by a decrease in velocity, observed across all discharges. Approximately 600 milliseconds after the release, bubbles reach the fluid surface with an air discharge of Q_a = 3 L/min and in a fluid mixture with a viscosity of μ_m/μ_w = 580, while the time that it takes for the air discharge of Q_a = 12 L/min is twice. As can be seen in Figure 11, the maximum bubble rising velocity for Q_a = 12 L/min is 2.3 m/s, and for Q_a = 3 L/min is 1.3 m/s. This indicates that the peak bubble rising velocity increases by more than 40% as air discharge increases by four times. Initially, the bubbles rapidly accelerate

upon the pinch-off due to the dominance of buoyancy and initial carrying force over viscous and inertial forces. Immediately following the pinch-off moment, increasing the buoyancy force due to accumulation of air in bubble and the primary momentum due to air flowrate dominate and quickly accelerate the bubble upwards to peak velocity, overcoming initial inertial and viscous resistance. Subsequently, viscous drag overcomes the other acting forces and lead the bubble rising velocity to gradually reduce.

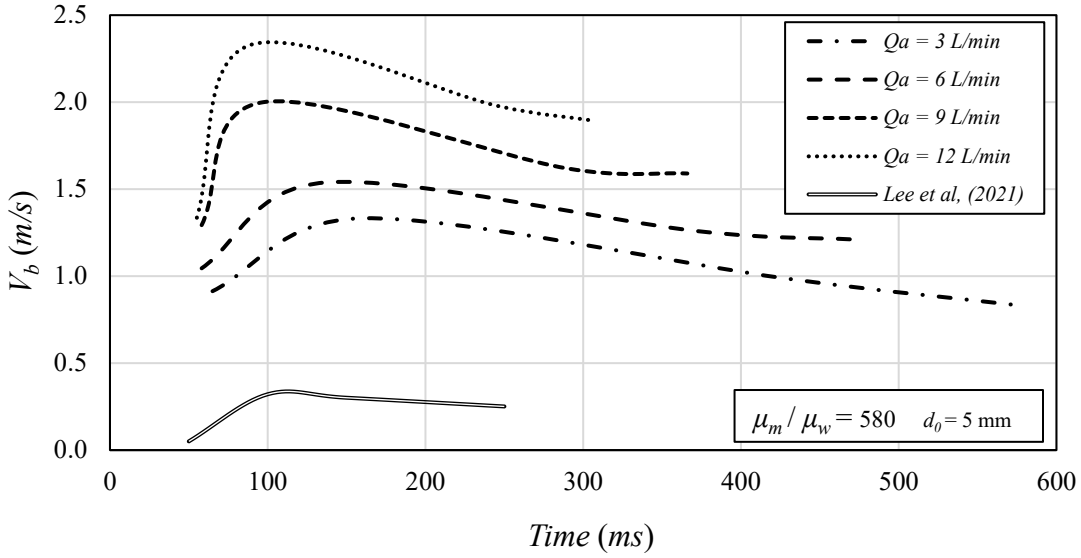

Figure 6.11: Effect of air discharge on the time-history of bubble rising velocity, V_b, in a water mixture with μ_m/μ_w = 580, which is made by the addition of C = 0.30 wt.% PAM. Nozzle diameter is d_o = 5 mm.

Figure 6.12 shows the effect of nozzle diameter in four subplots indicating the variations of the normalized average bubble rising velocity ($V_{b(ave)}/(gd_o)^{1/2}$) with the apparent viscosity of water-polymer mixture. Different data groups in each subplot represent the effect of air discharge on variations of time-averaged bubble rising velocity, $V_{b(ave)}$. Figure 6.12a shows the correlation between mixture viscosity with bubble rising velocity for a bubble plume issuing from a 2-mm nozzle. The average rising velocity increases while the ambient fluid changes from water to a fluid mixture with a fluid viscosity of μ_m/μ_w = 180. Such an increment in the bubble rising velocity is sharp, but the intensity of such augmentation varies over a different range of air discharges. As can be seen, bubble velocity is almost constant, and it is invariant with the mixture viscosity in

relatively small air discharge (i.e., Q_a = 1 L/min). The graph corresponding to the lowest discharge rate, Q_a = 1 L/min, exhibits the lowest fluctuations among the four curves. Conversely, an opposite trend is observed when the mixture's viscosity increases from μ_m/μ_w = 520 to μ_m/μ_w = 580, except in the cases where the nozzle size is d_o = 12.7 mm. However, the average bubble rising velocity increases with increasing mixture viscosity and becomes constant for $\mu_m/\mu_w \geq 180$.

At relatively high ambient viscosity, the rising bubble velocity decreases, and such velocity reduction intensifies with increasing air discharge and nozzle size. The viscous ambient holds up the air and forms larger bubbles, which increases the buoyancy force. As a result of the rising buoyancy force, the rising velocity increases with increasing ambient viscosity. It was observed that higher air discharge also causes a higher bubble rising velocity (see Figure 6.11). As apparent viscosity and yield stress of the ambient fluid mixture increase, the resistance to rising bubbles increases and, at a certain threshold, the resistive viscous force overcomes the active buoyancy force, and such an imbalance reduces the rising velocity of bubbles. This may be the reason for bubble velocity reduction for a fluid mixture with an apparent viscosity ratio of μ_m/μ_w = 580. The reduction in bubble rising velocity is significant in tests with relatively larger air discharges and nozzle diameters (see Figure 6.12d).

For the graphs with a nozzle size of d_o = 12.7 mm and discharge rates of Q_a = 9 and 12 L/min, the maximum bubble rising velocity is observed in the fluid with a viscosity ratio of μ_m/μ_w = 520. As the nozzle size increases in relatively high air discharges (Q_a = 9 and 12 L/min), the active force due to momentum transfer increases the bubble rising velocity and overcomes the resistive viscous force. This can be clearly seen in tests with the largest nozzle size of d_o = 12.7 mm and high air discharges of Q_a = 9 and 12 L/min. The peak bubble rising velocity is now shifted from μ_m/μ_w = 180 to 520. Such a shift indicates that the effects of nozzle size and air discharge surpass the influence of the mixture viscosity and yield stress.

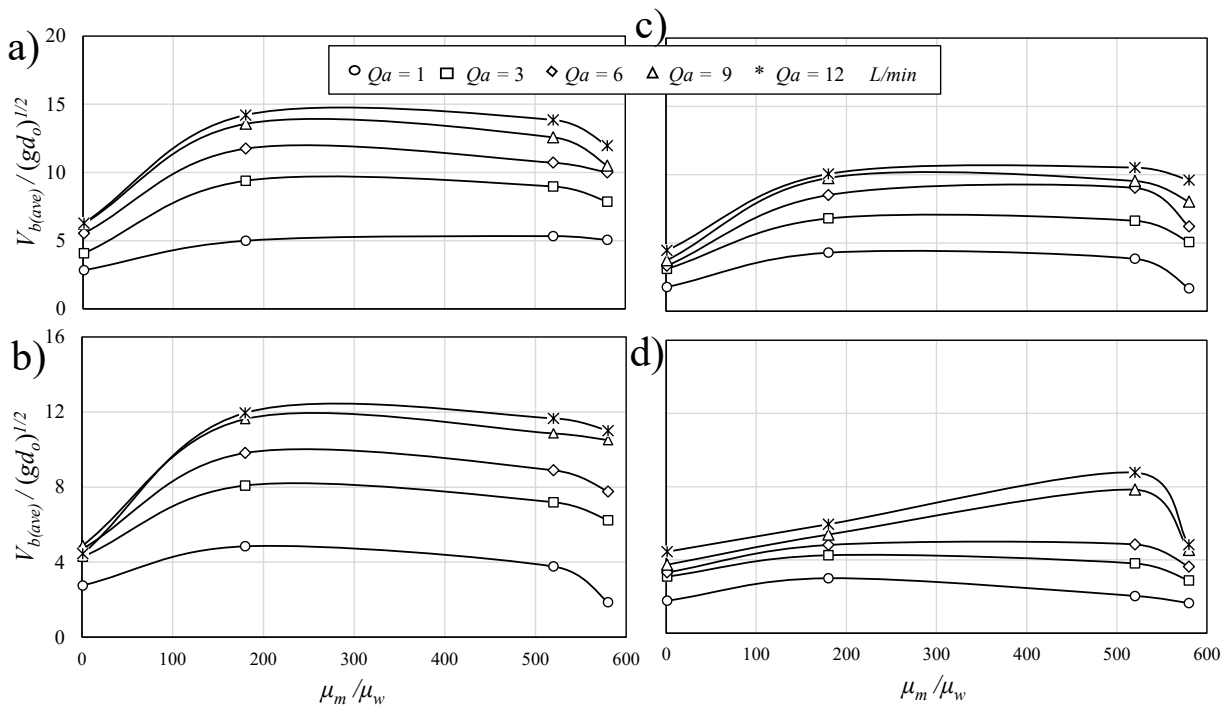

Figure 6.12: Effects of nozzle diameter, ambient viscosity, and air discharge on the average bubble rising velocity: a) d_o = 2 mm, b) d_o = 3 mm, c) d_o = 5 mm, d) d_o = 12.7 mm.

Figure 6.13a represents the variations of normalized mean bubble rising velocity ($V_{b(ave)}/(gd_o)^{1/2}$) with the nozzle size and air discharge for a constant apparent viscosity ratio of μ_m/μ_w = 520. Two experiment sets with air discharges of Q_a = 3 and 6 L/min are plotted in Figure 6.13a. As can be seen, the mean bubble rising velocity is higher in relatively high air discharge, and it reduces almost linearly with nozzle diameter. Regarding the potential influence of nozzle size on bubble rising velocity, increasing the nozzle size leads to two distinct trends. Initially, as the nozzle size increases from 2 mm to 3 mm, the average bubble rising velocity decreases sharply, while the reduction in the mean bubble velocity is mild when the nozzle size changes from 5 to 12.7 mm. Figure 6.13b shows the effect of air discharge on variations of average bubble rising velocity for different nozzle sizes and a constant viscosity ratio of μ_m/μ_w = 180. Three curves are plotted for different nozzle sizes of 2, 3, and 5 mm, which are standing in ascending order in agreement with the nozzle size. As it was shown in Figure 6.11, the normalized bubble rising velocity increases with increasing air discharge, and the correlation follows non-linear trends.

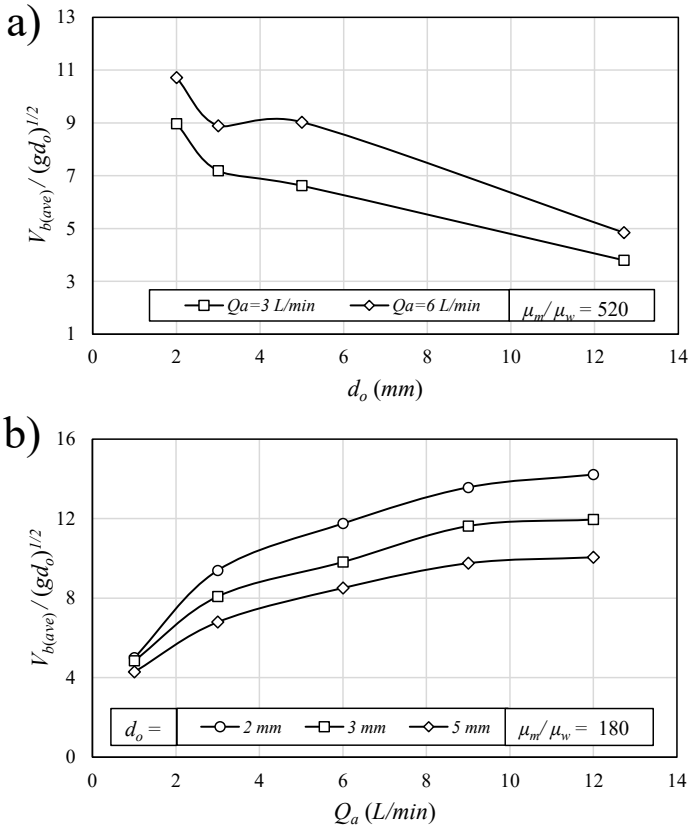

Figure 6.13: Effect of nozzle size and air discharge on variations of bubble rising velocity: a) μ_m/μ_w = 520. and Q_a =3 and 6 L/min, b) μ_m/μ_w = 180, and d_o = 2, 3, and 5 mm.

Figure 6.14 illustrates the effect of ambient viscosity on variations of normalized bubble diameter with average bubble velocity. The present results are compared with the observations of Baz-Rodríguez et al., (2012), Liu et al., (2015), Kure et al., (2021), and Behzadipour et al., (2022). The equivalent bubble diameter was calculated from the minor, a, and major, b, axis of the bubble as:

$$d_b = \sqrt[3]{a^2 \times b} \tag{6.7}$$

As can be seen, the results related to bubble formation in water from the present study follow the experimental results of Behzadipour et al. (2022) having similar air discharge and nozzle sizes to the present study. The results in the study of Liu et al. (2015) exhibited the lowest bubble rising velocities due to relatively higher ambient viscosities of up to 620 mPa·s. In contrast, the current study utilizes significantly higher air discharge (i.e., Q_a = 2–12 L/min) in comparison to previous

studies, leading to higher bubble rising velocities. As can be seen, the outcomes regarding the Baz-Rodríguez et al. (2012) are located at the bottom of the graph and have some overlap with the outcomes of Liu et al., (2015), Kure et al., (2021), and Behzadipour et al., (2022). The common feature among them is the water ambient as the liquid medium. The comparison of their outcomes with the ones in different fluid mixtures with higher viscosity indicates the importance of the fluid properties such as fluid viscosity and yield stress in the average bubble rising velocity.

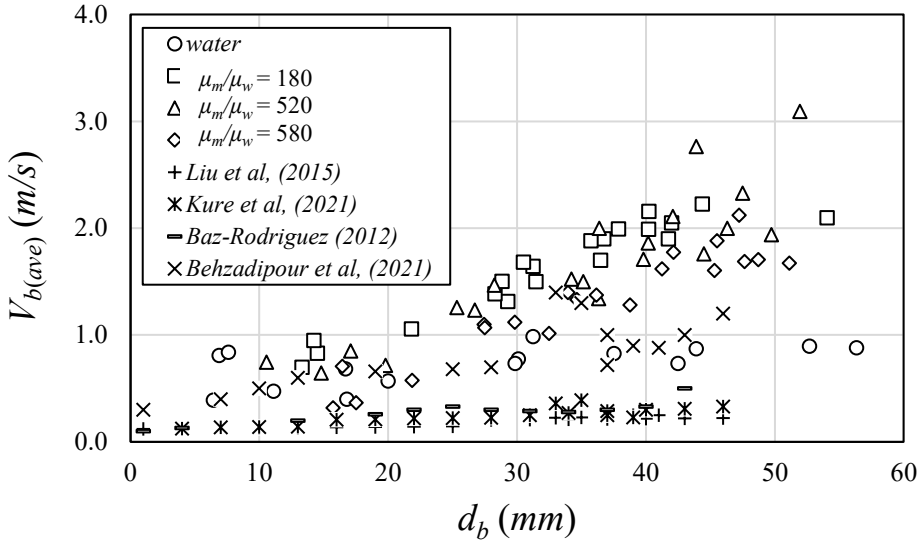

Figure 6.14: Effect of ambient viscosity on variations of normalized equivalent bubble diameter with mean bubble rising velocity.

6.3.4 Bubble Coalescence

Figure 6.15 elucidates the occurrence of bubble coalescence due to the wake effect of bubbles in a relatively viscous fluid mixture with a fluid viscosity ratio of $\mu_m/\mu_w = 580$. The nozzle diameter in Figure 6.15 is $d_o = 2$ mm, and air discharge is $Q_a = 9$ L/min. Four phenomena are identified in this figure which are named as the leading bubble, trailing bubble, conjunction section, and at-end coalescence. A coalescence occurs once the trailing bubble moves at a faster rate and reaches the leading bubble. In such a condition, the trailing bubble collides with the leading bubble, merges, and forms a larger bubble. The bubble coalescence process can be categorized into three stages, each originating from the interaction between the trailing and leading bubbles. In the first stage, the trailing bubble follows the leading bubble. Since the trailing bubble has a higher rising velocity than that of the leading bubble, due to the wake generated by the leading bubble, both bubbles

eventually contact and form one larger bubble. Such coalescence occurs at approximately 150 milliseconds after the release of the second bubble.

As can be seen in Figure 6.15, the velocity of the trailing bubble exponentially grows and reaches the maximum at 1.6 times of the rising velocity of the leading bubble before the collision between the two bubbles occurs. After the collision, the velocity of the trailing bubble decreases in contrast to the velocity of the leading bubble which experienced a slight increment. Approximately 120 milliseconds after the release, coalescence occurs, and the bubbles conjunct completely to form a new bubble with a larger dimension. After the collision stage, coalescence can be claimed to have formed thoroughly. The present results complement the outcomes of the research that was conducted by Feng et al. (2016). They demonstrated that the trends in the increasing and decreasing velocities of the trailing and leading bubbles, as well as their conjunction and coalescence behavior, align with the findings of the current study. However, the rising velocity in their study varied between 0.05 to 0.12 m/s, which was much smaller than the velocity observations in this study.

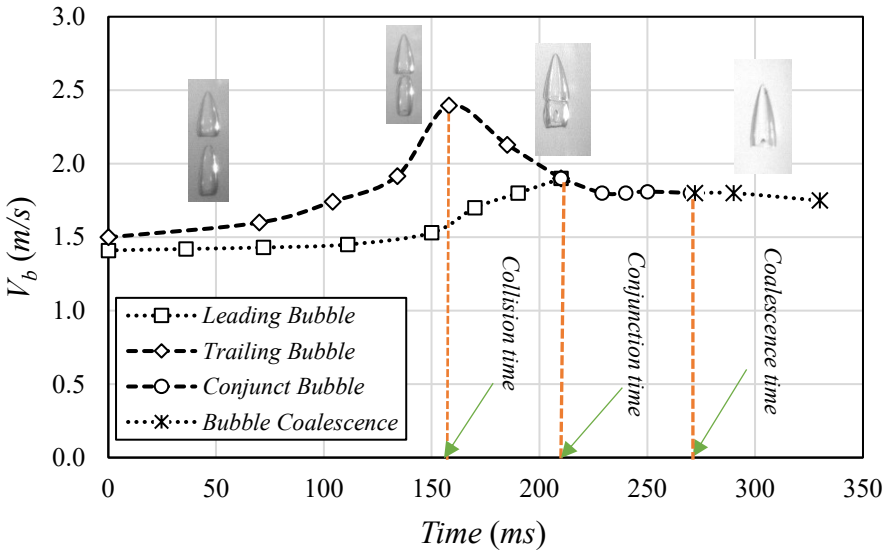

Figure 6.15: The occurrence of bubble coalescence due to wake effect in water-polymer mixture with a viscosity of $\mu_m/\mu_w = 580$ ($C = 0.30$ wt.% PAM). The nozzle diameter is $d_o = 2$ mm, and air discharge is $Q_a = 9$ L/min.

Under the conducted experimental conditions, the bubble chain breakup has not been seen in any Q_a. This is due to the existence of a strong damping force in the high-viscosity non-Newtonian fluid. Therefore, it requires a high flow rate for the occurrence of such a phenomenon. Thence, within the applied flow rate range up to 12 L/min, no such incident was observed. The probability of the occurrence of the bubble coalescence is correlated with different parameters. Figure 6.16 shows the effects of controlling parameters on the Probability Mass Function (PMF). To investigate coalescence under various experimental conditions and parameter values in a stable manner, a fixed time duration of 200 milliseconds was selected. Previous observations confirmed that the selected interval is sufficient for coalescence to occur, ensuring that any coalescence phenomena manifest within the initial 200 milliseconds. After observation of all conducted experiments and monitoring the coalescence occurrence over a relatively longer period, it was found that 200 milliseconds window is completely sufficient to observe the coalescence occurrence for all the cases even for tests with high air flowrates. The Probability Mass Function (PMF) for bubble coalescence quantifies the probability of bubble coalescence within a specified observation window. The values of PMF was determined by counting the number of coalescence occurrences observed through high-speed image sequences over the total number of potential bubble interactions identified within the field of view. The resulting PMFs offer a quantitative likelihood measurement of coalescence occurrences across varying experimental factors.

Figure 6.16a shows the effect of air discharge on variations of the Probability Mass Function (PMF) of coalescence occurrence at different frequencies. From this figure, it is evident that at an air discharge of Q_a = 1 L/min, bubble coalescence rarely occurs. The maximum coalescence occurrence is observed at a flow rate of 12 L/min, particularly for a fluid viscosity of μ_m/μ_w = 180. At intermediate range of air discharge (i.e., Q_a = 3 and 6 L/min), there is a reduced likelihood of zero coalescence, coupled with an elevated probability of one or two coalescence events per observation. At relatively higher air discharges (i.e., Q_a = 9 and 12 L/min), the distribution in frequency of coalescence shifts again, exhibiting notable contributions at both none (i.e., zero) and two coalescence events. The bubble coalescence occurs four times only at air discharge of 6, 9, and 12 L/min, but its occurrence is not frequent. It also represents that increasing air discharge increments the probability of bubble coalescence occurrence.

Figure 6.16b shows the effect of nozzle diameter on variations of PMF coalescence occurrence. The highest coalescence occurrence is visible for the smallest nozzle diameter (i.e., d_o = 2 mm). Figure 16c shows the effect of ambient viscosity on variations of PMF coalescence occurrence. Overall, the likelihood of bubble coalescence decreases as fluid viscosity increases. Higher ambient viscosity dampens the motion of bubbles and reduces the probability of bubble collisions. Additionally, the probability of bubbles maintaining their integrity without coalescence remains high in bubbles passing through highly viscous ambient fluids. It was seen that for the fluid with the fluid viscosity ratio of μ_m/μ_w = 580 and nozzle size of d_o = 2 mm, the coalescence happens over all range of air discharge. However, while the nozzle size increases to d_o = 12 mm, the coalescence does not occur at low air discharges. When the ambient viscosity of the fluid reduces to μ_m/μ_w = 180, the coalescence occurs in almost all experiments except in the lowest air discharge of Q_a = 2 L/min.

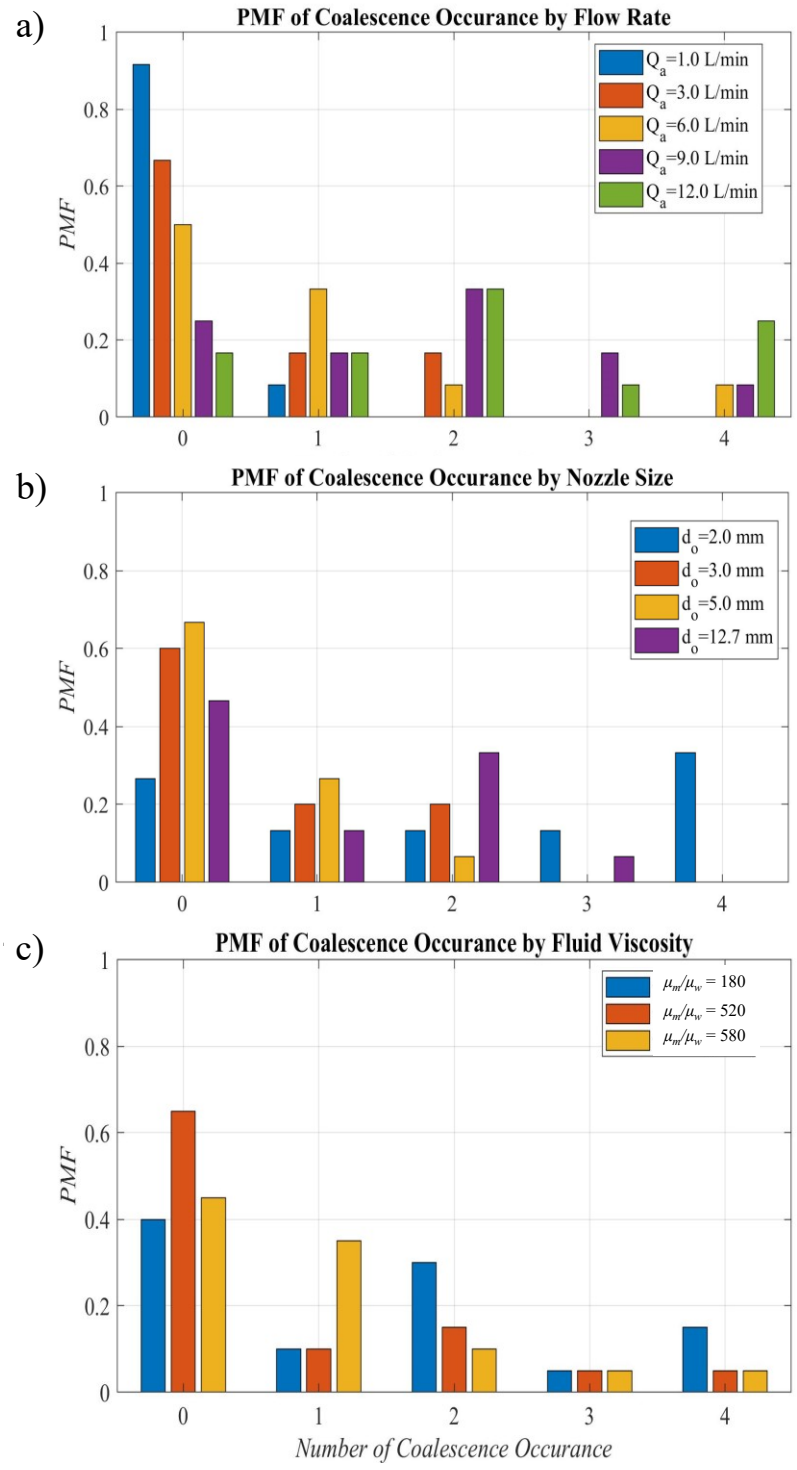

Figure 6.16: Effects of controlling parameters on the Probability Mass Function (PMF) of coalescence occurrence: a) effect of nozzle diameter, b) effect of air discharge, c) effect of ambient viscosity.

6.5 Conclusions

A series of laboratory experiments was carried out to investigate the effects of controlling parameters such nozzle size, and air discharge on bubble dynamics in non-Newtonian ambient with different rheological characteristics. Since the selected non-Newtonian fluid mixtures are shear thinning with yield stress, it is not possible to combine the values of air discharge, nozzle diameter, and apparent viscosity into a Reynolds number. Therefore, the effects of controlling parameters were shown in different subplots and data groups. Bubble dimensions and aspect ratios varied with both air discharge and nozzle size. Experimental results indicated that increasing air discharge from 1 to 12 L/min increased the bubble width ratio by approximately 50%. The normalized bubble height ranged between 1 and 6 in relatively low air discharge and it ranged between 5 and 37 in relatively large air discharge of 12 L/min. It can be concluded that for the same nozzle size and air discharge, bubbles became shorter and wider while passing through a fluid with higher viscosity.

The findings demonstrated that bubble height at the pinch-off was always higher than that of bubble height after the pinch-off. The nearly parallel linear correlations of the two trends indicated that air discharge affected both variables similarly at a relatively small viscosity ratio. Overall, the height of bubbles in low viscous ambient was reduced by 15%, while in the presence of high ambient viscosity, the suppression of bubble height after the pinch-off increased to 28%.

The bubble rising velocity had a direct correlation with the air discharge and the peak bubble rising velocity increased by more than 40% as the air discharge increased by four times. The viscous ambient holds up the air and forms larger bubbles, which increases the buoyancy force. As a result of rising buoyancy force, the rising velocity increased with increasing ambient viscosity. Four phenomena of leading bubble, trailing bubble, conjunction section, and end-of-coalescence were identified. Experimental results indicated that the velocity of the trailing bubble exponentially grew and reached a maximum value of 1.6 times of the rising velocity of the leading bubble before the collision.

The probability of the occurrence of bubble coalescence was quantified by Probability Mass Function (PMF). It was found that the maximum frequency of coalescence occurred at the maximum air discharge for a fluid viscosity of μ_m/μ_w = 180. The likelihood of zero coalescence reduced at the intermediate range of air discharge (i.e., Q_a = 3 and 6 L/min), and the probability of one or two coalescence events per observation increased in such a range of air discharge. In

addition, the highest coalescence occurrence was found in the smallest nozzle diameter and when the ambient fluid viscosity increases.

Chapter 7

7.1 Recommendation for future research

The investigations presented in this dissertation have established a systematic framework for understanding fluid-entry dynamics of rigid disks in Newtonian and non-Newtonian media. While the present work has clarified the roles of Froude number, rheological parameters, and geometric configuration on cavity formation, pinch-off, bubble-plume development, and energy dissipation, several fundamental and application-oriented questions remain open. The following research directions extend the findings of this thesis toward a unified predictive theory of impact in complex fluids and toward practical engineering applications in marine, environmental, and industrial systems.

Future work should therefore seek to incorporate rheological parameters such as the power-law index and consistency coefficient directly into generalized impact groups alongside classical inertial scaling parameters. Such a framework would allow the construction of a single regime map spanning Newtonian and shear-thinning fluids, clarifying whether impact dynamics transition smoothly between rheological classes or whether distinct scaling regimes emerge. The scientific outcome of such work would be a predictive map for cavity evolution and energy partitioning in complex fluids. This has direct relevance to marine impact in biologically active waters, to offshore structures operating in polymer-contaminated or cold environments, and to industrial systems involving slurries or shear-thinning suspensions.

While the present thesis focused on axisymmetric impacts, many natural and industrial events occur at oblique angles. Future investigations into tilted-disk entry would clarify how symmetry breaking interacts with rheology to produce skewed cavities, asymmetric side-jetting, or splash-dominated regimes. Shear-thinning fluids may damp lateral instabilities and suppress side-jet formation beyond a critical angle, leading to fundamentally different stability maps compared to Newtonian fluids. Establishing such stability diagrams would be valuable for predicting slamming loads on marine panels, understanding debris entry into natural waters, and optimizing impact angles in industrial processes where splash reduction is critical.

The annular disk results presented in this dissertation suggest that controlled ventilation significantly modifies cavity formation and energy loss. A systematic exploration of porosity, plate thickness, and edge geometry would allow the construction of a performance-based design map linking geometric parameters to cavity depth and dissipation characteristics. It is plausible that families of geometries exist that achieve equivalent cavity penetration at lower energy loss through regulated annular flow. Such findings would have immediate implications for splash suppression devices, perforated marine components, and engineered impact plates used in fluid–structure interaction systems.

Post-impact bubble plume development in shear-thinning media also warrants deeper investigation. The present results indicate that rheology alters plume morphology, but the entrainment coefficient and bubble size distributions remain insufficiently quantified. Extending plume measurements to extract rise velocity, half-width growth, and bubble size probability distributions would enable modification of classical integral plume models to include viscosity-dependent effects. A refined plume model applicable to shear-thinning fluids would be highly relevant for aeration in wastewater treatment reactors, gas dispersion in polymer-processing tanks, and environmental studies of gas entrainment following surface disturbances.

The energy-loss analysis conducted in this thesis can be expanded into a fully resolved impact energy budget. Decomposing total energy dissipation into splash kinetic energy, cavity formation work, viscous dissipation, and added-mass contributions would clarify how rheology redistributes losses over time. Preliminary observations suggest that non-Newtonian fluids may concentrate dissipation in early high-shear phases, with added-mass effects dominating later stages. A time-resolved energy framework would provide valuable insight for offshore structure design, impact mitigation materials, and slurry-based industrial processes where energy efficiency is critical.

Surface chemistry and micro-roughness effects represent another dimension not isolated in the current work. Since wettability influences air entrainment and cavity inception, systematic variation of surface coatings and controlled roughness would reveal whether cavity formation thresholds shift with contact angle. Superhydrophobic or textured surfaces may raise the critical Froude number required for coherent cavity formation or alter pinch-off pathways. Such findings would be applicable to anti-splash coatings, marine hull treatments, and protective tank linings in chemical processing industries.

Direct measurement of impact loads is another natural extension. While cavity behavior was characterized in detail, embedded pressure sensing would allow correlation between peak pressure, impulse duration, and rheological effects. Shear-thinning fluids may reduce peak pressure but extend impulse duration, offering potential strategies for load mitigation. Such results would have direct implications for offshore structural design and slamming analysis.

Further investigation into pinch-off singularity behavior in non-Newtonian fluids would address fundamental fluid-mechanics questions. Shear-thinning rheology may alter the near-singularity exponent and suppress satellite bubble formation, potentially modifying universal scaling laws derived for Newtonian fluids. Clarifying whether universality persists or breaks down in complex fluids would contribute to the broader understanding of nonlinear free-surface dynamics.

In summary, the research directions proposed in this chapter extend the present dissertation from controlled laboratory observations toward a comprehensive predictive framework for impact in complex fluids. By integrating rheology, geometry, surface chemistry, compliance, stratification, and data-driven modeling, future work can bridge fundamental fluid mechanics with practical marine and industrial applications. The goal is the development of a unified, physics-informed understanding of water-entry dynamics applicable across a wide range of real-world systems.

REFERENCES

Abdulmouti, H., 2022. Bubbly Two-Phase Flow: III-Applications. American Journal of Fluid Dynamics 2022, 16–119. https://doi.org/10.5923/j.ajfd.20221201.02

Akbarzadeh, P., Krieger, M., Hofer, D., Thumfart, M., Gittler, P., 2023. Parallel water entry: Experimental investigations of hydrophobic/hydrophilic spheres. Physics of Fluids 35. https://doi.org/10.1063/5.0167494

Akbarzadeh, P., Norouzi, M., Ghasemi, R., Daghighi, S.Z., 2022. Experimental study on the entry of solid spheres into Newtonian and non-Newtonian fluids. Physics of Fluids 34. https://doi.org/10.1063/5.0081002

Akers, B., Belmonte, A., 2006. Impact dynamics of a solid sphere falling into a viscoelastic micellar fluid. J Nonnewton Fluid Mech 135, 97–108. https://doi.org/10.1016/j.jnnfm.2006.01.004

Alharbi, A.F., Alhawiti, M., Usman, M., Ullah, I., Alam, M.M., Bilal, M., 2024. Enhancement of heat transfer in thin-film flow of a hybrid nanofluid over an inclined rotating disk subject to thermal radiation and viscous dissipation. Int J Heat Fluid Flow 107. https://doi.org/10.1016/j.ijheatfluidflow.2024.109360

Alif, M.E., Husain, A., Quizhpe, C., Maynor, E., Dickerson, A.K., 2023. Water entry of spheres with impact-axis channels. Physics of Fluids 35. https://doi.org/10.1063/5.0175406

Aoyama, S., Hayashi, K., Hosokawa, S., Lucas, D., Tomiyama, A., 2017. Lift force acting on single bubbles in linear shear flows. International Journal of Multiphase Flow 96, 113–122. https://doi.org/10.1016/j.ijmultiphaseflow.2017.07.003

Aparece-Scutariu, V., Shin, D. hyuk, 2022. Spatial characteristics and modelling of mixture fraction variance and scalar dissipation rate in steady turbulent round jets. Int J Heat Fluid Flow 98. https://doi.org/10.1016/j.ijheatfluidflow.2022.109048

Arigo, M.T., McKinley, G.H., 1997. The effects of viscoelasticity on the transient motion of a sphere in a shear-thinning fluid. J Rheol (N Y N Y) 41, 103–128. https://doi.org/10.1122/1.550803

Aristoff, J.M., Bush, J.W.M., 2009. Water entry of small hydrophobic spheres. J Fluid Mech 619, 45–78. https://doi.org/10.1017/S0022112008004382

Aristoff, J.M., Truscott, T.T., Techet, A.H., Bush, J.W.M., 2010. The water entry of decelerating spheres. Physics of Fluids 22, 1–8. https://doi.org/10.1063/1.3309454

Auguste, F., Magnaudet, J., Fabre, D., 2013. Falling styles of disks. J Fluid Mech 719, 388–405. https://doi.org/10.1017/jfm.2012.602

Barozzi, G.S., Dumas, A., Collins, M.W., 1984. Sharp entry and transition effects for laminar combined convection of water in vertical tubes. Int J Heat Fluid Flow 5, 235–241. https://doi.org/https://doi.org/10.1016/0142-727X(84)90060-2

Baz-Rodríguez, S., Aguilar-Corona, A., Soria, A., 2012. Rising velocity for single bubbles in pure liquids. Rev Mex Ing Quim 11, 269–278.

Behzadipour, A., Azimi, A.H., Lima Neto, I.E., 2022a. Effect of grid-screen on bubble characteristics of vertically discharged bubble plumes. Chem Eng Sci 253. https://doi.org/10.1016/j.ces.2022.117545

Behzadipour, A., Azimi, A.H., Lima Neto, I.E., 2022b. Effect of grid-screen on bubble characteristics of vertically discharged bubble plumes. Chem Eng Sci 253. https://doi.org/10.1016/j.ces.2022.117545

Behzadipour, A., Azimi, A.H., Neto, I.E.L., 2023a. Effects of air discharge on bubble dynamics in vertically discharged bubble plumes. Chem Eng Sci 268. https://doi.org/10.1016/j.ces.2022.118440

Behzadipour, A., Azimi, A.H., Neto, I.E.L., 2023b. Effects of air discharge on bubble dynamics in vertically discharged bubble plumes. Chem Eng Sci 268. https://doi.org/10.1016/j.ces.2022.118440

Belden, J., Speirs, N.B., Hellum, A.M., Jones, M., Paolero, A.J., Truscott, T.T., 2023. Water entry of cups and disks. J Fluid Mech 963. https://doi.org/10.1017/jfm.2023.330

Bergmann, R., van der Meer, D., Gekle, S., van der Bos, A., Lohse, D., 2009. Controlled impact of a disk on a water surface: Cavity dynamics. J Fluid Mech 633, 381–409. https://doi.org/10.1017/S0022112009006983

Besagni, G., Brazzale, P., Fiocca, A., Inzoli, F., 2016. Estimation of bubble size distributions and shapes in two-phase bubble column using image analysis and optical probes. Flow Measurement and Instrumentation 52, 190–207. https://doi.org/10.1016/j.flowmeasinst.2016.10.008

Besagni, G., Deen, N.G., 2020. Aspect ratio of bubbles in different liquid media: A novel correlation. Chem Eng Sci 215. https://doi.org/10.1016/j.ces.2019.115383

Besagni, G., Inzoli, F., 2017. The effect of liquid phase properties on bubble column fluid dynamics: Gas holdup, flow regime transition, bubble size distributions and shapes, interfacial areas and foaming phenomena. Chem Eng Sci 170, 270–296. https://doi.org/10.1016/j.ces.2017.03.043

Bi, D., Wei, Y., Theunissen, R., Xu, H., 2021. Study on the flow structure behind a freely falling annular disk using proper orthogonal decomposition. European Journal of Mechanics, B/Fluids 85, 90–101. https://doi.org/10.1016/j.euromechflu.2020.09.005

Bi, D.F., Wei, Y.J., Wang, C., Xu, H., 2018. Experimental study on the vortex structure and path instability of freely falling annular disks. Sci China Technol Sci 61, 853–866. https://doi.org/10.1007/s11431-017-9218-4

Bleier, R., 1990. Selecting a Drilling Fluid. Journal of Petroleum Technology 42, 832–834. https://doi.org/10.2118/20986-PA

Bodily, K.G., Carlson, S.J., Truscott, T.T., 2014. The water entry of slender axisymmetric bodies. Physics of Fluids 26. https://doi.org/10.1063/1.4890832

Bohne, T., Grießmann, T., Rolfes, R., 2020. Development of an efficient buoyant jet integral model of a bubble plume coupled with a population dynamics model for bubble breakup and coalescence to predict the transmission loss of a bubble curtain. International Journal of Multiphase Flow 132. https://doi.org/10.1016/j.ijmultiphaseflow.2020.103436

Bokman, G.T., Supponen, O., Mäkiharju, S.A., 2022. Cavitation bubble dynamics in a shear-thickening fluid. Phys Rev Fluids 7. https://doi.org/10.1103/PhysRevFluids.7.023302

Bombardelli, F.A., Buscaglia, G.C., Rehmann, C.R., Rincón, L.E., García, M.H., 2007. Modeling and scaling of aeration bubble plumes: A two-phase flow analysis. Journal of Hydraulic Research 45, 617–630. https://doi.org/10.1080/00221686.2007.9521798

Bryant, D.B., Seol, D.G., Socolofsky, S.A., 2009. Quantification of turbulence properties in bubble plumes using vortex identification methods. Physics of Fluids 21. https://doi.org/10.1063/1.3176464

Cachaza, E.M., Elena Díaz, M., Montes, F.J., Galán, M.A., 2011. Unified study of flow regimes and gas holdup in the presence of positive and negative surfactants in a non-uniformly aerated bubble column. Chem Eng Sci 66, 4047–4058. https://doi.org/10.1016/j.ces.2011.05.036

Cao, J., Sun, Q., Zhao, D., Xu, M., Shen, Q., Wang, D., Wang, Y., Ding, S., 2020. A critical review of the appearance of black-odorous waterbodies in China and treatment methods. J Hazard Mater. https://doi.org/10.1016/j.jhazmat.2019.121511

Chaudhry, A.Z., Shi, Y., Pan, G., 2022. Recent developments on the water entry impact of wedges and projectiles. Ships and Offshore Structures. https://doi.org/10.1080/17445302.2020.1835053

Chen, B., Zhou, S., Zhang, N., Liang, H., Sun, L., Zhao, X., Guo, J., Lu, H., 2022. Micro and nano bubbles promoted biofilm formation with strengthen of COD and TN removal synchronously in a blackened and odorous water. Science of the Total Environment 837. https://doi.org/10.1016/j.scitotenv.2022.155578

Cheny, J.-M., Walters, K., 1999. Rheological influences on the splashing experiment.

Cheny, J.M., Walters, K., 1996. Extravagant viscoelastic effects in the Worthington jet experiment 1, J. Non-Newtonian Fluid Mech.

Choi, K., Kim, S., Kim, H., Kim, C., 2023. Computational investigation on the non-isothermal phase change during cavitation bubble pulsations. Ocean Engineering 285. https://doi.org/10.1016/j.oceaneng.2023.115414

Clift, R., Grace, J.R., Weber, M.E., 2013. Bubbles, drops, and particles.

Cointe, R., Fontaine, E., Molin, B., Scolan, Y.M., 2004. On energy arguments applied to the hydrodynamic impact force, Journal of Engineering Mathematics.

Crowe, C.T., 2012. Multiphase flows with droplets and particles. CRC Press.

de Goede, T.C., de Bruin, K.G., Bonn, D., 2019. High-velocity impact of solid objects on Non-Newtonian Fluids. Sci Rep 9. https://doi.org/10.1038/s41598-018-37543-1

Dijkhuizen, W., van Sint Annaland, M., Kuipers, J.A.M., 2010. Numerical and experimental investigation of the lift force on single bubbles. Chem Eng Sci 65, 1274–1287. https://doi.org/10.1016/j.ces.2009.09.084

Dissanayake, A.L., Gros, J., Socolofsky, S.A., 2018. Integral models for bubble, droplet, and multiphase plume dynamics in stratification and crossflow. Environmental Fluid Mechanics 18, 1167–1202. https://doi.org/10.1007/s10652-018-9591-y

Du, Y., Wang, Z., Wang, Y., Wang, J., Qiu, R., Huang, C., 2022. Study on the cavity dynamics of water entry for horizontal objects with different geometrical shapes. Ocean Engineering 252. https://doi.org/10.1016/j.oceaneng.2022.111242

Duan, W., Shi, Z., Jiang, Z., Li, H., Huang, L., 2022. Experimental and numerical investigation of bubble evolution and bubble wall fluctuation mechanism during water entry of flared cavity. Ocean Engineering 266. https://doi.org/10.1016/j.oceaneng.2022.113030

Duclaux, V., Caillé, F., Duez, C., Ybert, C., Bocquet, L., Clanet, C., 2007. Dynamics of transient cavities. J Fluid Mech 591, 1–19. https://doi.org/10.1017/S0022112007007343

Ebrahimi, M., Azimi, A.H., 2025a. Cavity dynamics by the entry of annular disks into non-Newtonian ambient. Ocean Engineering 321, 120379. https://doi.org/10.1016/j.oceaneng.2025.120379

Ebrahimi, M., Azimi, A.H., 2025b. Energy losses due to entry of disks into water and viscous fluid mixtures. Int J Heat Fluid Flow 109943. https://doi.org/10.1016/j.ijheatfluidflow.2025.109943

Ebrahimi, M., Azimi, A.H., 2024. On the entry of cylindrical disks into non-Newtonian fluid mixtures. Physics of Fluids 36. https://doi.org/10.1063/5.0224156

Ebrahimi, M.A., Ahmadi, M., Ameri, M.J., 2020. Application of unconditional simulation methods for quantifying the uncertainties in mud window design of gas reservoirs based on 3-dimensional mechanical earth modeling. J Nat Gas Sci Eng 76. https://doi.org/10.1016/j.jngse.2020.103186

Ebrahimi, M.A., Ameri, M.J., Ahmadi, M., 2021. Application of Stochastic Method for Geomechanical Parameters under Uncertainty Quantification to Design Mud Window, in: 82nd EAGE Annual Conference & Exhibition. European Association of Geoscientists & Engineers, pp. 1–5. https://doi.org/10.3997/2214-4609.202010425

Ebrahimi, M.A., Sanati, A., 2021. On the potential of Alyssum as an herbal fiber to improve the filtration and rheological characteristics of water-based drilling muds. Petroleum. https://doi.org/10.1016/j.petlm.2021.04.005

Eshraghi, J., Jung, S., Vlachos, P.P., 2020. To seal or not to seal: The closure dynamics of a splash curtain. Phys Rev Fluids 5. https://doi.org/10.1103/PhysRevFluids.5.104001

Faltinsen, O.M., Landrini, M., Greco, M., 2004. Slamming in marine applications, Journal of Engineering Mathematics.

Feng, J., Li, X., Bao, Y., Cai, Z., Gao, Z., 2016a. Coalescence and conjunction of two in-line bubbles at low Reynolds numbers. Chem Eng Sci 141, 261–270. https://doi.org/10.1016/j.ces.2015.11.014

Feng, J., Li, X., Bao, Y., Cai, Z., Gao, Z., 2016b. Coalescence and conjunction of two in-line bubbles at low Reynolds numbers. Chem Eng Sci 141, 261–270. https://doi.org/10.1016/j.ces.2015.11.014

Feng, J., Li, X., Bao, Y., Cai, Z., Gao, Z., Evans, G.M., 2016c. Behaviour and dynamics of two bubbles in conjunct condition in high-viscosity liquids. Canadian Journal of Chemical Engineering 94, 1583–1591. https://doi.org/10.1002/cjce.22527

Feng, S., Mingzhen, W., Jiaxu, Z., Qi, H., 2020. Numerical Simulation Method for Wave Surface Landing of Seaplane, in: IOP Conference Series: Materials Science and Engineering. Institute of Physics Publishing. https://doi.org/10.1088/1757-899X/751/1/012061

Feng, X., Zhang, B., 2023. Applications of bubble curtains in marine oil spill containment: Hydrodynamic characteristics, applications, and future perspectives. Mar Pollut Bull 194. https://doi.org/10.1016/j.marpolbul.2023.115371

Fingas, M., 2010. Oil spill science and technology. Gulf professional publishing.

Fraga, B., Stoesser, T., 2016. Influence of bubble size, diffuser width, and flow rate on the integral behavior of bubble plumes. J Geophys Res Oceans 121, 3887–3904. https://doi.org/10.1002/2015JC011381

Gao, C., 2013a. Viscosity of partially hydrolyzed polyacrylamide under shearing and heat. J Pet Explor Prod Technol 3, 203–206. https://doi.org/10.1007/s13202-013-0051-4

Gao, C., 2013b. Viscosity of partially hydrolyzed polyacrylamide under shearing and heat. J Pet Explor Prod Technol 3, 203–206. https://doi.org/10.1007/s13202-013-0051-4

Gao, D., Li, X., Hou, B., Lu, F., Ye, M., Wang, A., Wang, X., 2022. Study of bubble behavior in high-viscosity liquid in a pseudo-2D column using high-speed imaging. Chem Eng Sci 252. https://doi.org/10.1016/j.ces.2022.117532

Gaudet, S., 1998. Numerical simulation of circular disks entering the free surface of a fluid. Physics of Fluids 10, 2489–2499.

Glasheen, J.W., McMahon, T.A., 1996. Vertical water entry of disks at low Froude numbers. Physics of Fluids 8, 2078–2083. https://doi.org/10.1063/1.869010

Gordillo, J.M., Gekle, S., 2010. Generation and breakup of Worthington jets after cavity collapse. Part 2. Tip breakup of stretched jets. J Fluid Mech 663, 331–346. https://doi.org/10.1017/S0022112010003538

Grace, J.R., 1973. Shapes and velocities of bubbles rising in infinite liquids. Trans. Inst. Chem. Eng. 54, 116–120.

Guillet, T., Mouchet, M., Belayachi, J., Fay, S., Colturi, D., Lundstam, P., Hosoi, P., Clanet, C., Cohen, C., 2020. The Hydrodynamics of High Diving. MDPI AG, p. 73. https://doi.org/10.3390/proceedings2020049073

Guleria, S.D., Dhar, A., Patil, D. V., 2021. Experimental insights on the water entry of hydrophobic sphere. Physics of Fluids 33. https://doi.org/10.1063/5.0063040

Guo, Z., Zhang, W., Xiao, X., Wei, G., Ren, P., 2012. An investigation into horizontal water entry behaviors of projectiles with different nose shapes. Int J Impact Eng 49, 43–60. https://doi.org/10.1016/j.ijimpeng.2012.04.004

Guo, Z.T., Zhang, W., Wang, C., 2012. Experimental and theoretical study on the high-speed horizontal water entry behaviors of cylindrical projectiles. Journal of Hydrodynamics 24, 217–225. https://doi.org/10.1016/S1001-6058(11)60237-0

Gupta, D.V.S., Leshchyshyn, T.T., Hlidek, B.T., 2005. SPE 97211 Surfactant Gel Foam/Emulsions: History and Field Application in the Western Canadian Sedimentary Basin.

Han, Y., Dong, J. yu, Li, R. xin, Wu, Y. yuan, Ji, M. lei, 2024. Numerical simulation of bubble wakes with mixed scales of underwater vehicles. Ocean Engineering 314. https://doi.org/10.1016/j.oceaneng.2024.119746

Hemphill, T., Campos, W., Pilehvari, A., 1993. Yield-power law model more accurately predicts mud rheology 91:34.

Hou, Y., Huang, Z., Chen, Z., Guo, Z., Han, L., 2021. Different closure patterns of the hollow cylinder cavities with various water-entry velocities. Ocean Engineering 221. https://doi.org/10.1016/j.oceaneng.2020.108526

Hou, Y., Huang, Z., Chen, Z., Guo, Z., Luo, Y., 2019. Investigations on the vertical water-entry of a hollow cylinder with deep-closure pattern. Ocean Engineering 190. https://doi.org/10.1016/j.oceaneng.2019.106426

Hou, Y., Huang, Z., Chen, Z., Guo, Z., Xu, Y., 2022. Experimental investigations on the oblique water entry of hollow cylinders. Ocean Engineering 266. https://doi.org/10.1016/j.oceaneng.2022.112800

Hu, Z., Haruna, M., Gao, H., Nourafkan, E., Wen, D., 2017. Rheological Properties of Partially Hydrolyzed Polyacrylamide Seeded by Nanoparticles. Ind Eng Chem Res 56, 3456–3463. https://doi.org/10.1021/acs.iecr.6b05036

Huang, Z., Hou, Y., Cai, X., Chen, Z., Xu, Y., Qin, J., 2024. Effects of entry angle on the water-entry cavity and motion hydrodynamics of a hollow cylinder. Physics of Fluids 36. https://doi.org/10.1063/5.0220325

Islam, A., Mahmood, Z., Khan, U., Muhammad, T., Aich, W., Eladeb, A., Kolsi, L., 2024. Lie scaling transformations for the analysis of MHD flow with radiation, Soret, and Dufour effects as well as viscous dissipation across a convective surface during triple diffusion. Int J Heat Fluid Flow 108. https://doi.org/10.1016/j.ijheatfluidflow.2024.109465

Jafari, M.A., Akbarzadeh, P., 2022. Experimental analysis of water entry problem considering hollow cylinders: The impact of hole geometry. Ocean Engineering 259. https://doi.org/10.1016/j.oceaneng.2022.111906

Janati, M., Azimi, A.H., 2023. On the crown formation and cavity dynamics of free-falling thick disks. Physics of Fluids 35. https://doi.org/10.1063/5.0126864

Janati, M., Hossein Azimi, A., 2022. Effects of impact energy on the crown formation and underwater cavity of free-falling thick disks. https://doi.org/10.21203/rs.3.rs-2076858/v1

Jiang, X.F., Zhu, C., Li, H.Z., 2017. Bubble pinch-off in Newtonian and non-Newtonian fluids. Chem Eng Sci 170, 98–104. https://doi.org/10.1016/j.ces.2016.12.057

Jirka, G.H., 2004. Integral Model for Turbulent Buoyant Jets in Unbounded Stratified Flows. Part I: Single Round Jet, Environmental Fluid Mechanics.

Jung, J.C., Zhang, K., Chon, B.H., Choi, H.J., 2013. Rheology and polymer flooding characteristics of partially hydrolyzed polyacrylamide for enhanced heavy oil recovery. J Appl Polym Sci 127, 4833–4839. https://doi.org/10.1002/app.38070

Kapsenberg, G.K., 2011. Slamming of ships: Where are we now? Philosophical Transactions of the Royal Society A: Mathematical, Physical and Engineering Sciences. https://doi.org/10.1098/rsta.2011.0118

Khabakhpasheva, T.I., Korobkin, A.A., Malenica, S., 2024. Water entry of an elastic conical shell. J Fluid Mech 980. https://doi.org/10.1017/jfm.2024.17

Kim, N., Park, H., 2019. Water entry of rounded cylindrical bodies with different aspect ratios and surface conditions. J Fluid Mech 863, 757–788. https://doi.org/10.1017/jfm.2018.1026

Kim, T., Chang, J., Kim, D., 2018. Free-fall dynamics of a pair of rigidly linked disks. Physics of Fluids 30. https://doi.org/10.1063/1.5023792

Korkmaz, F.C., Güzel, B., 2017. Water entry of cylinders and spheres under hydrophobic effects; Case for advancing deadrise angles. Ocean Engineering 129, 240–252. https://doi.org/10.1016/j.oceaneng.2016.11.021

Kumar, S., Tiwari, R., Husein, M., Kumar, N., Yadav, U., 2020. Enhancing the performance of HPAM polymer flooding using nano CuO/nanoclay blend. Processes 8. https://doi.org/10.3390/PR8080907

Kure, I.K., Jakobsen, H.A., La Forgia, N., Solsvik, J., 2021. Experimental investigation of single bubbles rising in stagnant liquid: Statistical analysis and image processing. Physics of Fluids 33. https://doi.org/10.1063/5.0061581

Lai, C.C.K., Socolofsky, S.A., 2019a. The turbulent kinetic energy budget in a bubble plume. J Fluid Mech 865, 993–1041. https://doi.org/10.1017/jfm.2019.66

Lai, C.C.K., Socolofsky, S.A., 2019b. The turbulent kinetic energy budget in a bubble plume. J Fluid Mech 865, 993–1041. https://doi.org/10.1017/jfm.2019.66

Laupsien, D., Cockx, A., Line, A., 2017. Bubble Plume Oscillations in Viscous Fluids. Chem Eng Technol 40, 1484–1493. https://doi.org/10.1002/ceat.201600690

Laupsien, D., Le Men, C., Cockx, A., Liné, A., 2019. Image processing for bubble morphology characteristics in diluted bubble swarms. Physics of Fluids 31. https://doi.org/10.1063/1.5088945

Laupsien, D., Men, C. Le, Cockx, A., Liné, A., 2022. Effects of liquid viscosity and bubble size distribution on bubble plume hydrodynamics. Chemical Engineering Research and Design 180, 451–469. https://doi.org/10.1016/j.cherd.2021.09.025

Laupsien, D., Men, C. Le, Cockx, A., Line, A., 2021. Labelled Object Velocimetry: Simultaneous Measurements of Bubble Size and Velocity. Chem Eng Sci 230. https://doi.org/10.1016/j.ces.2020.116180

Lee, C., Su, Z., Zhong, H., Chen, S., Zhou, M., Wu, J., 2013. Experimental investigation of freely falling thin disks. Part 2. Transition of three-dimensional motion from zigzag to spiral. J Fluid Mech 732, 77–104. https://doi.org/10.1017/jfm.2013.390

Lee, M., 2000. Water-Entry Induced Cavity Pressure, KSME International Journal.

Lee, S.J.Y., An, H., Wang, P.C., Hang, J.G., Yu, S.C.M., 2021. Effects of liquid viscosity on bubble formation characteristics in a typical membrane bioreactor. International Communications in Heat and Mass Transfer 120. https://doi.org/10.1016/j.icheatmasstransfer.2020.105000

Li, G., Wang, B., Wu, H., DiMarco, S.F., 2020. Impact of bubble size on the integral characteristics of bubble plumes in quiescent and unstratified water. International Journal of Multiphase Flow 125. https://doi.org/10.1016/j.ijmultiphaseflow.2020.103230

Li, W., Wang, C., Wei, Y., Xia, S., Ding, Y., 2024. Experimental study on vertical water entry of the projectile with canard-wing. Physics of Fluids 36. https://doi.org/10.1063/5.0199543

Li, Z., Hu, H., Wang, C., Xie, Z., Chen, X., Yuan, Z., Du, P., 2024. Hydrodynamics and stability of oblique water entry in waves. Ocean Engineering 292. https://doi.org/10.1016/j.oceaneng.2023.116506

Lima, D.D., Lima Neto, I.E., 2018. Effect of Nozzle Design on Bubbly Jet Entrainment and Oxygen Transfer Efficiency. Journal of Hydraulic Engineering 144. https://doi.org/10.1061/(asce)hy.1943-7900.0001493

Lima Neto, I.E., Zhu, D.Z., Asce, M., Rajaratnam, N., Asce, F., n.d. Air Injection in Water with Different Nozzles. https://doi.org/10.1061/ASCE0733-93722008134:4283

Liu, H., Zhou, B., Yu, J., Liu, K., Han, X., Zhang, G., 2023. Experimental investigation on the multiphase flow characteristics of oblique water entry of the hollow cylinders. Ocean Engineering 272. https://doi.org/10.1016/j.oceaneng.2023.113902

Liu, H., Zhou, Bo, Han, X., Zhang, T., Zhou, Beike, Gho, W.M., 2020. Numerical simulation of water entry of an inclined cylinder. Ocean Engineering 215. https://doi.org/10.1016/j.oceaneng.2020.107908

Liu, L., Yan, H., Zhao, G., 2015. Experimental studies on the shape and motion of air bubbles in viscous liquids. Exp Therm Fluid Sci 62, 109–121. https://doi.org/10.1016/j.expthermflusci.2014.11.018

Liu, Z., Shi, Y., Wu, K., Zhao, H., Pan, G., 2023. Experimental study on load characteristics of vehicle during high-speed water entry. Ocean Engineering 288. https://doi.org/10.1016/j.oceaneng.2023.116052

Lu, G., Zhao, J., Li, S., Chen, Y., Li, C., Wang, Y., Li, D., 2021. Incorporation of Partially Hydrolyzed Polyacrylamide With Zwitterionic Units and Poly(Ethylene Glycol) Units Toward Enhanced Tolerances to High Salinity and High Temperature. Front Mater 8. https://doi.org/10.3389/fmats.2021.788746

Lu, J.X., Wang, C., Wei, Y.J., Sun, T.Z., Liu, F., Xu, H., 2022. Experimental and theoretical investigation of the cavity dynamics of underwater launched projectiles. Ocean Engineering 254. https://doi.org/10.1016/j.oceaneng.2022.111291

Lu, L., Cheng, Y., Chen, K., Yu, Z., Yang, Z., 2024. Experimental investigation on the water-entry characteristics of the structure passing through the broken ice field. Ocean Engineering 313. https://doi.org/10.1016/j.oceaneng.2024.119348

Lynn, N.D., Sourav, A.I., Santoso, A.J., 2021. Implementation of Real-Time Edge Detection Using Canny and Sobel Algorithms. IOP Conf Ser Mater Sci Eng 1096, 012079. https://doi.org/10.1088/1757-899x/1096/1/012079

Lyu, X., Wang, X., Yun, H., Chen, Z., 2022. On water-entry modes of the latter sphere in tandem configuration with two spheres. J Fluids Struct 112. https://doi.org/10.1016/j.jfluidstructs.2022.103601

Lyu, X., Yun, H., Wei, Z., 2021a. Experimental Study of a Sphere Bouncing on the Water. Journal of Marine Science and Application 20, 714–722. https://doi.org/10.1007/s11804-021-00236-9

Lyu, X., Yun, H., Wei, Z., 2021b. Influence of time interval on the water entry of two spheres in tandem configuration. Exp Fluids 62. https://doi.org/10.1007/s00348-021-03300-w

Mansoor, M.M., Marston, J.O., Vakarelski, I.U., Thoroddsen, S.T., 2014a. Water entry without surface seal: Extended cavity formation. J Fluid Mech 743, 295–326. https://doi.org/10.1017/jfm.2014.35

Mansoor, M.M., Marston, J.O., Vakarelski, I.U., Thoroddsen, S.T., 2014b. Water entry without surface seal: Extended cavity formation. J Fluid Mech 743, 295–326. https://doi.org/10.1017/jfm.2014.35

McKinley, G.H., 2002. Steady and Transient Motion of Spherical Particles. Transport processes in bubbles, drops and particles 338.

Milgram, J.H., 1983. Mean flow in round bubble plumes. J Fluid Mech 133, 345–376. https://doi.org/DOI: 10.1017/S0022112083001950

Mishra, S., Mukul, A., Sen, G., Jha, U., 2011. Microwave assisted synthesis of polyacrylamide grafted starch (St-g-PAM) and its applicability as flocculant for water treatment. Int J Biol Macromol 48, 106–111. https://doi.org/10.1016/j.ijbiomac.2010.10.004

Mitsch, W.J., Gosselink, J.G., 2015. Wetlands. John wiley & sons.

Mohammadkhani, M., Kozinski, J., Pakzad, L., 2025. Atomization characteristics of soft mist inhaler (SMI) devices: aerosolized particle delivery through the respiratory tract—an innovative numerical and experimental study. J Aerosol Sci 188. https://doi.org/10.1016/j.jaerosci.2025.106593

Nigen, S., Walters, K., 2001. On the two-dimensional splashing experiment for Newtonian and slightly elastic liquids, J. Non-Newtonian Fluid Mech.

Niida, Y., Watanabe, Y., 2018. Oxygen transfer from bubble-plumes. Physics of Fluids 30. https://doi.org/10.1063/1.5040819

Olivieri, G., Grillo, S., D'errico, G., Marzocchella, A., Ružička, M., Salatino, P., 2013. Preliminary Assessments of Combined Effects of Surface Tension and Viscosity on Bubble Column Hydrodynamics.

Panciroli, R., Shams, A., Porfiri, M., 2015. Experiments on the water entry of curved wedges: High speed imaging and particle image velocimetry. Ocean Engineering 94, 213–222. https://doi.org/10.1016/j.oceaneng.2014.12.004

Pei, Y., Zhao, L., Du, G., Li, N., Xu, K., Yang, H., 2016a. Investigation of the degradation and stability of acrylamide-based polymers in acid solution: Functional monomer modified polyacrylamide. Petroleum 2, 399–407. https://doi.org/10.1016/j.petlm.2016.08.006

Pei, Y., Zhao, L., Du, G., Li, N., Xu, K., Yang, H., 2016b. Investigation of the degradation and stability of acrylamide-based polymers in acid solution: Functional monomer modified polyacrylamide. Petroleum 2, 399–407. https://doi.org/10.1016/j.petlm.2016.08.006

Ping, Y., Wang, J., Xie, H., Liu, F., Liu, X., 2025. Experimental and CFD analysis: Effects of bottom appendages on the slamming characteristics of rigid hull structures during water entry. Ocean Engineering 319. https://doi.org/10.1016/j.oceaneng.2024.120195

Poojitha Yapa, B.D., Zheng, L., Nakata, K., 1999. JOURNAL OF HYDRAULIC ENGINEERING / MAY 1999 / 481 FIG. 1. Ixtoc I Well Blowout in 1979 (Photo Courtesy of Jerry Galt, NOAA).

Prasad, B.S., Sastry, G.R.K., Das, H.N., 2024. A comprehensive review study on multiphase analysis of water entry bodies. Ocean Engineering. https://doi.org/10.1016/j.oceaneng.2023.116579

Rensen, J., Roig, V., 2001. Experimental study of the unsteady structure of a confined bubble plume.

Reseghetti, F., 2014. Experimental Verification of Drag Forces on Spherical Objects Entering Water. Journal of Marine Biology & Oceanography 03. https://doi.org/10.4172/2324-8661.1000126

Riboux, G., Risso, F., Legendre, D., 2010. Experimental characterization of the agitation generated by bubbles rising at high Reynolds number. J Fluid Mech 643, 509–539. https://doi.org/10.1017/S0022112009992084

Roig, V., De Tournemine, A.L., 2007. Measurement of interstitial velocity of homogeneous bubbly flows at low to moderate void fraction. J Fluid Mech 572, 87–110. https://doi.org/10.1017/S0022112006003600

Ruzicka, M.C., Drahoš, J., Mena, P.C., Teixeira, J.A., 2003. Effect of viscosity on homogeneous-heterogeneous flow regime transition in bubble columns. Chemical Engineering Journal 96, 15–22. https://doi.org/10.1016/j.cej.2003.08.009

Ruzicka, M.C., Vecer, M.M., Orvalho, S., Drahoš, J., 2008. Effect of surfactant on homogeneous regime stability in bubble column. Chem Eng Sci 63, 951–967. https://doi.org/10.1016/j.ces.2007.10.015

Sarpkaya, T., Isaacson, M., Wehausen, J. V, 1982. Mechanics of Wave Forces on Offshore Structures. J Appl Mech 49, 466–467. https://doi.org/10.1115/1.3162189

Sato, R., Hayashi, K., Tomiyama, A., 2015. Effects of liquid viscosity on flows inside and outside a bubble diffuser pipe. Exp Therm Fluid Sci 66, 197–205. https://doi.org/10.1016/j.expthermflusci.2015.03.025

Seddon, C.M., Moatamedi, M., 2006. Review of water entry with applications to aerospace structures. Int J Impact Eng 32, 1045–1067. https://doi.org/10.1016/j.ijimpeng.2004.09.002

Seol, D.-G., Duncan, ;, Bryant, B., Socolofsky, S.A., Asce, M., 2009. Measurement of Behavioral Properties of Entrained Ambient Water in a Stratified Bubble Plume. https://doi.org/10.1061/ASCEHY.1943-7900.0000109

Seol, D.-G., Tirtharaj Bhaumik, ;, Bergmann, ; Christian, Socolofsky, S.A., Asce, M., 2007. Particle Image Velocimetry Measurements of the Mean Flow Characteristics in a Bubble Plume. https://doi.org/10.1061/ASCE0733-93992007133:6665

Sharker, S.I., Holekamp, S., Mansoor, M.M., Fish, F.E., Truscott, T.T., 2019. Water entry impact dynamics of diving birds. Bioinspir Biomim 14. https://doi.org/10.1088/1748-3190/ab38cc

Shi, F., Liu, Z., Li, J., Gao, H., Qin, S., Guo, J., 2022. Alterations in microbial community during the remediation of a black-odorous stream by acclimated composite microorganisms. J Environ Sci (China) 118, 181–193. https://doi.org/10.1016/j.jes.2021.12.034

Shi, Y., Wang, G., Pan, G., 2019a. Experimental study on cavity dynamics of projectile water entry with different physical parameters. Physics of Fluids 31. https://doi.org/10.1063/1.5096588

Shi, Y., Wang, G., Pan, G., 2019b. Experimental study on cavity dynamics of projectile water entry with different physical parameters. Physics of Fluids 31. https://doi.org/10.1063/1.5096588

Shihab Ahmed, A., 2018. COMPARATIVE STUDY AMONG SOBEL, PREWITT AND CANNY EDGE DETECTION OPERATORS USED IN IMAGE PROCESSING. J Theor Appl Inf Technol 15, 19.

Shokri, H., Akbarzadeh, P., 2022. Experimental investigation of water entry of dimpled spheres. Ocean Engineering 250. https://doi.org/10.1016/j.oceaneng.2022.110992

Simiano, M., Zboray, R., de Cachard, F., Lakehal, D., Yadigaroglu, G., 2006. Comprehensive experimental investigation of the hydrodynamics of large-scale, 3D, oscillating bubble plumes. International Journal of Multiphase Flow 32, 1160–1181. https://doi.org/10.1016/j.ijmultiphaseflow.2006.05.014

Socolofsky, S.A., Asce, M., Tirtharaj Bhaumik, ;, Seol, D.-G., 2008. Double-Plume Integral Models for Near-Field Mixing in Multiphase Plumes. https://doi.org/10.1061/ASCE0733-94292008134:6772

Song, Z.J., Duan, W.Y., Xu, G.D., Zhao, B.B., 2020a. Experimental and numerical study of the water entry of projectiles at high oblique entry speed. Ocean Engineering 211. https://doi.org/10.1016/j.oceaneng.2020.107574

Song, Z.J., Duan, W.Y., Xu, G.D., Zhao, B.B., 2020b. Experimental and numerical study of the water entry of projectiles at high oblique entry speed. Ocean Engineering 211. https://doi.org/10.1016/j.oceaneng.2020.107574

Sooraj, P., Khan, M.H., Sharma, A., Agrawal, A., 2019. Wake analysis and regimes for flow around three side-by-side cylinders. Exp Therm Fluid Sci 104, 76–88. https://doi.org/10.1016/j.expthermflusci.2019.02.009

Sun, T., Wang, H., Zong, Z., Zhang, G., Wang, A., Xu, C., 2019a. Splash formation and cavity dynamics of sphere entry through a viscous liquid resting on the water. AIP Adv 9. https://doi.org/10.1063/1.5109252

Sun, T., Wang, H., Zou, L., Zong, Z., Li, H., 2019b. Experimental study on the cavity dynamics of oblique impact of sphere on a viscous liquid floating on water. Ocean Engineering 194. https://doi.org/10.1016/j.oceaneng.2019.106597

Tabuteau, H., Sikorski, D., De Vet, S.J., De Bruyn, J.R., 2011. Impact of spherical projectiles into a viscoplastic fluid. Phys Rev E Stat Nonlin Soft Matter Phys 84. https://doi.org/10.1103/PhysRevE.84.031403

Tavakoli, S., Khojasteh, D., Haghani, M., Hirdaris, S., 2023a. A review on the progress and research directions of ocean engineering. Ocean Engineering 272. https://doi.org/10.1016/j.oceaneng.2023.113617

Tavakoli, S., Mikkola, T., Hirdaris, S., 2023b. A fluid-solid momentum exchange method for the prediction of hydroelastic responses of flexible water entry problems. J Fluid Mech 965. https://doi.org/10.1017/jfm.2023.386

Tavakoli, S., Mikkola, T., Hirdaris, S., 2023c. A fluid-solid momentum exchange method for the prediction of hydroelastic responses of flexible water entry problems. J Fluid Mech 965. https://doi.org/10.1017/jfm.2023.386

Tripathi, M.K., Sahu, K.C., Govindarajan, R., 2015. Dynamics of an initially spherical bubble rising in quiescent liquid. Nat Commun 6. https://doi.org/10.1038/ncomms7268

Turton, R., Levenspiel, O., 1986. A short note on the drag correlation for spheres. Powder Technol 47, 83–86. https://doi.org/https://doi.org/10.1016/0032-5910(86)80012-2

Tveitnes, T., Fairlie-Clarke, A.C., Varyani, K., 2008. An experimental investigation into the constant velocity water entry of wedge-shaped sections. Ocean Engineering 35, 1463–1478. https://doi.org/10.1016/j.oceaneng.2008.06.012

Vayig, Y., Rosenberg, Z., 2025. On the penetration of rigid projectiles in water. Int J Impact Eng 197. https://doi.org/10.1016/j.ijimpeng.2024.105185

Vincent, L., Shambaugh, W.S., Kanso, E., 2016. Holes stabilize freely falling coins. J Fluid Mech 801, 250–259. https://doi.org/10.1017/jfm.2016.432

Vincent, L., Xiao, T., Yohann, D., Jung, S., Kanso, E., 2018. Dynamics of water entry. J Fluid Mech 846, 508–535. https://doi.org/10.1017/jfm.2018.273

Wang, B., Lai, C.C.K., Socolofsky, S.A., 2019. Mean velocity, spreading and entrainment characteristics of weak bubble plumes in unstratified and stationary water. J Fluid Mech 874, 102–130. https://doi.org/10.1017/jfm.2019.461

Wang, B., Socolofsky, S.A., 2019. Characteristics of mean flow and turbulence in bubble-in-chain induced flows. Phys Rev Fluids 4. https://doi.org/10.1103/PhysRevFluids.4.054302

Wang, B., Socolofsky, S.A., 2015. A deep-sea, high-speed, stereoscopic imaging system for in situ measurement of natural seep bubble and droplet characteristics. Deep Sea Res 1 Oceanogr Res Pap 104, 134–148. https://doi.org/10.1016/j.dsr.2015.08.001

Wang, C., Huang, Q., Lu, L., Pan, G., Gao, S., 2024. Numerical investigation of water entry characteristics of a projectile in the wave environment. Ocean Engineering 294. https://doi.org/10.1016/j.oceaneng.2024.116821

Wang, G., Guo, L., Chang, X., Gao, H., Wang, C., He, Yuan, Du, J., Chen, P., Pan, J., He, Yong, 2024. Analysis of hydrodynamic ram and cavity evolution characteristics during high-velocity penetration of Zr55Cu30Al10Ni5 fragments into water-filled containers. Int J Impact Eng 187. https://doi.org/10.1016/j.ijimpeng.2024.104900

Wang, M., Yurikusa, T., Sakai, Y., Iwano, K., Ito, Y., Zhou, Y., Hattori, Y., 2022. Interscale transfer of turbulent energy in grid-generated turbulence with low Reynolds numbers. Int J Heat Fluid Flow 97. https://doi.org/10.1016/j.ijheatfluidflow.2022.109031

Wang, P.R., Shi, D.Y., Cui, X.W., Ma, C.L., Su, B., Li, G.L., 2023. Study on bubble pulsation process of underwater explosion between parallel plates with various distances. Ocean Engineering 278. https://doi.org/10.1016/j.oceaneng.2023.114512

Wang, X., Lyu, X., 2021. Experimental study on vertical water entry of twin spheres side-by-side. Ocean Engineering 221. https://doi.org/10.1016/j.oceaneng.2020.108508

Wang, X., Qi, C., Liu, C., Sun, R., Lyu, X., 2024a. Experimental study on the cavity dynamics of a sphere entering flowing water. Physics of Fluids 36. https://doi.org/10.1063/5.0191484

Wang, X., Qi, C., Liu, C., Sun, R., Lyu, X., 2024b. Experimental study on the cavity dynamics of a sphere entering flowing water. Physics of Fluids 36. https://doi.org/10.1063/5.0191484

Wang, X., Wu, G., Zheng, X., Du, X., Zhang, Y., 2022. Theoretical investigation and experimental support for the cavitation bubble dynamics near a spherical particle based on Weiss theorem and Kelvin impulse. Ultrason Sonochem 89. https://doi.org/10.1016/j.ultsonch.2022.106130

Wang, Y., Wang, Z., Du, Y., Wang, J., Wang, Yiwei, Huang, C., 2022. The mechanism of surface-seal splash during water entry. Physics of Fluids 34. https://doi.org/10.1063/5.0085761

Willmarth, W.W., Hawk, N.E., Harvey, R.L., 1964. Steady and unsteady motions and wakes of freely falling disks. Physics of Fluids 7, 197–208. https://doi.org/10.1063/1.1711133

Winterwerp, J.C., van Kesteren, W.G.M., 2004. Introduction to the Physics of Cohesive Sediment Dynamics in the Marine Environment, Developments in Sedimentology. Elsevier Science.

Wong, S.S., Teng, T.T., Ahmad, A.L., Zuhairi, A., Najafpour, G., 2006. Treatment of pulp and paper mill wastewater by polyacrylamide (PAM) in polymer induced flocculation. J Hazard Mater 135, 378–388. https://doi.org/10.1016/j.jhazmat.2005.11.076

Worthington, A.M., 1908. A study of splashes. Longmans, Green, and Company.

Wu, H., Wang, B., DiMarco, S.F., Tan, L., 2021. Impact of bubble size on turbulent statistics in bubble plumes in unstratified quiescent water. International Journal of Multiphase Flow 141. https://doi.org/10.1016/j.ijmultiphaseflow.2021.103692

Xia, S., Wei, Y., Wang, C., Cao, W., Hu, X., 2023. Numerical investigation of the high-speed vertical water entry of a cylindrical shell. Physics of Fluids 35. https://doi.org/10.1063/5.0142393

Xu, T., Li, J., Li, Z., Liao, S., 2021. Accurate predictions of chaotic motion of a free fall disk. Physics of Fluids 33. https://doi.org/10.1063/5.0039688

Xu, X., Zhang, J., Liu, F., Wang, X., Wei, W., Liu, Z., 2017. Rising behavior of single bubble in infinite stagnant non-Newtonian liquids. International Journal of Multiphase Flow 95, 84–90. https://doi.org/10.1016/j.ijmultiphaseflow.2017.05.009

Yan, W.L., Wang, Y.L., Chen, Y.J., 2013. Effect of conditioning by PAM polymers with different charges on the structural and characteristic evolutions of water treatment residuals. Water Res 47, 6445–6456. https://doi.org/10.1016/j.watres.2013.08.016

Yang, C., Wang, X., Li, H., Lyu, X., Chen, Z., 2023. Numerical study on the fluid dynamics for tandem water entries of two cylinders. Ocean Engineering 286. https://doi.org/10.1016/j.oceaneng.2023.115633

Yang, L., Sun, T. zhi, Wei, Y. jie, Wang, C., Xia, W. xue, Wang, Z. lu, 2021a. Hydroelastic analysis of water entry of deformable spheres. Journal of Hydrodynamics 33, 821–832. https://doi.org/10.1007/s42241-021-0065-1

Yang, L., Wei, Y., Li, J., Wang, C., Xia, W., 2021b. Experimental study on splash behaviors and cavity shape of elastic spheres during water entry. Applied Ocean Research 113. https://doi.org/10.1016/j.apor.2021.102754

Yang, L., Wei, Y., Wang, C., Xia, W., Li, J., Chen, C., 2020. Numerical study on the deformation behaviors of elastic spheres during water entry. J Fluids Struct 99. https://doi.org/10.1016/j.jfluidstructs.2020.103167

Yin, H., Yang, P., Kong, M., 2019. Effects of nitrate dosing on the migration of reduced sulfur in black odorous river sediment and the influencing factors. Chemical Engineering Journal 371, 516–523. https://doi.org/10.1016/j.cej.2019.04.095

Yu, J., Liu, J. hu, Wang, H. kun, Wang, J., Zhang, L. ping, Liu, G. zhen, 2021. Numerical simulation of underwater explosion cavitation characteristics based on phase transition model in compressible multicomponent fluids. Ocean Engineering 240. https://doi.org/10.1016/j.oceaneng.2021.109934

Yu, J., Liu, J.H., Wang, H.K., Wang, J., Zhou, Z.T., Mao, H. Bin, 2022. Application of two-phase transition model in underwater explosion cavitation based on compressible multiphase flows. AIP Adv 12. https://doi.org/10.1063/5.0077517

Yuan, Q., Hong, Y., Zhao, Z., Gong, Z., 2022. Water-air two-phase flow during entry of a sphere into water using particle image velocimetry and smoothed particle hydrodynamics. Physics of Fluids 34. https://doi.org/10.1063/5.0084790

Yun, H., Lyu, X., Wei, Z., 2020. Experimental study on oblique water entry of two tandem spheres with collision effect. J Vis (Tokyo) 23, 49–59. https://doi.org/10.1007/s12650-019-00602-4

Zahradnmh, J., Kuncovah, G., Fialovah, M., 1999. The e!ect of surface active additives on bubble coalescence and gas holdup in viscous aerated batches, Chemical Engineering Science.

Zhang, A.M., Li, S.M., Cui, P., Li, S., Liu, Y.L., 2023. A unified theory for bubble dynamics. Physics of Fluids 35. https://doi.org/10.1063/5.0145415

Zhang, A.-M., Li, S.-M., Xu, R.-Z., Pei, S.-C., Li, S., Liu, Y.-L., 2024. A theoretical model for compressible bubble dynamics considering phase transition and migration. https://doi.org/10.1017/jfm.2024.954

Zhang, D., Yang, H., Lan, S., Wang, C., Li, X., Xing, Y., Yue, H., Li, Q., Wang, L., Xie, Y., 2022. Evolution of urban black and odorous water: The characteristics of microbial community and driving-factors. J Environ Sci (China) 112, 94–105. https://doi.org/10.1016/j.jes.2021.05.012

Zhang, L., Yang, C., Mao, Z.S., 2008. Unsteady motion of a single bubble in highly viscous liquid and empirical correlation of drag coefficient. Chem Eng Sci 63, 2099–2106. https://doi.org/10.1016/j.ces.2008.01.010

Zhang, Q., Zong, Z., Li, H.T., Sun, T.Z., 2022. Experimental study of the impact of splash closure on the cavity evolution behind a sphere entering water. Physics of Fluids 34. https://doi.org/10.1063/5.0088333

Zhang, Q., Zong, Z., Sun, T.Z., Yu, Y.Q., Li, H.T., 2021a. Characteristics of cavity collapse behind a high-speed projectile entering the water. Physics of Fluids 33. https://doi.org/10.1063/5.0053409

Zhang, Q., Zong, Z., Sun, T.Z., Yu, Y.Q., Li, H.T., 2021b. Characteristics of cavity collapse behind a high-speed projectile entering the water. Physics of Fluids 33. https://doi.org/10.1063/5.0053409

Zhao, C., Wang, Q., Lu, H., Liu, H., 2023. Vertical water entry of a hydrophobic sphere into waves: Numerical computations and experiments. Physics of Fluids 35. https://doi.org/10.1063/5.0160041

Zhao, Z.X., Hong, Y., Gong, Z.X., Liu, H., 2023. Numerical analysis of cavity deformation of oblique water entry using a multi-resolution two-phase SPH method. Ocean Engineering 269. https://doi.org/10.1016/j.oceaneng.2022.113456

Zhong, H., Lee, C., Su, Z., Chen, S., Zhou, M., Wu, J., 2013. Experimental investigation of freely falling thin disks. Part 1. the flow structures and Reynolds number effects on the zigzag motion. J Fluid Mech 716, 228–250. https://doi.org/10.1017/jfm.2012.543

Zhou, X., Yuan, S., Zhang, G., 2021. Eccentric disks falling in water. Physics of Fluids 33. https://doi.org/10.1063/5.0045163

Ziegenhein, T., Lucas, D., 2017. Observations on bubble shapes in bubble columns under different flow conditions. Exp Therm Fluid Sci 85, 248–256. https://doi.org/10.1016/j.expthermflusci.2017.03.009